AERODYNAMIC PERFORMANCE AND HEAT TRANSFER CHARACTERISTICS OF HIGH PRESSURE RATIO TRANSONIC TURBINES

by

HAROLD OLUSEGUN DEMUREN

M.S. in Aeronautics, Kiev Institute of Civil Aviation Engineers

February 1972

SUBMITTED IN PARTIAL FULFILLMENT
OF THE REQUIREMENTS FOR THE
DEGREE OF DOCTOR OF SCIENCE
IN AERONAUTICS

at the

MASSACHUSETTS INSTITUTE OF TECHNOLOGY

February 1976

Signature of Author ______________________________

Certified by ______________________________
Thesis Supervisor

Certified by ______________________________
Thesis Supervisor

Certified by ______________________________
Thesis Supervisor

Accepted by ______________________________
Chairman, Departmental Graduate Committee

AERODYNAMIC PERFORMANCE AND HEAT TRANSFER CHARACTERISTICS OF HIGH PRESSURE RATIO TRANSONIC TURBINES

by

HAROLD OLUSEGUN DEMUREN

Submitted to the Department of Aeronautics and Astronautics on December 5, 1975, in partial fulfillment of the requirements for the degree of Doctor of Science in Aeronautics.

ABSTRACT

Reduction of engine weight and specific fuel consumption are driving gas turbine engine inlet temperature towards higher values and demanding an increase in turbine stage loading. One major avenue for large scale improvement of turbine stage loading is through increased working-fluid velocity. This means going to high pressure ratio transonic and supersonic turbines.

A family of blades suitable for high temperature high pressure ratio transonic turbine has been designed, built and tested. They included, a reference wholly convergent blade profile with straight suction back and thick trailing edge; a profile with convergent-divergent cross-section, a convergent profile with expansion on the suction side just like a plug nozzle and finally another wholly convergent profile with straight back but thin trailing edge.

Tests to determine the aerodynamic performance of these bladings have shown that each profile has a superior performance in different Mach number range and diverse potentialities when cooling and structural problems are carefully examined along with optimization of efficiency. Up to Mach number 1.2, the profile with straight back and thin trailing edge has the best performance while for higher Mach number $M > 1.3$, the convergent-divergent profile came out with the minimum profile loss.

Heat transfer characteristics of the bladings have also been obtained. Heat transfer distribution around the blades indicates a high level of heat transfer, evidence of early transition from laminar to turbulent flow. A high level of heat transfer caused by the thinning of the boundary layer was recorded around the trailing edge especially on the pressure side and amounted to about 75% or more of the average heat transfer to the blade at stagnation leading edge zone.

Comparison between the experimental data and an available NASA theoretical prediction did show a good agreement for most of the surface. A comparison of the average heat transfer (Stanton number) to all the blades has shown that the convergent-divergent blade has a higher Stanton number while the heat transfer to the other blades was about the same.

A quick evaluation of the potential worth of transonic turbines is made. Analysis showed that by replacing two subsonic stages with a single highly loaded transonic stage to produce the same work output, the amount of heat that has to be removed from the turbine stage has decreased by as much as 21%. Similar analysis showed savings of about 20% in coolant mass fow rate when two subsonic stages are replaced with a single transonic stage. And also while analysing the effect of cooling on stage efficiency, it was found that, efficiency degradation in the single high pressure ratio transonic stage is less than that of the two-stage subsonic turbines.

Thesis Supervisor: Jean F. Louis
Title: Professor of Aeronautics and Astronautics

Thesis Supervisor: Edward S. Taylor
Title: Professor of Flight Propulsion

Thesis Supervisor: David G. Wilson
Title: Professor of Mechanical Engineering

ACKNOWLEDGEMENTS

First giving honor and praises to God for truly it is good to trust in God.

I owe a special debt of gratitude to my thesis committee Professor Jean F. Louis, Chairman; Professor Edward S. Taylor and Professor David G. Wilson. Their words of wisdom have kept me from going astray, and their constant words of encouragements especially at the dark hours of the experiments have always renewed my strength.

To the entire members of the Gas Turbine Laboratory, faculty, staff and students alike I would like to express my appreciation for their help and cooperation all the way round.

I am in particular very grateful to Alan Epstein, Ara Demirjian, Bill Patrick, Milton Ortiz, James Fabunmi, Segun Adebayo , Rosemary, T. Christensen, Roy Andrews and Ray Johnson.

I will like to extend my sincere appreciation to the entire Turbomachinery Group of VKI and in particular Professor Chauvin and Professor Claus Sieverding for their cooperation throughout the joint program; and for their great hospitality during my stay at V.K.l.

I will also like to thank Fola Shonukan who set aside several nights to type and retype the entire manuscript. My love to Osa and our baby-boy, Olusegun.

Lastly this work was funded by the Office of Naval Research under contract No. N00014-67-A-0204-0079 and a travel grant was provided by NATO Research Grant No. 691 to whom I am duly grateful.

TABLE OF CONTENTS

5. Heat Transfer To Transonic Turbine Blade Surface

6. Prospects for Transonic Turbines

7. Conclusion and Recommendation

Appendices

Figures

<u>References</u>

SYMBOLS

A	Cross-sectional area
a	acoustic velocity = $\sqrt{\gamma R T}$
b	Blade axial chord
C	Absolute Velocity
c	Blade chord
C_p	Specific heat at constant pressure
f	Blade passing frequency $f = Z \cdot n$
g	Blade spacing
h	heat transfer coefficient
k	Thermal conductivity
Kf	Reduced Frequency
L	Characteristic length
M	Mach number
$\dot{m}$	Mass flow rate
N	R.p.m.
Nu	Nusselt number
P	Pressure
Pr	Prandlt Number
R	Gas constant
π	Pressure ratio
Re	Reynolds number
S	Surface Area
s	Blade pitch
St	Stanton number

S_f	Temperature Scaling Factor
T	Temperature
Tu	Absolute Fraction of Turbulence Level
Tu'	Turbulence Level expressed in percentage form
te	Trailing Edge Thickness
t	Time
U	Blade Speed
V	Flow Velocity
W	Relative Velocity
ω	Losses = $1 - \eta = \omega$
x	Coordinate direction (axial)
y	Coordinate direction (tangential)
z	Number of blades
ϵ	Internal cooling effectiveness
α	Blade angle in absolute coordinates measured in relation to the axial direction
β	Blade angle in relative coordinates measured in relation to the axial directions.
γ	Ratio of specific heats(Cp/Cv)
η	Efficiency
θ	Compromise angle
μ	Dynamic viscosity
ν	Kinematic viscosity
ρ	Density
η_{iso}	Isothermal film cooling effectiveness

Φ	Flow coefficient
Ψ	Load coefficient

Subscripts

$(\ )_x$	axial component
$(\ )_\theta$	tangential component
$(\ )_{op}$	Operating (actual condition)
$(\ )_{ex}$	Experimental condition
$(\ )_o$	Stagnation parameter
$(\ )_w$	Parameters at the wall (blade surface)
$(\ )_g$	Parameters (T) at the gauge surface
$(\ )_1$	Static parameters at Nozzle inlet
$(\ )_2$	Static parameters at Rotor inlet
$(\ )_3$	Static parameters at Rotor exit
$(\ )_{01}$	Stagnation parameters at Nozzle inlet
$(\ )_{02}$	Stagnation parameters in Rotor inlet
$(\ )_{03}$	Stagnation parameters at Rotor exit
$(\ )_c$	Parameters (Nu, Re) based on chord
$(\ )_d$	Parameters (Nu,re) based on the leading edge diameter
$(\ )_{is}$	Isentropic condition

CHAPTER 1

INTRODUCTION

Reduction of engine weight and specific fuel consumption have been the over-riding goal of most of the present advanced gas turbine studies and will continue to be in future.

In certain turbodrive power-generation systems, it is desired to obtain a high specific work output with the result that a large pressure ratio across the turbine is required. This can be accomplished with either many-stage subsonic turbines with supersonic or transonic turbines having fewer stages.

High-pressure-ratio supersonic turbines with one or two stages are now being employed in special applications where the use of simple, low-weight systems, with increased stage specific work output, can offset the lower efficiency realised from them.

In general the desire to reduce turbo-engine weight and complexity, along with recent development of fan engines with very large by-pass ratios, has generated a great need to increase turbine stage-loading. Several methods are being studied in an effort to increase work output by increased turning. Although the results of these programs are encouraging, there is an obvious limit of 180° turning and a performance limit. Since increasing blade loading by increasing blade speed is also limited by structural integrity, there remains one main avenue for large-scale improvement of turbine stage loading and that is through increased working-fluid velocity. This means going to transonic and supersonic turbines.

Another reason for developing the high-pressure-ratio turbine is the necessity for future turbo-engines to feature a very high turbine-inlet temperature and concomitantly a high compression ratio. The transonic and supersonic turbines not only offer the real opportunity to reduce the number of stages but also the amount of cooling work required, and consequently may achieve better specific fuel consumption and specific power.

In supersonic transport aircraft for instance the weight of power plants and fuel is about 60% of the gross-weight of the whole aircraft. Any improvement of the overall engine efficiency results in decreased engine size and weight or in reduced fuel consumption. Both possibilities lead directly to a higher pay load which is about 8% of the gross weight.

For several applications and in particular for the aeronautical industry, very high performance turbomachine are required with small weight and volume. Therefore a bigger and bigger enthalpy drop per stage must be obtained. Increasing the fluid velocity to supersonic levels introduces new problems peculiar to supersonic flows.

Technical information is available on the fluid-dynamic behavior of the supersonic impulse turbine long used in the first stage of steam turbines. Indeed, supersonic fluid velocities have been used in some industrial steam turbines (Curtis and DeLaval stages), in auxiliary power units, in turbo-pump drives, etc; but the efficiencies of these machines have been quite low. There have been only a few laboratory examinations of the supersonic turbine stage. References 1, 2 and 3 report NASA configurations while Reference 4 describes one at the British National Gas Turbine Establishment, but these also resulted in dissapointingly low efficiencies. However, Deych in References 5, 6 & 7 and Colclough in Reference 8 have reported low but promising levels of efficiency.

The poor efficiency of such machines comes from simple fluid-dynamic consideration - shocks at rotor inlet and exit, shock-boundary-layer interactions within the blade channel coupled with unfavourable pressure gradients on the blades, and strong mixing losses. This low level of component efficiency has severely limited the application of the supersonic turbine and makes it unattractive even for large-scale industrial application.

For the high pressure ratio turbine, with its significant advantages, to find widespread application the very low efficiency now being realised must be improved to at least a level comparable to the present subsonic turbine. This can be achieved by using transonic turbines.

And the aim of the present study is to gather necessary aerodynamic and heat-transfer data and develop the data-base for the design procedure of high-performance high-pressure-ratio transonic turbine stages.

In the pursuit of this goal the following tasks were undertaken:

--determination of high-performance transonic blade profiles for a turbine stage providing high work output;

--an experimental investigation of the aerodynamic performance and heat-transfer characteristics of these bladings; and

--an evaluation of the potential worth of transonic turbines.

CHAPTER 2

HIGH-PRESSURE-RATIO TURBINES

2.1 Review of Earlier Work

The military and space use of liquid-fueled rockets since the 1940s has increased interest in turbines of high pressure ratio, as previously used in, for example, the Curtis and the De Laval steam turbines. The purpose of such turbines is usually to achieve a high work output per stage, while an associated advantage of impulse turbines is the ability to use steam or gas of initially high temperature and pressure without obtaining either a large end thrust from the disc face or high temperature in the main structure of the turbine.

But until recently, there appears to have been very little published on the design of rotor blades for supersonic turbines. Kantrowitz[9] and Ferri[10] developed the theory for a supersonic rotor and diffusing stator combination for compressors while Stodola[11] and Shapiro[12] refer to blades for supersonic flow but give no design method. Liccini[13,14], however, used the method of characteristics to determine the flow field in a passage and successfully applied it to the design of a 90° turning passage, but the method suffers from drawbacks that blade design and optimization are difficult since the general shape of the blade cannot be predicted and there are no usable design criteria.

It is considered that the most promising method of designing supersonic blades is based on vortex flow. The original concept of a supersonic vortex flow field appears to be due to Busemann[15] and was verified by Oswatitsch[16], while Boxer et al[17] have applied the theory to the problem of converting a parallel supersonic flow into a potential vortex flow to produce a channel with a large turning angle.

The application of this theory to the design of the blades consisted essentially in converting the parallel supersonic flow from the turbine nozzles which was assumed to be uniform and free-flow ahead of the cascade into a potential vortex flow by means of transition sections. After this the major part of the flow was turned through the required angle by concentric circular streamlines and transition sections were used to convert the flow at the channel exit back to free-flow conditions. The blade channels were joined and the adjacent areas in between represent the blades. These were cusped at either end and it was necessary to create finite leading and trailing edges. (Figure 2.1 and 2.2)

Also around this time Stratford, B.S., and Sansome, G.E.,[19,20] investigated the performance of supersonic turbine blades using a semi-empirical method of blade design. Unacceptably high levels of loss were recorded. But then came the rather encouraging results of Colclough[8] and Deych[5,6,7, & 21] on detailed experimental results which gave the necessary optimism to further the research in this area.

Because of the significant importance and great potentials of supersonic turbines, research has continued, more heavily though, in the steam-turbine industry to improve the overall efficiency of these supersonic impulse stages which are used mostly in the first stages.

2.2 Present Status of Supersonic Turbine Blading

At present [22,23, &25] the most efficient blading being used in supersonic turbines is the supersonic impulse blading. The design method is based on a two-dimensional isentropic flow and consists of converting the uniform parallel flow at the blade inlet into a vortex flow field, turning the vortex flow and reconverting to a uniform parallel flow at the blade exit. Computer programs for the blade design with boundary-layer correction[24] are now available.

One major problem with this supersonic impulse blading is the necessity of maintaining relatively very sharp leading and trailing edges. Even though some blunting of the rotor-blade leading edge has been carried out by Colclough[8] and Deych[5,6,7 & 21] they have shown a drop in the already low efficiency level by as much as 10%, while the serious problem of structural integrity and cooling such blade shapes is still very severe.

These serious drawbacks have severely curtailed the application of supersonic turbines in advanced gas turbines. As of now supersonic turbines with one or two stages are usually employed in special applications where the use of simple, low-weight system can offset the low efficiency they offer. They incluse the first stages of steam turbines, stationary power-plant auxiliary units; and hydrogen-fueled open-cycle auxiliary space power systems.

For supersonic turbines to be attractive and to find wide spread application in all turbo-drive power-generation proper design methods must be available to obtain the highest practical efficiency, at least a level comparable to present subsonic turbines, and even higher, while eliminating the serious problems of structural integrity and cooling associated with present supersonic impulse bladings.

2.3 Transonic Turbine Stage

The transonic reaction stage is proposed as an alternative to the present supersonic impulse stage.

The reaction stage by allowing the static enthalpy drop (expansion) across the stage to be divided between the stator and rotor blades offers a flexible means of choosing cascade parameters such that rotor inlet velocity could be kept in the subsonic range. The flow is then accelerated in the wholly convergent rotor blade channel to choking condition and from the throat downwards undergoes a fast expansion to the required exit supersonic velocity.

The subsonic rotor inlet velocity removes the necessity of having a thin rotor-blade leading edges and this eliminates its associated problems, namely:-

- difficulties in cooling the very thin leading edge;
- structural ingegrity of the blade; and
- losses due to shock and shock-boundary-layer interaction at the rotor inlet.

The blade design is split into two parts; first a subsonic region where all the flow turning occurs, followed by purely supersonic section.

The subsonic part is designed jointly with V.K.I. using both the Deych[21] lemniscate curve and the modified NASA/Dunavant and Erwin method. The method of characteristics [26,27,28] as applied to a two-dimensional isentropic flow of a perfect gas is used in the design of the supersonic section. Since reduction of wetted-surface area and the minimization of hub and shroud boundary-layer build-up are of utmost importance, "minimum-length supersonic-section" blade designs are prescribed, with expansion carried out only on the blade suction side.

A high-pressure-ratio ($\pi = 4$), high-turbine-inlet-temperature (1800^{o}K), 50%-reaction stage is chosen for detailed investigation. For comparison purposes, four different designs of the reaction blade are retained (Figure 2.3).

All four blades were designed from a reference Blade 1 such that the subsonic part of the blade passage remained the same in all cases. The only difference occurs downstream of the throat.

- Blade 1: the reference blade has a wholly convergent blade channel with straight suction back downstream of the throat. It has a thick trailing-edge thickness of 4% (relative to the chord).
- Blade 2 is almost identical to Blade 1: a wholly convergent channel with straight suction back downstream of the throat. But it has a thinner trailing-edge thickness (equal to that of blade 3) of 2%. This gives

the opportunity to study the effect of trailing-edge thickness on the performance of a transonic blade and allows a realistic comparison to be made with other blade profiles.

- Blade 3 has a convergent channel with convex suction side downstream of the throat, thus providing an unguided expansion just like a plug nozzle. It has the same trailing-edge thickness as Blade 2 of 2%.

- Blade 4 has a convergent-divergent blade passage with trailing-edge thickness of 1.5%.

CHAPTER 3

TRANSONIC REACTION-BLADE PROFILE

The object of this work was not to design a stage for a particular engine or application but rather to provide a general understanding of the effects of transonic flow on turbomachine elements so that an efficient stage could be developed.

In all cases, only two-dimensional blade flow considerations have been used. Aspect-ratio, secondary-flow and tip-clearance effects have not been considered, since they depend mainly on the particular size and configuration of the application.

3.1 Basic Assumptions and Design Parameters

For design considerations, high-temperature, high-pressure-ratio impulse and 50%-reaction stages are chosen for investigation. These are extreme cases of practical importance.

Design parameters typical of advanced gas turbines are chosen:

(i) turbine inlet stagnation temperature, $T_{01} = 1800^{o}K$;

(ii) stagnation pressure ratio across the stage $P_{01}/P_{03} = 4$; and

(iii) blade speed, $U = 550$ m/sec.

The specific-heats ratio ($\gamma = C_p / C_v$) is taken to be 1.3 and assumed constant; while a target total-to-total polytropic efficiency of 0.9 is set.(from the nozzle inlet to rotor exit).

3.2 Stage Thermo & Gasdynamical Analysis

The following parameters are calculated both for the impulse and 50%-reaction stages.

3.2.1 Stagnation Temperature Drop across the Stage, ΔT_0

$$\frac{\overline{T}_{01}}{\overline{T}_{03}} = \left[\frac{P_{01}}{P_{03}}\right]^{\frac{\gamma-1}{\gamma}\eta}$$

$$= \left[4\right]^{\frac{1\cdot3-1}{1\cdot3}(0\cdot9)}$$

$$= 1\cdot334$$

$$\overline{T}_{03} = \frac{\overline{T}_{01}}{1\cdot334} = 1350\,^\circ K$$

$$\Delta T_0 = \overline{T}_{01} - \overline{T}_{03}$$

$$= 450\,^\circ K.$$

3.2.2 Specific Work Output, ΔW

The specific work output, for adiabatic reversible process, is equal to the drop in stagnation enthalpy across the stage i.e.

$$\Delta W = \bar{C}_p \cdot \Delta T_0$$

$$= \frac{\gamma}{\gamma-1} \frac{R}{m} \qquad \frac{J \cdot mole \ {}^\circ K \cdot}{Kg \cdot mole \ {}^\circ K} .$$

$$= \frac{1.3}{(1.3-1)} \cdot \frac{8314}{29} \cdot 450$$

$$= 559040.5 \quad \frac{M^2}{Sec^2} .$$

3.2.3 Change in Tangential Velocity, ΔC_y

From the momentum equation applied to a control surface enclosing the rotor, the total tangential force developed on all the rotor blades is equal to the change in tangential momentum across the rotor i.e. $\dot{m}(C_{y2} + C_{y3})$, where the flow rate $\dot{m} = \rho_1 C_{x1} A_1 = \rho_2 C_{x2} A_2 = \rho_3 C_{x3} A_3$. The blades are moved at constant velocity U, so that the work per unit time is $\dot{W} = \dot{m} U (C_{y2} + C_{y3})$

The specific work, work per unit flow rate, is

$$\Delta W = U (C_{y2} + C_{y3})$$

Thus the change in tangential velocity $\Delta C_y = \frac{\Delta W}{U} = 1016.44 \ M/sec.$

3.2.4 Axial Velocity C_x.

In choosing the axial velocity care is taken to ensure that the maximum axial Mach number obtained in the stage is never greater than 0.6. This limit is set simply to avoid supersonic axial flow at off-design and because increasing Mach number over 0.6 can not provide any substantial increase in mass flow.

Along with this constraint, for impulse stage, the axial velocity is chosen such that the compromise angle θ, lies between 15 & 20°,

$$\text{where } \theta = \text{arctg} \frac{C_{x2}}{C_{y2}}$$

while for reaction stage, axial velocity is chosen such that θ lies between 20° & 30°.

A value of $\theta = 16^\circ$ is chosen for the impulse stage while a value of $\theta = 25^\circ$ is chosen for the reaction stage.

3.2.5 Gas Velocity Triangles

The flow velocity triangles are drawn both for the Impulse and 50% Reaction Stages using the geometrical peculiarities of each stage while assuming a constant axial velocity thru the stage (Figure 3.1).

For the impulse stage, first the base CG of the flow velocity triangle is drawn, the length being equal to $(U + \Delta C_y)$

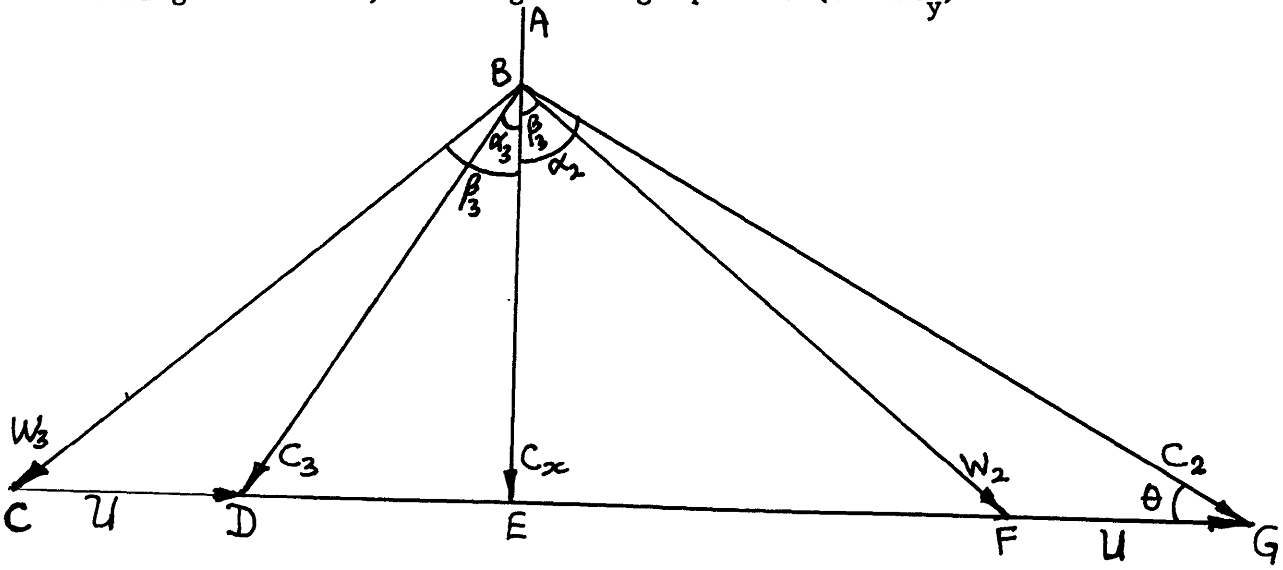

-- then, the locations of points D and F are marked out, with CD = FG = blade speed, U.

-- for the impulse stage, both the rotor relative velocity and angle at inlet are equal to those at the exit i.e. $W_2 = W_3$ and $\beta_2 = \beta_3$ This property is used to determine the location of point E which is simply the mid point of CF.

-- from point E, a straight line AE perpendicular to CG is drawn.

-- from point G, a line is drawn making an angle θ (compromise angle) with line CG and cutting line AE at point E. ($\hat{CGB} = \theta = 16^\circ$).

-- Point B is the apex of the velocity triangle and points B & C; B & D and E & F are simply joined together to complete the sides.

From the graphical construction, the values of the rotor inlet and exit, absolute and relative velocities and angles are found. The corresponding Mach numbers and temperatures at each station are also calculated. The complete analysis is given in Table 1.

A similar analysis is carried out for the 50% Reaction Stage:

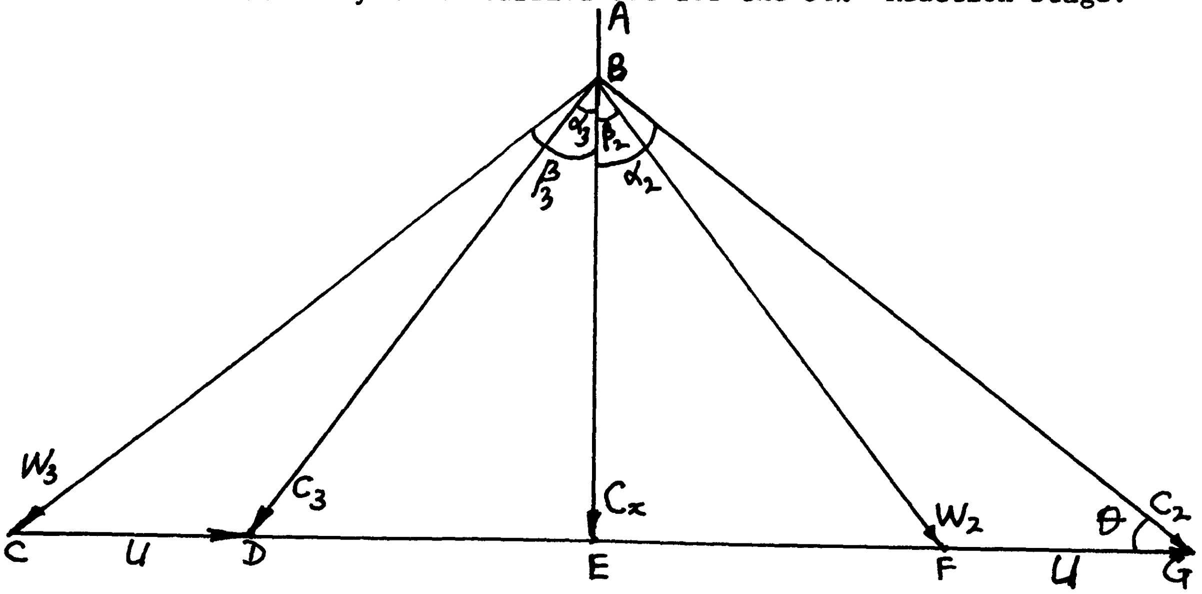

-- First, the base CG of the velocity triangle is drawn, the length equal also to $U + \Delta C_y$.

-- the locations of points D and F are marked out with CD = FG = blade speed, U,

-- the similarity of the velocity triangles for the 50%-reaction stage dictate the location of point E - which is the midpoint of CG.

-- From point E, a straight line AE perpendicualr to CG is drawn.

-- From point G, a line is drawn making an angle (compromise angle) with base line CG and cutting line AE at point E. (CGB = 0 = 25°).

-- Point E is the apex of the velocity triangle and again points B & C, B & D and E & F are simply joined together to complete the sides.

As in the impulse case, the values of the velocities and angles (relative & absolute) are found from the graphical construction. Corresponding Mach numbers and temperatures at each station are, then calculated. The complete analysis is given in Table 1.

Analytically the stage degree of reaction R, load coefficient ψ , and flow coefficient ϕ, are related to the inlet and exit angles (α_2, β_3) through the following expressions.

$$\psi = \phi(\tan\alpha_2 + \tan\beta_3) - 1 \qquad (3.2.1)$$

$$R = \frac{1}{2} + \frac{\phi}{2}(\tan\beta_3 - \tan\alpha_2) \qquad (3.2.2)$$

For the impulse stage, R = 0

$$\psi = \frac{C_p \Delta T_0}{U^2} = 1.8481$$

$$\phi = \frac{C_x}{U} = 0.6182$$

Solving equations 3.2.1 and 3.2.2. simultaneously, we obtained

$$\alpha_2 = 72.2^\circ$$

$$\beta_3 = 56.2^\circ$$

Similarly for the 50%-reaction stage, with $R = 0.5$, $\psi = 1.8481$ and $\Theta = 0.664$, solving the equation gave

$$\alpha_2 = \beta_3 = 65^\circ.$$

These values are identical to those obtained from the graphical construction.

TABLE 1

	STAGE PARAMETERS	IMPULSE STAGE	50% REACTION STAGE
1.	**Design Parameters**		
a.	Turbine Inlet Stagnation Temperature T_{01}	1800°K	
b.	Stage Stagnation Pressure Ratio, P_{01}/P_{03}	4	
c.	Blade Speed, U	550 m/sec.	
d.	Target Total-to-Total Polytropic Efficiency η_{TT}	0.9	
e.	Specific heats ratio $(\gamma = C_p/C_v)$	1.3	
2.	Stagnation Temperature Drop across the stage $\Delta T_0 = T_{01} - T_{03}$ $\Delta T_0 = T_{01} - \frac{T_{01}}{\left[\frac{P_{01}}{P_{03}}\right]^{\frac{\gamma-1}{\gamma}\eta_{TT}}}$	450°K	
3.	Stage Specific Work Output, ΔW $\Delta W = C_p \Delta T_0 = \frac{\gamma}{\gamma-1}\frac{R}{m}\Delta T_0$	559040.5 $\frac{\text{J.mole °K}}{\text{kg mole °K}}$	
4.	Change in Tangential Velocity, ΔC_y $\Delta C_y = \frac{\Delta W}{U}$	1016.44 m/sec.	
5.	Compromise angle, θ $\theta = \arctan \frac{C_{x2}}{C_{y2}}$	16°	25°

	STAGE PARAMETERS	IMPULSE STAGE	50% REACTION STAGE
6.	Axial Velocity, Cx. for Impulse: $C_x = tg\theta[0.5\Delta C_y + U]$	309 m/sec	365.2 m/sec.
	for 50% Reaction $C_x = tg\theta[0.5(\Delta C_y + U)]$		
7.	Tangential Components of the velocities		
a.	for impulse: $W_{y3} = \frac{\Delta C_y}{2}$ for 50% Reaction $W_{y3} = \frac{(\Delta C_y + U)}{2}$	508.22 m/sec	783.22 m/sec.
b.	$C_{y2} = W_{y3} - U$	-41.78 m/sec	233.22 m/sec.
c.	For Impulse $W_{y2} = W_{y3}$	508.22 m/sec	233.22 m/sec.
d.	$C_{y2} = W_{y2} + U$	1058.22 m/sec	783.22 m/sec.
8.	Rotor Inlet and Exit Velocities		
a.	Absolute $C_2 = C_x^2 + C_{y3}^2$	1111.5 m/sec	864.2 m/sec.
b.	Relative $W_2 = W_x^2 + W_{y2}^2$	594.8 m/sec	433.3 m/sec.
c.	Absolute $C_3 = C_x^2 + C_{y3}^2$	311.8 m/sec	433.3 m/sec.
d.	Relative $W_3\ W_x^2 + W_{y3}^2$	594.8 m/sec	864.2 m/sec.

	STAGE PARAMETERS	IMPULSE STAGE	50% REACTION STAGE
9.	Static Temperatures & Acoustic Velocities at Rotor Inlet and Exit		
a	$T_2 = T_{02} - \frac{C_2^2}{2C_p}$	1302.8°K	1499.4°K
b.	$a_2 = \sqrt{\gamma R T_2}$	696.8 m/sec	747.55 m/sec.
c.	$T_3 = T_{03} - \frac{C_3^2}{2C_p}$	1302.8°K	1270.1°K
d.	$a_3 = \sqrt{\gamma R T_3}$	696.8 m/sec.	699.01/m sec.
10.	Mach number at Rotor Inlet and Exit.		
a.	Absolute Inlet Mach no, $M_{c2} = C_2/a_2$	1.6	1.15
b.	Relative Inlet Mach no; $M_{w2} = W_2/a_2$	0.9	0.58
c.	Axial Inlet Mach no $M_{cx2} = C_x/a_2$	0.444	0.4885
d.	Absolute Exit Mach no $M_{c3} = C_3/a_3$	0.492	0.62

	STAGE PARAMETERS	IMPULSE STAGE	50% REACTION STAGE
e.	Relative Exit Mach no $M_{w_3} = W_3/a_3$	0.9	1.3
f.	Axial Exit Mach no $M_{cx_3} = C_x/a_3$	0.488	0.52
11.	Rotor Inlet and Exit Angles		
a.	Inlet absolute angle ; α_2	74°	65°
b.	Inlet relative angle ; β_2	68°	32.3°
c.	Exit absolute angle , α_3	56.2°	32.3°
d.	Exit relative angle , β_3	68°	65°
12.	Stagnation temperature at Rotor Inlet.		
	Absolute $\overline{T_{o2}}^{abs}$	1800°K	
	Relative $\overline{T_{o2}}^{relat}$	1449	1575°K
13.	Stagnation Temperature at rotor Exit		
	Absolute $\overline{T_{o3}}^{abs.}$	1350°K	
	Relative $\overline{T_{o3}}^{relat.}$	1449	1575°K
14.	Stage Loading Coefficient $\Psi = \frac{C_p \Delta T_0}{U^2}$	1.8481	1.8481
15.	Stage Flow coefficient $\Phi = C_x/U.$	0.6182	0.664

3.3 BLADE DESIGN

3.3.1 SEVERAL METHODS OF BLADE DESIGN

A large number of investigations have been devoted to profiling and designing turbine blade rows. Methods for direct and inverse problems are well known, based on solving differential and integral equations of fluid flow in a row, together with methods using conformal transformation, hodographs, analogy and modelling.

Approximate methods utilizing solutions of the problem of flow in the blade passage (blade-passage methods) are widely used. The methods of solving the inverse problem (designing blade profiles for a given velocity distribution) have been greatly improved and speeded-up by the use of computers.

But usually, in practice, extensive use is made of approximate geometrical methods for designing profiles, based on a large volume of empirical data. One of these methods consists of bending a basic axially symmetrical profile in respect to a mean line (the mean line being the geometric locus of the centers of circles inscribed within the profile). The mean line taken is usually a parabola, the tangent to which makes the angle β_2, with the front of the cascade inlet and angle β_3 at the exit.

The method of constructing profiles proposed by M.I. Zhukovskii is based on the use of a series of well designed cascades. When designing a new profile, small changes are made to the geometry at the entrance and exit portions of two adjacent blade sections. Since the geometry of the new section is close to that of the established efficient profiles, its characteristics are also very similar.

In this study, both Deych's method of profiling turbine blades with respect of lemniscate curves, and a modified NASA method using Dunavant and Erwin's thickness distribution were used.

3.3.2 Design of the Reference Blade

All the different blade profiles were designed from a reference blade such that the subsonic part of the blade passage remained the same in all cases, the only difference occuring downstream of the throat.

The design parameters are for an inlet Mach number $M_2 = 0.5$; exit Mach number $M_3 = 1.3$. Inlet angle $\beta_2 = 32°$, exit angle $\beta_3 = 65°$; with space to chord ratio $g/c = 0.75$.

The blade design in itself is split into two parts, first a subsonic region where all the flow turning occurs, followed by a purely supersonic section.

The present reference blade evolved as a compromise between two design methods. The first method is the modified Russian lemniscate[21] method proposed by Deych, whereas the second method used a single parabolic arc "camber-line" (as opposed to two parabolic arcs usually used on NACA profiles) with Dunavant and Erwin[30] thickness distribution.

A lemniscate (equation $(x^2 + y^2)^2 = a^2(x^2 - y^2)$) is a very convenient curve for determining subsonic blade profiles because it allows the point of maximum curvature to be selected at any cross-section of the blade passage and ensures a smooth change in curvature along the section and contour and over the blade height. Both Russian[5,6,7,21] and foreign[33] experimental investigations of these profiles have indicated a satisfactorily low level of losses over a wide range of subsonic Mach numbers, Reynolds numbers, inlet and exit angles. The details of the design procedure are given in Appendix A.

The curvature of the second profile was obtained by curving the center line (camber line) of the profile according to a single parabolic arc. The method of construction of the camber line set out in Reference 39 is used. According to this method, if two tangents and their contact points with the desired curve are given it is possible to draw an arbitrary number of additional tangents by dividing the two distances between the contact points and the point of intersection between the two tangents into the same number of equal parts. The tangents to the desired curve are then obtained by cross-connecting the division points as shown in Figure 3.2.

It is obvious that a given profile thickness distribution and a given curved center line can readily be combined into a curved profile by plotting the given thickness at right angles to the camber line of the profile. Dunavant and Erwin thickness distribution, highly recommended for accelerating reaction turbine blades with rapid turning, was used here.

These two blade profiles were combined (Figure 3.3) and one compromise blade was obtained from the two methods. This compromise profile became the reference blade and acted as a base over which the family of blades was developed.

This reference blade has a wholly convergent blade channel with straight suction back downstream of the throat.

3.3.3 Supersonic Section of the Remaining Profiles

The supersonic section is designed using the method of characteristics as applied to two-dimensional isentropic flow of a perfect gas (Reference 28) Since reduction of wetted surface area and the minimization of hub and shroud boundary layer build up are of utmost importance, "minimum length supersonic section" blade design is chosen with expansion carried out only on the blade suction side, using the inner rhombus. (Figure 3.4)

Supersonic section with sharp-edged throat is characterised by concentrated expansions at the throat (Busemann type of concentrated expansion nozzle). The sharp-edged throat initiates a Prandtl-Meyer expansion (flow around a corner). The waves (characteristics lines) emanating from the sharp edge have a negative slope (waves of family II) and are reflected at the center line into waves with positive slopes (waves of family I). These reflected waves then extend across to intersect the supersonic section contour, which is shaped so as to cancel these waves. (Figure 3.5)

An expansion wave incident on a channel wall will, in general, require that a secondary wave be emitted at the point of incidence in order to keep the flow against the wall. But if the wall is curved in the way a streamline would be turned under the influence of the incident wave, however, no secondary wave arises to keep the flow along the wall. This method of suppression of secondary wave is the principle used to obtain theoretically, uniform, wave-free parallel flow in the exit section.

The problem then reduces to locating the point of incidence of the waves on the section wall, while the difference in value of the characteristics bounding the incident wave gives the change of wall inclination required to suppress secondary waves. Definitely, the accuracy of the wall contour obtained improves as the number of characteristics drawn to represent the incident expansion waves is increased.

Shapiro and Edelman[26,27] have long established the coordinates of these sharp-cornered supersonic sections for a wide range of discharge Mach numbers and specific-heats ratio $\gamma = 1.4$. Recently NASA came up with a computer program[28] listing of the lay-out design for any exit Mach number and any specific-heat ratio(γ).

Slight modifications necessary to run this program on the MIT-IBM 370 were carried out and this program was then used in this blade design to obtain the coordinates of the supersonic section of the blades,

This supersonic section was then used to replace the straight-back section on the reference base-profile to evolve the convergent-divergent blade profile. (Figure 3.6) Expansion here is controlled by the walls.

The next series in the family of blades was the "plug nozzle" having an unguided expansion on the suction side. This blade evolved directly from the convergent-divergent blade but instead of having the expansion controlled by the downstream pressure (Figure 2.3)

In order to be able to make a realistic comparison between the different blade profiles, the influence of the trailing-edge thickness had to be considered. Thus, there was a necessity for another series in the family of blades, having a straight suction back, wholly convergent channel with trailing-edge thickness equal to that of the plug nozzle. (Figure 2.3)

3.4 Blade Manufacturing

The blades, 2 inches high, are made out of structural heat-treated aluminum (2024-T-351 1-¼" X 3" aluminum rectangular stock) on M.I.T. Gas Turbine Laboratory blade copying machine using master blades as templates. The master blades, four times the actual sizes of the blades, were designed and machined on a tape-controlled milling machine to a tolerance of about 1/1000th of an inch.

Because of the large radius of the follower used on the blade copying machine the rapid changes in curvature of the master blades could not be followed correctly and consequently the cutter on the other end could not do a perfect job on the blades. The final blades thus came out with bumps on their suction sides. Figure 3.7 shows the difference between the blade profile we wanted and what we actually got. The physical size of non-uniformity is about 0.015" and may be enough to trigger transition from laminar to turbulent and subsequent separation.

In cutting new blades, definetely a smaller follower and corresponding smaller cutter must be used. This may entail making up a special cutter to obtain the right size needed.

CHAPTER 4

AERODYNAMIC PERFORMANCE OF TRANSONIC TURBINE BLADES

Tests to determine the aerodynamic performance of all the four turbine blade profiles designed were carried out in a linear cascade attached to an open-cycle supersonic wind tunnel.

4.1 Test Facility

The test facility used for the turbine cascade investigation was the von Karman Institute high-speed cascade tunnel. This tunnel is of the blow-down type (exhaust to atmosphere) and is supplied with dry air from high-pressure tanks (Figure 4.1)

The air enters the settling chamber through perforated pipe bent backwards (to suppress any inlet swirl). The flow then passes through a honeycomb screen and a wooden contour into a rectangular channel.

The test section outlet is formed by a diffuser equipped with a back-pressure valve and a flexible exhaust duct into the atmosphere.

4.2 Tunnel and Test Section Instrumentation

The settling-chamber pressure was measured with a mercury-filled U-tube manometer. The pressure could be kept constant within ± 1 mm Hg. The static pressure on the blades and on the wall was measured with a mercury multimanometer (a blocking device allows readings to be made after each blowdown). Mid-span traverses were performed at the inlet and outlet plane of the cascade by the use of three different probes.

The probes are introduced into the test section through slots in the Perspex discs and moved by a remote-controlled carriage. These probes are:

for the inlet - pitot-directional probe; and

for the outlet - a pitot-directional probe combined with
a single-needle static probe (VKI probe)
in the range of Mach numbers up to
1.2 - 1.3 at exit;
- an AVA-tube probe in the range of Mach
number above 1.2. (Figure 4.2)

Strain-gauge pressure tranducers with a linearity of better than 0.1% full scale are used to measure the required flow parameters. These measurements are then recorded on paper recorders. The facility is also equipped with a standard Schlieren system in continuous operation for flow observation and pictures are obtained by using a short-duration 15,000V electric discharge.

4.3 Measuring and Data-Reduction Procedure

The investigation was started with a flow survey by means of the Schlieren system to verify the periodicity of the outlet angle. Schlieren pictures and shadow-graphs were taken at various outlet Mach numbers. The outlet Mach number was varied by increasing the supply pressures with a sudden area enlargement downstream of the cascade for the lowest range of Mach numbers (up to 1.2). For Mach numbers above 1.2, changes in M_2 were obtained by varying the inclination of a tailboard which was linked to the trailing edge of the last blade of the cascade.

The blade performance was determined from inlet and outlet traverses and blade pressure distribution measurements. The downstream traverses were carried out behind several blades including the instrumented ones. The pressure distributions were taken without any probe in the test section to avoid disturbances due to the probe.

In the downstream traverses, the following values were continuously being recorded:

P_0 = difference between settling chamber pressure and total pressure of the probe;

P_S - difference between static pressure of the probe and atmospheric pressure; and

P_{LR} - pressure difference measured by the directional probe.

The following values were computed at several points distributed equally over one pitch:

$\left.\begin{array}{l} P_{03}) \\ P_{S3}) \end{array}\right\}$ downstream total and static pressures taking into account the probe calibration and the shock in front of the pitot- tube;

$P_{02})$ inlet stagnation pressure;

Efficiency;
$$\eta = \frac{1 - \left[\dfrac{P_{S3}}{P_{03}}\right]^{\frac{\gamma-1}{\gamma}}}{1 - \left[\dfrac{P_{S3}}{P_{02}}\right]^{\frac{\gamma-1}{\gamma}}} ;$$

Losses, $\omega = 1 - \eta$;

M_3 - local outlet mach number = $\sqrt{\frac{2}{\gamma-1}\left[\left(\frac{P_{03}}{P_{s3}}\right)^{\frac{\gamma-1}{\gamma}}-1\right]}$; and

BETA 3 - β_3 outlet flow angle

Area-(A) and Mass (M)-averaged values were computed for all the above values.

(1) For example, the mass-average value for the exit stagnation pressure P_{03} is computed as follows:-

Outlet mass flows $\dot{m}_3 = \int_0^g y(1)_{\text{local}}\, dg$

with $y(1)_{\text{local}} = \frac{P_{3\,\text{local}}}{R\,T_3} \cdot M_{3\,\text{local}} \cdot \sqrt{\gamma R T_3}\, \cos \beta_{3\,\text{local}} \cdot dg$

then P_{03} mass average = $\frac{\int_0^g P_{03\,\text{local}} \cdot y(1)_{\text{local}} \cdot dg}{\dot{m}_3}$

The area average, on the other hand, is

$$P_{03\ \text{area average}} = \int_0^g P_{03\ \text{local}} \cdot dg$$

The inlet Mach number was based on the total pressure and the area-averaged static wall pressure at the cascade inlet.

(2) $M_2 = C_2/A_2 = \sqrt{\frac{2\left(\overline{T}_{02}-\overline{T}_2\right)C_p}{\gamma R\,\overline{T}_2}} = \sqrt{\left[\left(\frac{P_{02}}{P_2}\right)^{\frac{\gamma-1}{\gamma}}-1\right]\frac{2}{\gamma-1}}$

The Reynolds number was based on inlet parameters and referred to 1 cm length.

(3) $$R_e = \frac{M_2\sqrt{\gamma R T_2}\cdot p_2}{\mu_0\left(\frac{T_2}{273}\right)^n R\,T_2}$$

where μ - viscosity = $1.753.10^{-6}$ kg.S.m^{-2} at 0°C

n - exponent for viscosity-temperature ratio and is equal to 0.76 for air.

$=\left(\frac{T_2}{273}\right)^n$ valid for -20°C + 500°C.

The outlet Mach number was based on local stagnation and static exit pressure

$$M_3 = \sqrt{\frac{2}{\gamma-1}\left[\left(\frac{p_{03}}{p_3}\right)^{\frac{\gamma-1}{\gamma}} - 1\right]}$$

Critical outlet Mach number is:

$$M_{3cr} = \frac{c_3}{a_{cr}} = \sqrt{\frac{M_3^2}{1+\frac{(\gamma-1)}{(\gamma+1)}\left(M_3^2-1\right)}}$$

4.4 Blade and Cascade Geometry

4.4.1 Reference Convergent Transonic Blade with Straight Suction Back and Thick Trailing Edge (Blade 1)

Blade chord c= 66.0 mm

Blade spacing g = 49.5 i.e. g/c = 0.75

Stagger angle $\gamma = 51^{\circ}$

Inlet flow angle $\beta_3 = 30^{\circ}$

Exit angle $\beta_3 = 65^{\circ}$

Trailing-edge thickness, te = 2.8 mm te/c = 0.0424

Number of blades in the cascade = 6

with blade 3 suction side and blade 4 pressure side instrumented with static-pressure taps (Figure 4.3).

4.4.2 Wholly Convergent Blade with Straight Suction Back but Thin Trailing Edge (Blade 2)

Blade chord c = 64.2 mm

Blade spacing g = 48.15 mm i.e. g/c = 0.75

Stagger angle γ = 51°

Inlet flow angle β_2 = 30°, exit angle = 65°

Trailing-edge thickness, te = 1.3 mm te/c = 0.02025

Number of blades in the cascade = 6

with blade 3 suction side and blade 4 pressure side instrumented with static-pressure taps (Figure 4.4)

4.4.3 Transonic Turbine Blade with Unguided Expansion on the Suction Side (Plug Nozzle) Blade 3)

Blade chord c = 66.0 mm

Blade spacing g = 49.5 mm i.e. g.c = 0.75

Stagger angle γ = 51°

Inlet flow angle β_2 = 30°; exit angle β_3= 65°

Trailing-edge thickness, te = 1.46 mm te/c = 0.0221

Number of blades in the cascade = 6

with blade 3 suction side and blade 4 pressure side instrumented with static-pressure taps.

4.4.4 Blade With Convergent-Divergent Channel

Blade chord c = 76.0 mm; Throat 0 = 18.30 mm.

Blade spacing g = 49.6 mm i.e. g/c=0.64

Stagger angle $\gamma = 46.5^{\circ}$

Inlet flow angle $\beta_2 = 30^{\circ}$, Exit angle $\beta_3 = 65^{\circ}$

Trailing-edge thickness te = 1.14, i.e. te.C = 0.015

Number of blades in the cascade = 6

with blade 3 suction side and blade 4 pressure side instrumented with static-pressure taps.

4.5 Blade Instrumentation

The blade velocity distribution was measured at the mid-span by pressure taps on the pressure side and suction side of two neighboring blades such that the instrumented blade surfaces formed the blade passage. The locations of the pressure taps are shown in Tables 2 and 3, and in Figure 4.5.

4.6 Inlet Flow Field

The Mach-number distribution at the cascade inlet was derived from wall static pressure in a plane "0.1C" ahead of the leading-edge plane. Inlet Mach number variation as a function of exit Mach number is shown in Figure 4.6. The inlet-angle variation in the transverse direction was also measured. No influence of the outlet Mach number was observed.

4.7 Cascade Flow

The blade velocity is expressed by the local Mach number calculated from the local static pressure on the blade and the total pressure upstream of the cascade. Measurements were taken on the suction side of the blade and the pressure side of the blade. The Mach number distributions are plotted in Figures 4.7 thru 4.10.

The Schlieren pictures and shadow-graphs of the flow at different pressure ratios are shown in Figures 4.11 thru 4.14

4.8 Blade Performance

The blade performance was evaluated from the downstream wake traverses behind the blades at an axial distance of "0.3c" behind the trailing edge in all cases. A typical computer output of the traverse detailed analyses is shown in Table 4.

4.9 Losses

The variation of blade losses as a function of the outlet Mach number for all the blades are plotted in Figures 4.15 thru 4.18.

For Blade 1, the convergent reference blade with straight suction back, for exit Mach number up to $M_3 = 0.7$ blade losses, ran up to 8%. This high level of loss was apparently caused by trailing edge thickness (te/c = 4% compared to te/c = 2.025% in the second blade, and te/c = 2.2% in the third blade).

Local supersonic zones, lamda "λ" shocks and diffusion losses cause a sudden rise in the level of the losses from $M_3 > 0.7$ with maximum loss of about 11% occuring at about $M_3 = 0.85$.

The decrease in the level of losses from $M_3 = 0.85$ to around $M_{3\ \text{design}} = 1.3$ is linked with the fact that the shocks became more oblique and flow reattachment occured. The new increase of ω for

Table 4 **Computer output of the downstream traverse detailed analysis.**

```
 TN= 12.0    DATE 10.24.75      TU.U7407             MIT-VKI BL-3  PR-VKI
-------------------------------------------------------------------------------

          I= -0.7  M1=0.271  P01=1548.0  PS1=1471.0  RE=0.129E 06
          ---------------------------------------------------------
 N  P02       PS2    P0201   P01S2    ETA      W      THL      M2      BLD    BETA2
 1 1532.4   558.4   0.990   2.772   0.991   0.009   0.011   1.293     0.3    24.6
 2 1533.6   581.8   0.991   2.661   0.992   0.008   0.011   1.263     0.1    24.8
 3 1537.5   598.0   0.993   2.589   0.994   0.006   0.008   1.244    -0.2    25.1
 4 1541.3   629.2   0.996   2.460   0.996   0.004   0.005   1.208    -0.4    25.3
 5 1543.6   654.4   0.997   2.365   0.997   0.003   0.004   1.179    -0.4    25.3
 6 1545.2   683.8   0.998   2.264   0.998   0.002   0.003   1.145    -0.4    25.3
 7 1541.8   718.1   0.996   2.156   0.995   0.005   0.006   1.105    -0.6    25.5
 8 1524.3   751.2   0.985   2.061   0.981   0.019   0.024   1.058    -1.0    25.9
 9 1491.2   780.1   0.963   1.984   0.950   0.050   0.060   1.008    -1.4    26.3
10 1419.0   787.8   0.917   1.965   0.882   0.118   0.140   0.957    -1.3    26.2
11 1346.6   793.0   0.870   1.952   0.807   0.193   0.224   0.904    -0.0    24.9
12 1296.6   789.0   0.838   1.962   0.755   0.245   0.282   0.873     1.3    23.6
13 1291.0   782.6   0.834   1.978   0.753   0.247   0.285   0.877     2.0    22.9
14 1333.0   776.5   0.861   1.993   0.800   0.200   0.234   0.914     1.7    23.2
15 1391.0   760.7   0.899   2.035   0.862   0.138   0.164   0.970     0.8    24.1
16 1436.9   692.2   0.928   2.236   0.917   0.083   0.102   1.077     0.2    24.7
17 1471.6   555.5   0.951   2.787   0.957   0.043   0.057   1.267     2.0    22.9
18 1513.7   481.8   0.978   3.213   0.984   0.016   0.023   1.391     2.8    22.1
19 1508.1   480.9   0.974   3.219   0.981   0.019   0.026   1.390     2.4    22.5
20 1494.0   481.0   0.965   3.218   0.974   0.026   0.036   1.383     1.8    23.1
21 1471.9   481.2   0.951   3.217   0.963   0.037   0.050   1.372     1.1    23.8
22 1473.4   482.9   0.952   3.206   0.964   0.036   0.050   1.370     0.5    24.4
23 1481.2   487.0   0.957   3.179   0.968   0.032   0.045   1.368    -0.1    25.0
24 1485.8   492.5   0.960   3.143   0.970   0.030   0.042   1.362    -0.6    25.5
25 1495.2   496.8   0.966   3.116   0.974   0.026   0.036   1.360    -1.0    25.9
-------------------------------------------------------------------------------
 W2A= 0.054   THL2A=0.069   M2A=1.162 MCR2A= 1.13 MCRX2A= 1.03 MCRU2A= 0.47
   M= 0.053         M=0.067     M=1.163       M= 1.13        M= 1.03       M= 0.47

 P02/P01A=0.947   PS1/PS2A= 2.315  P01/PS2A= 2.436
       M=0.949          M= 2.312          M= 2.433

 BETA1= 60.7  BETA2A= 24.5   TETA2A= -36.3   E2=0.593  F2=0.266  E2/F2=2.23
                    M= 24.6        M= -36.2
*******************************************************************************
```

$M > M_{design}$ up to the limit loading $M_{limit} = 1.59$, is due to the increasing strength of the left-running T.E. shock which caused the boundary layer to separate without reattachment on the suction side.

Losses recorded for $M_3 > M_{limit}$ depend on the total pressure losses due to the blade boundary layer $(\Delta P_0)_{B.L.}$, the trailing-edge shocks (ΔP_0) shock, and the mixing process between the T.E. plane and the measuring plane as well as the outlet velocity. The $(\Delta P_0)_{B.L}$ remains roughly constant, while $(\Delta P_0)_{shock}$ and mixing losses increase as the exit Mach number increase.

For Blade 2, the convergent blade with straight suction back and thin trailing-edge thickness (te/c = 2.025%) for exit Mach number up to $M_3 = 0.75$, losses were decreasing until they reached a value of 4.7%. This again is probably due to flow acceleration and thinning of the boundary layer.

As in Blade 1, local supersonic zones, lamda "λ" shocks, and diffusion losses cause a sudden rise in the level of the losses for $M_3 > 0.75$ with maximum loss of about 6% occuring at about $M_3 = 0.95$.

The losses then decrease as in the first blade form $M_3 = 0.95$ to around $M_{3\ design} = 1.3$ as the shock becomes oblique and possible flow reattachment occurs after separation. The pattern in which the losses decrease from $M_{3\ design}$ is very similar to that of blade 1 (straight suction back with thick trailing edge).

The new increase in W for $M > M_{design}$ up to the limit-loading M_{limit} loading is both due, to the increasing strength of the left running trailing edge shock which causes the boundary layer to separate without reattachment on the suction side, and mixing losses. The very sharp increase in the level of the losses after M_{design} is also similar to that of blade 1 and around $M_2 = 1.5$ reaching level of losses comparable to each other.

For Blade 3, the plug nozzle blade with expansion on the suction side, (te/c = 2.21%) - for exit Mach numbers up to $M_3 = 0.7$, losses were decreasing and reached their minimum value of 5.5% - probably due to flow acceleration and thinning of the boundary layer.

As in other blades, local supersonic zones, lamda "λ" shocks and flow diffusion cause a sudden rise in the level of the losses for $M_3 > 0.7$, with maximum loss of about 7.5% occuring at $M_3 = 0.9$.

The losses then decrease as in the first and second blades from $M_3 = 0.9$ to $M_{design} = 1.3$ as the shock becomes oblique and possible flow reattachment occurs after separation. The decrease is pretty sharp unlike in blades 1 and 2 and the losses flatten out between $M_3 = 1.2$ and $M_3 = 1.4$ providing a reasonable operating zone with ($\omega = 5\%$). This region loss lies between 5% and 5.3%.

Losses increase for $M_3 > M_{design}$ up to the limit-loading $M_{limit} = 1.67$ but not as steep as in the first and second blades. This is probably due to the fact that the increasing strength of left running T.E. shock is smaller in this blade than in the first and second blades.

For Blade 4, the convergent-divergent blade (te/c = 1.5%) losses were first decreasing apparently due to flow acceleration and thinning of the boundary layer and it reached a low value of 6.5% at $M_{exit} =$

0.75.

As the pressure ratio increases, local sonic bubbles, lamda "λ" shocks, and flow diffusion increased the loss level to a maxinum of 8.25% at $M_{exit} = 0.86$.

The losses then start to decrease as in all the three other blades but very sharply from $M_{exit} = 0.86$ to around $M_3 = M_{design} = 1.3$ as shock becomes oblique, weaker and flow reattachment occurred after separation. A very low level of losses, 3.5%, recorded at the design exit Mach number region, and stayed that low, below 4% between $M_{exit} = 1.2$ to $M_{exit} = 1.5$, providing a good working range of low-loss exit Mach number.

A comparison of the loss curves (Fig. 4.19a) has shown clearly that each profile has a superior performance in different Mach number range, and diversing potentialities when cooling problems and problems of structural integrity are carefully examined along with optimization of efficiency. Remembering also that lower blade chord "c" means increase secondary losses tends to suggest a more broadly based assessment of losses to determine an optimum profile for a particular application.

4.10 Outlet Angles

The outlet angles shown on the performance curves were measured with reference to the tangential direction(Figures 4.15 thru 4.18).

For Blade 1 the convergent reference blade with straight suction back, β_3 decreased slightly from 25.5^o to 24^o between $M_3 = 0.6$ and $M_3 = 1.3$ ($\beta_{3\ design} = 25^o$); for $M_3 > M_{design}$, the exit angle increases slowly up to $M_3 = 1.4$ in a linear fashion. At $M_3 = M_{limit\ loading} = 1.59$, the deviation was about 10^o.

For blade 2 the convergent blade with straight suction back but thin trailing edge, β_3 decreased slightly from 25.5^o to 23.5^o between $M_3 = 0.5$ and $M_3 = 1.1$. A gradual increase was noticed from $M_3 = 1.1$ to $M_{3\ design} = 1.3$ when β_3 increased back to 25^o, the design exit angle. For $M_3 > M_{3\ design}$, the exit angle increases very sharply as in the Blade 1.

For blade 3 the plug nozzle, β_3 decreased from 28^o to $\beta_3 = 24.5^o$ between $M_3 = 0.6$ and $M_3 = 1.3$. For $M_3 > M_{design}$, the exit angle increases very sharply as in blades 1 and 2 in a linear form. At $M_3 = M_{limit\ loading} = 1.67$, the deviation of about 10^o was again recorded.

For blade 4, the exit angle β_3 changes very little for all the ranges of the M_{exit} up till $M_{3\ design}$, fluctuating by about 0.5^o from a mean of 24.5^o. (The desing exit angle is 25^o). After $M_{3\ design}$ ($M = 1.3$), a sharp increase in the value of is noticed, already amounting to a 2^o deviation at $M_{exit} = 1.47$, which suggests possible large deviation of the exit angle at higher exit Mach numbers just like the remaining blades.

There are noticeable differences in the exit angle behavior for each blade in the Mach number range investigated (Fig. 4.19b).

The striking one is the rather big deviation in Blade 3, close to 3^{o}, at low Mach numbers. This is not surprising remembering that Blade 3 is the plug nozzle with unguided expansion. This deviation then disappears as we approach the design supersonic exit Mach number.

Another striking point is that very sharp and high deviation is noted in all the cases at $M_{exit} > 1.4$, i.e. just a little over M_3 design. This is associated with the over expansion at the T.E. corner and the effect is even seen on the wake inclination.

4.11 Effect of Reynolds-Number Variation

In addition to the normal test series performed at Reynolds numbers between 10^5 and 10^6, the reference blade (Blade 1) was tested at constant inlet total pressure of P_{01} =Patmosp + 1000 mm Hg, constant Reynolds number of 10^6(corresponding to the highest total pressure for the highest Mach number in the normal test series), while the downstream pressure was varied with a back pressure valve.

4.11.1 Blade and Cascade Geometry

The blade geometry is the same as tested earlier on with g/c = 0.75 but the cascade geometry has changed. The Reference Blade with straight suction back wholly convergent channel is now being tested at g/c = .81

Blade chord c = 66.0 mm

Blade spacing g = 53.6 mm   i.e. g/c = 0.81

Stagger angle, γ = 59.5° - (tangential direction)

Inlet flow angle β_2 = 38.5°

Exit flow angle β_3 = 57°

o/g = 0.495

te/c = 0.0424

Number of blades in the cascade remained 6 with blade 3 suction side and blade 4 pressure side instrumented with static pressure taps.

4.11.2 Test Results

The results of these tests showed that the Reynolds number effect was neglibible in the test range of 10^5 to 10^6. No noticeable change was seen on the pressure distribution. Both the peak position and its value remained practically unchanged. The pattern of the shock-system remained exactly the same. Figure 4.20 carries the Schlieren pictures of the flow field for the Reference Blade 1 at g/c = 0.81 taken at constant Reynolds number while varying the back pressure to vary exit Mach numbers. Figure 4.21 carried the Mach number distribution. When Figures 4.20 and 4.21 are compared with Figure 4.7 and 4.11, (which were obtained while varying the Reynolds number) it confirmed the statement that no noticeable change was seen in the velocity distribution while the Schlieren pictures showed no variation in shock pattern.

Thus it was concluded that the Reynolds number effect was neglibible in the range that tests were conducted.

Further aerodynamic tests were carried out on M.I.T. Hot Blowdown Cascade Facility which has a very high level of tubulence (10%) and a significant effect of this turbulence on the pressure distribution was seen. Detailed results of these tests are described in Chpater 5 of this thesis.

4.12 Effect of Blade Solidity on Performance

Tests were also carried out to determine the effect of stage solidity on cascade performance. Reference Blade 1 was tested at $g/c = 0.81$ and $g/c = 0.695$ (former tests were conducted at $g/c = 0.75$). In addition Blade 3 (Plug) was tested at $g/c = 0.695$.

Careful examination of the blade velocity distribution (compare figures 4.7 and 4.9 with figures 4.22 and 4.23) and the Schlieren pictutes (figures 4.24 and 4.25) did show a considerable change in the locations and inclined angles of the left-running shocks for the same values of M_{is} (but varying blade spacing "g"). As the blade spacing increased, the shock got weaker and some flow separations resulting the shock-boundary-layer interactions were avoided.

4.13 Downstream Wake

Analysis of the downsream wake using the downstream traverse taken at 0.3C behind the blades and Schlieren photos shows an interesting effect of Mach number on the wake. All the plots of the stagnation pressure ratio P_{02}/P_{01} across pitch & β_3 distribution along the pitch (figures 4.26 thru 4.31) show that as M_{exit} increases the flow non-uniformity increases. A characteristic effect is the increase in the wake depth during the transition from subsonic to supersonic exit Mach number. The width of the wake changes also.

For the different blade profile, the effect of T.E. thickness can also be seen clearly in the relative width of the wake.

Careful examination of the Schlieren photos of wake flow shows that it consists, under certain flow condition, of von Karman vortex streets. Because of the long exposure time an estimate of the shedding frequency of the vortices cannot be made from the evaluation of the present Schlieren pictured obtained.

Further experiment is planned in conjuction with V.K.I. to determine the shedding frequencies by directly measuring the pulsating wake pressure with a high-frequency-response Kulite Pressure transducer.

CHAPTER 5

HEAT TRANSFER TO TRANSONIC TURBINE BLADE SURFACE

Tests to determine the pressure and heat-transfer distributions around the turbine blades were carried out on M.I.T. Gas Turbine Laboratory Hot Blowdown Cascade Facility. (Figure 5.1)

Detailed study of heat transfer to turbine components in the highly three-dimensional and unsteady flow in turbomachinery are usually hampered on the theoretical side by the singular complexity of the problem and on the experimental side by the severity of engine operating conditions. Short-duration experimental studies on a hot-blowdown cascade facility provide a practical, low-cost and flexible means to solve these problems while providing rigorous modeling of the flow and temperature fields to simulate turbine design and off-design operating conditions.

5.1 FLOW AND TEMPERATURE MODELING

Because accurate heat-transfer measurements are extremely difficult to take at the high pressures and temperatures which exist in the turbine at design conditions, scaling down of operating condition is necessary. This offers the opportunity to test high-temperature turbine elements at reduced temperatures and pressures. The short test time (one second) makes it reasonable to assume an isothermal-wall model.

The principle of similarity is used in this modelling. Accordingly to this model law, the behavior of two systems will be similar if the ratios of their linear dimensions, forces, velocities, etc, are the same. Under conditions of forced convection in geometrically similar systems, the velocity fields will be similar provided the ratio of inertia forces to viscous forces is the same, in both fluids. The Reynolds number is the ratio of these forces and consequently we expect similar flow conditions in forced convection for a given value of the Reynolds number. The Prandlt number is the ratio of two molecular-transport properties, the kinematic viscosity $\nu=\mu/\rho$, which affects the velocity distribution, and thermal diffusivity $K/\rho C_p$ which affects the temperature profile. In other words, it is a dimensionless group which relates the temperature distribution to the velocity distribution. Hence, in geometrically similar systems having the same Prandtl and Reynolds numbers, the temperature distribution will be simialr. According to its definition the Nusselt number is numerically equal to the ratio of the temperature gradient at a fluid - to-surface interface to a reference-temperature gradient. We expect therefore, that in systems having similar geometries and temperature fields, the numerical values of the Nusselt number will be identical.

The flow and temperature modeling first scales down the operational temperature of the blade surface (T_{0p}) to room temperature (T_{ex}). Thus, a temperature scaling factor, S_f, may be defined as:

$$S_f \equiv T_{0P}/T_{ex} \qquad 5.1.1$$

For present day technology, T_{0p} is of order of 1200°K while room temperature, T_{ex} = 300°K, thus stating that S_f will have a value like 4.

It is assumed in this analysis that the working fluid in both operating and experimental cases is air acting as an ideal gas with constant specific heats.

In order to match the test (experimental) conditions with the actual operating condition the following dimensionless parameters must be identical.

a. Mach Number, M

b. Reynolds Number, Re

c. Prandlt Number, Pr

d. Reduced Frequency, K_f

e. Nusselt Number, Nu

a. Mach number

The Mach number is the ratio of the square root of the inertia force to the square root of the force steming from the compressibility of the fluid

$$M = \frac{\sqrt{(\rho V^2/L)}}{\sqrt{\rho c^2/L}} = \frac{V}{c} = \frac{V}{\sqrt{\gamma R T}} \tag{5.1.2}$$

Requiring that $M_{OP} = M_{ex}$ results in the following

$$\frac{V_{ex}}{\sqrt{(\gamma R T)_{ex}}} = \frac{V_{op.}}{\sqrt{(\gamma R T)_{op}}} \tag{5.1.3}$$

where $(\quad)_{op}$ indicates actual operating condtions and

$(\quad)_{ex}$ indicates experimental condtions

Assuming $\gamma_{ex} = \gamma_{op}$ and $R_{ex} = R_{op}$ equation (5.1.3) becomes

$$\frac{V_{op}}{V_{ex}} = \frac{\sqrt{T_{op}}}{\sqrt{T_{ex}}} = S_f^{\frac{1}{2}} \qquad (5.1.4)$$

Thus the velocity is scaled down as the square root of S_f.

b. Reynolds number

The Reynolds number is the ratio of inertia force to the friction force

$$R_e = \frac{\rho V^2/L}{\mu V/L^2} = \frac{\rho V L}{\mu} \qquad (5.1.5)$$

For equal Reynolds number

$$\frac{\rho_{ex} \cdot V_{ex} \cdot D_{ex}}{\mu_{ex}} = \frac{\rho_{op} \cdot V_{op} \cdot D_{op}}{\mu_{op}} \qquad (5.1.6)$$

Using the perfect gas relationship ($P = \rho RT$) to eliminate ρ in equation (5.1.6), results in

$$\frac{P_{ex}}{P_{op}} = \frac{\mu_{ex}}{\mu_{op}} \cdot \frac{V_{op}}{V_{ex}} \cdot \frac{L_{op}}{L_{ex}} \cdot \frac{R_{ex}}{R_{op}} \cdot \frac{T_{ex}}{T_{op}}$$

-- Since the viscosity varies approximately as the square root of the temperature

$$\mu = f(T^{0.64})$$

-- From equation (5.1.4), identical Mach numbers require

$$\frac{V_{op}}{V_{ex}} = S_f^{1/2}$$

-- and assuming $R_{ex} = R_{op}$

$$\frac{P_{ex}}{P_{op}} = \frac{L_{op}}{L_{ex}} \cdot \frac{1}{S_f} \qquad (5.1.8)$$

i.e. by using the geometrical ratio L_{op} P_{ex} can be lowered to amenable values.

The mass flow through the turbine is changed in the following way:

$$\frac{m_{op}}{m_{ex}} = \frac{\rho_{op} \cdot A_{op} \cdot V_{op}}{\rho_{ex} \cdot A_{ex} \cdot V_{ex}}$$

$$= \left(\frac{\mu_{op}}{\mu_{ex}} \cdot \frac{V_{ex}}{V_{op}} \cdot \frac{L_{ex}}{L_{op}}\right) \frac{A_{op}}{A_{ex}} \cdot \frac{V_{op}}{V_{ex}}$$

reducing finally to

$$\frac{M_{op}}{M_{ex}} = S_f^{1/2} \cdot \frac{L_{op}}{L_{ex}} \qquad (5.1.9)$$

c. Prandtl number

The Prandtl number is the ratio of two molecular transport properties, the kinematic viscosity $\nu \equiv \mu/\rho$

which affects the velocity distribution, and the thermal diffusivity; $K/\rho C_p$, which affects the temperature profile

i.e. $$P_r \equiv \frac{\mu C_p}{K}$$

For equal Prandtl number.

$$\frac{\mu_{ex}\cdot C_{p_{ex}}}{K_{ex}} = \frac{\mu_{op}\cdot C_{p_{op}}}{K_{op}} \qquad (5.1.10)$$

Since constant specific heats were assumed, equation (5.1.10) becomes:

$$\frac{\mu_{op}}{\mu_{ex}} = \frac{K_{op}}{K_{ex}} = S_f^{1/2} \qquad (5.1.11)$$

Note that the thermal conductivity varies like the viscosity, approximately as the square root of the temperature, and so the relation (5.1.11) holds and Prandtl number is in fact constant.

d. Reduced frequency

Reduced frequency is defined as $K_f = LF/V$.

Keeping the reduced frequency constant in both cases require

$$\frac{L_{ex}\cdot f_{ex}}{V_{ex}} = \frac{L_{op}\cdot f_{op}}{V_{op}} \qquad (5.1.12)$$

thus

$$\frac{f_{ex}}{f_{op}} = \frac{L_{ex}}{L_{op}}\cdot\frac{V_{ex}}{V_{op}} = \frac{L_{ex}}{L_{op}}\cdot S_f^{-1/2} \qquad (5.1.13)$$

that is, the ratio of the blade passing frequency varies as

$$\frac{L_{ex}}{L_{op}}\cdot S_f^{1/2}$$

Since the frequency ratio is equal to the N_{rpm} ratio, turbine rotational speed in the experiment must be reduced by the product of the geometrical ratio and the velocity scaling factor of $S_f 1/2$

$$\frac{N_{op}}{N_{ex}} = S_f^{1/2} \cdot \frac{L_{op}}{L_{ex}} \tag{5.1.14}$$

e. Nusselt number

The Nusselt number is a dimensionless coefficient of heat transfer and is defined as:

$$Nu = \frac{h_c \cdot L}{K}$$

If heat transfer data are to be the same for the experiment as for the actual turbine operating condition, it is very important that the Nusselt number remains the same i.e.

$$\frac{h_{c_{ex}} \cdot L_{ex}}{K_{ex}} = \frac{h_{c\,op} \cdot L_{op}}{K_{op}} \tag{5.1.15}$$

or
$$\frac{h_{c\,op}}{h_{c\,ex}} = \frac{L_{ex}}{L_{op}} \cdot \frac{K_{op}}{K_{ex}} = S_f^{1/2} \frac{L_{ex}}{L_{op}} \tag{5.1.16}$$

5.2 Test Conditions

For today's technology, the maximum allowable blade temperature is 1200°K while the room temperature is 300°K. Thus, the maximum scaling factor is:

$$S_f = \frac{1200}{300} = 4$$

The geometrical ratio, $\frac{L_{ex}}{L_{op}}$ = 2 is chosen

The pressure at the inlet to the cascade during the experiment is found to be: $P_{ex} = \frac{L_{ex}}{L_{op}} \cdot \frac{P_{op}}{S_f} = \frac{P_{op}}{2\, S_f}$

reducing to $P_{ex} = \frac{P_{op}}{8} = \frac{26 \text{ atm}}{8}$

$= 46$ psia.

The temperature at the inlet to the linear cascade is:- =

$$\bar{T}_{ex} = \frac{\bar{T}_{op}}{4} = \frac{1800}{4} = 450^\circ K.$$

5.3 HOT BLOWDOWN CASCADE FACILITY

The cascade tunnel, designed and built specifically for these investigations, is attached to an existing high pressure air supply through a pebble bed heater [29] to form the Hot Blowdown Cascade Facility shown schematically in Figure 5.2. The major components include the following:

Air supply system: Air is supplied from storage of 11 bottles holding a total of 420lb of air at 2400 psia. The bottles are charged by an oil-free air compressor. A two-inch pipe leads from the air tanks to a dome-loading-type pressure regulator, which controls the flow so that the pressure will never exceed the dome's pressure. After the dome, there is a two-inch ball valve which is operated by pneumatic actuator. Its purpose is to shut off the flow immediately at the end of the experiment. The pebble-bed bleed valve is for the purpose of bleeding the system if the test should be cancelled.

Peeble bed heater: The pebble-bed heater is a high-pressure steel tank, 6 feet long and 1.5 feet in diameter, filled with 3500 lb. of soft steel balls. Prior to a run, the pebble bed is heated by means of a propane burner and a steam ejector draws the hot air from the burner through the pebble bed. The burners and two steam ejectors are used in order to heat the pebble bed from both direction and thus achieving a uniform temperature distribution. The bed is designed to keep the mass flow at a constant temperature during the test time. Operating at high pressures help minimized the the cross-section of the bed, while the distance a diffusive cooling wave would travel during the test time basically determined the length of the bed.

Filter Trap: Right at the end of the pebble-bed heater, an in-line fiberglass filter is placed in the pipe, to collect dust particles and particles of iron oxide (3 microns or larger), which get into the air flow from the piping of the air supply system and from the pebble-bed.

Diaphragm Section: The bursting of the main 6" diaphragm with a pneumatically actuated plunger initiates the hot flow thru the cascade.

Metering throat: Just downstream of the diaphragm is located a metering throat, 1.5 ins. in diameter, normally choked under operating conditions. It is instrumented to measure the mass flow.

Supersonic Nozzle and Diffuser. Since the pebble bed heater has to operate at high pressure (up to 1000 psi) to provide the necessary mass flow at a specified cascade inlet pressure (generally less than 100 psia); means of reducing the stagnation pressure is necessary. A supersonic nozzle located downstream of the choked throat and a diffuser accomplish this task. The flow leaving the metering throat expands supersonically through a 7°

cone. At the downstream area corresponding to the correct Mach number for desired pressure reduction thru a normal shock, a supersonic diffuser is installed. A seven to one pressure reduction is obtained across this diffuser.

The compact diffuser is constructed out of 0.25" diameter steel tubes, 6" long. The device is axially movable in the nozzle, so that the diffuser can be adjusted for the desired pressure diffeential.

Transitional-Piece

The subsonic flow coming out of the supersonic diffuser settles down in a long pipe 6 ft. long, 6" in diameter and enters the transitional piece; where the flow is changed from cylindrical form to rectangular. To enhance a healthy flow transition, some area contraction is introduced.

$$\frac{A_{exit}}{A_{inlet}} = \frac{2 \times 12}{\pi 3^2} = 0.84$$

and the exit Mach number is generally in the range of 0.35. From here the flows enters into the cascade section.

Cascade Section

The test section is formed by two rotatable, steel disc side walls (15 inches diameter and 1 inch thick) in which the blades are fixed and cascade section changeable steel-end walls. The end passages of the cascade are full blade passages, the boundaries being either the suction side or the pressure side of a normal blade. The rotatable side walls with changeable end walls allow changes of the stagger angle.

The two side walls are equiped with Pyrex optical window for taking the shadowgraphs of the trailing-edge shock system.
The cascade outlet is formed by a diffuser formed with two adjustable tail boards with sudden area enlargement just downstream of the cascade. A mobile traversing mechanism is installed in one of the tail boards, on which a total pressure-directional probe can be installed to the survey the downstream flow field.

The facility is equipped with a thermal boundary-layer control system. Through an attachment to M.I.T. High-Pressure Steam Ejector, the walls of the tunnels, including all the pipings, up to the cascade inlet, are preheated to the gas temperature by drawing hot air from the gas burners through the pebble-bed heater, while the blades are kept at room temperature by drawing cold air through the cascade at the same time.

5.4 Operation of the Cascade Blowdown Facility

The sequence of operation of the test facility is as follows:
(1) The pebble-bed heater right up to the cascade inlet is preheated to the gas temperature, while venting cold air thru the blades to keep them at room temperature, using the steam ejector. (ii) A diaphragm is quickly put in while the pebble-bed heater and the pipe section leading up to the diaphragm is pressurized.
(iii) The diaphragm is burst and hot test air enters the cascade.
(iv) The test is terminated by a delay switch which initiates the closing of the main valves and bleeding of the dome regulators.

5.5 Tunnel and Cascade Instrumentation

Pressure (P), temperature (T) and heat-transfer rate (q) are the three quantities being measured. From where all the required parameters (M, Re, Nu) are determined in order to monitor the performance of the test facility and evaluate the characteristics of the cascade.

5.5.1 Tunnel Instrumentation

Using pitot tubes and fast-response pressure transducers, total pressures were recorded at the pebble-bed heater, nozzle, and cascade inlet. Static pressures were also measured at the metering throat and cascade inlet using pressure taps on the walls.

Total temperatures were measured using fast-response thermocouples at the nozzle and cascade inlet.

Several thermocouples are also installed along the pebble bed heater, and also in the tunnel wall to record the wall temperature distribution up to the cascade inlet.

Using the measured total pressure and temperature at the nozzle and the known throat area (A^*) the mass flow through the cascade is calculated.

$$\dot{m} = 0.532\ A^*\ P_o / T_o^{0.5}$$

The following mass flow rate ($\dot{m}$) were calculated for the various test conditions:

Tests	T_o ° °R	P_o psia	$\dot{m}$ lbm/sec
1	810	100	3.3
2	810	150	4.95
3	810	2200	6.6
4	810	250	8.25
5	810	300	9.9
6	810	350	11.55
7	810	500	16.5

5.5.2 Cascade Instrumentation

A. Cascade Inlet

Inlet instrumentation consists of total temperature rakes, total pressure rakes and static pressure ports (Figure 5.3). They are located two-chord lenghts in front of the blades.

The total pressure measurements are stagnation readings from pitot tubes, total temperature measurements are with .003" diameter copper constantan thermocouples placed in a .094" diameter cavity drilled in a .166" diameter cylindrical rod with a small bleed hole.

The above measurements were used to determine the temperature and pressure spanwise distribution at the cascade inlet.

B. Blade Instrumentation

Each of the cascades carrying the different blade profiles has 9 blades, and the central blade has been instrumented with 25 pressure and 25 heat-transfer gauges all around the blade profile, using 0.032" O.D. stainless steel tubing buried flush in the blade surface for static pressure distribution measurements and 3/32" diameter x 0.020" thick, aluminum discs for heat transfer measurements. The aluminum discs are joined (spot-welded) to copper-constantan thermocouples and placed in a Teflon FEP insulator cup (.020" thickness all around), and buried flush in the blade surface. (Figure 5.4).

The diffusion time through the aluminum slugs and the time response of the copper-constantan small thermocouples are less than 10 msec.

These gauges have good time response to measure the average heat-transfer rates during the test time of 1 sec. Fast-response Entran pressure transducers are used to read the steady-state pressure. All data are recorded on Bell and Howell oscillographs using sensitive galvanometers.

With these calorimetric gauges, the average heat-transfer rate is determined from the temperature time response of the thermocouples joined to the small aluminum slugs.

5.6 Blade and Cascade Geometry

5.6.1 Reference Convergent Transonic Blade with Straight Suction Back and Thick Trailing Edge (Blade 1)

Blade chord c = 66.0 mm

Blade spacing g = 45.87 i.e. g/c =0. 95

Stagger angle $\gamma = 51^{o}$

Inlet flow angle $\beta_2 = 30^{o}$

Trailing edge thickness, te = 2.8 mm te/c = 0.0424

Number of blades in the cascade = 9

with the central blade instrumented with static pressure taps and heat-transfer gauges.

5.6.2 Transonic Turbine Blade with Unguided Expansion on the Suction Side (Plug Nozzle (Blade 3)

Blade chord c = 66.0 mm

Blade spacing g = 45.87 mm i.e. g/c = 0.695

Stagger angle $\gamma = 51^{o}$

Inlet flow angle $\beta_2 = 30^{o}$

Trailing edge thickness, te = 1.46 mm te/c = 0.0221

Number of blades in the cascade = 9

with the central blade instrumented with static pressure taps and heat transfer gauges.

5.6.3 Blade With Convergent-Divergent Channel (Blade 4)

Blade chord c = 76.0 mm

Blade spacing g = 45.87 mm i.e. g/c = 0.6036

Stagger angle $\gamma = 46.5$

Inlet flow angle $\beta_2 = 30^{o}$

Trailing Edge thickness te = 1.14 i.e. te/c = 0.015

Number of blades in the cascade = 9

with the central blade instrumented with static pressure taps and heat transfer gauges. (Figure 5.4)

5.7 MEASURING AND DATA REDUCTION PROCEDURE

The level of turbulence in the cascade tunnel was first determined. The inlet flow field is determined from measurements of the total pressure and temperature rakes located upstream of the cascade.

During the tests, the mass flow is constant and metered at the upstream choked throat. All the tests were performed at constant inlet stagnation temperature of 450^{o}K while varying the upstream stagnation pressure.

The blade velocity distribution is expressed by the local isentropic Mach number calculated from the local static pressure on the blade and the total pressure upstream of the cascade.

5.7.1 Heat Transfer Measurements

The heat transfer rate is measured by the calorimetric heat transfer gauge, a thin aluminum disc (insulated with Teflon) with copper - constantan thermocouple joined to it.

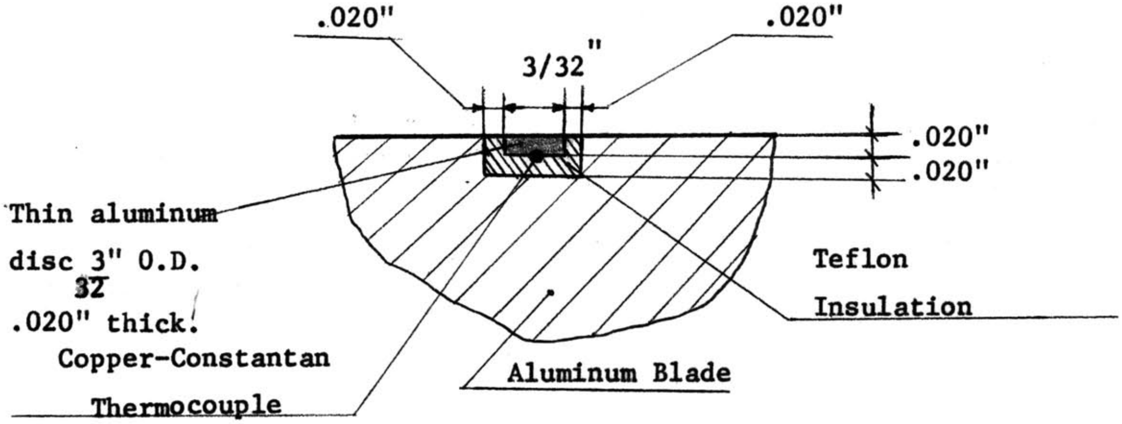

From an ideal case, with zero heat loss through the insulation, the rate at which the gauge internal energy (mCT_g) is changing will be equal to the rate at which heat is being transfered to the gauge

$$\dot{q}_{gauge} = \frac{d}{dt}(m \cdot C \cdot T_g) = h \cdot A \cdot (T_f - T_g) \tag{5.7.1}$$

Taking the mass of the gauge m, its specific heat c, and fluid temperature, T_f as constants, the equation reduces on integration to

$$h = \frac{m \cdot c}{A \cdot t} \ln\left(\frac{T_f - T_w}{T_f - T_g}\right) \tag{5.7.2}$$

Correction For Heat Loss Through Insulation

In actual fact, during the test, heat is lost through the insulating material. $\dot{q}_{gauge} = \dot{q}_{in} - \dot{q}_{lost} = \frac{d}{dt}(m \cdot C \cdot T_g)$ (5.7.3)

Estimate of $\dot{q}_{lost}$.

As the gauge temperature rises; a temperature gradient develops between the gauge and the surrounding insulating material, and heat is lost thru the insulation at the following rate:

$$\dot{q}_{lost} = \frac{K \cdot A \cdot (T_g - T_w)}{\Delta x} \tag{5.7.4}$$

where K - Thermal conductivity of the Teflon insultation

A - Surface area at the gauge-insulation interface.

Δx - Diffusion distance of the heat wave into the insulation.

$$\text{i.e.}\quad \frac{d}{dt}(m \cdot C \cdot T_g) = \dot{q}_{in} - \frac{K \cdot A \cdot (T_g - T_w)}{\Delta x} \tag{5.7.5}$$

$$\frac{d\,(T_g - T_w)}{dt} + \frac{(T_g - T_w)}{\tau} = \frac{\dot{q}_{in}}{m\,C}$$

where $\tau \equiv \dfrac{\Delta x \cdot m \cdot C}{K \cdot A}$.

—— diffusion time through the teflon insulation and is calculated to be 3.2 seconds for the gauge used in the experiment.

The above equation integrates (taking q in/mc as constant) to

$$(T_g - T_w) = \frac{q_{in} \cdot \tau}{m \cdot c}\left(1 - e^{-t/\tau}\right) \tag{5.7.6}$$

The derivative of which is

$$\frac{d}{dt}(T_g - T_w) = \frac{\dot{q}_{in}}{m \cdot c}\, e^{-t/\tau} \tag{5.7.7}$$

Combining with equation 5.7.1, gives

$$\dot{q}_{gauge} = \dot{q}_{in} e^{-t/\tau}$$

$$\therefore \quad \dot{q}_{in} = e^{t/\tau} \cdot \dot{q}_{gauge} \qquad (5.7.8)$$

The correct heat transfer coefficient will then be

$$h = \frac{m \cdot c}{A \cdot t} \ln \left[\frac{T_f - T_w}{T_f - T_g} \right] e^{t/\tau} \qquad (5.7.9)$$

From this the Nusselt number (based on blade chord c) is then calculated.

$$Nu_c = \frac{h \cdot c}{K}$$

Typical readings from the gauges are shown in Figure 5.5a. These are four of the gauges on the reference blade 1. They include the gauge at the stagnation leading edge, the gauge at the trailing edge, a gauge on the blade suction side and one on the pressure side. The curves show that after the correction for heat loss, the scatter in the results is very small (< 3%) except for the first data point (taken at one tenth of a second) where the scatter was large (≃ 10%). This large scatter is due to the fact that up to a tenth of a second a steady condition has not yet been reached in the cascade.

5.8 Tunnel Turbulence Level

The level of turbulence intensity in the tunnel was measured using a Disa Hot Wire Anenometer Set (Disa 55D05 Hot Wire, Disa 55D15 Linearizer and Disa 52A40 Power Supply). A conical hot film probe (SSA81) was used and output signals were recorded on an oscilloscope.

As proposed by King and verified in many subsequent studies, a wire with resistance R, and temperature coefficient α will obey the following law when immersed in a fluid moving at a velocity U, normal to the wire.

$$\frac{I^2 R \alpha}{a} A_1 + B_1 \sqrt{U} \qquad (5.8.1)$$

where A_1, B, - empircal constants

R_o - resistance of hot wire at fluid temperature

I - heating current

According to this formula, the rate of heat loss Q and flow velocity are related

$$Q = \left(A_1 + B_1 \sqrt{U}\right)\left(T - T_o\right) \qquad (5.8.2)$$

where T - wire temperature

T_o - fluid temperature

For thermal equilibrium conditions, the rate of heat loss from the wire must equal the heating power $P = I^2R$, generated in the wire by electric current.

Incorporating the temperature difference between the wire and the fluid in the constants A and B, Kings formula takes this simple form

$$\frac{E^2}{R} = A + BU^n \qquad (5.8.3)$$

where E - bridge voltage

U - mean flow velocity

R - probe operating resistance

A,B - constants

at $U = 0$, $A = Eo^2/R$

Therefore, $E^2/R = Eo^2/R + BU^n$ (5.8.4)

differentiating both sides of equation 5.8.4.

$$2E\frac{dE}{R} = nBU^{n-1}dU = nBU^{n}\frac{dU}{U}.$$

$$\therefore \frac{dU}{U} = \frac{2E\,dE}{R\cdot nBU^{n}} = \frac{2E\,dE}{Rn\left[\frac{E^{2}}{R}-\frac{E_0^{2}}{R}\right]}$$

$$= \frac{2E\,dE}{n(E^{2}-E_0^{2})}$$

$$\text{for } n=\frac{1}{2}\,; \quad \frac{\Delta U}{U} = \frac{4E\,\Delta E}{E^{2}-E_0^{2}}$$

where U - RMS of the fluctuating velocity

E - RMS voltage (from true RMS Voltmeter)

U - Average velocity

$$\frac{\Delta U}{U} = \frac{4(2.0)(0.05)}{2^{2}-0^{2}} = 0.10 \pm 0.02$$

Therefore percentage of the turbulence level = 10% ± 2%

5.9 Inlet Flow Field

From the readings of the total pressure and temperature rakes, the spanwise pressure and temperature profiles at the cascade inlet are calculated and shown in Figure 5.5b.

They show a relatively uniform inlet flow field spanwise except close to the walls where exist a defect in the pressure profile near the wall, due to the boundary layer.

5.10 BLADE PRESSURE DISTRIBUTION

Plots of the blade pressure (Mach number) distributions are shown in figures 5.6 thru 5.8. A very fast expansion takes place or the suction side with the Mach number reaching its first peak, at a location where the first surface roughness (bump) is located on the blade. The flow decelerates a bit and quickly starts to accelerate again, until when it hits the left-running shock, from the neighbouring blade, downstream of which the flow decelerates and later accelerates.

towards the trailing edge on the suction-side.

As the pressure ratio increases, the shock moves downwards towards the blade trailing edge and this represents a typical pattern of pressure distribution on the suction side for all the blades.

On the pressure side, a rapid acceleration follows up from stagnation point; that quickly stops close to the leading edge and later gradually accelerate to its maximum value, which occurs at the blade trailing edge. Once the flow was choked there was very little change (almost insignificant) in the pressure side pressure distribution.

All the blade profiles tested featured the same typical variation in Mach number (pressure) distribution-differing only in absolute values of the peaks; strength and locations of the shocks hitting the suction sides. Since all the blades showed the same tendency to peak at nearly the same place on the suction surface, it would seem more logical to attribute this peak to the geometry (large curvature) of the blade.

5.11 COMPARISON BETWEEN BLADE PRESSURE DISTRIBUTION OBTAINED IN THE HOT BLOWDOWN CASCADE FACILITY AND THAT OBTAINED IN V.K.I. HIGH SPEED WIND - TUNNEL

A detailed comparison is made between the Mach number distribution around the blade obtained on the Hot Blowdown Cascade facility with those obtained in VKI High Speed Wind -tunnel. (Figures 4.7 thru 4.10, and 5.6 thru 5.8). On the whole the overall pattern of the Mach number distribution was similar. Fast acceleration from stagnation point on the suction side leads to the first peak of Mach number. But here the location and absolute value (magnitude) of the peak were different in both cases. The peak shifted forward in the tests conducted on the Hot Blowdown Cascade Facility. There are several possible reasons for this. First, it must be recalled that the experiment on the Wind-tunnel at VKI was a cold flow investigation ($T_g/T_b = 1$) with low level of turbulence 0.7%, whereas experiments on MIT Cascade Facility was a hot flow, (Inlet stagnation temperature of 450°K, $T_g/T_b = 1.5$) and high turbulence level (10%). Schlieren photos taken at VKI showed a distinct region with separation bubble on the blade suction side. A combined effect of large blade curvature and surface roughness (bump) could have triggered this separation while the distinct region served to generate the necessary turbulence in the shear layer to reattach the flow. Unlike the tests at MIT, the high freestream turbulence provided the turbulence necessary for a quick turbulent flow reattachment and thus created an earlier transition.

Another possible reason could be argued if we remember that there are fewer pressure taps on the blade tested here in the Hot Blowdown Cascade facility. There were 25 pressure taps and 25 Heat Transfer gauges evenly distributed all around a single instrumented blade as compared to instrumenting two blades (that formed the central channel) with 36 pressure taps on the suction side and 22 on the pressure side in the tests in VKI Wind Tunnel. Thus pressure taps were not as closely located and the exact location of the peak could have been missed.

But on the whole the overall pattern of the pressure distribution were the same. The correct peaks of the Mach number before, at and after the shock could not be exactly located but the distribution still shows the existence and movement of the shocks correctly.

A good agreement is seen on the pressure side with gradual Mach number increase up till the trailing edge.

5.12 Blade Heat Transfer Distribution

The Blade Heat Transfer Distributions are plotted in Figure 5.9 thru 5.16. Plots of the local Nusselt number N_u as a function of the relative coordinate $\bar{X} = X/c$; and plots of $N_u/Re^{0.8}$ versus $\bar{X}$ are all shown -- (Additional curves of $\frac{N_u}{Re^{0.5}}$ versus $\bar{X}$ and $\frac{N_u}{Re^{0.6}}$ versus $\bar{X}$ were drawn for the Reference Blade 1)

To aid the understanding of the curves for heat transfer and static pressure distributions, a typical pattern of heat transfer and of dimensionless pressure coefficient have been drawn on polar diagrams round the blade surface. (Figures 5.17 thru 5.20).

On the whole the external flow pressure distribution and level of turbulence as expected, have greatly influenced the boundary layer flow which in turn, practically dictate the heat transfer structure on the blade surface. It is remarkable to see similar effect of shock boundary layer interaction on both the pressure and heat transfer distribution around the blade.

Generally the pattern is like this. On the suction side from the leading edge, the pressure distribution indicate a very fast acceleration up to a minimum pressure, a condition very favourable for the formation of a laminar boundary layer and thus the Nusselt number decreases. Transition from laminar to turbulent flow then jumped up the Nusselt number sharply. The Nusselt number thereafter fluctuates up and

and down similar to the behavior of the pressure distribution in this area, until it hits the left running shock coming from the trailing edge of the neighbouring blade. Downstream of the shock, the Nusselt number drops significantly and later starts to increase as the flow accelerates toward the trailing edge.

On the pressure side, from the leading edge, the pressure distribution indicates again a rapid acceleration conducive to the maintenance of laminar boundary layer, and as a result, the Nusselt number first falls. Transitional boundary layer occurs at $x/c = .3$ and further the Nusselt number increases all the way towards the trailing edge similar to the rapid decrease in pressure up to the trailing edge on the pressure side. This increase in Nusselt number is merely caused by the thinning of the boundary layer due to favourable pressure gradient.

It must be mentioned that a high level of heat transfer is recorded close to the trailing edge, amounting to about 75% of the mean value measured at the leading-edge region. And on the whole it is generally noticed that zones with variation in heat-transfer rate coincide with zones of variation in pressure (Mach number) distribution.

In all the cases, straight lines have been used to connect all the data points. And because of the relative distances between the data points, the true picture of the heat-transfer distribution, in particular the exact values and locations of the peak would not be exactly the same as here. The heat transfer gauge (3/32" diameter) itself is averaging over a certain area, across which the Nusselt number could have varied very significantly, reminding us that the so-called local-heat-transfer distribution is in fact an average over a certain small area in that region or location.

5.13 COMPARISON BETWEEN EXPERIMENTAL HEAT-TRANSFER DATA AND AN AVAILABLE NASA THEORETICAL PREDICTION

5.13.1 Theoretical Prediction Based on Hot-Blowdown-Cascade Blade Pressure Distribution(as input)

A comparison between the experimental results and values obtained by available theoretical method is shown in Figures 5.21 thru 5.26. A modified NASA Compressible Laminar and Turbulent Boundary Layer Program (Reference 63) is used to predict the heat transfer distribution (Appendix B).

As input into the program, the experimental pressure distribution obtained from the Hot Blowdown Cascade Tests were used.

The curves (Fig. 5.21 thru 5.26) did not agree point by point but on the whole the general pattern was the same, and it was an agreement good enough for such a complex quantity as the heat-transfer coefficient. There are obvious reasons for the differences in the curves. On the part of the NASA program, there are principal limitations. Surface curvature, surface roughness, initial turbulence level of the freestream and shock-boundary-layer interactions are not taken into account by the program.

From the experimental side, the physical size of the gauge (3/32" diameter X0.020" thick aluminum discs) reminds us that we are averaging over a certain surface area, across which the heat transfer could have varied sharply.

The most obvious discrepancy between the two results occured as a result of two different locations for the transitional point. The experimental data showed an earlier transition to turbulent flow than the theoretical prediction.

There are several possible reasons for this. The theoretical prediction, as mentioned earlier does not take into account the freestream turbulence, while it assumes an adiabatic wall. The experiment on the other hand is experiencing two opposing effects. High level of freestream turbulence tends to destabilize the laminar boundary layer and forces an earlier transition, while the heat transfer across the boundary layer to the blade acts to stabilize the boundary layer by dissipating the energy of turbulence. This will tend to delay transition. The net effect when coupled with the effect of the blade surface roughness (the blades in fact do have bumps in this region of interest) and could have caused the early transition.

On the pressure side though, the experimental data on the heat transfer suggest that instead of having a transitional point, a transitional region in fact existed. This is possible under the favourable pressure gradient in this region and indicating that spread spread of turbulence through the boundary layer is probably gradual

5.13.2 Theoretical Prediction using VKI Wind Tunnel Cold Flow Blade Pressure Distribution.

Another series of theoretical predictions were done, this time using the experimental pressure distribution obtained from cold flow

VKI Wind Tunnel tests. This is of particular interest since in the absence of theoretical potential-flow solution, the next available is the experimental pressure distribution from the cold-flow wind-tunnel, normally with low level (1%) of turbulence.

The three curves (experimental data, theoretical prediction based on high-turbulence hot-flow blade pressure distribution and theoretical prediction using low turbulence cold flow) are shown in Figures 5.27 thru 2.59.

The prediction based on low turbulence cold flow is very similar to that based on high-turbulence hot flow except for the location of the suction-side transition point. There were differences in absolute and location of peaks but apart from this, they almost match point by point (almost no difference in the predictions for the pressure side).

The low turbulence cold flow has the most delayed transition as expected. This is definitely the effect of the difference in the free-stream on the transition of the boundary layer.

5.13.3 TRANSITION POINT

Several investigations[52,53,54 and 56] carried out have shown that the main flow level of turbulence exerts considerable influence on the stability of laminar boundary layer and on heat transfer. Effect of turbulence on losses in turbine cascades is shown in the structure of the boundary layer. Friction losses and intensity of heat exchange can alter several-fold, of course, depending on whether the flow regime in the boundary layer is laminar or turbulent. Hence it is essential to know the true location of transition.

Normally in the absence of high scale surface roughness flow in the boundary layer changes from laminar to turbulent either through instability resulting from the growth in thickness of the laminar boundary layer or through turbulent reattachment after laminar separation. Studies on the behavior of turbulent boundary layers in accelerating flows[41,42] have shown that when the acceleration is severe enough and acceleration parameter $K=\frac{\nu}{U_e^2}\frac{dU_e}{dx}>3\times10^{-6}$, the originally turbulent layer undergoes a reversion towards laminar just as in this experiment.

Unfortunately, quantitative datas on the influence of freestream turbulence level on transition, heat transfer[52,53] and losses are scanty and the few that are available substantially differ.

Zysina-Molozhen[54,55] and others have been studying the effect of turbulence on transition in the boundary layer of gas turbine blades. They came up with an empirical formula for calculating the Reynolds number at the beginning of transition R_{exit}; as a function of the level of turbulence Tu, wall to gas temperature ratio; and Mach number.

$$R_{extr} = 0.71\ X10^{6}(1 + 3M_o{}^{1.7})\ Tu^{-1.76}\psi^{-2.3}(1 + 38M_1{}^{0.6})$$

where M_o - is the Mach number of the flow at maximum velocity before transition.

M_1 - is the Mach number of the flow at cascade inlet.

ψ = Tw/Tg

A plot[54] of R_{extr} versus Tu (turbulence level) for typical valves of M_1, M_0, ψ - have shown that R_{extr} decreases rapidly when Tu increases from 1.5 to 3% indicating that transition point moves forward and then remains at a relatively fixed position. (Figure 5.30)

The authors of ref. 54 & 55 however noticed that for Tu $>$ 4.5% the dependence alters and some stabilization is observed in R_{extr}, having reached the value of $R_{extr} = 1.2 \times 10^5$, noticeably ceases to decline with a further increase in turbulence. It is as though it reaches the maximum possible displacement of the transitional point upstream.

But the quantity Re_{xtr} cannot truely be a good measure of the transition point since it takes no account of acceleration of the flow. Re_{θ} would have been a much better measure.

In the experiment, transition is controlled by the streamwise pressure history (turbulent reattachment after laminar separation). The rapid rise in Nusselt number which occurs at $x/c = 0.20$ on the suction surface and $x/c = 0.35$ on the pressure surface is taken as evidence of transition.

Whatever could have shifted the transition-point to its present location, it is clear that knowing its exact location, and forcing the theoretical program to start to calculate turbulent boundary layer from there will greatly improve the quality of the theoretical heat transfer prediction.

5.14 Heat Transfer at the Blade Leading Edge Region

It has been shown by numerous investigators that with increasing flow turbulence, heat transfer is intensified over the entire leading surfaces of cylinders of sphere traverse to the flow, particularly in the vicinity of the frontal stagnation point.

Kestin and others[52,60,61] have correlated heat transfer in the frontal stagnation point of a cylinder as

$$\frac{Nu}{\sqrt{Re}} = f(Tu\sqrt{Re}) \qquad (5.14.1)$$

This relationship is based on the assumption that heat transfer is intensified in this case by eddies generated in the boundary layer near the stagnation curve by flow turbulence, with the distance between the eddies (wavelength) being inversely proportional to the Re number.

Dyban and other[51] suggested, from general consideration of similarity theory, the use of the turbulent Re number (Tu Re) and correlation data by the expression.

$$Nu_{Tu} = \varepsilon_{Tu} \, Nu_{Tu=0} = f(Re_{Tu}) \, Nu_{Tu=0} \qquad (5 \cdot 14 \cdot 2)$$

A comparison is made between the experimental heat transfer data obtained at the leading edge with predictions based on empirical and semi-empirical formulation of other workers listed below.

5.14/1 Correlation of Kestin and Wood[52]

Kestin and Wood formulated that in the range $0 < (Tu \, Re^{1/2}) < 40$, heat transfer at the leading edge could be expressed as

$$\frac{Nu}{Re^{0.5}} = 0.945 + 3.48 \left(\frac{Tu \cdot Re^{1/2}}{100} \right) - 3.99 \left(\frac{Tu \cdot Re^{1/2}}{100} \right)^2 \qquad (5 \cdot 14 \cdot 3)$$

here, the turbulence level, Tu, is expressed as an absolute fraction (as opposed to a percentage) and Re number is based on leading-edge diameter and inlet flow stagnation parameters. All the tests described in this thesis lie in the range $16.3 \leq Tu \, Re^{1/2} < 27.6$

5.14.2 Smith and Kuethe's.[60] Correlation

On basis of a semi-empirical theory, Smith and Kuethe were first to suggest the use of single correlation parameter Tu $Re^{1/2}$. According to their theory:

$$\frac{Nu}{Re^{1/2}} = 0.9762 + 0.0138\, Tu \left(Re \times 10^{-3}\right)^{1/2} - 1.32 \cdot 10^{-6} \left(Tu\, Re^{1/2}\right)^{2} \qquad (5.14.4)$$

5.14.3 Mujumdar A.S. and Douglas W.J.M[62]s Correlation

Mujumdar and Douglas observed that a better correlation could be made in terms of turbulent Reynolds number, Re_T(= Tu Re) instead of the single parameter, Tu$Re^{1/2}$, and gave this correlation.

$$\frac{Nu}{Re^{1/2}} = 0.981 + 1.017 \times 10^{-4} Re_T + 2.74 \times 10^{-9} Re_T^{2} \qquad (5.14.5)$$

5.14.4 Dyban E.P; Epik E.Ya, and Kozlova L.G.[51] Correlation

Judging from the results of their wide range experimental investigations on heat transfer in the vicinity of the front stagnation point of a cylinder in traverse flow, Dyban, Epik and Kozlova concluded that freestream turbulence affects heat transfer in that critical point in the same manner as Reynolds number does.

Using turbulent Reynolds number, $Tu'Re$, they came out with emperical formulation:

$$\varepsilon_0 = \frac{Nu_0}{Nu_{Tu=0}} = 1 + \frac{0.8\, Re\, \overline{Tu}'}{1500 + Re\, \overline{Tu}'} \qquad (5.14.6)$$

where Nu_o - Nusselt number at stagnation point in turbulent flow

$Nu_{Tu=o}$ - Nusselt number at stagnation point in zero turbulence

$\mathcal{E}_o$ - the ratio of the two valves above

Tu' - percentage level of turbulence

and Re = Reynolds number based on leading-edge diameter and inlet flow conditions.

Computed results using these empirical formulations are compared with results of experimental datas obtained here. (Table 8, and Figure 5.31)

The results show that the measured Nu_d at the blade leading edge were consistently lower by as much as 30% than the predicted values in all the cases except for the Smith and Kuethe semi-empirical correlation, where the differrence have decreased to less than 7%.

It must be remembered that there is a generally noted disagreement with Smith and Kuethe correlation for $Tu\, Re^{1/2} > 20$. As Kuethe, himself has indicated[52], the theory would require modifications for $TuRe^{1/2} > 20$. Since the experiments reported here were in range $16.3 \leq TuRe^{1/2} \leq 27.6$; it means the agreement between the experimental datas and Smith/ Kuethe correlation should not be taken seriously.

There is no doubt that the measured Nu_d were consistently lower than its true value. An explanation for this is the possibility that the leading-edge gauge could not have exactly been placed at the stagnation point and even, if it was, we are averaging over an area in the leading edge zone, where there is a very sharp gradient of pressure and heat transfer. Ratio of gauge diameter to leading edge diameter =0.5.

It is therefore not unreasonable to indicate that the maximum heat transfer at the L.E. may not have been recorded but instead just averaged out over a certain area of the leading edge region.

TABLE NO. 8

Test	Re_d $X10^{-4}$	Kestin and Wood's Correlation ←	Smith and Kuethe's semi-emperical Theory Nu_d	Mujumdar and Douglas Correlation →	Dyban, Epik and Kozlova Experimental Correlation →	Test Results Reference Blade Nu_d
1	2.657	229.215	160.226	207.105	276.58	160.15
2	3.4875	271.859	183.74	255.66	317.05	190.99
3	4.2348	307.075	202.622	300.62	349.49	223.68
4	4.9821	339.944	219.92	347.24	379.17	260.74
5	6.1447	387.322	244.466	423.73	421.2	295.56
6	7.6392	442.787	272.87	272.87	530.06	330.96

5.5 Effect of Mach Number on Blade Mean Nusselt Number

An attempt was made to correlate the effect of Mach number on the blade heat transfer. Variations of Nu/Re^n, for various values of n (n = 0.5,0.66,0.8 & 1.0) and Stanton number as a function of the dimensionless chordwise location x/c were investigated and shown in Figures 5.33 through 5.36.

Unfortunately the shock movement on the suction side makes it impossible to arrive at a meaningful quantitative correlation.

A plot of mean Nu/Re^n, obtained from the area measurements of the heat transfer distribution curves, for the entire blade surface is plotted as a function of exit Mach number in Figure 5.37. It shows that the mean heat transfer to the blade increases with Mach number.

A comparison is also made between the measured blade mean Nusselt number with several available experimental data. As shown in Figure 5.38; our experimental data lie in the upper region (high valves) which is expected as a result of the high level of turbulence at which we operated.

Finally a comparison of the mean heat transfer (Stanton number) to all the blades tested as a function of exit Mach number is made. It shows that the average heat transfer coefficient to blades 1 & 3 is about the same while the convergent-divergent blade has a higher stantum number. (Figure 5.39).

CHAPTER 6

PROSPECTS FOR TRANSONIC TURBINES

6.1 Overall Assessment

For transonic turbines to be attractive and compete very well with the present subsonic turbines it must show clear advantages and promising potentialities in the two foremost areas of interest to gas-turbine - namely, reduction of engine weight and specific fuel consumption (i.e. higher efficiency).

As far as weight reduction is concerned, there is no question about the superiority of high-pressure ratio transonic (and supersonic) stages over subsonic ones. Several studies, including this one, have demonstrated that with higher and higher enthalpy drop across the stage and the corresponding jump in fluid velocity to supersonic regime, large improvement in stage loading can be achieved, resulting in fewer stages. But the very important factor that can influence the future of these highly-loaded transonic turbine stages are both the level of efficiency at which they will operate in supersonic flows and the amount of cooling air flow required.

The desire for higher specific thrust (specific power) has always provided a powerful incentive to increase the turbine inlet temperature T_{01}. Fuel consumption, a crucial problem in these days of energy-crisis, also improves if the increased temperature is accompanied by an increase in compressor pressure ratio. It will not be an exaggeration to state that the main course of development of gas turbine engines and powerplants of all types is to increase the turbine inlet temperature.

Although improvements in the high temperature properties of materials have allowed gas temperature to rise steadily since the initial development of the gas turbine, cooling techniques of varying degrees of sophistication have made practicable operating conditions which otherwise would have remained metallurgically impossible for many years to come.

However cooling is accompanied by energy losses which counteract the gains resulting from increased temperature [64,65]. The question then is this.: Is the cooled-highly-loaded transonic stage more desirable, than the cooled subsonic turbine stage, efficiency wise.

At least two important parameters that will greatly affect the decision as to which is more desirable are:-

(1) the efficiency of the cooled stages (transonic and subsonic)

(2) the amount of coolant mass flow required in each case (for the same work-output), $\dot{m}_c$

But before investigating each of this parameters (η_{stage}; $\dot{m}_c$), a word is needed on the type of cooling technique being anticipated. Out of all the several schemes being anticipated, and of all the several schemes being proposed for turbine cooling[38,39,40,46,47,48], transpiration (effusion) cooling in the most promising for application in advanced high temperature engines since it offers the largest reduction in coolant mass flows for any given blade temperature. So far, problems of structural integrity, and plugging of the porous wall have prevented its application in production engines. Film cooling, next best to transpiration, offers a more engineeringly viable solution and a study[65] of a model of combined convection and film cooling schemes came to the conclusion that it is important to utilize the maximum thermodynamic internal convective cooling potential of the coolant before its utilization for film-cooling.

It is therefore not unreasonable to anticipate a combined internal convective cooling with film cooling for these high temperature turbine blades.

6.2 Comparative Studies

For this comparative study, let us consider a case where one highly loaded transonic turbine stage is used to replace two conventional subsonic turbine stages.

It is assumed that the mass flow rate $\dot{m}g$, turbine inlet stagnation temperature T_{01} and pressure P_{01}, work-output and tip speed are the same in both cases. In addition, the axial velocity is assumed constant in both cases .

For the Transonic Turbine:-

Number of stages = 1

Stage Stagnation Pressure Ratio = 4

Turbine Inlet Stagnation Temperature = 1800°K.

For the Subsonic Turbine:-

Number of stages = 2

1st. Stage :- Stage Pressure Ratio = 2

Turbine Inlet Stagnation Temperature = 1800°K

2nd Stage:- Stagnation Pressure Ratio = 2.

Gasdynamic Analysis of the two Turbines

Gasdynamic analysis of the Transonic Turbien Stage has been carried out and the results given in Table Number 1. A similar analysis is now carried out here for the two stages of the Subsonic Turbines.

Turbine 1st Stage:-

$$T_{01} = 1800^{\circ}$$

$$\frac{P_{01}}{P_{03}} = 2$$

$$\frac{T_{01}}{T_{03}} = \left(\frac{P_{01}}{P_{03}}\right)^{\frac{\gamma-1}{\gamma}\eta} = 1{\cdot}155$$

$$\therefore T_{03} = 1560^{\circ}K$$

$$\Delta T_0 = 1800 - 1560^{\circ}K$$
$$= 240^{\circ}K.$$

Specific Work Output

$$\Delta W = \bar{C}_p \cdot \Delta T_0 = \frac{\gamma}{\gamma-1}\frac{R}{M}\Delta T_0$$
$$= 299154{\cdot}93 \ \frac{M^2}{Sec^2}$$

For the 2nd Stage

$$T_{01} = 1560^{\circ}K$$

$$\frac{P_{01}}{P_{03}} = 2 \quad ; \quad \frac{T_{01}}{T_{03}} = 1{\cdot}155$$

$$T_{03} = 1350^{\circ}K.$$

$$\Delta T_0 = 210^{\circ}K.$$

The detailed multi-stage analysis is shown in Table 9.

Table 9

	Stage Parameter	1st. Stage	2nd. Stage
1.	Design Parameters		
(a)	Turbine Inlet Total Temperature	1800°K	1560°K
(b)	Stage Stagnation Pressure Ratio	2	2
(c)	Blade Speed, U	550 m/s	550 m/s
(d)	Target Total to total polytropic efficiency	0.9	0.9
2.	Stagnation Temperature Drop across Stage $\Delta T_0 = T_{01} - T_{03}$	240°K	210°K
3.	Stage Specific Work Output. $\Delta W = \bar{C}_p \Delta T_0$	299154.9	260887.6
4.	Change in Tangential Vel, $\Delta C_y = \frac{\Delta W}{U}$	543.92	474.34
5.	Tangential Components of the Velocities		
	$W_{y3} = \left(\frac{\Delta C_y + U}{2}\right)$	546.47	512.17
	$C_{y3} = Wy_3 - U$	-3.53	-37.83

Stage Parameter	1st. Stage	2nd. Stage
$W_{y2} = C_{y3}$	-3.53	-37.83
$C_{y2} = W_{y2} + U$	546.47	512.17
6. Rotor Inlet and Exit Velocities		
$C_2 = \sqrt{C_x^2 + C_{y2}^2}$	657.16 m/s	628 m/s
$W_2 = \sqrt{W_x^2 + W_{y2}^2}$	365.02 m/s	367 m/s
$C_3 = \sqrt{C_x^2 + C_{y3}^2}$	365.02 m/s	367 m/s
$W_3 = \sqrt{W_x^2 + W_{y3}^2}$	657.16 m/s	628 m/s
7. Static Temperatures & Acoustic Velocities at Rotor Inlet and Exit		
(a) $T_2 = T_{02} - \frac{C_2^2}{2C_p}$	1626.19°K	1401.27°K
(b) $a_2 = \sqrt{\gamma \frac{R}{m} T_2}$	778.51	722.67
(c) $T_3 = T_{03} - \frac{C_3^2}{2C_p}$	1506.37	1295.79
(d) $a_3 = \sqrt{\gamma \frac{R}{m} T_3}$	749.28	694.94
8. Mach Number at Rotor Inlet & Exit		
(a) Absolute Inlet Mach No, $M_{c2} = C_2/a_2$	0.84	0.87

	Stage Parameter	1st. Stage	2nd. Stage
(b)	Relative Inlet Mach No. $M_{w2} = W_2/a_2$	0.47	0.51
(c)	Axial Inlet Mach No; $M_{cx2} = Cx/a_2$	0.47	0.51
(d)	Absolute Exit Mach No, $M_{c3} = c_3/a_3$	0.49	0.53
(e)	Relative Exit Mach No. $M_{w3} = W_3/a_3$	0.88	0.90
(f)	Axial Exit Mach No. $M_{cx3} = c_x/a_3$	0.49	0.53
9.	Stagnation Temperature at Rotor Inlet		
	Absolute T_{02}^{ab}	$1800^{\circ}K$	$1560^{\circ}K$
	Relative T_{02}^{rel}	1679.81	$1455.48^{\circ}K$
10.	Stagnation Temperature at Rotor Exit		
	Absolute T_{03}^{ab}	$1560^{\circ}K$	$1350^{\circ}K$
	Relative T_{03}^{rel}	1679.81	$1455.48^{\circ}K$
11.	Stage Loading Coefficient $\psi = \frac{C_p \Delta T_0}{U^2}$	0.99	0.86
12.	Stage Flow Coefficient $\phi = \frac{C_x}{U}$.	0.66	0.66

6.2.1 Estimate Of The Coolant Flow Requirements Using Film Cooling

As mentioned above in section 6.1, film cooling of varying degrees of sophistication offers a more practical and engineeringly viable solution for high temperature turbine blade cooling.

According to film-cooling effectiveness data on flat plates gathered at M.I.T. Gas Turbine Lab. by Louis and others, a correlation[83] incorporating the effect of geometry on film cooling effectiveness, shows that for double row of holes, with injection angle of 20°, gives

$$\eta_{isoth} = 156.17\left(\pi^{*1.41}\cdot\frac{4}{\pi}\right)^{-.24}\left(m^{-1.35}\,\theta^{-0.68}\right)^{-.24}\left(\frac{x}{D}\cdot\frac{y_1}{D}\right)^{-.24} \qquad (6.2.1)$$

$$= 156.17\left(\pi^{*1.41}\frac{4}{\pi}\right)^{-.24}\left(K_o^{-1.35}\right)\left(\frac{x}{D}\cdot\frac{y_1}{D}\right)^{-.24}$$

where $m = \dfrac{\rho u_c}{\rho u_g}$;

$\theta = \dfrac{T_{c\,exit}}{T_g}$

$K_o^2 = \dfrac{\rho u_c^2}{\rho u_g^2}$; $K_o = m\sqrt{\theta} = \dfrac{M_c}{M_g}$.

$\pi^* = \pi$

The main flow $\dot{m}_g = \rho_g U_g \cdot A_g = (\rho_g \cdot U_g)\, S \cos\beta_{throat} \cdot h$.

Coolant flow $\dot{m}_c = 2.48\dfrac{C}{x} \cdot \dfrac{\pi D^2}{4} \cdot \dfrac{h_1}{y_1}\, \rho_c \cdot U_c$.

here the perimeter of the blade profile is taken as 2.48C, just as in the case of reference blade 1

$$\therefore \frac{\dot{m}_g}{\dot{m}_c} = \frac{4}{2.48\pi} \cdot \frac{S}{C} \cdot \cos\beta\, \frac{\rho U_{g\,throat}}{\rho U_c} \cdot \frac{x}{d} \cdot \frac{y_1}{d} \qquad (6.2.2)$$

Combining equations 6.2.1 and 6.2.2, we get the following expressions:-

For $\eta_{isoth.} > 62\%$ i.e. $A_2 < 45$

$$\frac{\dot{m}_c}{\dot{m}_g} = 1.944\,\eta^{4.17}\,\frac{m'}{m}\,m^{-0.35}\,\theta^{-0.68}\left(s/c\,\cos\beta\right)^{-1} \qquad (6.2.3)$$

where $m' = \dfrac{\rho u_c}{\rho u_{g\,throat}}$.

For $33.4\% < \eta_{isoth.} < 62\%$; i.e. $45 < A_2 < 180$

$$\frac{\dot{m}_c}{\dot{m}_g} = 0.833\,\eta^{2.273}\,\frac{m'}{m}\,m^{-0.35}\,\theta^{-0.68}\left(s/c\,\cos\beta\right)^{-1} \qquad (6.2.4)$$

For $\eta_{isoth.} < 33\%$. i.e. $A_2 > 180$

$$\frac{\dot{m}_c}{\dot{m}_g} = 0.380\,\eta^{1.538}\,\frac{m'}{m}\cdot m^{-0.35}\,\theta^{-0.68}\left(s/c\,\cos\beta\right)^{-1} \qquad (6.2.5)$$

where $A_2 = \pi^{*\,1.41}\,m^{-1.35}\,\theta^{-0.68}\,\dfrac{x}{S_{eq}}$.

with $\dfrac{x}{S_{eq}} = \dfrac{4}{\pi}\cdot\dfrac{x}{d}\cdot\dfrac{y_1}{d}$ for double row of holes

$$\frac{m'}{m} = \frac{\dfrac{\rho u_c}{\rho u_{g\,throat}}}{\dfrac{\rho u_c}{\rho u_{g\,injection}}} = \frac{(\rho u_g)_{injection}}{(\rho u_g)_{throat}} = \frac{A^*}{A_{inject^n}} = 0.63$$

for the reference blade 1

Equation 6.2.3, which is of high values of $\eta_{isothermal}$ is used in this analysis.

According to the definition of film cooling isothermal effectiveness

$$\eta_{isoth} = \frac{q' - q''}{q'} \qquad (6.2.6)$$

where q' - heat transfer to the blade in the absence of film cooling

q' - heat transfer to the blade with film cooling

$q'' = (1-\eta_{isothermal})q'$ and this must be handled by the internal cooling

$$\text{i.e. } q'' = \dot{m}_c\,\bar{C}p_c\,(T_{c.exit} - T_{c.m}) \qquad (6.2.7)$$

Let us define an internal cooling effectiveness

$$\epsilon = \frac{T_{c\,exit\cdot} - T_{c\cdot in\cdot}}{T_{blade} - T_{c\cdot in}} \qquad (6.2.8)$$

ϵ varies from 0.0 to 1, higher values of ϵ generally $>$ 0.5 are of interest. ϵ is a strong function of the type of internal cooling; its configuration, coolant flow Reynold number, etc.

Tc_{in}, Tc_{exit} - coolant inlet and exit temperatures respectively

combining equation 6.2.7 and 6.2.8 results in

$$q'' = \dot{m}_c \cdot \bar{C}_{p_c} \cdot \epsilon \left(T_{blade} - T_{c\cdot in}\right)$$

$$\dot{m}_c = \frac{\dot{q}''}{\bar{C}_{p_c} \cdot \epsilon \left[T_{blade} - T_{c\cdot in}\right]}$$

$$= \frac{(1-\eta)\, q'}{\bar{C}_{p_c} \cdot \epsilon \left[T_{blade} - T_{c\cdot in}\right]}$$

$$= \frac{(1-\eta)\, 2.48\, \sigma\, St \cdot \rho \cdot U \cdot \bar{C}_{p_g}\, S \left(T_g - T_b\right) K_1}{\bar{C}_{p_c}\ \epsilon \left[T_{blade} - T_{c\cdot in}\right]}$$

where St - blade mean Stanton number

$$\frac{\dot{m}_c}{\dot{m}_g} = \frac{(1-\eta)\, \frac{A^*_{throat}}{A_{exit}}\, (2.48)\, \sigma \cdot St \cdot C_{p_g} \cdot K_1 \left(T_g - T_b\right)}{\bar{C}_{p_c} \cdot \epsilon \left[T_b - T_{c\cdot in}\right] \cos\beta\,\cdot} \qquad (6.2.9)$$

where the ratio $\frac{A^*_{throat}}{A_{exit}}$ comes from $\frac{(\rho U)_{g.exit}}{(\rho U)_{g.throat}} = \frac{A^*_{throat}}{A_{exit}} = 0.86$

for the reference blade.

k_1 - is the coefficient that takes into account the effect of blade rotation. Using experimental correlation of references 38, 39 & 40 k_1 is taken to be 1.5.

β — exit angle at the throat.

$$\left[\frac{\dot{m}_c}{\dot{m}_g}\right]_{\substack{film\\cooling}} = k_2 \left[\frac{\dot{m}_c}{\dot{m}_g}\right]_{\substack{internal\\cooling}}$$

where k_2 - fraction of internal cooling being used for film cooling and taken to be 1 in this analysis.

Equations 6.2.3 and 6.2.9 are coupled and solved simultaneously.

$$\frac{\dot{m}_c}{\dot{m}_g} = 1.2247\, \eta^{4.17}\, m^{-0.35}\, \theta^{-0.68} \left(S/c \cos\beta\right)^{-1}. \quad (6.2.3)$$

$$\frac{\dot{m}_c}{\dot{m}_g} = \frac{(1-\eta)(2.1328)\, \sigma \cdot St \cdot C_{p_g} \cdot K_1 \left[T_g - T_b\right]}{\bar{C}_{p_c} \cdot \epsilon \cdot \left[T_b - T_{c.in}\right] \cos\beta}. \quad (6.2.9)$$

$$\theta = \frac{T_{c.exit}}{T_g} = \left[\frac{\epsilon\left(T_b - T_{c.in}\right) + T_{c.in}}{T_g}\right]$$

Curves of $\eta_{isothermal}$ as a function of $\frac{\dot{m}_c}{\dot{m}_g}$ are drawn for various values of $m = \frac{\rho U_c}{\rho U_g} = 0.5$, 1.0 and 1.5 while varying internal cooling internal cooling effectiveness ϵ. ($\epsilon = 0.5$, 0.75 and 0.9)

For the single high pressure ratio transonic turbine stage the coolant mass flow requirements for the rotor blade row alone is considered. The coolant mass flow requirement for the nozzle row is not included as the nozzle is considered as part of the combustion chamber.

The turbine inlet stagnation absolute temperature defined here is for the rotor inlet To_2^{ab} (= 1800°K)

Blade Row: For the rotor blade row, equations 6.2.3 & 6.2.9 are solved simultaneously

$$\theta = \frac{T_{c.exit}}{T_g} = \frac{\left[\epsilon\left(T_b - T_{c.in}\right) + T_{c.in}\right]}{T_{02}^{rel.}} \qquad (6.2.12)$$

$T_b = 1200^{o}k$ allowable blade temperature

$T_{c.in} = 750^{o}k$

$T_{02}^{rel} = 1575^{o}k$

$S/c \cos \beta = (0.7)(0.42) = 0.315$

$\sigma = c/s = ;.4286$

$St = 0.00187$

$k_1 = 1.5$ accounting for the effect of rotation

$T_g = T_{02}^{rel}$

Computations are carried out for m = 0.5, 1.0, & 1.5 while varying ϵ . (ϵ = 0.5, 0.75 and 0.9)

a_1 is defined as the ratio of coolant to gas flow rate.

$$a_1 = \frac{\dot{m}_{cr}}{\dot{m}_g} = a_{\substack{transonic \\ stage}}$$

and is determined from figures 6.1, 6.2 and 6.3.

Two-Stage Subsonic Turbine

Equation 6.2.3 and 6.2.9 are solved simultaneously to determine the coolant to gas flow rate.

As in the transonic stage; the first nozzle is not included. This is regarded as part of the combustion chamber.

The coolant mass flow requirements for the rotor of the first stage, the nozzle and rotor of the second stage are estimated.

1^{st} Stage Rotor

θ is defined as in equation 6.2.12

$T_b = 1200^o k$ - allowable blade temperature

$T_{c.in} = 750^o K$

$T_{02}^{rel} = T_g = 1680^o K$

$(s/c \cos \beta) = (0.7)(0.554) = 0.3878$

$\sigma = c/s = 1.4286$

$S_t = 0.00194$

$K_1 = 1.5$ accounting for the effect of rotation. Computations carried out for m = 0.5, 1.0, and 1.5 and ϵ = 0.5, 0.75 and 0.9

a_1 is defined as the ratio of coolant to gas flow rate

$$a_1 = \frac{\dot{m}_{cr}}{\dot{m}_g} \quad \text{determined from figure 6.4}$$

2nd Stage Nozzle

The 2nd Stage nozzle inlet temperature is computed using energy conservation.

$$\dot{m}_g C_{p_g} \overline{T}_{02}^{ab} + \dot{m}_{c.r1} C_{p_c} \overline{T}_{c.exit} = (\dot{m}_g + \dot{m}_{c.r1}) C'_{p_g} \overline{T}_{03}^{ab} + (\dot{m}_g + \dot{m}_{c.r1}) \overline{C}_p \cdot \Delta \overline{T}_0$$

$$\dot{m}_g C_{p_g} \cdot \overline{T}_{02}^{ab} + \dot{m}_{c.r1} C_{p_{c.exit}} \overline{T}_{c.exit} = (\dot{m}_g + \dot{m}_{c.r1}) \left(C'_{p_g} \overline{T}_{03}^{ab} + \overline{C}_p \cdot \Delta \overline{T}_0 \right) \quad (6.2.14)$$

where $\dot{m}g$ - main (hot) gas mass flow entering the first rotor

$\dot{m}_{c.r1}$ - coolant mass flow for rotor baldes of Stage 1

$(\dot{m}_g + \dot{m}c.r1)$ - mass flow leaving the rotor stage

ΔT_o - stagnation temperature drop across the first stage.

Equation 6.2.14 then reduces to

$$T_{03}^{ab} = \frac{\left[\frac{C_{p_g}}{C'_{p_g}} T_{02}^{ab} + a_1 \frac{C_{p_{c.exit}}}{C'_{p_g}} T_{c.exit}\right]}{(1 + a_1)} - \frac{\bar{C}_p}{C'_{p_g}} \Delta T_{o_I} \qquad (6.2.14)$$

$$T_{03}^{ab} = \frac{\left[\frac{C_{p_g}}{C'_{p_g}} T_{02}^{ab} + a_1 \frac{C_{p_{c.exit}}}{C'_{p_g}} \left[\epsilon(T_g - T_{c.in}) + T_{c.in}\right]\right]}{(1 + a_1)} - \frac{\bar{C}_p}{C'_{p_g}} \Delta T_{o_I} \qquad (6.2.15)$$

knowing T_{03}^{ab}, θ can be calculated.

$$\theta = \frac{T_{c.exit}}{T_g} = \frac{\left[\epsilon(T_b - T_{c.in}) + T_{c.in}\right]}{T_{03}^{ab}} \qquad (6.2.16)$$

$k_1 = 1$, - stationary row

s/c Cos β = (0.7)(0.5812) =.4068

$\sigma = c/s = 1.4286$

$St = 0.00194$

$T_g = T_{03}^{ab}$ expressed by equation 6.2.14

$T_b = 1200^\circ K$

$T_{c.in} = 600^\circ K$

The equations are solved again for $\dot m = 0.5$, 1.0 and 1.5 and $\epsilon = 0.5$, 0.75 and 0.9.

a_2 is defined as the ratio of the coolant to gas flow rate for the 2nd stage nozzle.

$$a_2 = \frac{\dot m_{c.n2}}{\dot m_g + \dot m_{c_{r1}}}$$ determined from figure 6.5

2nd Stage Rotor

Equations 6.2.3 and 6.2.9 are solved simultaneously to determine coolant mass flow.

The mean absolute stagnation temperature T_{04}^{ab} at 2nd rotor inlet is found using conservation of energy.

$$(\dot m_g + \dot m_{c.r1})\bar T_{03}^{ab} + m_{c.n2} C_{pc} T_{c.exit} = (\dot m_g + \dot m_{c.r1} + \dot m_{c.n2}) C_{p4} \cdot \bar T_{04}^{ab} \tag{6.2.17}$$

$$\bar T_{04}^{ab} = \frac{\frac{C_{p3}}{C_{p4}} T_{03}^{ab} + a_2 \frac{C_{pc}}{C_{p4}} \left[T_{c.exit} \right]}{(1 + a_2)} \tag{6.2.18}$$

$$\bar T_{04}^{ab} = \frac{\frac{C_{p3}}{C_{p4}} \cdot T_{03}^{ab} + a_2 \frac{C_{pc}}{C_{p4}} \cdot \left[\epsilon (T_b - T_{c.in}) + T_{c.in} \right]}{(1 + a_2)}$$

$$\bar T_{04}^{rel} = \bar T_{04}^{ab} - \frac{(C_4^2 - W_4^2)}{2 \bar C_p} \tag{6.2.19}$$

where C_4 and W_4 - are the absolute and relative velocities (taken from the velocity triangle)

$$\theta = \frac{T_{c.exit}}{T_{04}^{rel}}$$

$$\theta = \frac{\left[\epsilon\left(T_b - T_{c.in}\right) + T_{c.in}\right]}{T_{04}^{ab} - \frac{\left(C_4^2 - W_4^2\right)}{2C_p}} \qquad (6.2.20)$$

$k_1 = 1.5$

$s/c \cos\beta = (0.7)\ (0.5812) = 0.4068$

$\sigma = c/s = 1.4286$

$St = 0.00191$

$T_g = T_{04}^{rel}$ compressed as in equation 6.2.19

$T_{c.in} = 600\,^\circ K.$

The equations are solved for m = 0.5, 1.0 and 1.5 and ϵ = 0.5, 0.75 and 0.9.

a_3 is defined as $\dfrac{\dot{m}_{c.r2}}{\dot{m}_g + \dot{m}_{c.r1} + \dot{m}_{c.n2}}$ determined from figure 6.6

and $a_{subsonic} = \dfrac{\dot{m}_{c.r1} + \dot{m}_{c.n2} + \dot{m}_{c.r2}}{\dot{m}_g + \dot{m}_{c.r1} + \dot{m}_{c.n2} + \dot{m}_{c.r2}}$

From this analysis, we now have the total percentage coolant flow for both the single stage high pressure ratio transonic turbine, ($a_{transonic}$) and for the two-stage subsonic turbine. ($a_{subsonic}$)

Savings In Coolant Mass Flow

Savings in coolant mass flow rate by replacing two subsonic turbine stage with a single high pressure ratio transonic stage for the same work output.

$$\Delta\dot{m} = \frac{a_{transonic} - a_{subsonic}}{a_{subsonic}} \times 100\%$$

Omissions and limitations of the analysis:

It ought to be mentioned that majority of unanswered questions in advanced cooling techniques rest, unfortunately, in the area of film cooling, which is the area of greatest technoligical interest. The behavior of the both the mainstream and the coolant flows because of the mixing and complex 2-D and 3.D effects, will be difficult to predict. The analytical problems are compounded by the fact that very few relevant data now exist as a guide to modelling.

The data used in this analysis are from flat plate experiments. Curvature effect and effect of preceeding coolant injection on a row of holes are still to be investigated.

It would be unfair to fail to point out that many other considerations must go into the final design of the high performance turbine, and that these are strongly coupled to the aerodynamics with cooling injection, detail heat transfer and structural analysis. And since the ultimate constraint in the evolution of a given turbine design is often the survival or endurance of the airfoils rather than the precise aerodynamic performance; one cannot fail to expand the necessary effort on these problems too.

6.2.2 Stage Efficiency η_{stage}

For the cooled stage, the efficiency is defined as the ratio of the actual turbine work per unit of total air flow (primary plus cooling) to the ideal work which would be attained in expanding the total airflow through the actual pressure ratio.

Assuming that the cooling flow expands through the same pressure ratio as the primary flow

$$\eta_{Stage} = \frac{(1-a)(T_{01} - T_{03}) + a(T_{0c} - T_{03})}{\left[(1-a)T_{01} + aT_{0c}\right]\left[1 - \left(\frac{P_{03}}{P_{01}}\right)^{\frac{\gamma-1}{\gamma}}\right]} \qquad (6.2.21)$$

where a - ratio of cooling airflow to total airflow

T_{oc} - coolant stagnation temperature

T_{03} - mean exit stagnation temperature.

There are several ways in which cooling flow, especially with injection, can influence η_{stage}: -

(1) The cooling air itself suffers a pressure loss in passing through the cooling passages, so that it definetely has a lower stagnation pressure when mixed into the downstream flow.

(2) The entropy of the flow as a whole is increased by the transfer of heat from hot primary flow to the cooling flow.

(3) The film cooling injections (depending on the location and the rate of injection) change the blade drag characteristics substantially.

The entropy is related to the temperature and pressure of the fluid by

$$S - S_{ref} = C_p \ln \frac{T}{T_{ref}} - R \ln \frac{P}{P_{ref}}.$$

where $(\quad)_{ref}$ denotes some reference state. In stagnation state

$$S - S_{ref} = C_p \ln \frac{T_o}{T_{ref}} - R \ln \frac{P_o}{P_{ref}}.$$

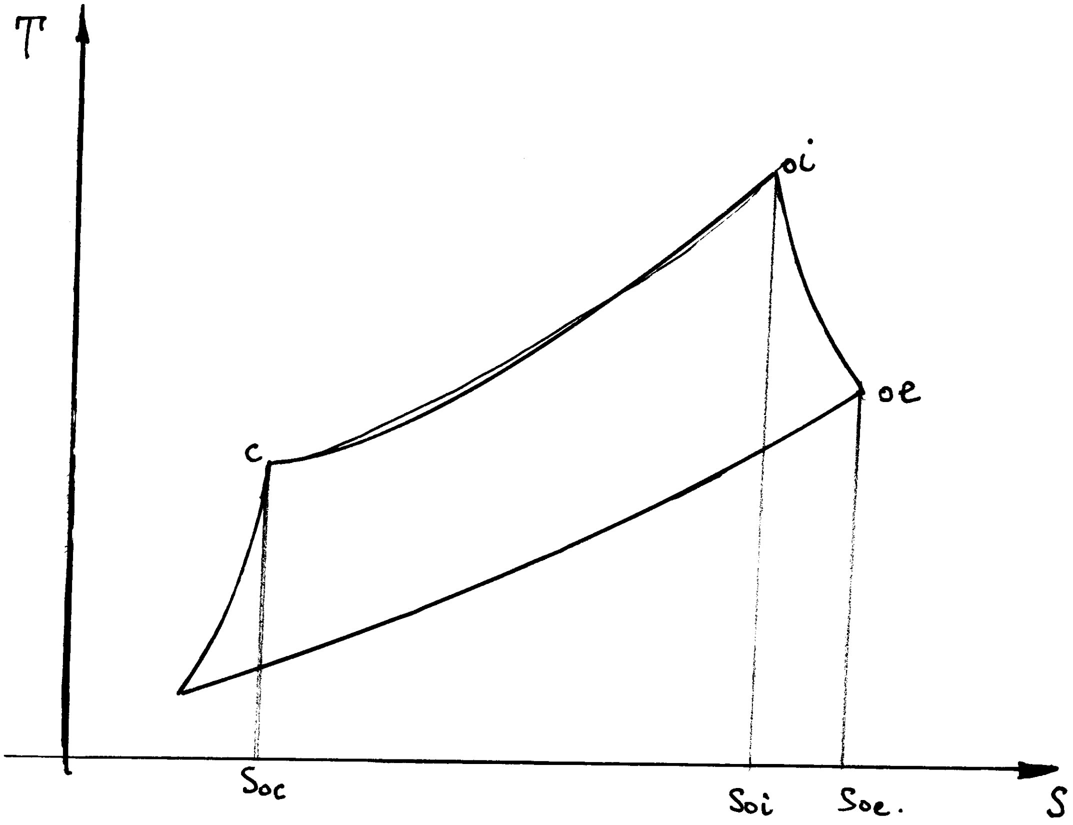

The entropy change of the hot main flow in a cooled turbine stage is given by

$$S_{oe} - S_{oi} = \Delta S_h = C_p \ln \frac{T_{oe}}{T_{oi}} - R \ln \frac{P_{oe}}{P_{oi}} \qquad (6.2.22)$$

while the entropy change for the coolant flow is given by

$$S_{oe} - S_{c} = \Delta S_c = C_p \ln \frac{T_{oe}}{T_{oc}} - R \ln \frac{P_{oe}}{P_{oc}} \qquad (6.2.23)$$

and

$$S_{oe} = S_{oc} + \Delta S_c = S_{oi} + \Delta S_h .$$

The total temperature term, which largely reflects the effect of thermal mixing can be computed for each stream by conservation of energy, the total pressure term, which largely reflects the effects of viscous dissipation, cannot be obtained without a detailed understanding of the flow field.

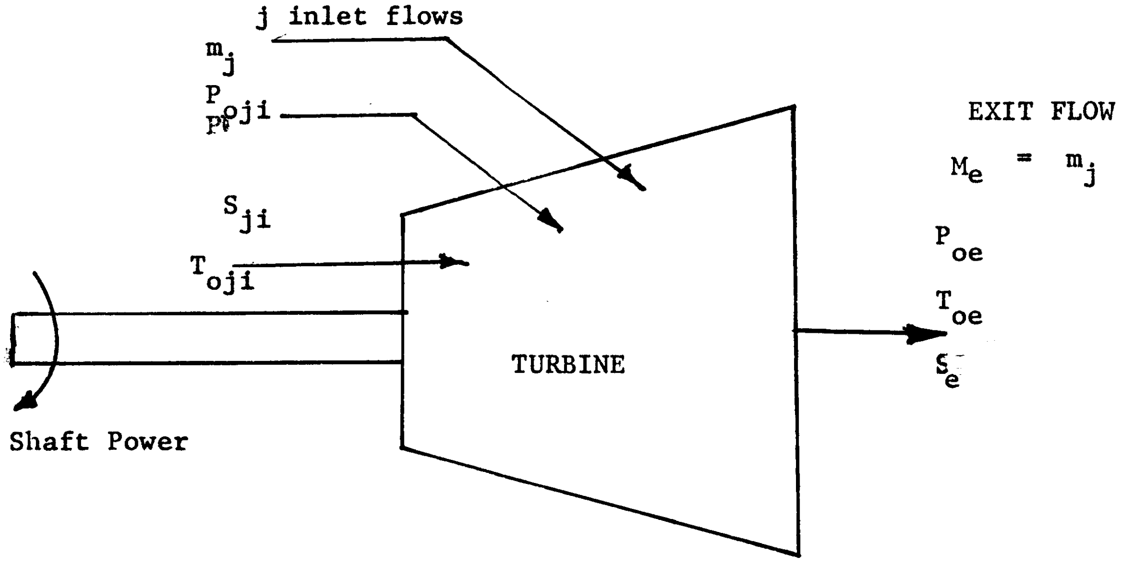

Schematic representation of a multipleflow, multistage cooled turbine.

Let us look at the performance in the most general terms, of the multiple-flow, multi-stage turbine. The usual analysis of single flow, multistage, uncooled turbine performance assumes that the exit stagnation pressure is fixed and that the flow is uniform at inlet and exit.

Efficiency is then defined as the ratio of actual work output ot the work that would have been obtained in the corresponding reversible process, exhausting to the same exit total pressure.

Applying the foregoing reasoning to the multiple-flow, multi-stage, cooled turbine shown above, the resulting expression for efficiency becomes

$$\eta_{stage} = \frac{\sum_j \left[\overline{T}_{oji} - \overline{T}_{oe}\right] \dot{m}_j \overline{c}_{p_1}}{\sum_j \left[\overline{T}_{oji} - \overline{T}_{oe}\, e^{-\left(\frac{S_{oe} - S_{oji}}{c_p}\right)}\right] \dot{m}_j \overline{c}_{p_2}} \leq 1 \qquad (6.2.24)$$

where it has been assumed in computing the actual work output that the exit conditions are entirely uniform. Furthermore, in computing the ideal work output, it has been assumed that exit total pressure is the same for all streams and that the individual flows are isentropic.

The exact definition of the inlet plane for each flow will vary from designer to designer depending on whether or not turbine efficiency occur within the cooling air ducts and airfoils.

Equation 6.2.24 can be rewritten as:

$$\eta_{turbine} = \frac{\sum \dot{m}_j \overline{c}_{p_1} \left(\overline{T}_{oji} - \overline{T}_{oe}^{\,actual}\right)}{\sum \dot{m}_j \overline{c}_{p_2} \left(\overline{T}_{oji} - \overline{T}_{oe}^{\,ideal}\right)}.$$

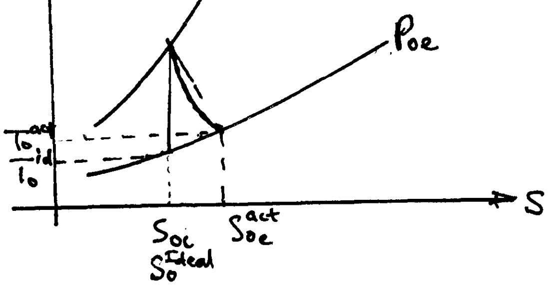

For the ideal isentropic case

$$\frac{\overline{T}_{oe}^{\,ided}}{\overline{T}_{oi}} = \left(\frac{P_{oe}}{P_{oi}}\right)^{\frac{\gamma-1}{\gamma}}$$

$$\overline{T}_{oe}^{\,Ideal} = \overline{T}_{oi}\cdot\left(\frac{P_{oe}}{P_{oi}}\right)^{\frac{\gamma-1}{\gamma}}$$

For the actual process

$$\frac{S_{oe}^{act} - S_{oi}}{C_p} = \ln\frac{\overline{T}_{oe}^{\,act}}{T_{oi}} - \frac{\gamma-1}{\gamma}\ln\frac{P_{oe}}{P_{oi}}.$$

$$\therefore\ \overline{T}_{oe}^{\,actual} = \overline{T}_{oi}\left(\frac{P_{oe}}{P_{oi}}\right)^{\frac{\gamma-1}{\gamma}} e^{\frac{S_{oe}^{actual} - S_{oi}}{C_p}}$$

$$\eta_{turbine} = \frac{\sum \dot{m}_j \overline{C}_{p_1}\left[\overline{T}_{oji} - \overline{T}_{oji}\left(\frac{P_{oe}}{P_{oji}}\right)^{\frac{\gamma-1}{\gamma}} e^{\frac{S_{oe}^{actual} - S_{oji}}{C_p}}\right]}{\sum \dot{m}_j \overline{C}_{p_2}\left[\overline{T}_{oji} - \overline{T}_{oji}\left(\frac{P_{oe}}{P_{oji}}\right)^{\frac{\gamma-1}{\gamma}}\right]}$$

$$\eta_{turbine} = \frac{\sum \dot{m}_j \overline{C}_{p_1}\left[1 - \left(\frac{P_{oe}}{P_{oji}}\right)^{\frac{\gamma-1}{\gamma}} e^{\frac{\Delta S_j}{C_p}}\right]}{\sum \dot{m}_j \overline{C}_{p_2}\left[1 - \left(\frac{P_{oe}}{P_{oji}}\right)^{\frac{\gamma-1}{\gamma}}\right]}$$

where $\Delta S_j = \Delta S_{jI} + \Delta S_{jII} + \Delta S_{jIII}$

ΔS_{jI} — entropy generation due to thermal mixing.

$$= \ln\frac{\overline{T}_{oji}}{\overline{T}'_{oi}}$$

$$\overline{T}'_{oi} = \frac{\sum T_{oji}\, m_{ji}\, C_p}{\overline{C}_p \sum \dot{m}_{ji}}$$

$\Delta S_{jII} = -R\ln\frac{P_{o2}}{P_{o1}}$ entropy generation due to friction and shocks.

P_1/P_{02} is taken from detailed results of the downstream traverse (Fig. 4.19)

$\Delta S_{\gamma_{III}}$ entropy generation due to film cooling and secondary flow.

The entropy generation due to film cooling and secondary flow is expressed as

$$\frac{\Delta S_{\gamma_{III}}}{\Delta S_{\gamma_I} + \Delta S_{\gamma_{II}}} = \epsilon$$

where ϵ = -0.2, 0.0, 0.1, 0.3 and 0.5.

$$\begin{aligned} \Delta S_\gamma &= \Delta S_{\gamma_I} + \Delta S_{\gamma_{II}} + \epsilon\left(\Delta S_{\gamma_I} + \Delta S_{\gamma_{II}}\right) \\ &= \Delta S_{\gamma_I} + \Delta S_{\gamma_{II}}\left(1 + \epsilon\right) \end{aligned}$$

This is computed for both the subsonic and transonic turbines.

Curves of turbine efficiency η_{turbine} as a function of coolant mass flow $\dot{m}_c$ are plotted while assuming different values of ϵ (-0.2, 0.0, 0.1, 0.3 and 0.5) and shown in figures 6.7 and 6.8.

Efficiency gains if any is then computed thus

$$\Delta\eta = \frac{\eta_{\substack{\text{transonic}\\ \text{turbine}}} - \eta_{\substack{\text{subsonic}\\ \text{turbine}}}}{\eta_{\substack{\text{subsonic}\\ \text{turbine}}}} .$$

6.3 Desirability

Without specifying any cooling technique to be used a general approach to determine the desirability of using transonic turbine to replace subsonic turbine can be roughly estimated by considering the ratio of the amount of heat that has to be removed from the stage to the work output from the stage.

Like before, it is assumed that both the transonic and subsonic turbine have the same turbine inlet total temperature and total pressure; operate with the same mass flow, axial velocity and tip speed. And we are considering the case, when oen highly loaded tranosonic stage $\frac{P_{01}}{P_{03}} = 4$ is used to replace, two stages, say moderately loaded $\frac{P_{01}}{P_{03}} = 2$ subsonic stages. For the Single Transonic Stage,

$$d_{transonic} = \frac{\sum q_{transonic}}{\dot{m}\left(\bar{C}_p\,\Delta T_0\right)_{transonic}}$$

where $\sum q_{transonic} = q_{nozzle} + q_{\substack{rotor\\blade}} + q_{disc} + q_{casing}$

= sum of all the heat that has to be removed from the turbine components.

For simplicity, let us consider only the nozzle and blade rows.

Using the example we are dealing with here, let us first compare the highly loaded single stage transonic turbine with the moderately loaded subsonic one.

Transonic Stage : pressure ratio of 4, turbine inlet temperature of 1800°K

$$d = \frac{q_{nozzle} + q_{rotor}}{\dot{m}\bar{C}_p \Delta T_0} .$$

$$\doteq \frac{\dfrac{q_{nozzle}}{\dot{m}\bar{C}_p} + \dfrac{q_{rotor}}{\dot{m}\bar{C}_p}}{\Delta \bar{T}_0}$$

$$\doteq \frac{\dfrac{2.48\,\sigma\,St\cdot\left[\rho u_1 C_p (\bar{T}_4 - \bar{T}_g) g\right]}{\rho u_1 g \cos\beta\,\bar{C}_p} + \dfrac{2.48\,\sigma\,St\cdot K\cdot\left[\rho u_3 \bar{C}_p (\bar{T}_{02}^{rel} - \bar{T}_b) g\right]}{\rho U_3 g \cos\beta\,\bar{C}_p}}{\Delta \bar{T}_0}$$

$$\doteq \frac{\dfrac{(2.48)(1.33)(0.00188)(600)}{0.423} + \dfrac{(1.5)(2.48)(1.333)(0.00188)(1575-1200)}{0.423}}{450}$$

$$= 0.0367$$

Subsonic Stage with pressure ratio of 2, turbine inlet temperature of 1800°K.

For the subsonic stage, let us consider the first stage of the two-stage subsonic turbine.

$$d = \frac{\dfrac{2.48\sigma\, St\,(\bar{T}_{01} - \bar{T}_b)}{\cos\beta} + \dfrac{2.4\sigma\, St \cdot K_1\,(\bar{T}_{02}^{rel} - \bar{T}_b)\,g}{\cos\beta}}{\Delta T_{0_I}}$$

$$= 0.0602$$

Second Subsonic Stage With pressure ratio of two, with turbine inlet temperature of $1560^{\circ}K$

$$d_{\text{subsonic II}} = \frac{3.7659 + 2.6727}{210^{\circ}}$$

$$= 0.0307$$

For the Multistage Subsonic Turbine

$$d_{\substack{\text{multistage}\\ \text{subs.}}} = \frac{q_{\substack{\text{nozzle}\\ \text{stage 1}}} + q_{\substack{\text{rotor}\\ \text{stage 1}}} + q_{\substack{\text{nozzle}\\ \text{stage 2}}} + q_{\substack{\text{rotor}\\ \text{stage 2}}}}{\dot{m}\,\bar{C}_p\,\Delta T_{0_I} + \dot{m}\,\bar{C}_p\,\Delta T_{0_{II}}}$$

$$= \frac{\frac{q_{nozzle\ I}}{\dot{m}\bar{C}_p} + \frac{q_{rotor\ I}}{\dot{m}\bar{C}_p} + \frac{q_{nozzle\ II}}{\dot{m}C_p} + \frac{q_{rotor\ II}}{\dot{m}\bar{C}_p}}{(\Delta T_{o1} + \Delta T_{o2})}$$

$$= \frac{6 \cdot 5681 + 7 \cdot 8817 + 3 \cdot 7659 + 2 \cdot 6727}{450}$$

$$= 0 \cdot 0464$$

$$D = \frac{d_{multistage} - d_{transonic}}{d_{multistage}}$$

$$= \frac{0 \cdot 0464 - 0 \cdot 0367}{0 \cdot 0464} = 20 \cdot 95\%$$

i.e. by replacing two subsonic stages with a single highly loaded transonic stage to produce the same work output, the amount of heat that has to removed from the turbine stage has been decreased by as much as 21%

It also worth mentioning that for a fixed rotor blade temperature, the turbine nozzle inlet temperature can be raised (overall cycle temperature) since the blade relative stagnation temperature is generally lower in transonic turbine than in subsonic ones.

And when this increased temperature is matched with a corresponding increase in compressor pressure ratio, the overall cycle - efficiency will definetly improve.

This analysis on the whole has shown unique potentialities and promising future for high pressure ratio transonic turbines.

CHAPTER 7

7.1 Summary and Conclusion

The aerodynamic performance and heat-transfer characteristics of different transonic turbine bladings have been investigated.

Transonic turbine blades were designed, built and tested. Aerodynamic tests carried out to investigate the performance of these bladings have shown:

(a) that, on the whole, by using proper blade design methods, highly loaded transonic turbine stage can operate at an efficiency level comparable to the best existing subsonic stages;

(b) that for exit Mach number $\angle 1.2$, the blade suction-side downstream of the throat must be specially designed contoured to minimize the losses; and

(c) that at high exit Mach number $M > 1.3$ the biggest sources of entropy generation are the shocks, shock-boundary-layer interaction and the mixing.

The MIT Hot Blowdown Cascade Facility was designed, built and used for the turbine blade aerodynamic and heat-transfer investigations. Very good agreement between the pressure distribution around the blade obtained on the facility with those obtained at the VKI conventional transonic wind tunnel confirms that the facility can and is offering a practical, low-cost and flexible means to solve rather complicated heat-transfer problems while providing fairly rigorous modeling of the flow and temperature fields to simulate turbine operating conditions.

Heat-transfer characteristics of the turbine blades have been obtained. The tunnel's level of turbulence has some influence on both the pressure and heat-transfer distribution around the blade. An early transition to turbulence occured on both sides of the blade. Variations in heat-transfer distribution around the blade followed a pattern similar to that of the pressure distribution.

On the whole, a high level of heat transfer was measured around the blade apparently being the result of high turbulence level in the tunnel. On the blade suction-sides, the movement of the shocks as the pressure ratio across the cascade is varied, made any quantitative correlation impossible. But they did exhibit a systematic pattern-downstream of the shock, a very sharp drop in heat transfer was recorded, and later started to rise as the flow accelerates towards the trailing edge.

A very high level of heat transfer was recorded around the trailing edge especially on the pressure side, amounting to about 75% or more of the average heat transfer to the blade at the stagnation leading-edge zone.

Comparisons between the experimental data and an available NASA theoretical prediction showed a good agreement for most of the surface.

Obvious discrepancies occured as to the location of the transition point and consequently on the heat-transfer distribution in that region.

Comparisons between the data obtained here and the experimental data of other workers showed a very good correlation.

It must also be mentioned that due to the physical size of the heat-transfer gauges and their spacings, the exact distribution of the heat transfer could not be measured. Instead an average over the gauge face area was being measured and straight lines were just being used to connect the points.

And finally a look at the future of transonic turbine was made. It was found that by replacing two subsonic stages with a single highly loaded transonic stage to produce the same work output, the amount of heat that has to be removed from the turbine stage has decreased by as much as 21%. Similar analysis showed savings of about 25% in coolant mass flow rate when two subsonic turbine are replaced with single transonic stage. And also while analysing the effect of cooling on stage efficiency, it was found that, without considering the entropy generated as a result of coolant injection into the main flow. (mixing losses), about 4.28% degradation in turbine stage efficiency existed in the single highly loaded transonic stage compared to an 8.11% efficiency degradation that existed in the two stage subsonic turbine.

7.2 Suggestions for Further Work

1. So far, the aerodynamic performances of these transonic blades have been investigated at zero incidence; we still need the necessary information about the performance of these bladings at off-design inlet angles.

2. The blade aerodynamic performance was obtained with no coolant injection. Information on the effect of coolant injection on the aerodynamic performance of the transonic blades is needed and this is recommended for immediate investigation.

3. Further works are also recommended on the theoretical side. It will be of great assistance if a good solution of the transonic blade potential-flow pressure-distribution calculation is available (mixed flow problem). Even the present NASA boundary layer program that was used here has several limitations. Surfaces curvature, surface roughness, initial freestream turbulence, shock and shock-boundary-layer interactions are not taken into account. Improvements in these areas, and a combination of the two approaches (potential flow and boundary layer) will improve the predicting capability of the theoretical approach.

4. It is not clear whether the high blade curvature influenced the transition or not. But the Deych lemniscate method has a lower curvature than the NASA/Dunavant method (Figure 3.3) which is based on using a single parabolic arc "camber-line" with Dunavant and Erwin thickness distribution. The large curvature obtained using the NASA/Dunavant method may favor laminar separation whereas the low curvature obtained using the lemniscate method might alleviate this occurrence.

APPENDIX A

DEICH'S LEMNISCATE METHOD FOR CONSTRUCTING SUBSONIC TURBINE BLADE PROFILES

A lemniscate equation $(x^2 + y^2)^2 = a^2(x^2 - y^2)$ is one of the most convenient curves for determining subsonic blade profiles because it allows the point of maximum curvature to be selected at any cross-section of the blade passage and ensures a smooth change in curvature along the section contour (Fig. A.1). By changing the scale of ordinate $k_1 (y^1 = k_1 y)$ it is possible to move point E in either direction along the line $x = 0.625a$ and thus provide the required shape of the blade back for different entrance and leaving angles.

Flow over the concave surface of a blade usually occurs with negative pressure gradients and, consequently, the profile need not be so exact here. For some parts of the blade face, therefore, lemniscates are replaced by arcs of a circle.

Any blade profile consists of the following parts (Fig. A.1):

1. The blade back: $00'$ - a straight line (existing only when $\alpha_0 > 90^\circ$) which is the lemniscate produced through point 0 since curvature at this is zero; 0E $(0'E)$, which is lemniscate L_1; and EC, which is lemniscate L_2 formed from EF (L_1) as defined.
2. The blade face: AD, being lemniscate L_3; DC, an arc of a circle with radius R_1; when $\alpha_0 > 90^\circ$ there is no section AD but only the arc AC (R_1).
3. The entrance and exit portions of the profile, formed by arcs of

circles (R_z and R_3).

For sections with flow inlet angles $\alpha_0 < 100^\circ$, the tangent to the backbone at the leading edge was taken as 5° larger than the theoretical angle. This difference is justified by the results of numerous experimental studies of cascades in static conditions.

When constructing the profile given quantities are angles of entry $\alpha_0(\beta_1)$ and exit $\alpha_{1eff}(\beta_{2eff})$, and the section's chord (or width b). The velocities are subsonic. The scale is chosen arbitrarily. All the figures and tables in this article are given in relative quantities.

Constructing the profile:

1. For a given leaving angle α_1 or β_2, the coefficient k_1 is selected from Table 11 and the lemniscate L_1 plotted to the formula $y^1 = k_1 y$ (Fig. A.1) (interpolation must be used for intermediate angles).

2. Coefficient k_2 is defined:

   when $\alpha_0 \leq 90^\circ$ $\quad K_2 = K_2' = \chi'(90 - \alpha_0)$

   when $\alpha_0 \geq 90^\circ$ $\quad K_2 = K_2'' = \chi''(\alpha_0 - 90^\circ)$

3. Point C (Fig. 1) lies on the curve L_2. Its coordinates x_c, y_c are determined from Table 2. For accuracy, the coordinate x_c is given for angles of $\alpha_0(\beta_1) \geq 90^\circ$ and coordinate y_c for $\alpha_0(\beta_1) \leq 90^\circ$.

4. The straight line 00' (for angles $\alpha_0(\beta_1) > 90^\circ$) is plotted in terms of the equation tan $y = k_1$.

5. The coordinates of point A^1 ($x_A 1$, $y_A 1$) are determined in relation to angles of entry $\alpha_0(\beta_1)$ and exit $\alpha_1(\beta_2)$ by reference to Fig. A.2 or Table 11. Having the throat a($A'L_1$) we find point A ($AA^1 = t = a/\sin a_1$)

The cascade's angle of attack and pitch are defined in essentially the same way. If it is necessary to alter the pitch (within narrow limits), the angle of attack must also be altered in order to maintain the design leaving angle.

6. The thickness of the trailing edge OA ($0'A$ or $0''A$) is chosen with regard to structural and engineering conditions.

7. Coordinates of point B are determined in relation to $\alpha_1 (\beta_2)$ [coordinates of B ($\bar{x}_B$ and $\bar{y}_B$) are ginven in Table 11 .].

8. A circle of radius $R_1 = \bar{R}_1$ is drawn through points B and C or A and C (if the coefficient k_3 is not given). Values for this radius are found from the data in Table 11.

9. The lemniscate L_3, which should touch the circle of radius R_2, is drawn thfough point A. To construct the lemniscate L_3 we use the right-hand part of lemniscate FE (Fig. A.1) in which case point F is transferred and combined with point A. The scale for k_3 of lemniscate L_3 is selected with the aid of Table 12. Extrapolation is not possible. For other cases (when, for example, $\alpha_0 = 120°$, $\alpha_1 = 30°$) the face of the profile is composed only of an arc of the circle R_1. Radius R_1 and lemniscate L_3 are selected in such a way that it is possibel in all cases to achieve a small change of curvature at their junction.

10. The radius of the leading edge R_2 is governed by the angles of entry $\alpha_0 (\beta_1)$ and exit $\alpha_1 (\beta_2)$, and is found from Table 12.

Experimental [5,6, and 21] and analytical[33] investigations of several profiles designed using Lemniscate curves have indicated a satisfactorily low level of losses over a wide range of Mach and Reynolds number.

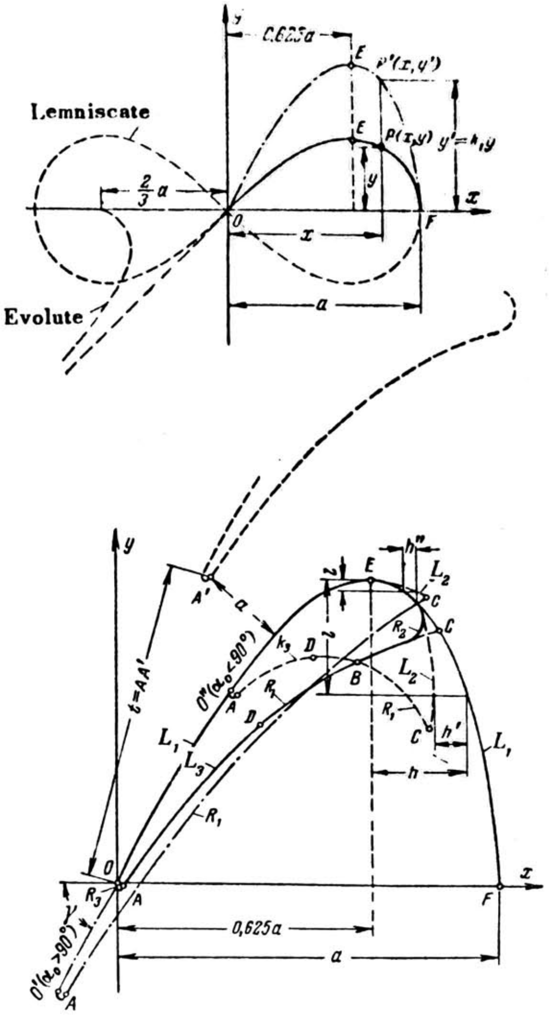

Figure A.1

Diagram for constructing lemniscate blade sections

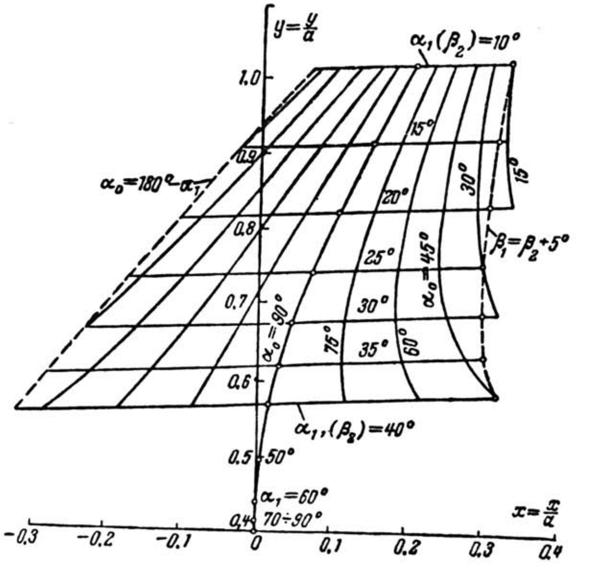

Coordinates of *A* in relation to α_0 (β_1) and α_1 (β_2)

Figure A.2

Source: Reference 21

Lemniscates for subsonic blade sections

Table 11

	α_1 (β_2), degrees	10	15	20	25	30	35	40	50	60	75	90
k_1		3.2	2.75	2.38	2.05	1.75	1.48	1.25	0.88	0.6	0.275	0.05
$\varkappa' \cdot 10^3$		7.3	6.8	6.85	7.3	8.0	9.0	10.4	—	—	—	—
$\varkappa'' \cdot 10^3$		21	19	15.8	10.3	0	—	—	—	—	—	—
$\overline{x}_B = \frac{x_B}{a}$		0.525	0.56	0.585	0.608	0.63	0.65	0.658	—	—	—	—
$\overline{y}_B = \frac{y_B}{a}$		0.795	0.685	0.603	0.53	0.46	0.396	0.34	—	—	—	—
$\alpha_0 = 90°$	$\overline{x}_{A'}$	0.204	0.148	0.104	0.071	0.045	0.027	0.014	0.005	0.001	0	0
	$\overline{y}_{A'}$	1.02	0.914	0.822	0.743	0.677	0.618	0.568	0.494	0.44	0.415	0.415
$\beta_1 = \beta_2 + 5°$	$\overline{x}_{A'}$	0.332	0.315	0.305	0.293	0.239	0.302	0.32	—	—	—	—
	$\overline{y}_{A'}$	1.026	0.922	0.833	0.755	0.69	0.635	0.534	—	—	—	—

TABLE 12

α_0 (β_1), degrees			$\beta_1=\beta_2+5°$	30	45	60	75	90		105	120	135	150	165	$\alpha_0=180-\alpha_1$
$\overline{x}_c = \frac{x_c}{a}$ ($\alpha_0 \geqslant 90°$) $\overline{y}_c = \frac{y_c}{a}$ ($\alpha_0 \leqslant 90°$)	α_1 (β_2), degrees	10	0.585	0.65	0.71	0.775	0.81	0.905	0.855	0.858	0.825	0.77	0.685	0.5	0.365
		15	0.495	0.535	0.59	0.65	0.71	0.77	0.855	0.852	0.81	0.74	0.62	0.36	0.36
		22	0.415	0.425	0.475	0.525	0.575	0.625	0.855	0.845	0.733	0.695	0.525	—	0.35
		30	0.325	—	0.355	0.4	0.44	0.485	0.855	0.82	0.728	0.537	0.34	—	0.34
		40	0.235	—	0.235	0.275	0.31	0.35	0.855	0.75	0.62	0.425	—	—	0.325
$\overline{R}_1 = \frac{R_1}{a}$	α_1 (β_2), degrees	10	0.27	0.312	0.37	0.41	0.535	0.69		1.0	1.8	4.0	8.75	24	∞
		15	0.32	0.35	0.405	0.483	0.59	0.76		1.15	2.15	4.7	11	∞	∞
		22	0.37	0.38	0.445	0.525	0.64	0.835		1.35	2.65	6.0	20	—	∞
		30	0.43	—	0.475	0.56	0.682	0.91		1.6	3.3	8.25	∞	—	∞
		40	0.5	—	0.5	0.595	0.725	1.0		1.9	4.3	12.5	—	—	∞
k_3	α_1 (β_2), degrees	10	1.2	1.6	2.0	2.4	2.8	3.2		3.6	4.0	—	—	—	—
		15	1.2	1.42	1.74	2.07	2.4	2.72		3.05	3.37	—	—	—	—
		22	1.23	1.28	1.55	1.82	2.08	2.35		2.61	—	—	—	—	—
		30	1.3	—	1.45	1.67	1.9	2.12		2.34	—	—	—	—	—
		40	1.4	—	1.4	1.6	1.8	2.0		—	—	—	—	—	—
$\overline{R}_2 = \frac{R_2}{a}$	α_1 (β_2), degrees	10	0.021	0.03	0.04	0.05	0.059	0.065		0.068	0.066	0.06	0.017	0.025	0.015
		15	0.021	0.027	0.036	0.045	0.054	0.06		0.062	0.06	0.052	0.038	0.015	0.015
		22	0.02	0.021	0.029	0.033	0.016	0.052		0.054	0.05	0.041	0.026	—	0.014
		30	0.016	—	0.021	0.028	0.036	0.043		0.045	0.04	0.028	0.012	—	0.012
		40	0.012	—	0.012	0.018	0.025	0.03		0.03	0.024	0.014	—	—	0.01

Source: Reference 21

APPENDIX B

Theoretical Prediction of Blade Heat-Transfer

NASA computer program[63] which gives the solution of the two-dimensional compressible laminar and turbulent boundary layer equations in an arbitrary pressure gradient was used in this studies. Cohen and Reshotko's method is used for the calculation of the laminar boundary layer and Sasman and Cresci's method for the turbulent boundary layer. Both are "integral" methods. In the laminar regime, a single ordinary differential equation, the momentum integral equation, is solved numerically. For turbulent flow, coupled first-order ordinary differential equations, the momentum and moment-of-momentum integral equations, are solved using Runge-Kutta techniques.

Transition from laminar to turbulent boundary layer is predicted by the Schlichting-Ulrich-Granville method; or by specifying a transition point, thus forcing transition. Separation is predicted in the laminar regime when negative skin friction occurs. Separation is predicted for turbulent flow when the level of incompressible form factor reaches a specified limit.

Laminar Solution

The Cohen-Reshotko method[77] used to solve the laminar boundary layer; involves the momentum integral equation for compressible laminar cases with arbitrary pressure gradient and heat transfer. Cohen and Reshotko's method was chosen because it does not have the restrictions on compressibility, pressure gradient, heat transfer, Prandtl number, or type of free-stream velocity distribution which many of the other laminar methods have. It is one of the most accurate, programmable, general methods available for the laminar case. This momentum integral equation is derived as follows: Prandtl's boundary-layer equation are transformed for compressible flow by Stewartson's transformation[80]. The resulting first-order differential equations are then expressed in terms of dimensionaless parameters related to wall shear, surface heat transfer, and free-strem velocity gradient. This gives two equations with three unknowns. Thwaite's concept[81] that these three quantities are related in a unique way without specifying a type of velocity profile is then assumed. The relations are obtained by examining exact solutions for the incompressible laminar boundary layer. A unique correlation relating the variables is chosen, reducing the problem to the solution of one first-order, ordinary, nonhomochosen, reducing the problem to the solution of one first-order, ordinary, nonhomogeneous differential equation in terms of a freestream velocity gradient parameter.

Turbulent Solution

The Sasman-Crest method[78] is used for the solution of the turbulent boundary layer. It involves momentum and moment-of-momentum integral boundary-layer equations for compressible turbulent cases with arbitrary gradients and heat transfer. It extends Reshotko and Tucker's analysis[79] by using more recent empirical data to avoid some of the problems with strong adverse pressure gradients. The momentum integral equation is obtained by applying a Mager-type transformation[82] to Prandtl's equations in which flow variables appear as time-averaged quantities. The momentum equation is then integrated across the boundary layer to give the momentum integral equation.

Transition

The Schlichting-Ulrich-Granville method[44] is used for the theoretical prediction of transition from laminar to turbulent flow. Details of the method are summarized in reference 44.

Schlichting and Ulrich[44] used sixth-degree Pohlhausen velocity profiles to calculate curves of neutral stability for laminar boundary layers in various pressure gradient. From these curves, a single curve of critical momentum-thickness Reynolds number against shape factor K was obtained. This curve is used by the program for predicting the point of instability of the laminar boundary layer. The distance between the point of instability and the point of transition is predicted by means of an experimental curve by Granville. This curve represents the difference in momentum-thickness Reynolds numbers at the instability and transition points plotted against a mean Pohlhausen parameter $\bar{K}$. Once an instability point is located, $\bar{K}$ can be calculated and the location of transition determined.

Separation

Laminar case. - In the laminar boundary layer, separation is assumed to occur at the station where skin friction coefficient C_f or wall shear stress passes from positive to negative indicating backflow. The values of C_f are checked at the separation station and the previous station in order to more exactly determine the point of separation.

Turbulent case. - In the turbulent boundary layer, separation is predicted by the program at the station where H_1 achieves a value greater than 2.8. This is a relatively high value for H_1, and H_1 grows rapidly near separation. A lower value of H_1 (2.0 to 2.5 is typical) could be specified instead. (H_1 is the incompressible form factor).

Limations of Program

The following are the principal limitations of the program:

(1) Surface curvature, surface roughness, initial turbulence level of the flow, and shock-boundary-layer interactions are not taken into account by the program.

(2) The program cannot be used along surfaces where relative total pressure is changing from point to point, such as a turbomachine rotor with change in radius along streamlines.

(3) The program is valid only for air. However, it can be easily altered for use with other gases. These alterations are described in reference 63.

AB	Inlet upper transition arc
FG	Outlet upper transition arc
CD	Inlet lower transition arc
HI	Outlet lower transition arc
AF	Upper circular arc
CH	Lower circular arc
BE and GJ	Straight lines

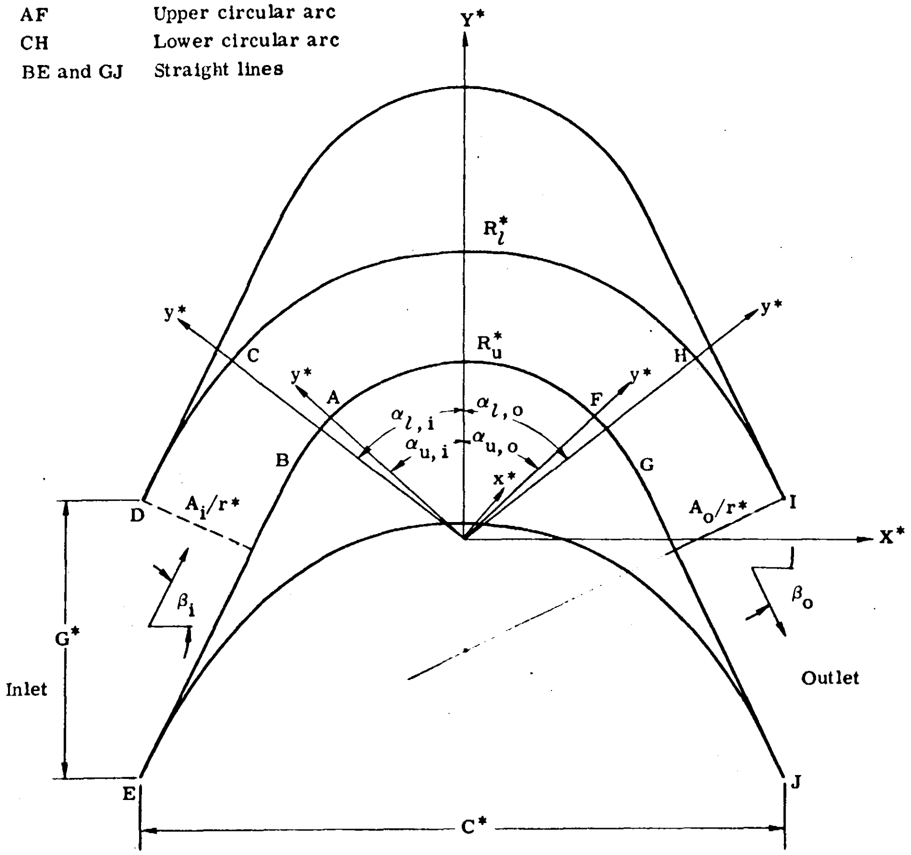

Figure 2.1 - Typical supersonic blade section. (All coordinates are made dimensionless by dividing by r*.)

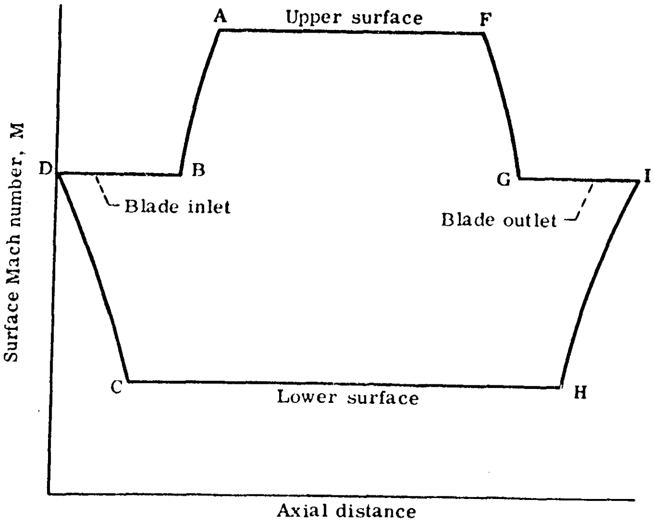

Figure 2.2 - Surface Mach number variation for typical blade section.

Figure 2.3 Transonic Reaction Blade Profiles

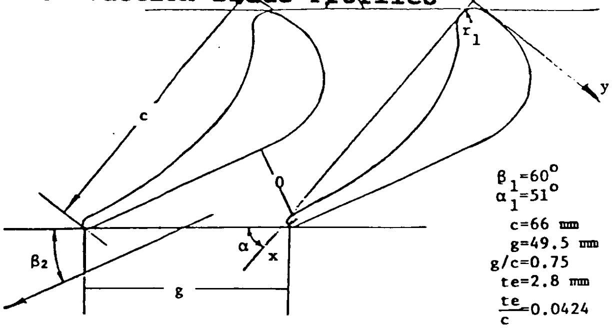

(a) Convergent Reference Blade with Straight Suction Back and Thick Trailing Edge

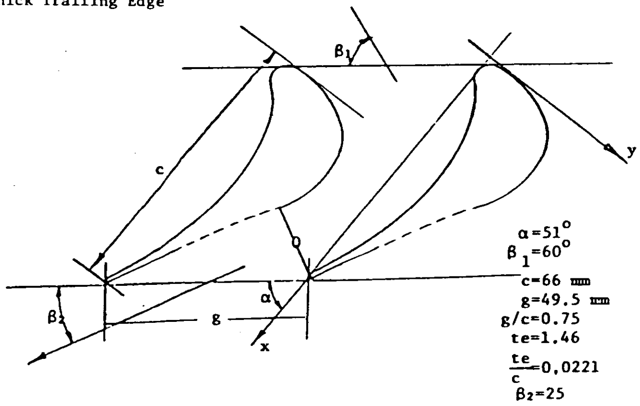

(b) Blade Profile with Unguided Expansion on the Suction Side

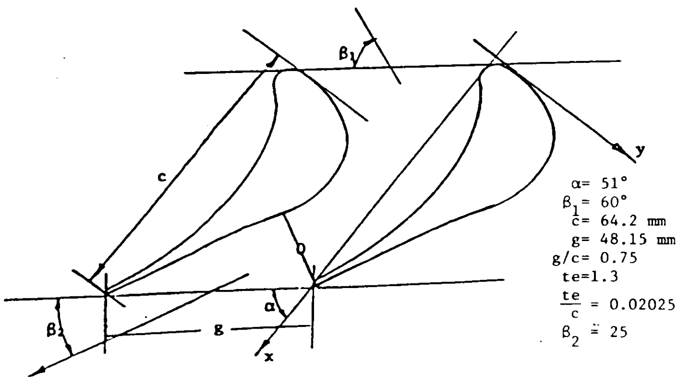

(c) Convergent Blade with Straight Suction Back but Thin Trailing Edge

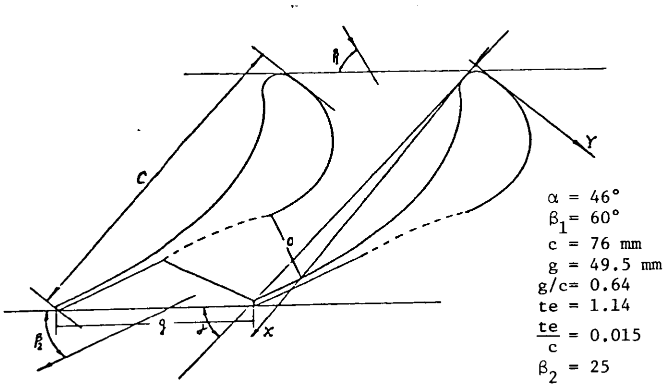

(d) Convergent-Divergent Blade

Figure 3.1 High Pressure Ratio 50% Reaction Blade Velocity Triangle

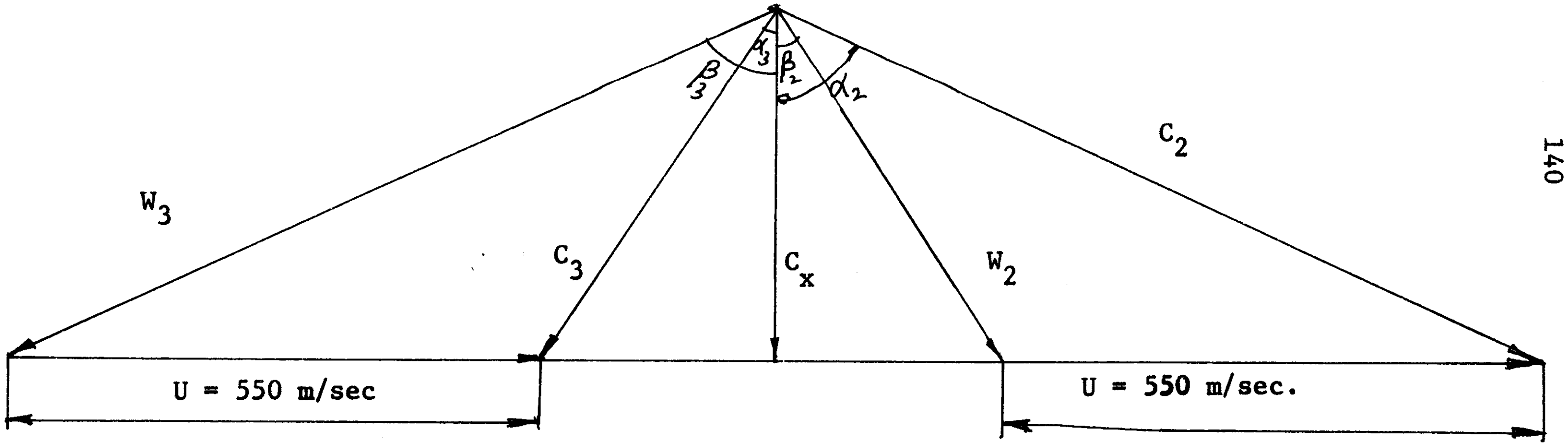

$M_{w2} = 0.56$

$M_{w3} = 1.3$

$\beta_2 = 32^\circ$

$\beta_3 = 65^\circ$

Figure 3.2 Graphical construction of the camber-line

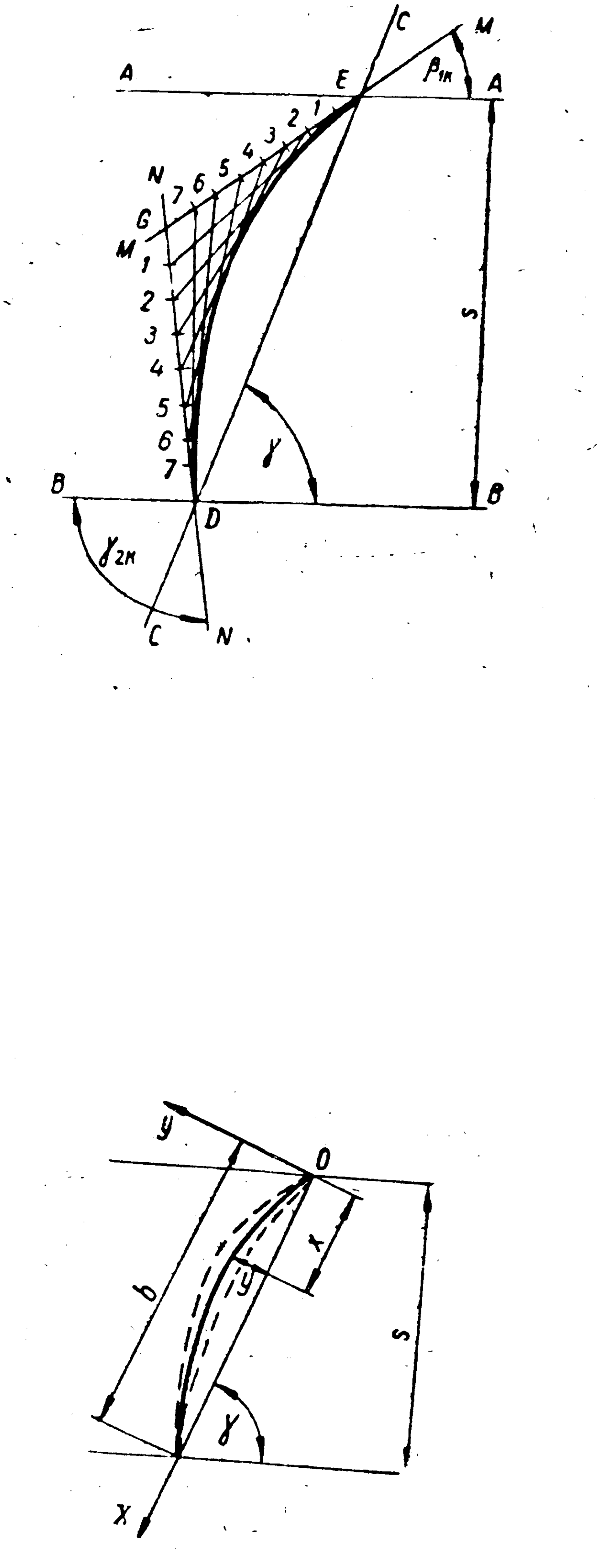

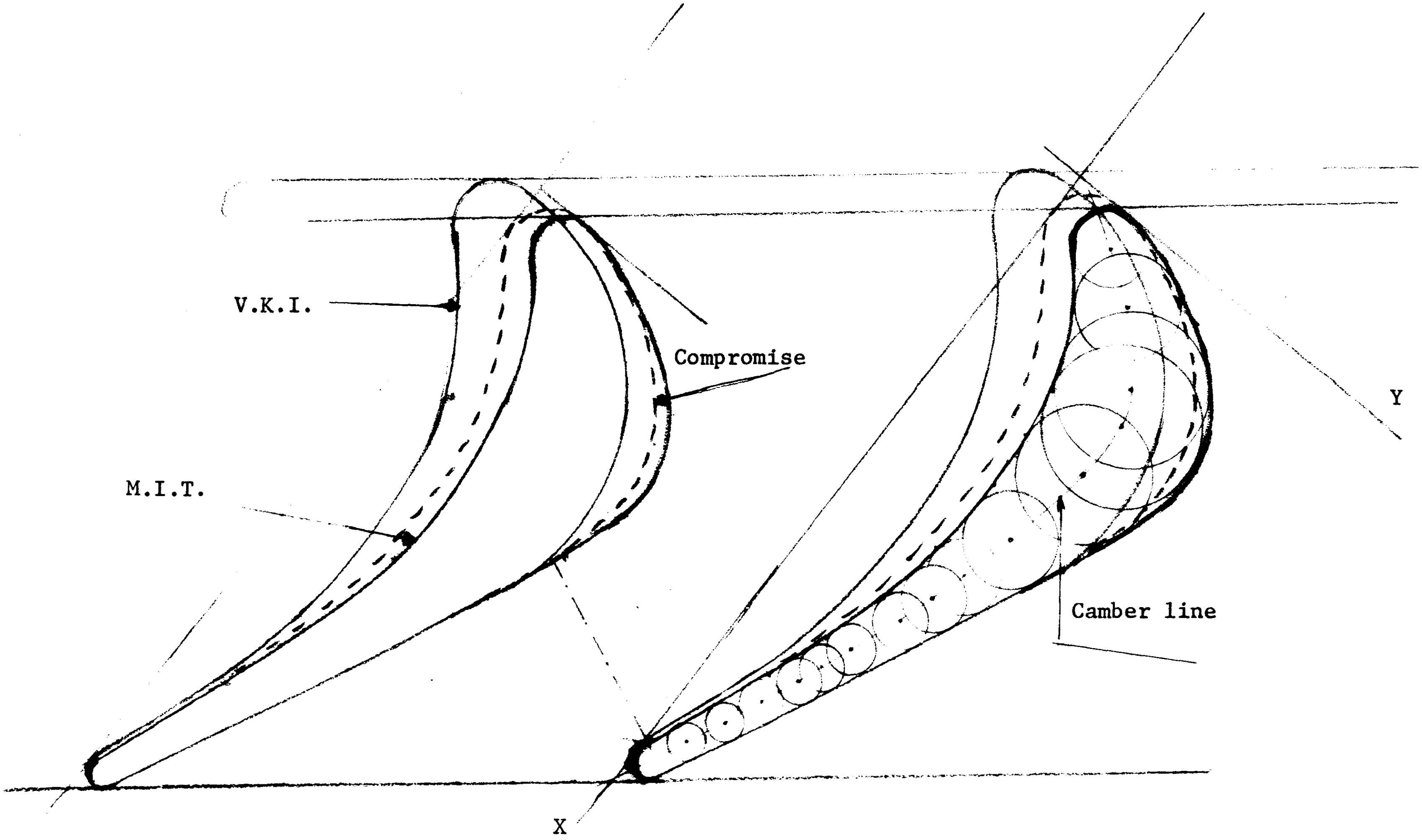

Figure 3.3 Compromise Blade

Figure 3.4a Design of the Supersonic Blade Section

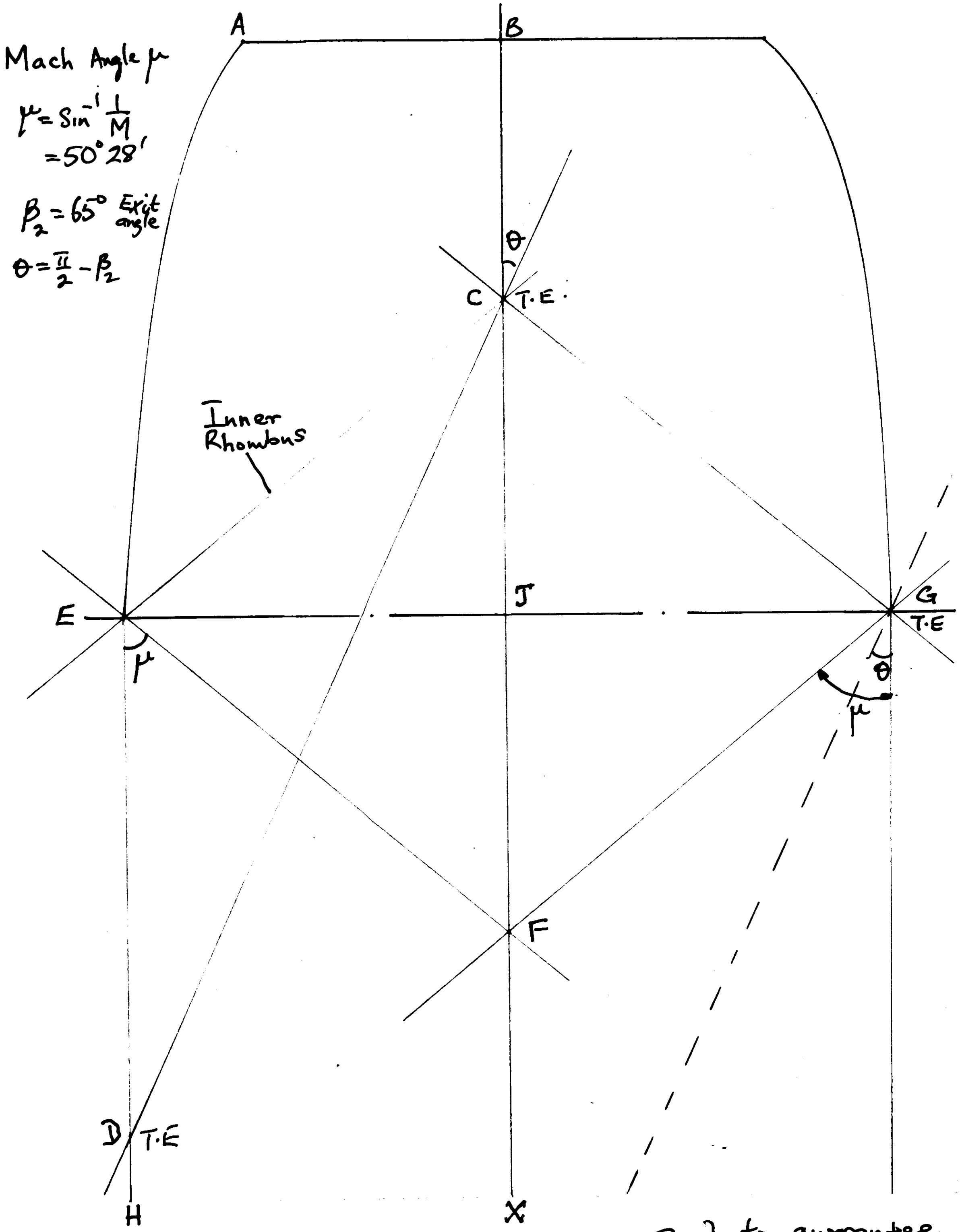

Mach Angle μ

$\mu = \sin^{-1}\frac{1}{M}$

$= 50°28'$

$\beta_2 = 65°$ Exit angle

$\theta = \frac{\pi}{2} - \beta_2$

If $\theta < \mu$, start T.E. from point C. } to gurrantee complete expansion.
If $\theta > \mu$. start T.E. from point E

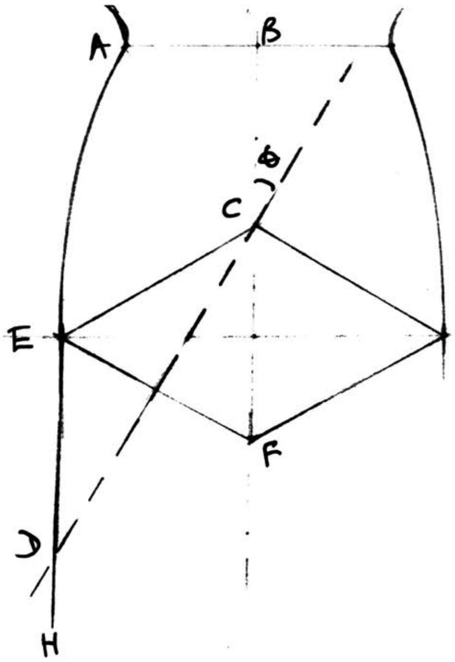

$\theta = \frac{\pi}{2} - \beta_2$.

β_2 — blade exit angle.

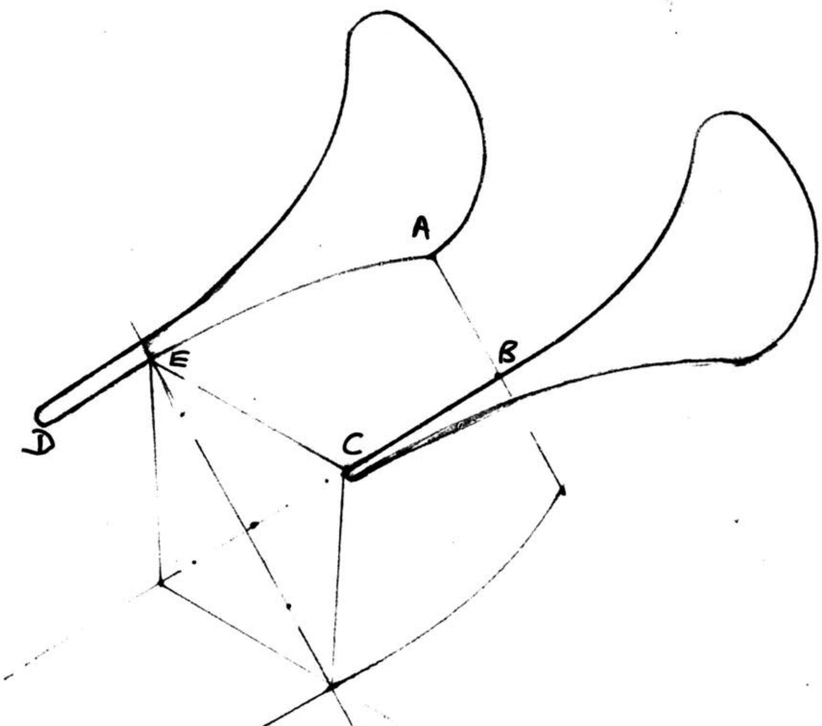

Figure 3.4b Design of the Supersonic Blade Section

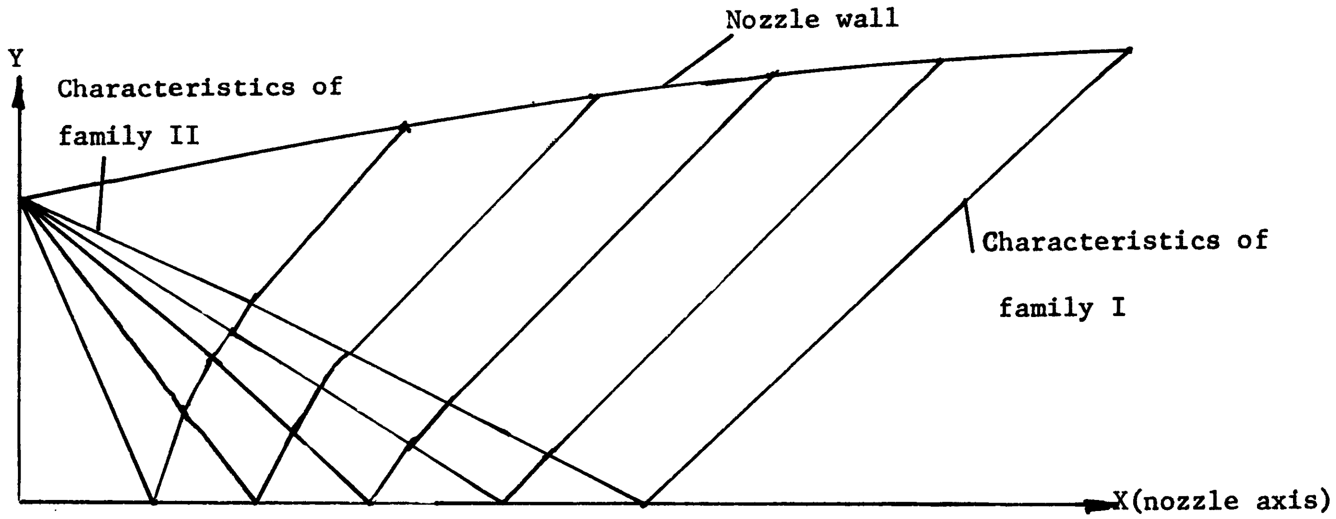

Figure 3.5 Wave diagram for Supersonic Nozzle With Sharp-Edged Throat.

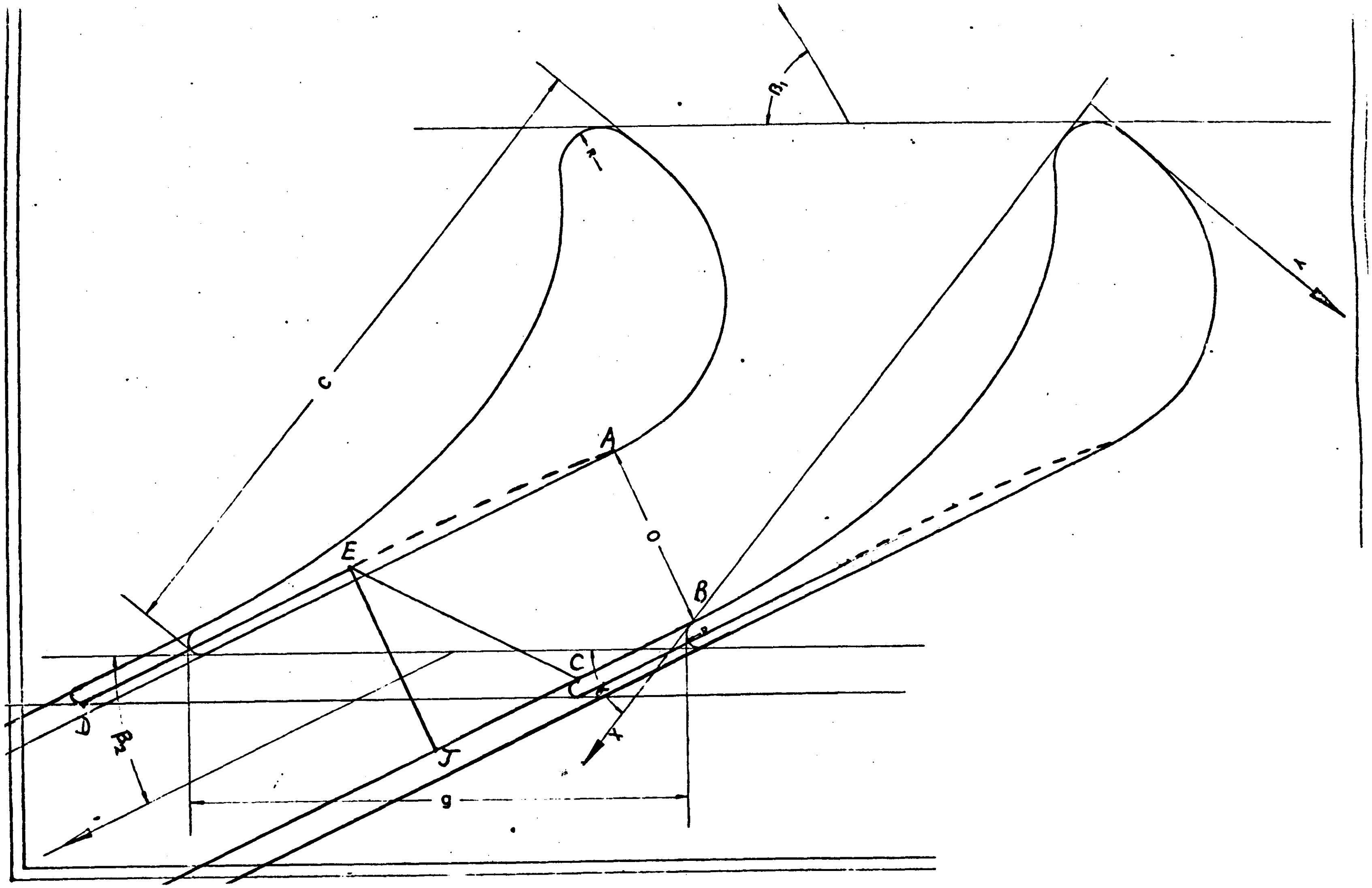

Figure 3.[illegible] Design of the Supersonic Blade Section (Convergent-Divergent)

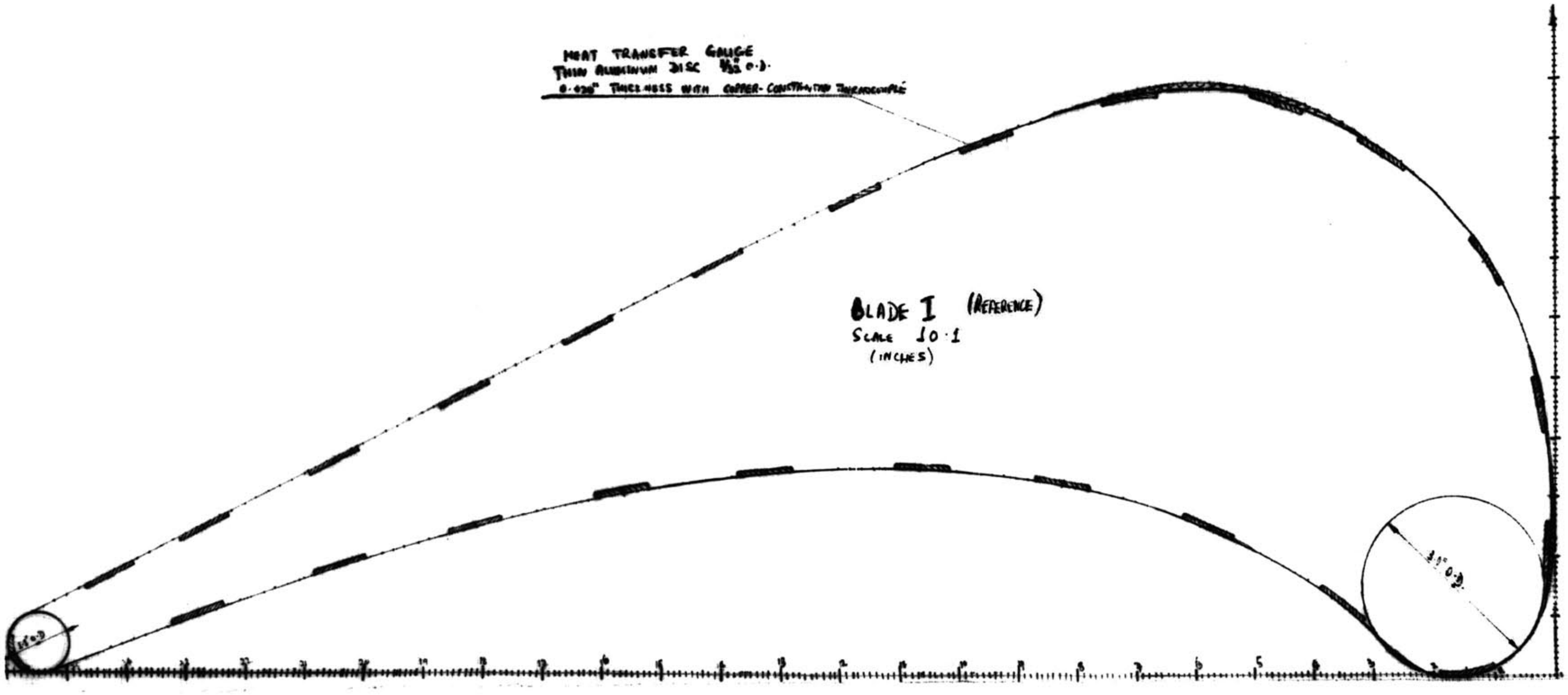

Figure 3.7 *Error incurred during blade manufacturing*

1. settling chamber
2. honeycomb
3. upper nozzle block (interchangeable)
4. cascade
5. upper cascade end wall
6. Perspex side wall (rotatable)
7. transition from rectanpular to angular section
8. flexible outlet pipe

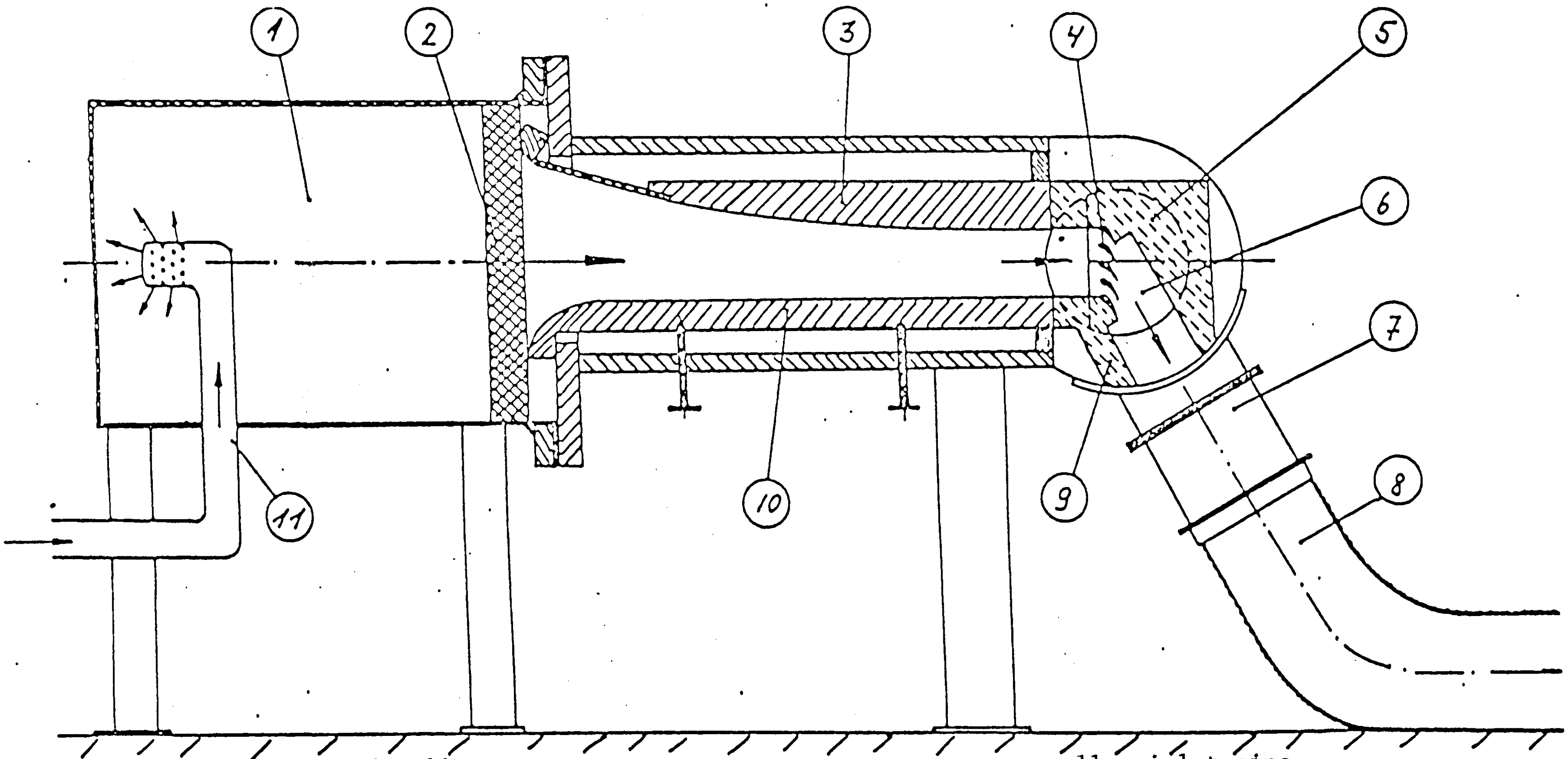

9. lower cascade end wall
10. lower nozzle block (movable)
11. inlet pipe

Figure 4.1 V.K.I. Test Facility

AVA-TYPE PROBE

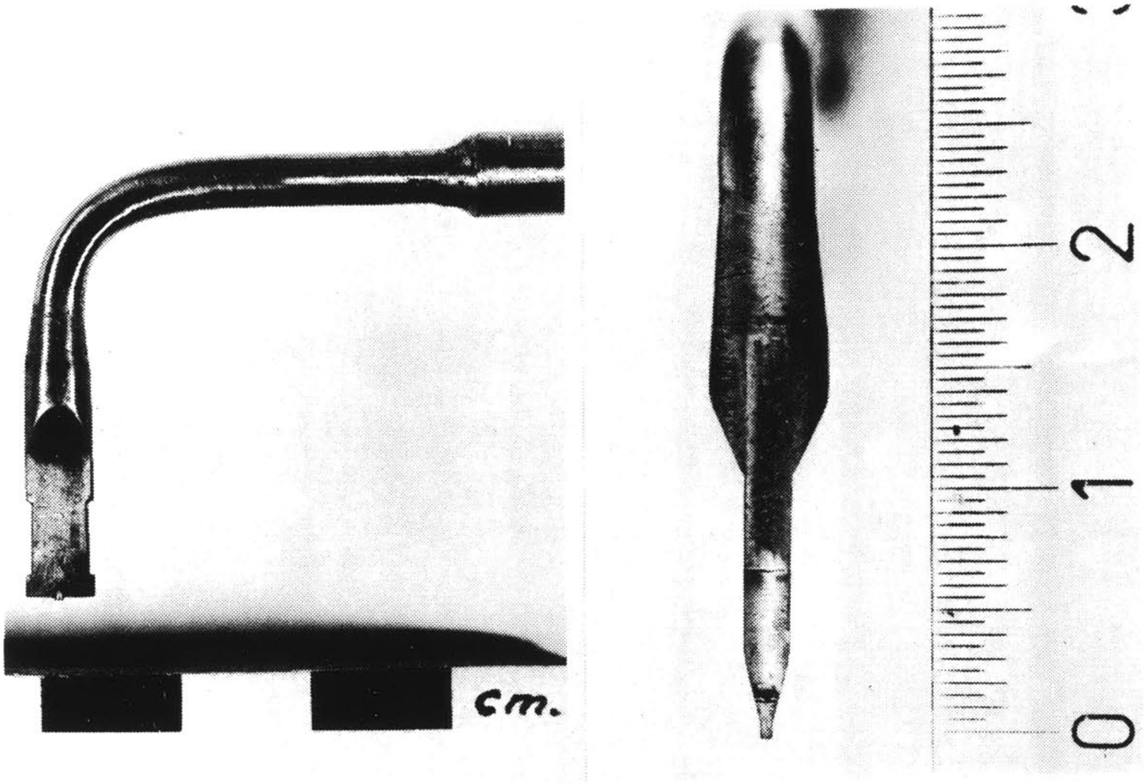

Combined Total-Directiional Probe with Separated Needle Static Probe (VKI)

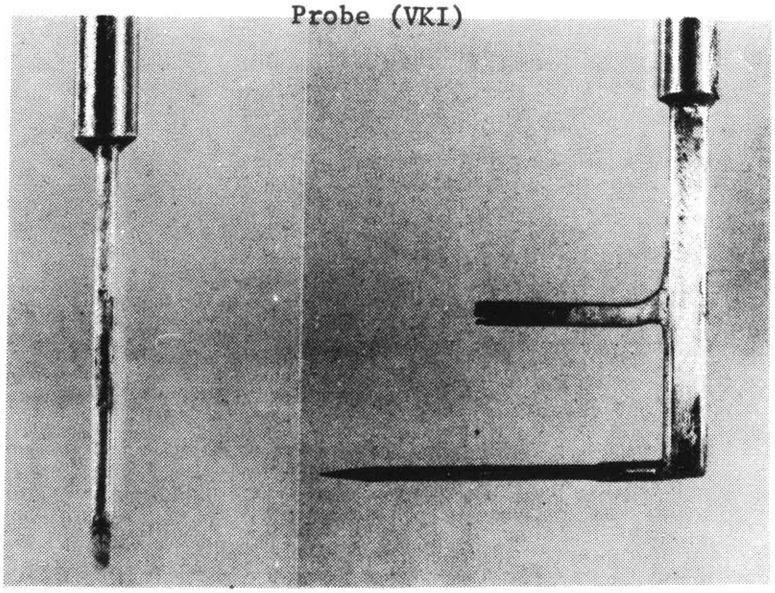

Figure 4.2

Figure 4.3 Location of pressure taps on Reference Blade 1.

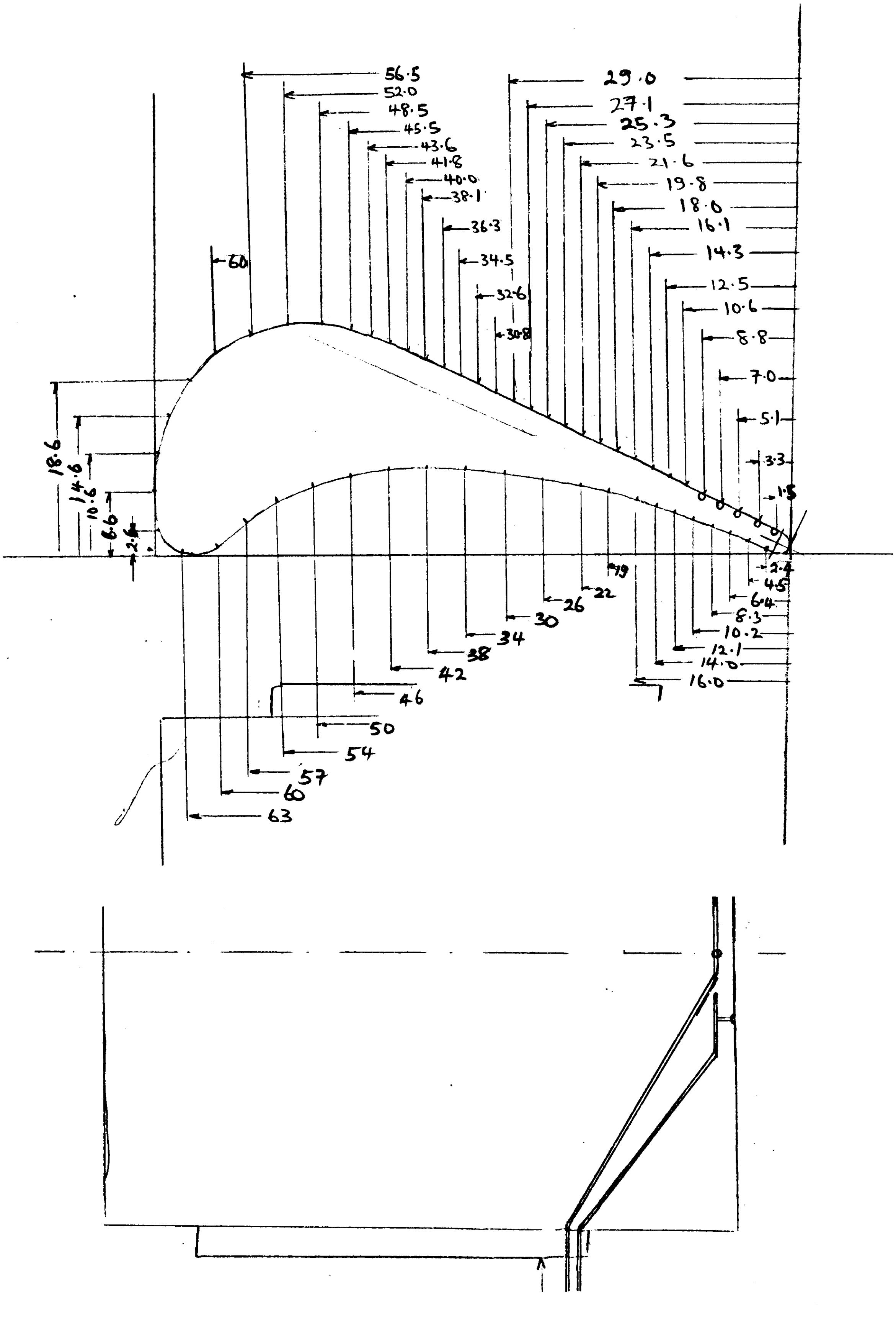

Figure 4.4 Location of Pressure Taps (Blade 2)

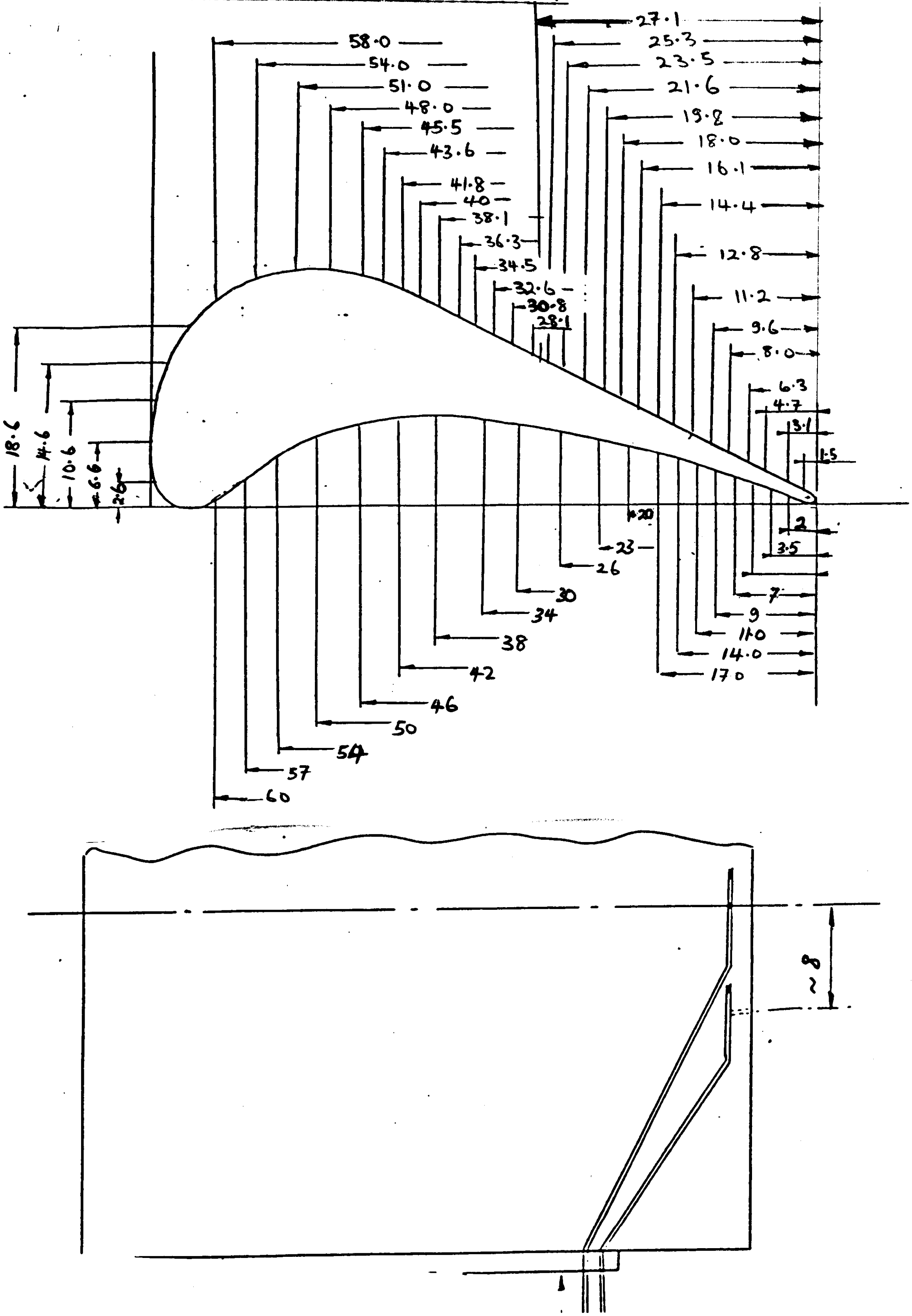

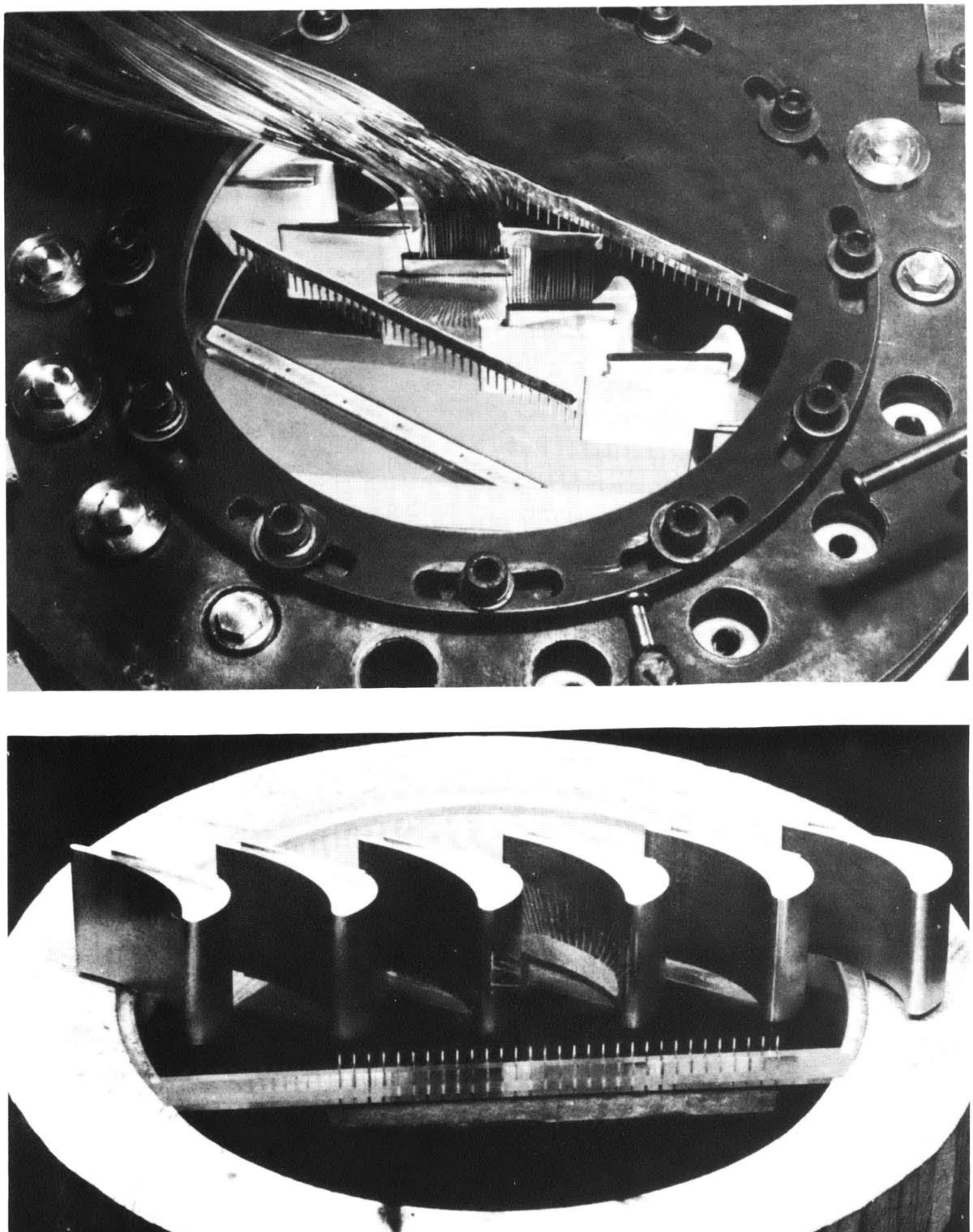

Figure 4.5 Linear Cascade

Figure 4.6 Inlet Mach Number versus Exit Mach number

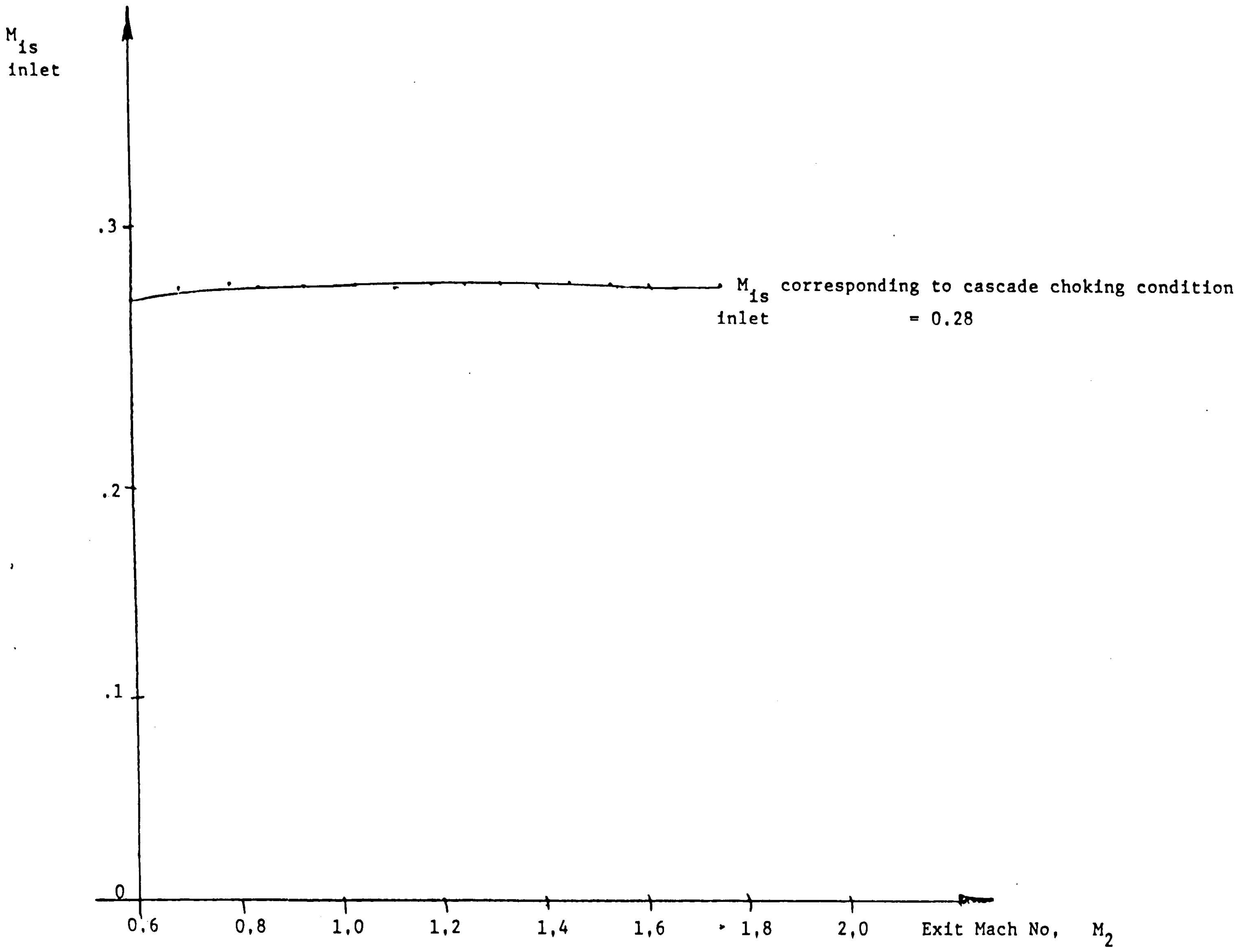

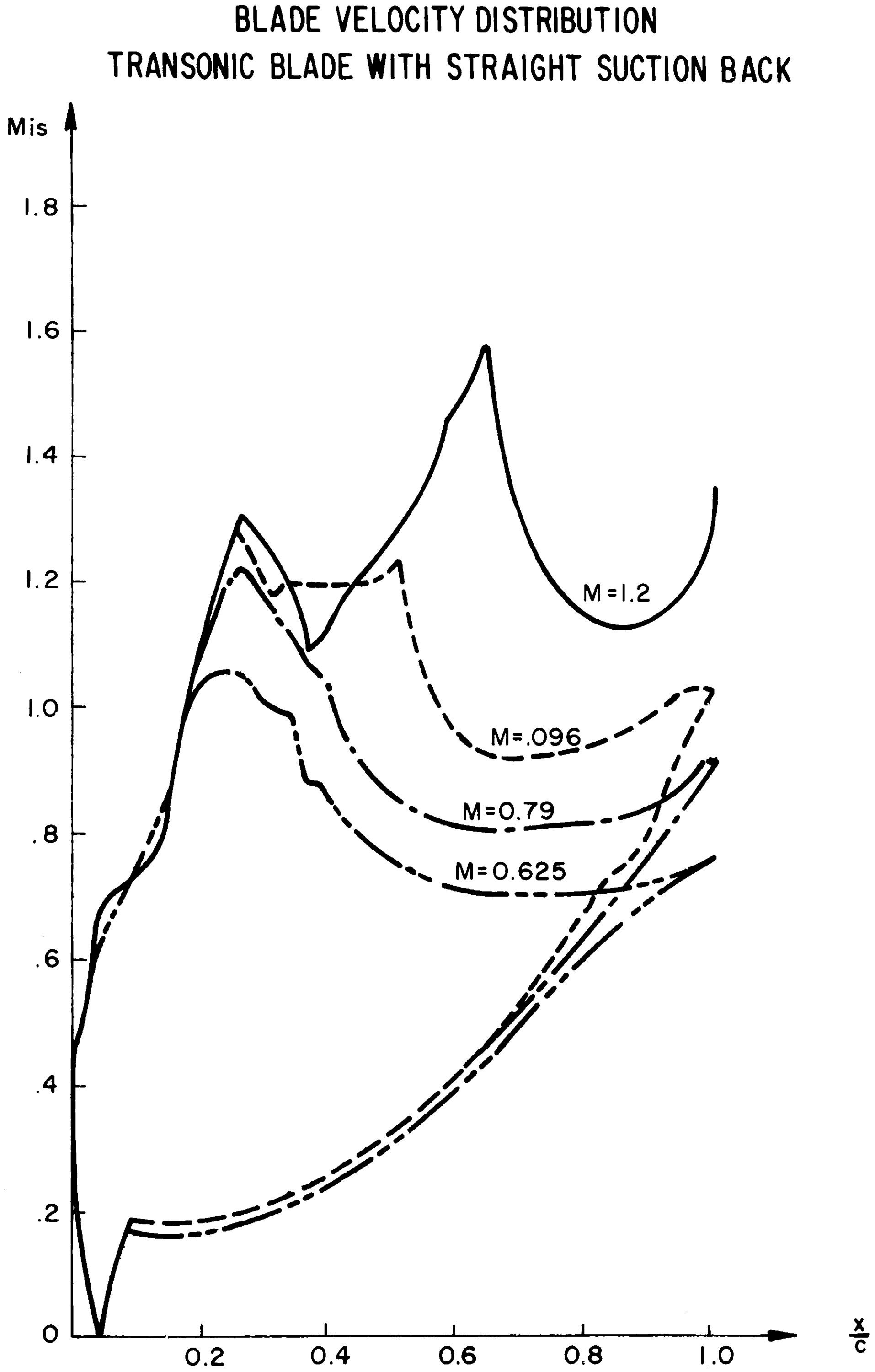

Figure 4.7 Blade 1 Surface Mach Number Distribution g/c = 0.75

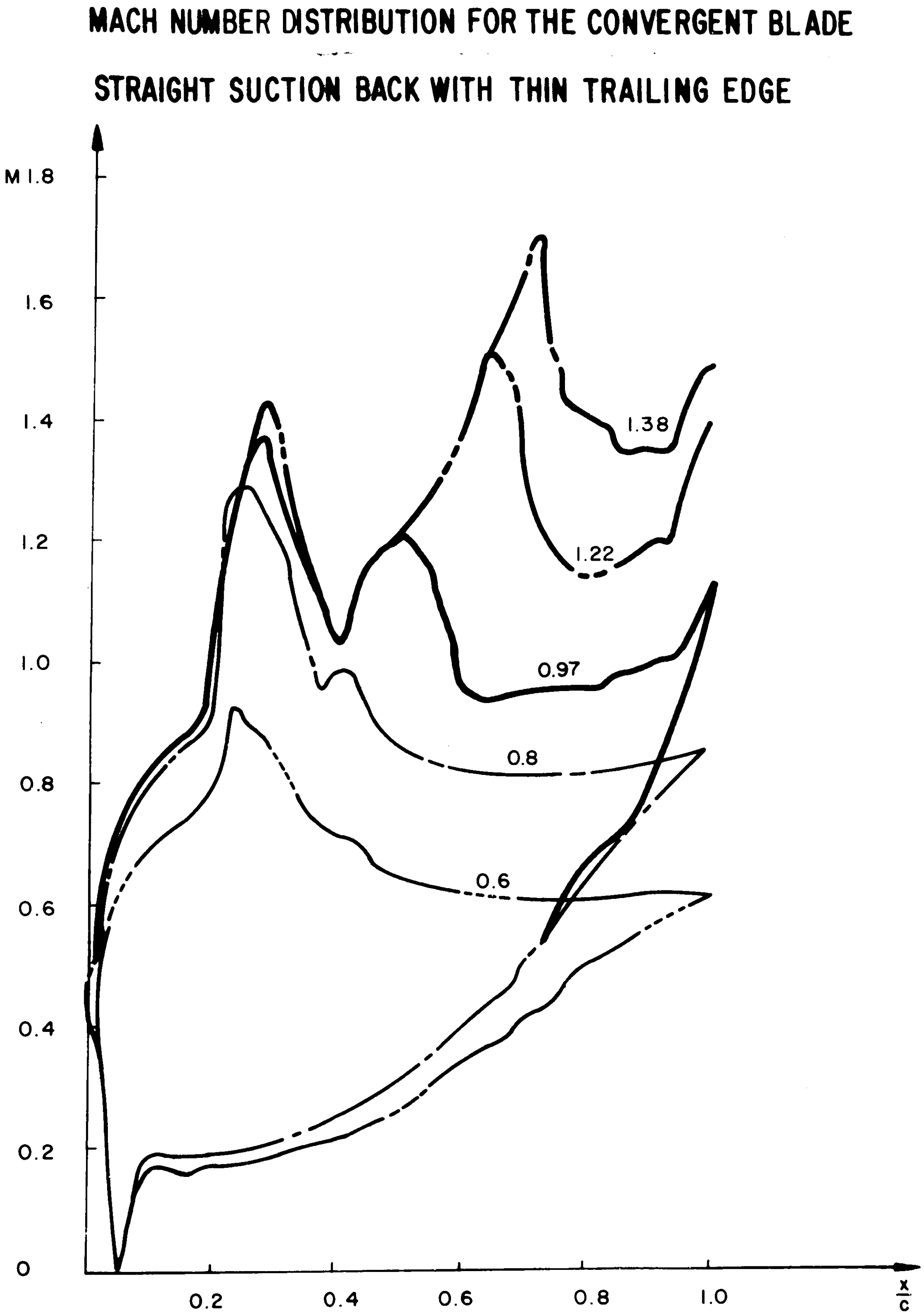

Figure 4.8 Blade 2 Surface Mach Number Distribution g/c = 0.75

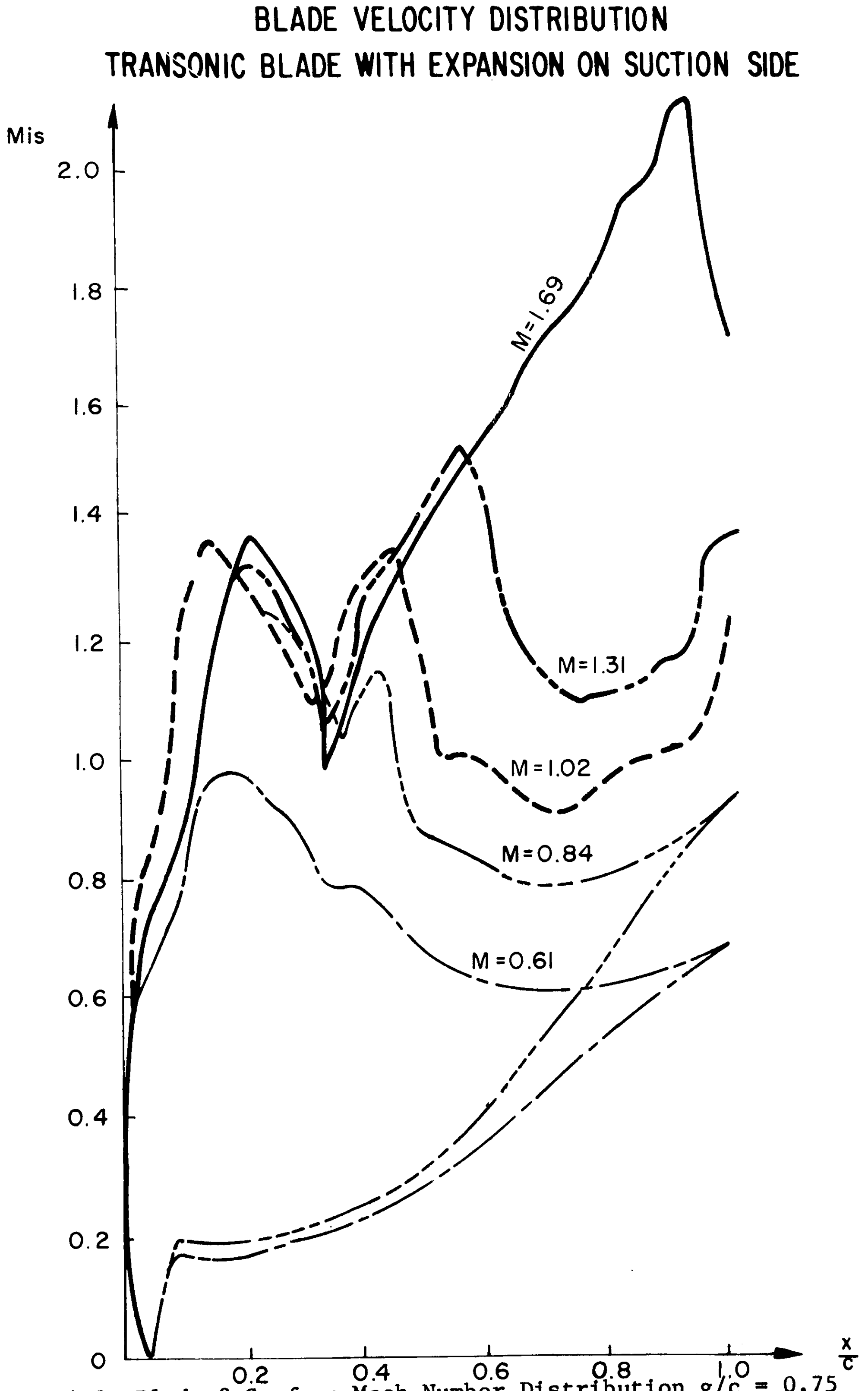
BLADE VELOCITY DISTRIBUTION
TRANSONIC BLADE WITH EXPANSION ON SUCTION SIDE

Figure 4.9 Blade 3 Surface Mach Number Distribution g/c = 0.75

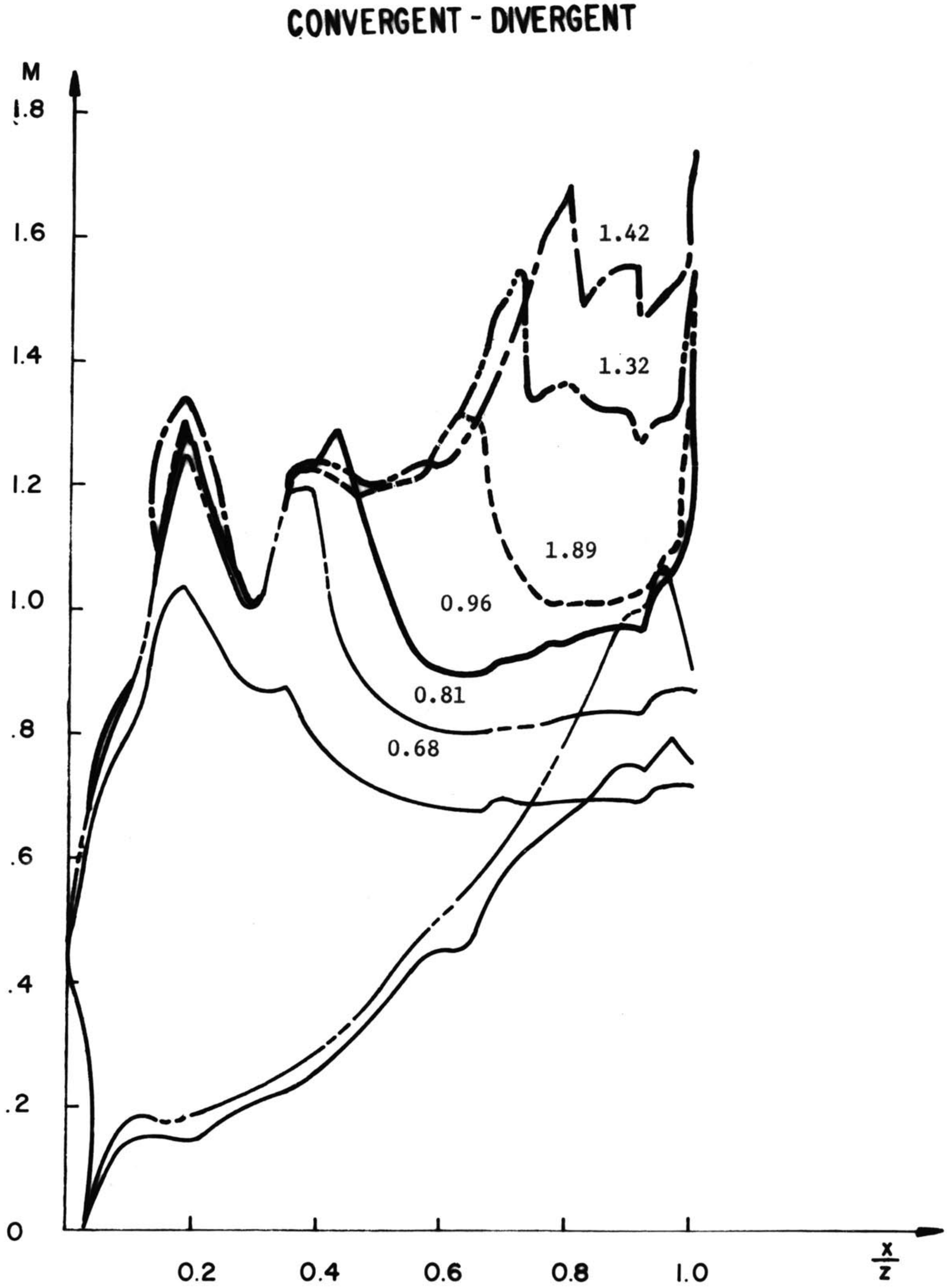

Figure 4.10 Blade 4 Surface Mach Number Distribution g/c = 0.75

Figure 4.11a Schlieren photos of Referen-e Blade 1 (straight suction back) g/c = 0.75

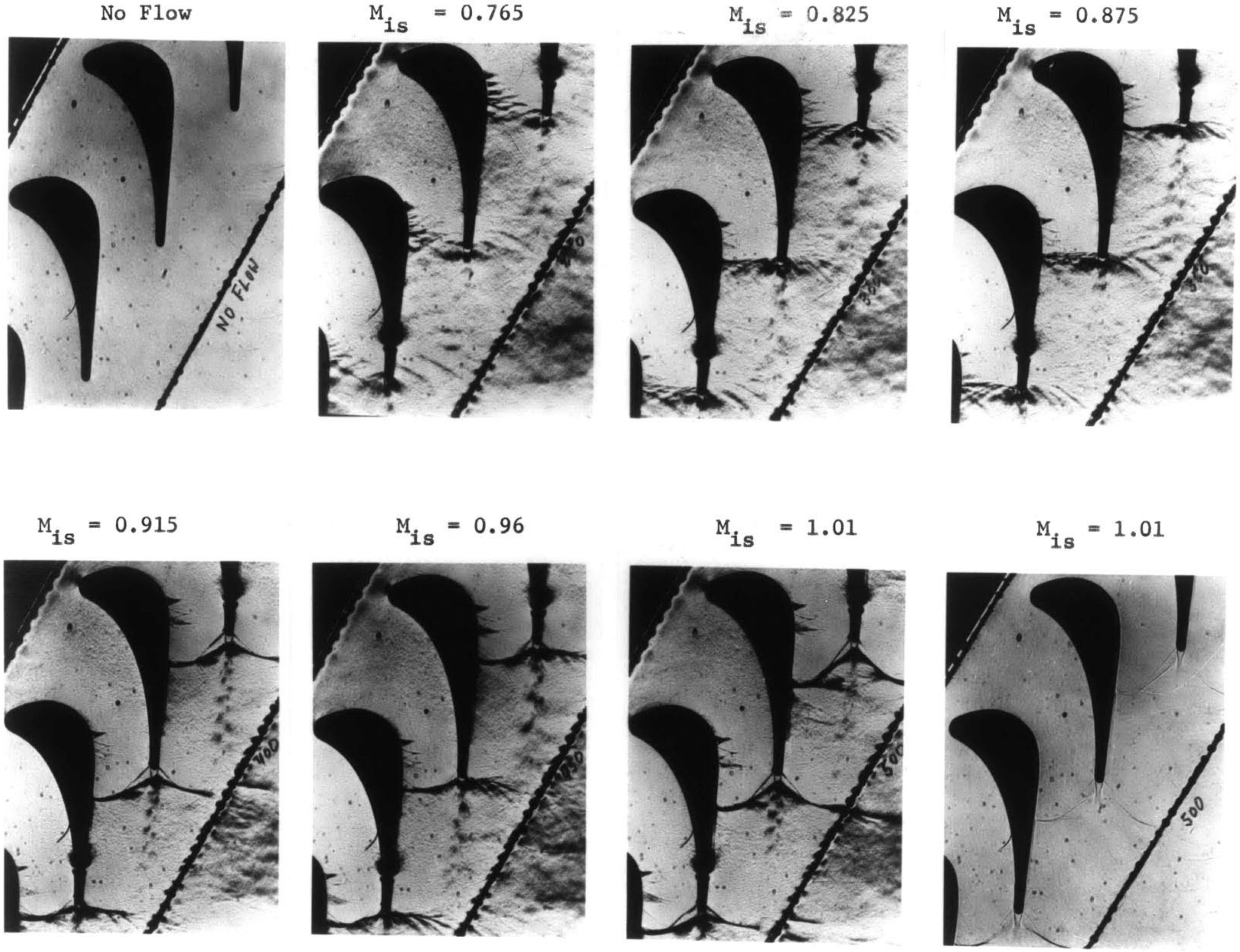
No Flow

$M_{is} = 0.765$

$M_{is} = 0.825$

$M_{is} = 0.875$

$M_{is} = 0.915$

$M_{is} = 0.96$

$M_{is} = 1.01$

$M_{is} = 1.01$

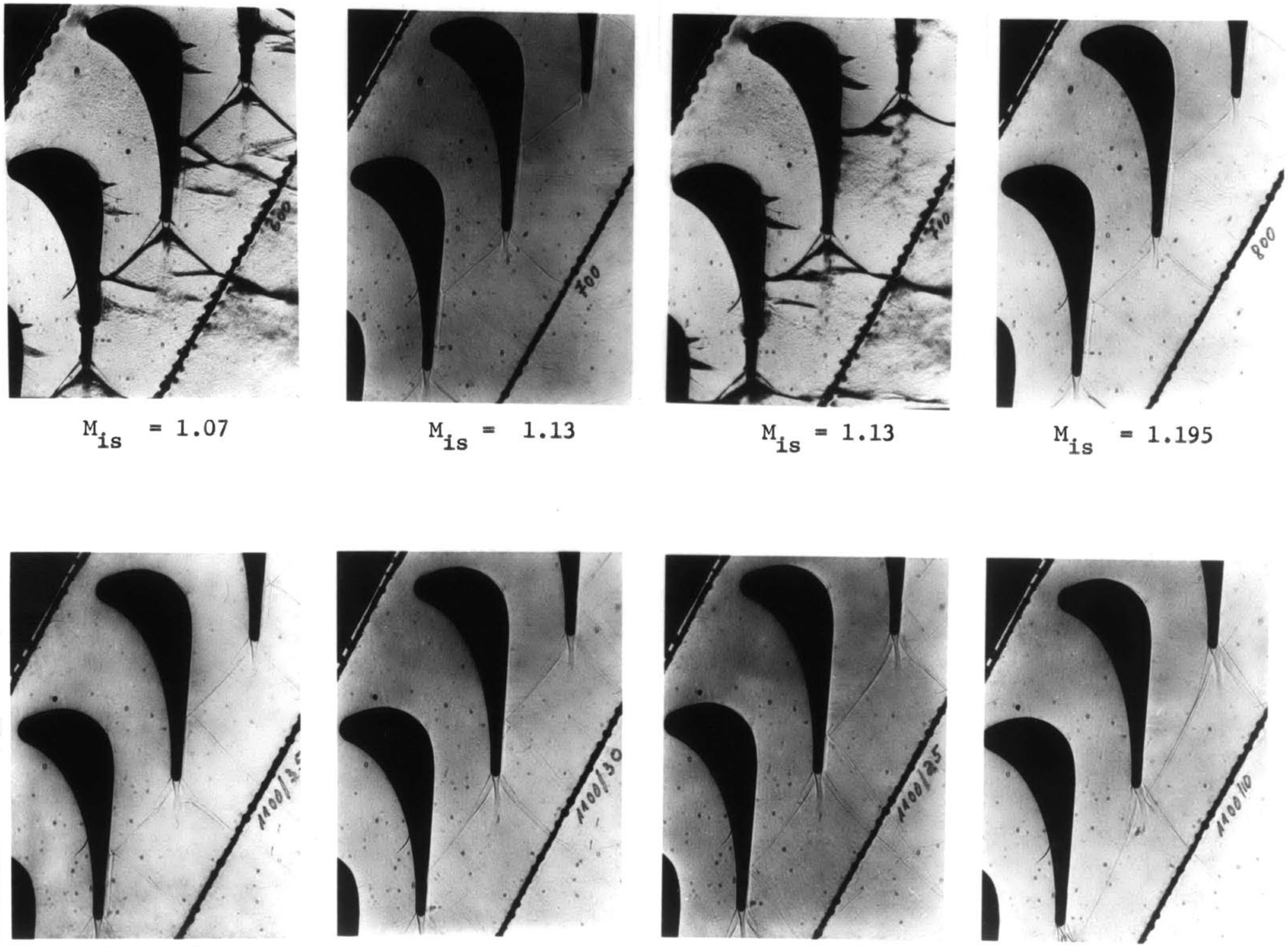

$M_{is} = 1.07$ $M_{is} = 1.13$ $M_{is} = 1.13$ $M_{is} = 1.195$

$M_{is} = 1.235$ $M_{is} = 1.34$ $M_{is} = 1.42$ $M_{is} = 1.67$

Figure 4.11b Schlieren photos of Reference Blade 1 contd. (straight suction back) g/c = 0.75

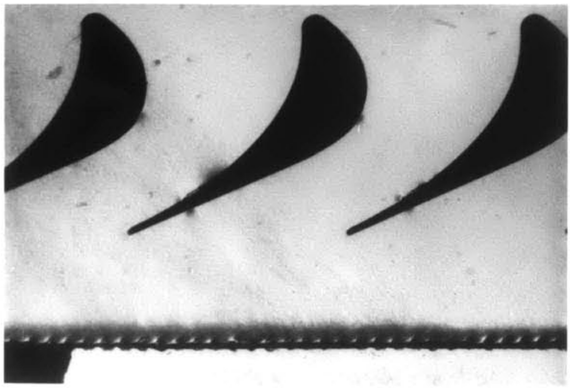

No Flow

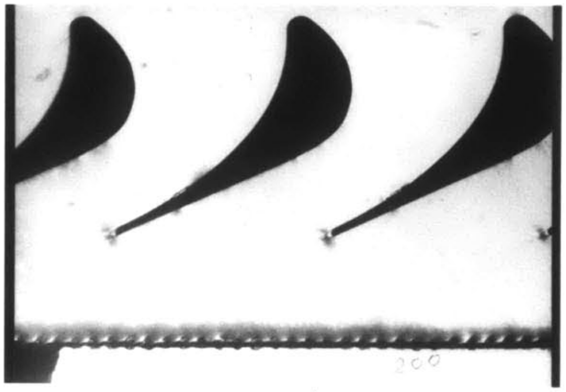

$M_{is} = 0.6$

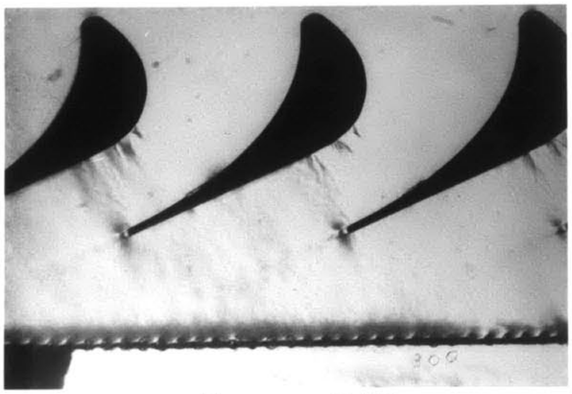

$M_{is} = 0.85$

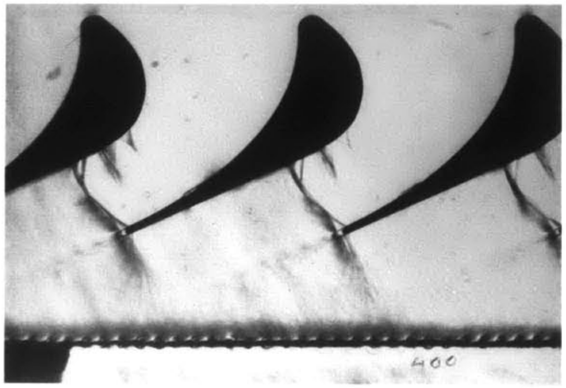

$M_{is} = 1.01$

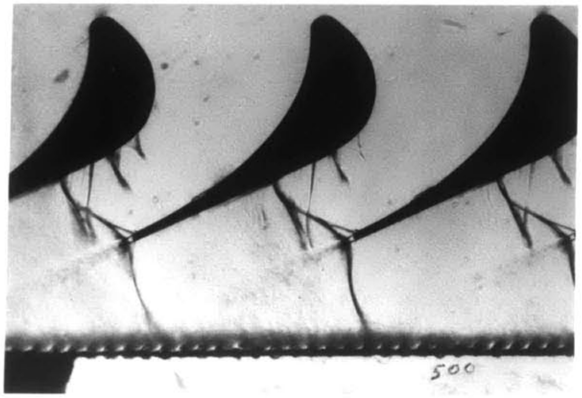

$M_{is} = 1.10$

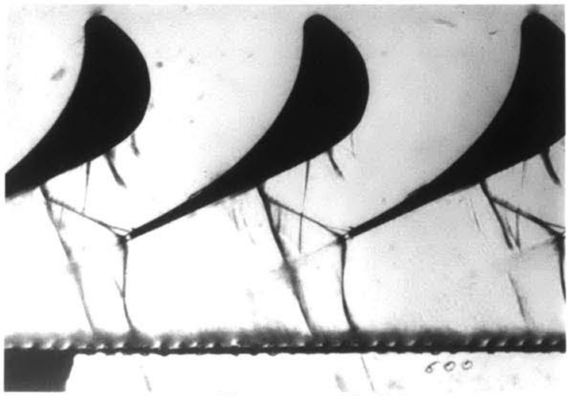

$M_{is} = 1.22$

Figure 4.12a Schlieren photos of Blade 2, g/c = 0.75
(Straight back with Thin Trailing Edge)

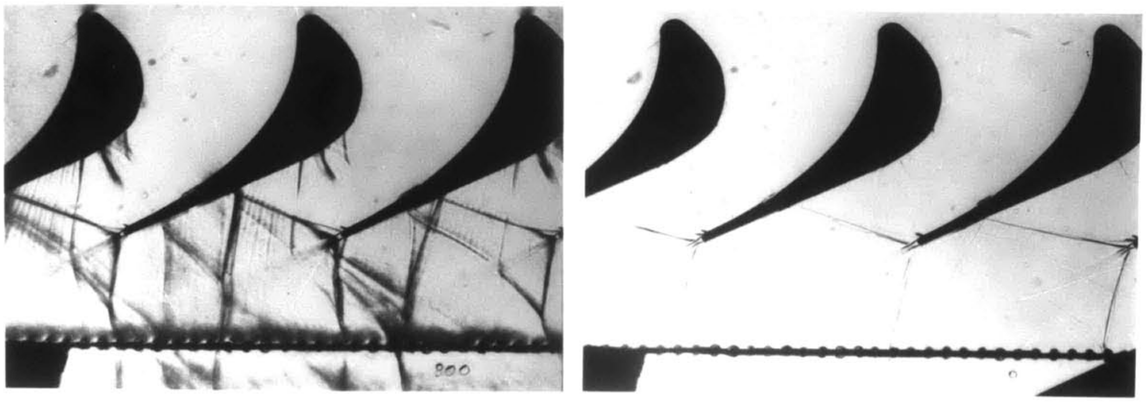

$M_{is} = 1.31$ $M_{is} = 1.38$

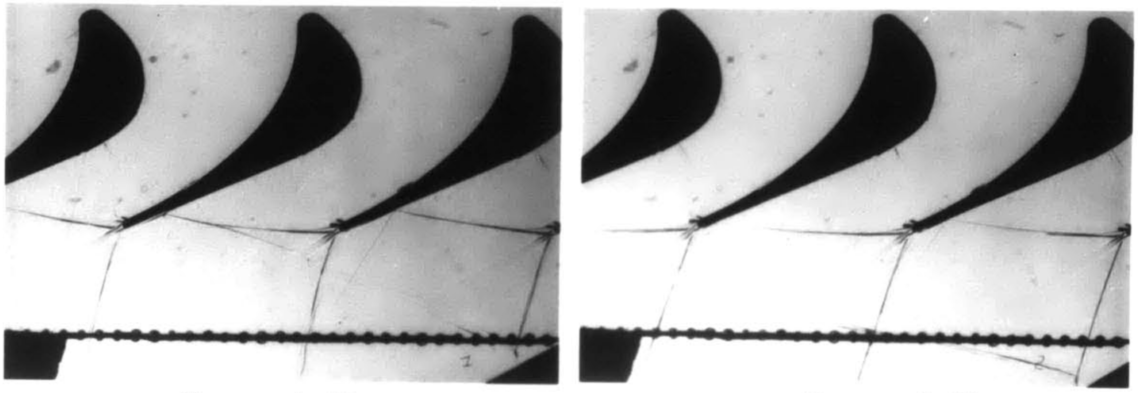

$M_{is} = 1.44$ $M_{is} = 1.50$

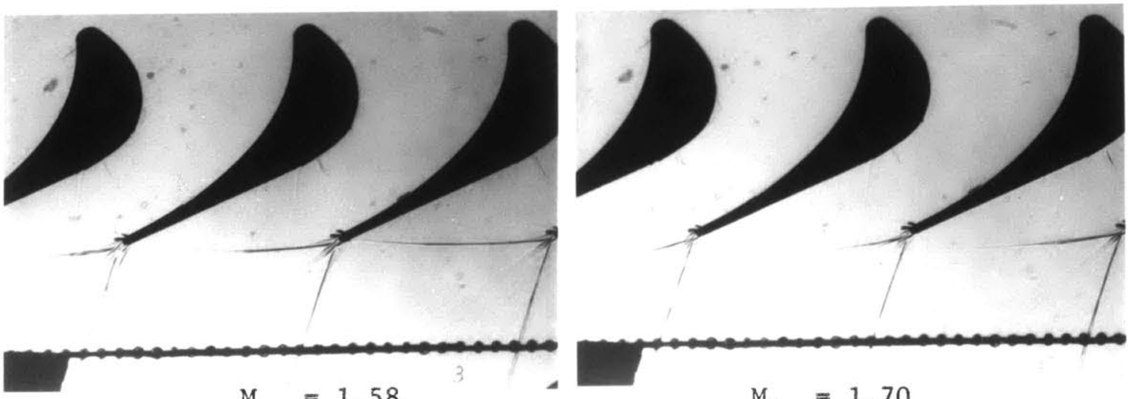

$M_{is} = 1.58$ $M_{is} = 1.70$

Figure 4.12b Schlieren photos of Blade 2 (contd) g/c = 0.75
(Straight back with Thin Trailing Edge)

Figure 4.13a Schlieren photos of the Plug Nozzle Blade 3 (unguided expansion) g/c = 0.75

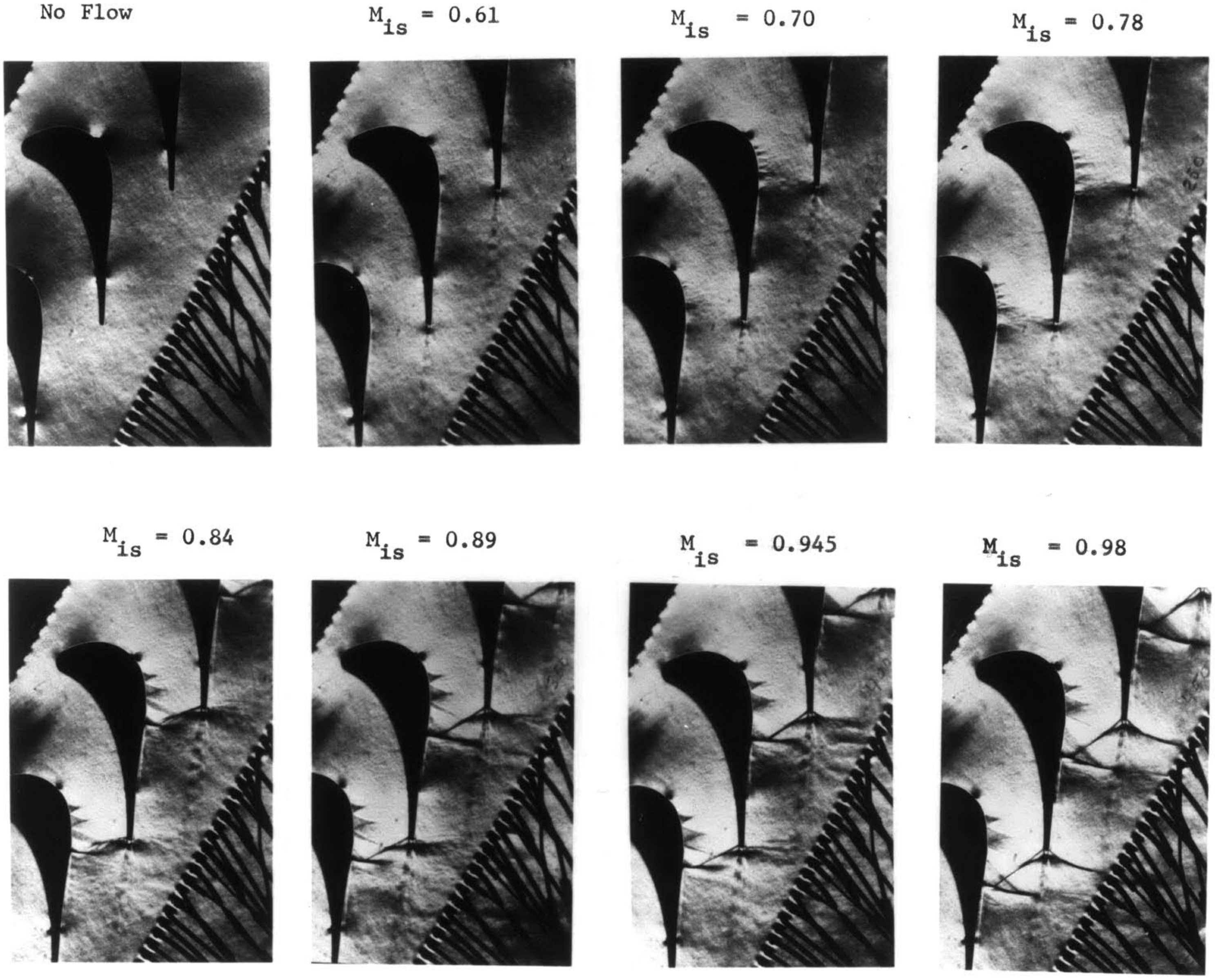

No Flow

$M_{is} = 0.61$

$M_{is} = 0.70$

$M_{is} = 0.78$

$M_{is} = 0.84$

$M_{is} = 0.89$

$M_{is} = 0.945$

$M_{is} = 0.98$

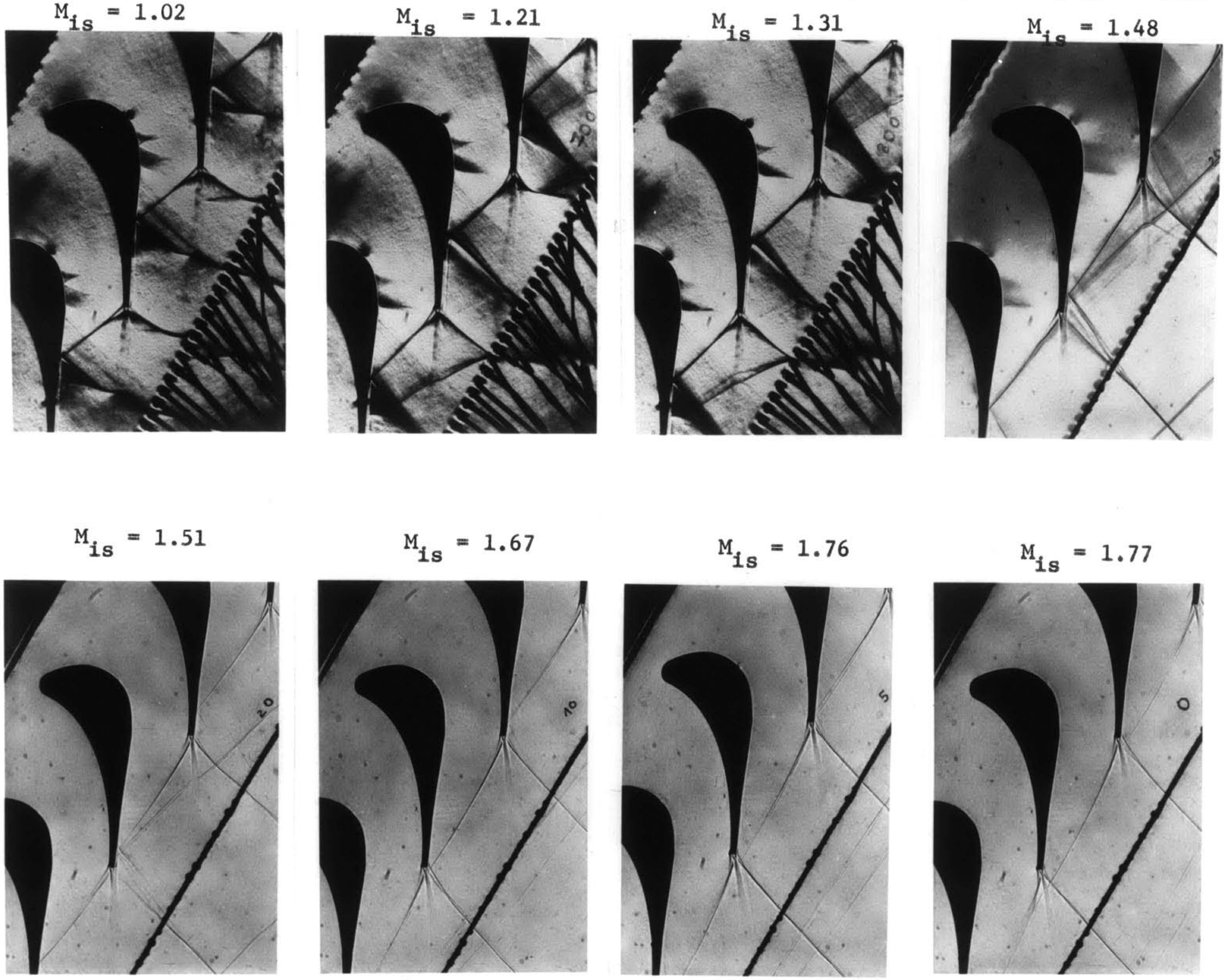

Figure 4.13b Schlieren photos of the Plug Nozzle Blade 3 contd. (unguided expansion) g/c = 0.75

$M_{is} = 1.02$ $M_{is} = 1.21$ $M_{is} = 1.31$ $M_{is} = 1.48$

$M_{is} = 1.51$ $M_{is} = 1.67$ $M_{is} = 1.76$ $M_{is} = 1.77$

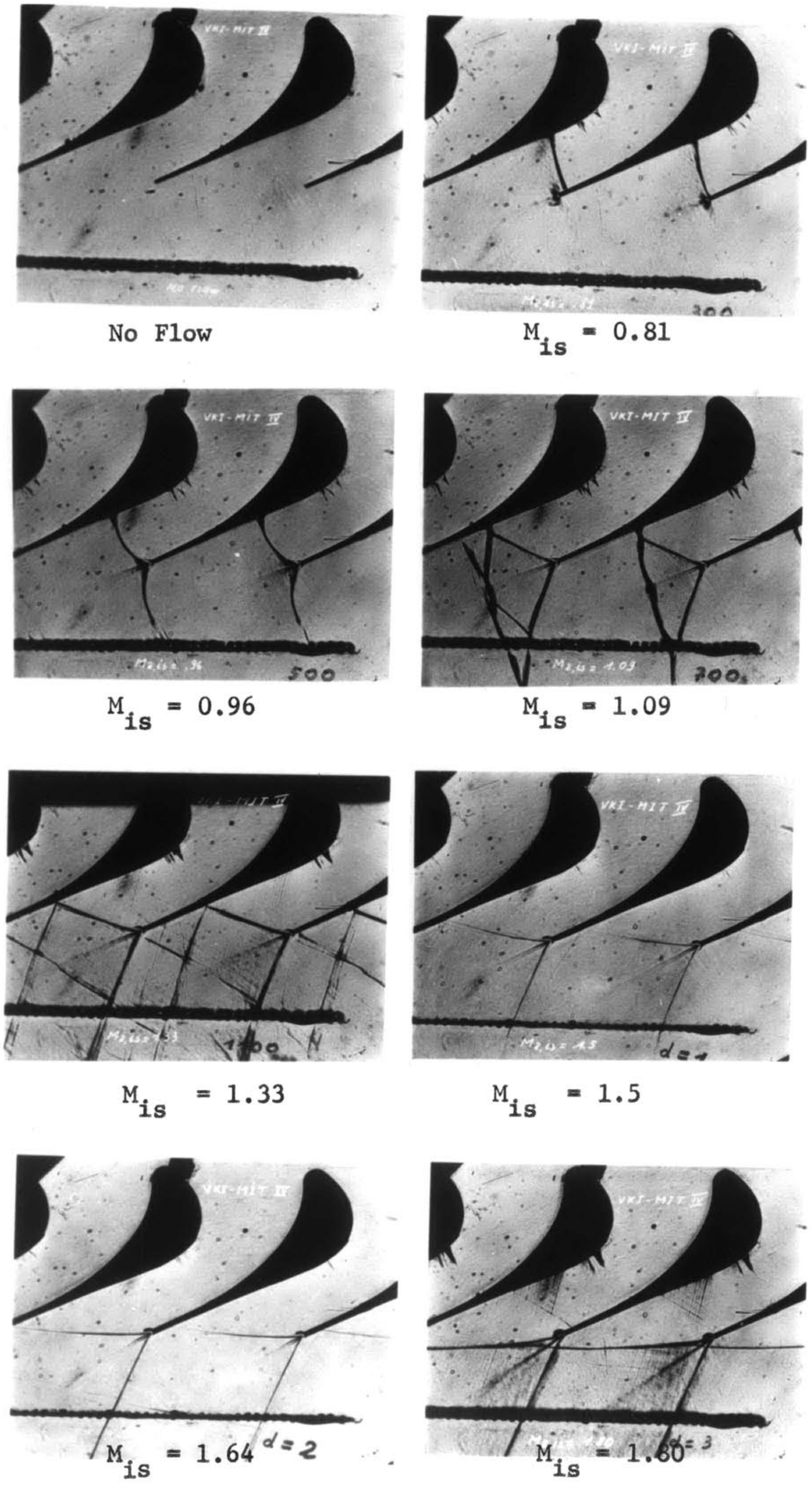

No Flow

$M_{is} = 0.81$

$M_{is} = 0.96$

$M_{is} = 1.09$

$M_{is} = 1.33$

$M_{is} = 1.5$

$M_{is} = 1.64$

$M_{is} = 1.80$

Figure 4.14 Schlieren photos of the Convergent-Divergent Blade 4
g/c = 0.75

Figure 4.15 PERFORMANCE CURVE BLADE WITH STRAIGHT SUCTION BACK

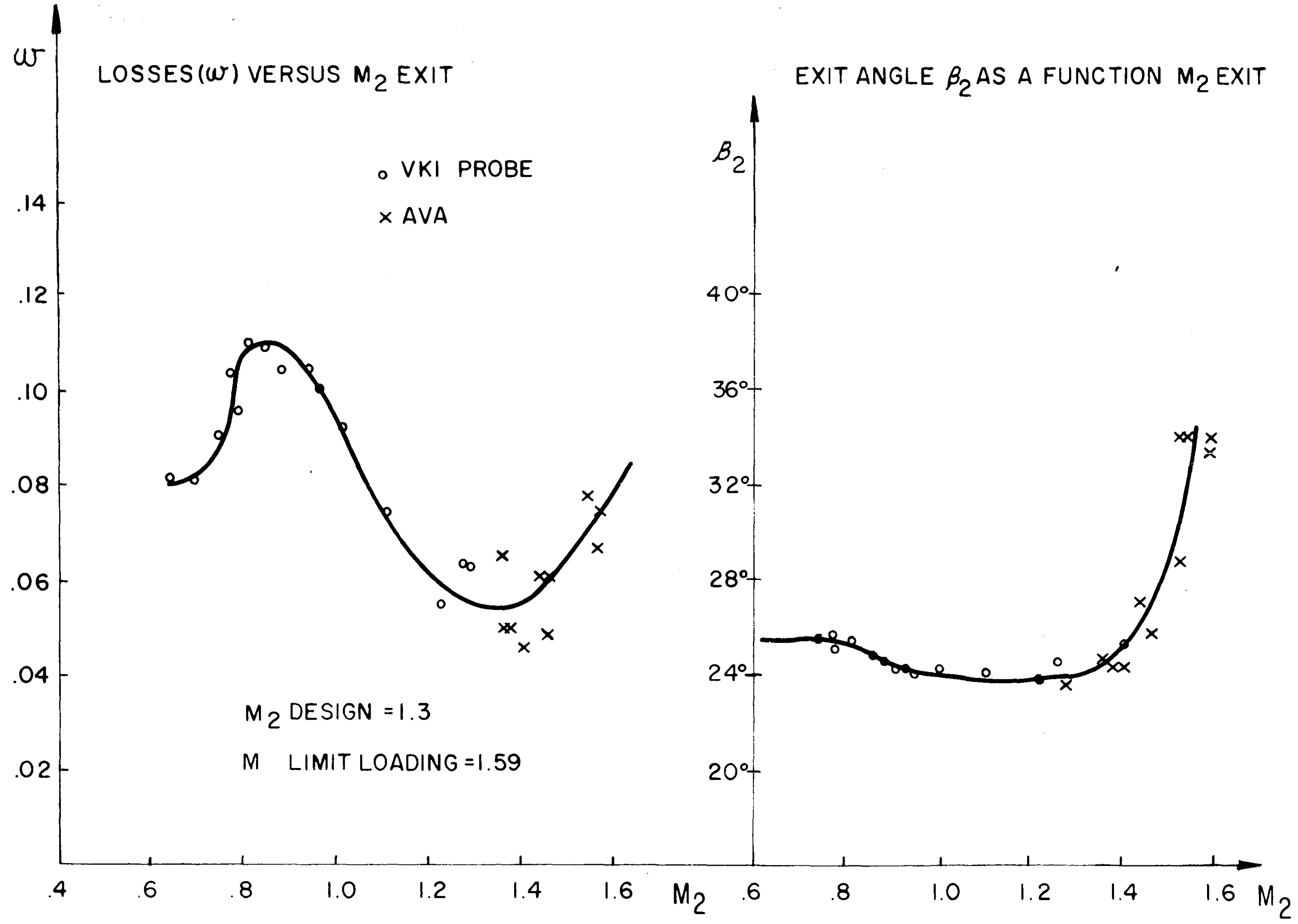

Figure 4.16 PERFORMANCE CURVE-CONVERGENT BLADE STRIGHT SUCTION BACK WITH THIN TRAILING EDGE

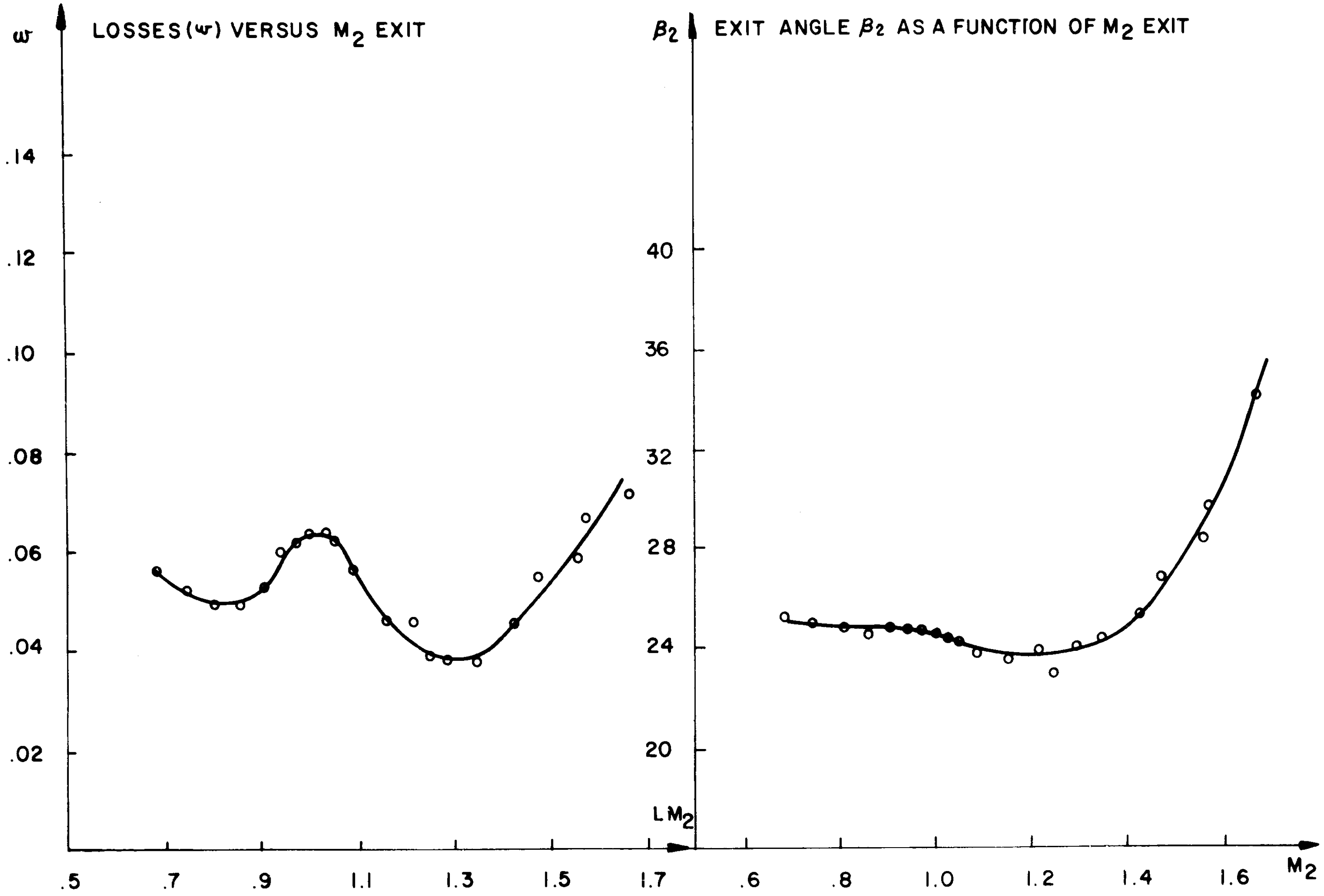

Figure 4.17 PERFORMANCE CURVE BLADE WITH EXPANSION ON SUCTION SIDE (PLUG)

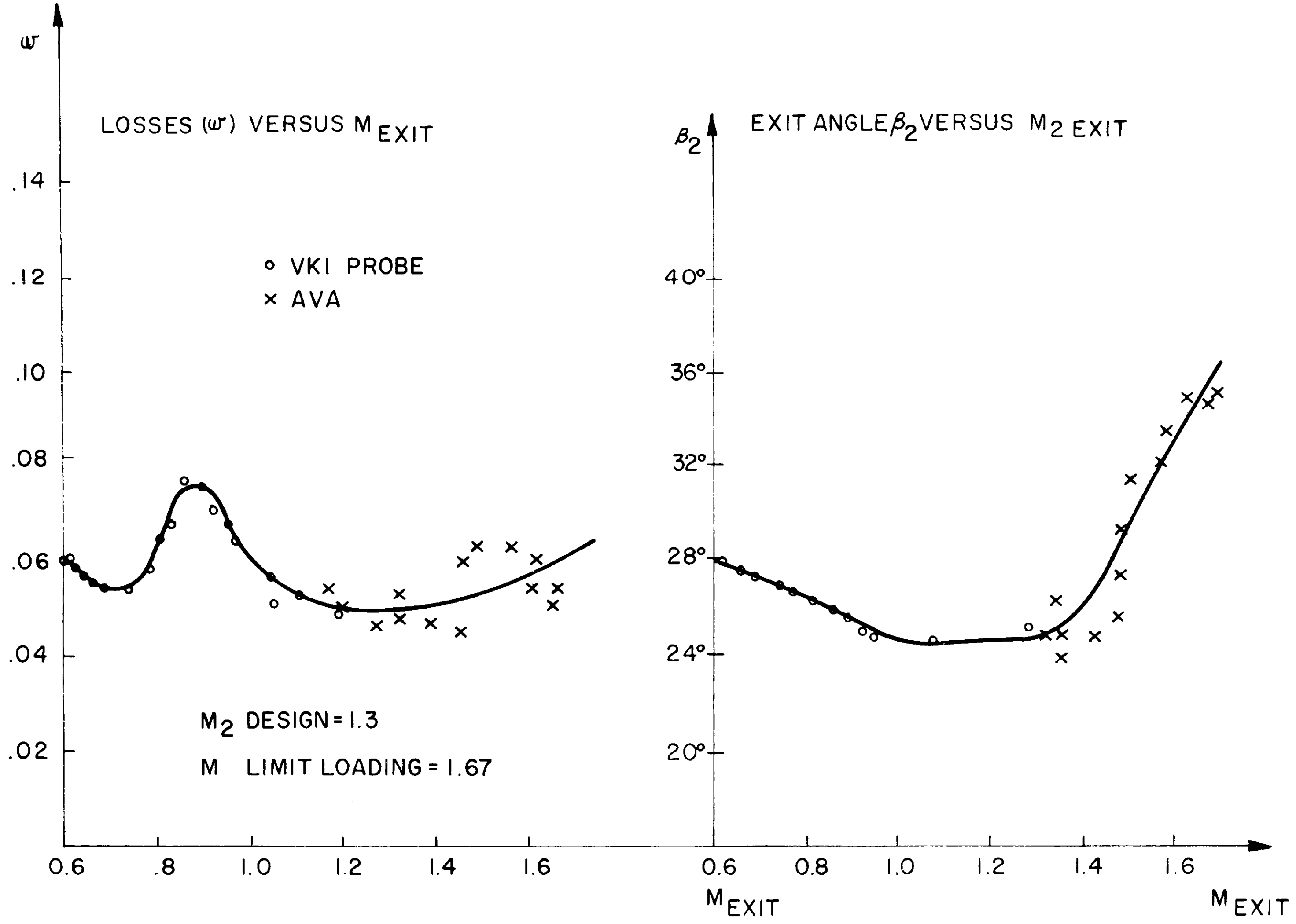

Figure 4.18 **CONVERGENT AND DIVERGENT BLADE PROFILE**

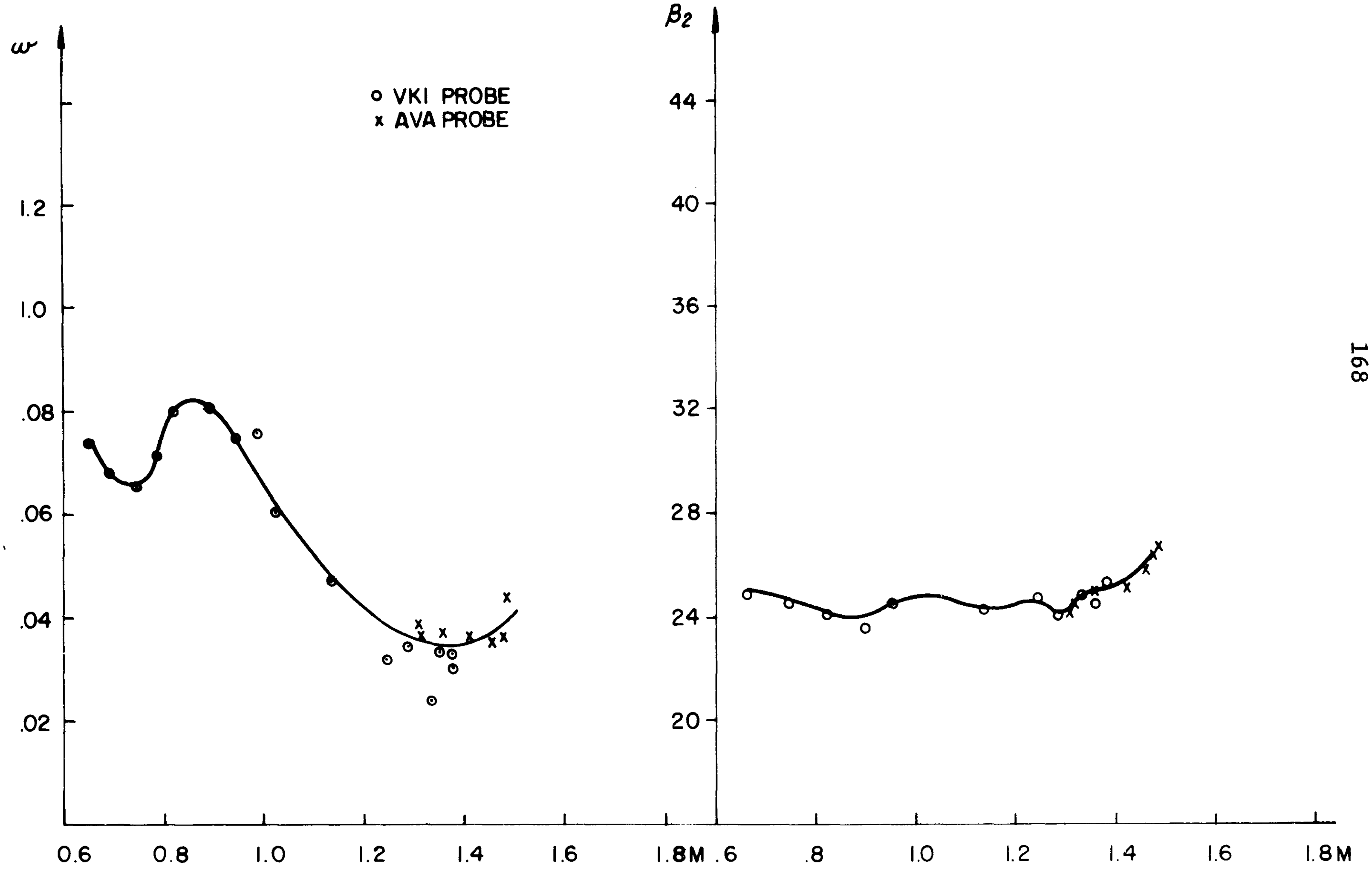

Figure 4.19

COMPARISON OF AERODYNAMIC PERFORMANCE OF DIFFERENT TRANSONIC TURBINE BLADE PROFILES

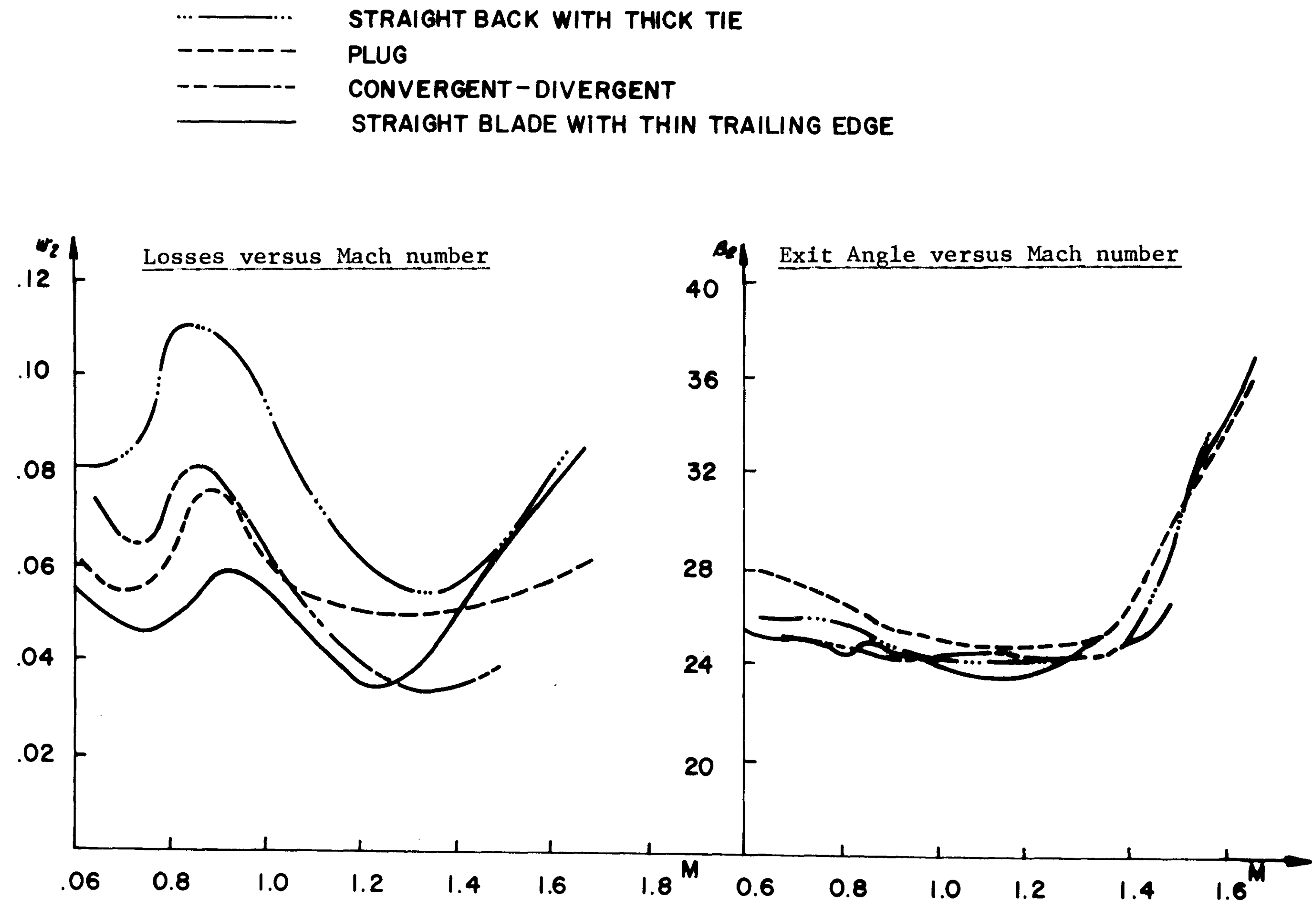

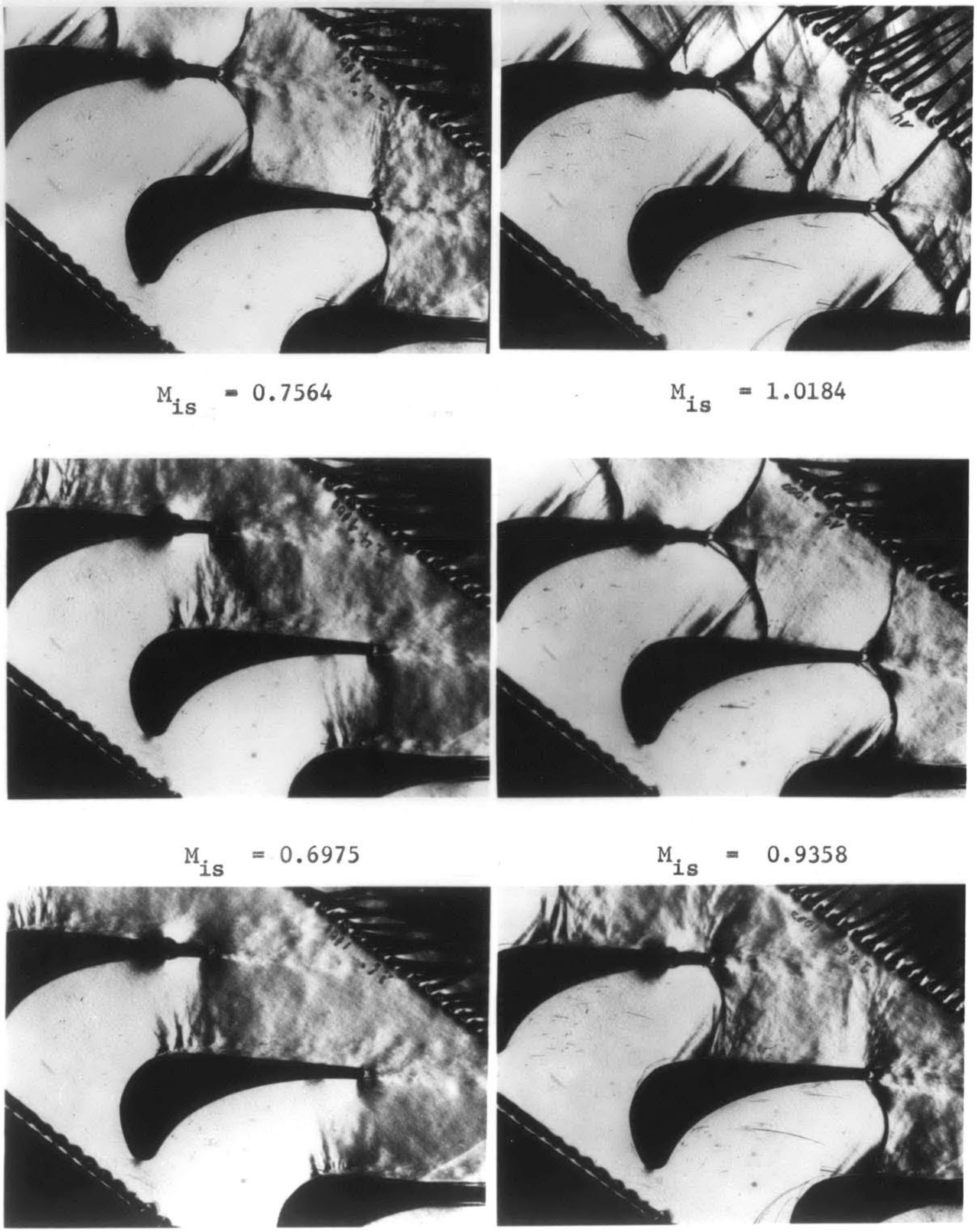

M_{is} = 0.9029

M_{is} = 1.1716

M_{is} = 0.7564

M_{is} = 1.0184

M_{is} = 0.6975

M_{is} = 0.9358

Figure 4.20 Reference Blade 1 Schlieren photos g/c = 0.81 with varying back pressure to change Reynolds number

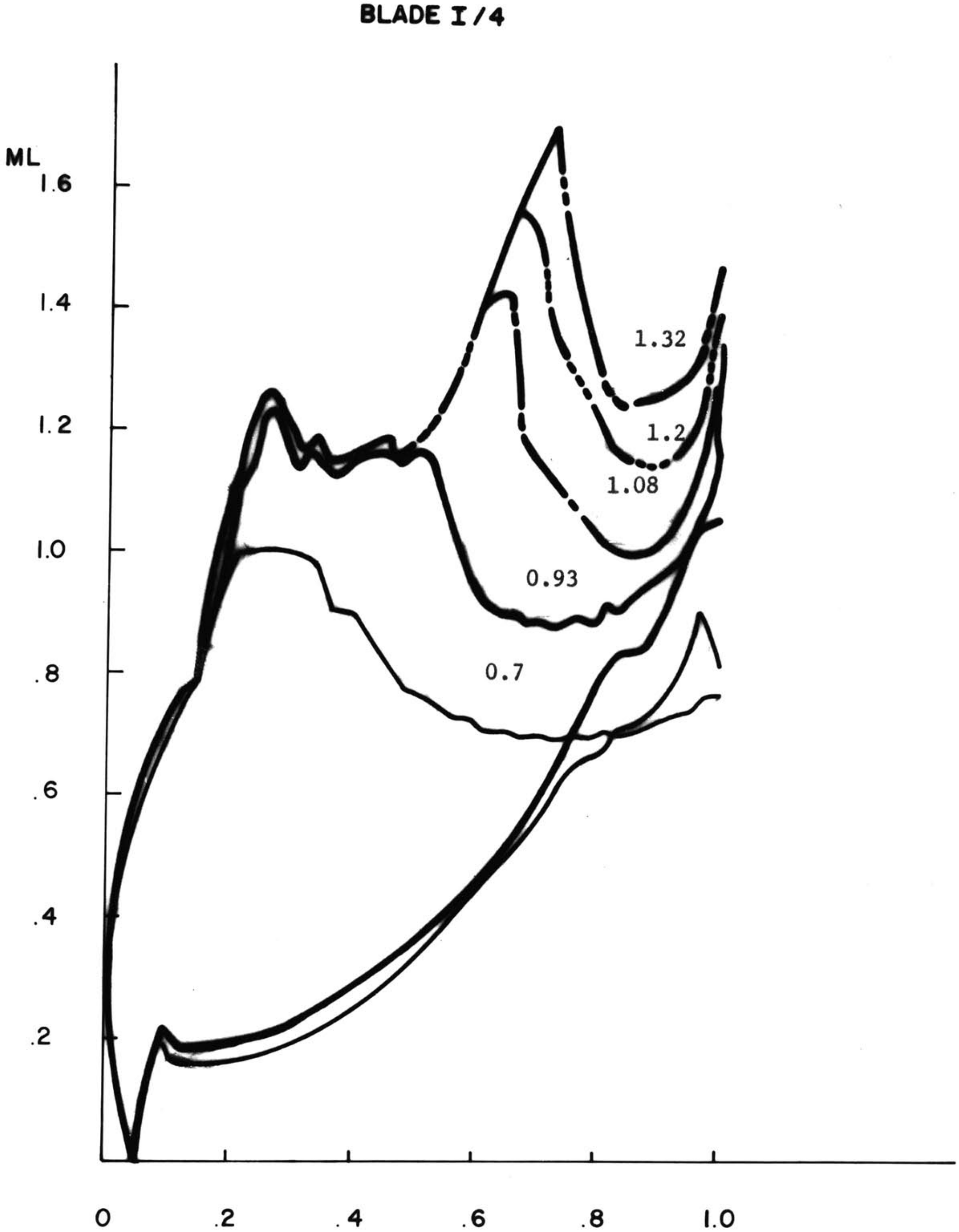

Figure 4.22 Blade 1 Mach number distribution g/c = 0.695

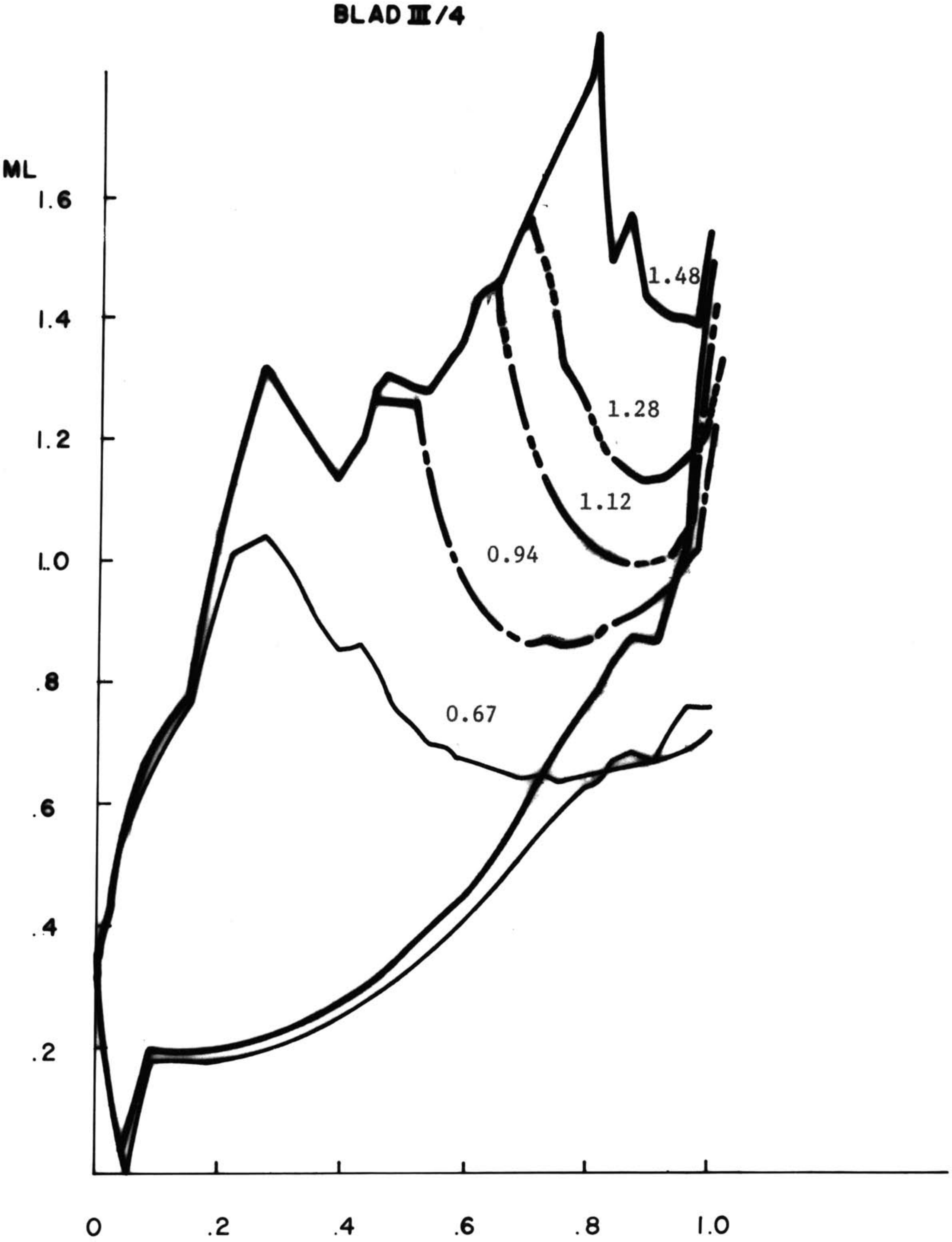

Figure 4.23 Blade 3 Mach number distribution g/c = 0.695

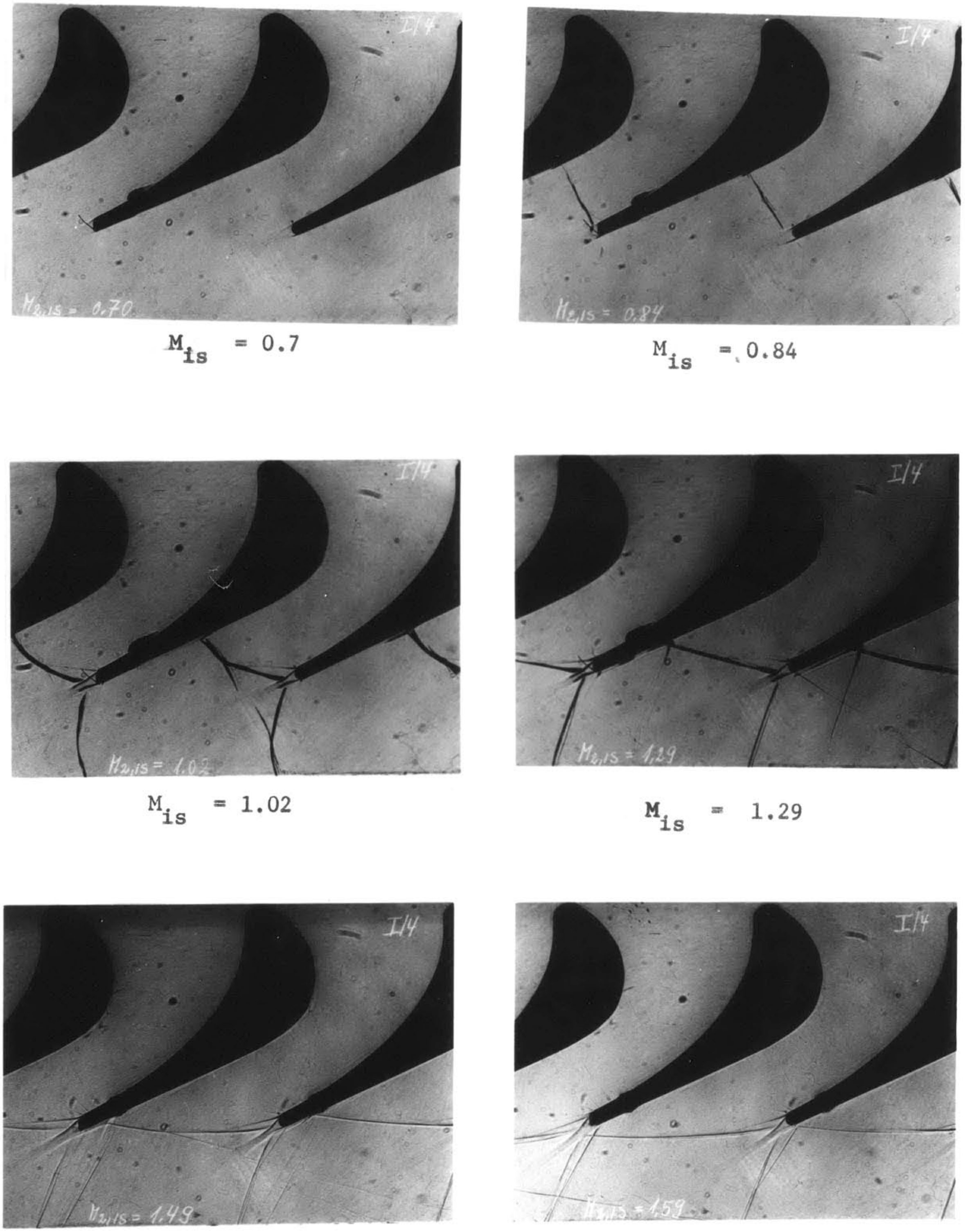

M_{is} = 0.7

M_{is} = 0.84

M_{is} = 1.02

M_{is} = 1.29

M_{is} = 1.49

M_{is} = 1.59

Figure 4.24 Reference Blade 1 Schlieren photos g/c = 0.695

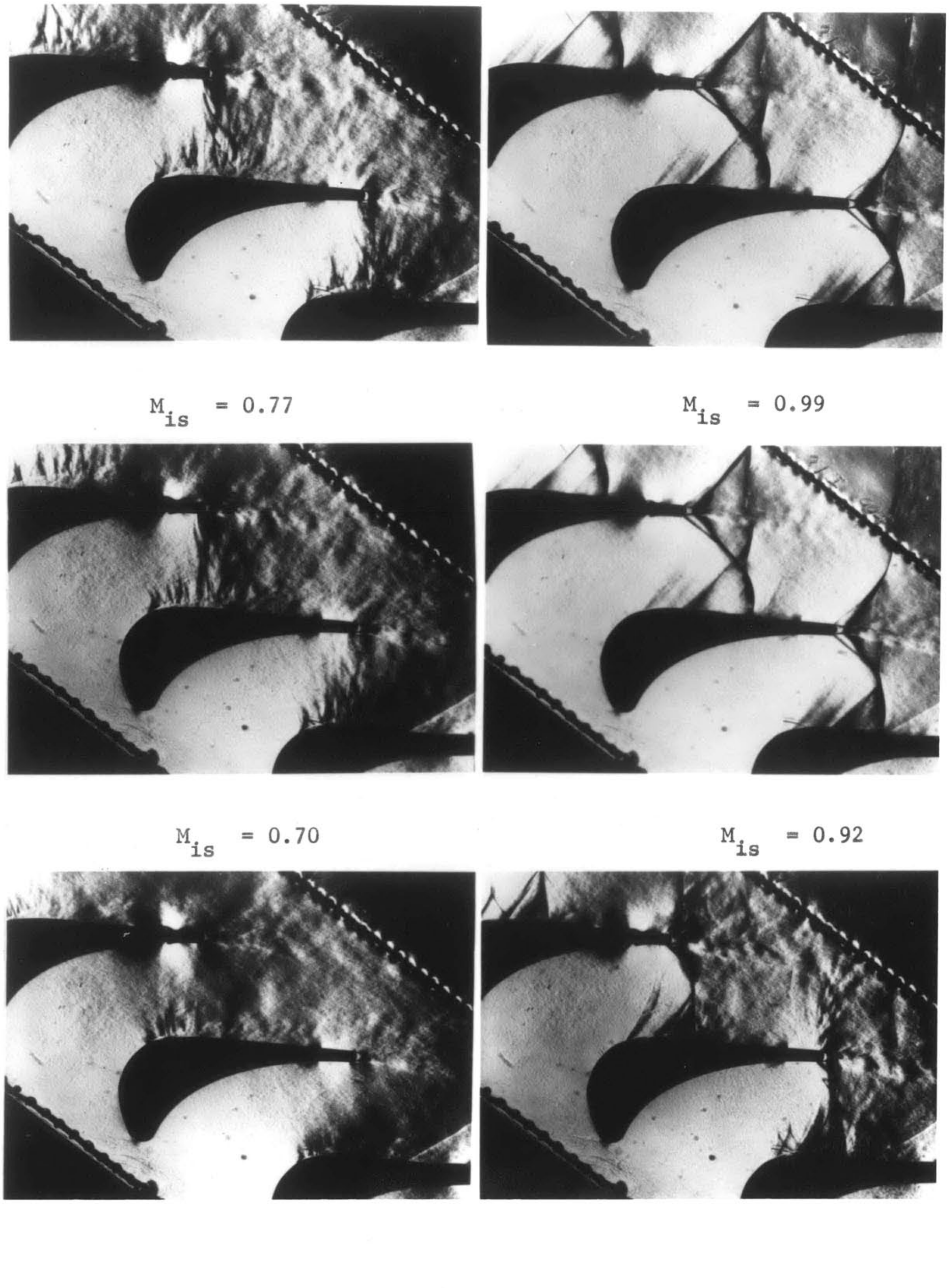

$M_{is} = 0.83$

$M_{is} = 1.06$

$M_{is} = 0.77$

$M_{is} = 0.99$

$M_{is} = 0.70$

$M_{is} = 0.92$

Figure 4.24b Reference Blade 1 Schlieren photos g/c = 0.81

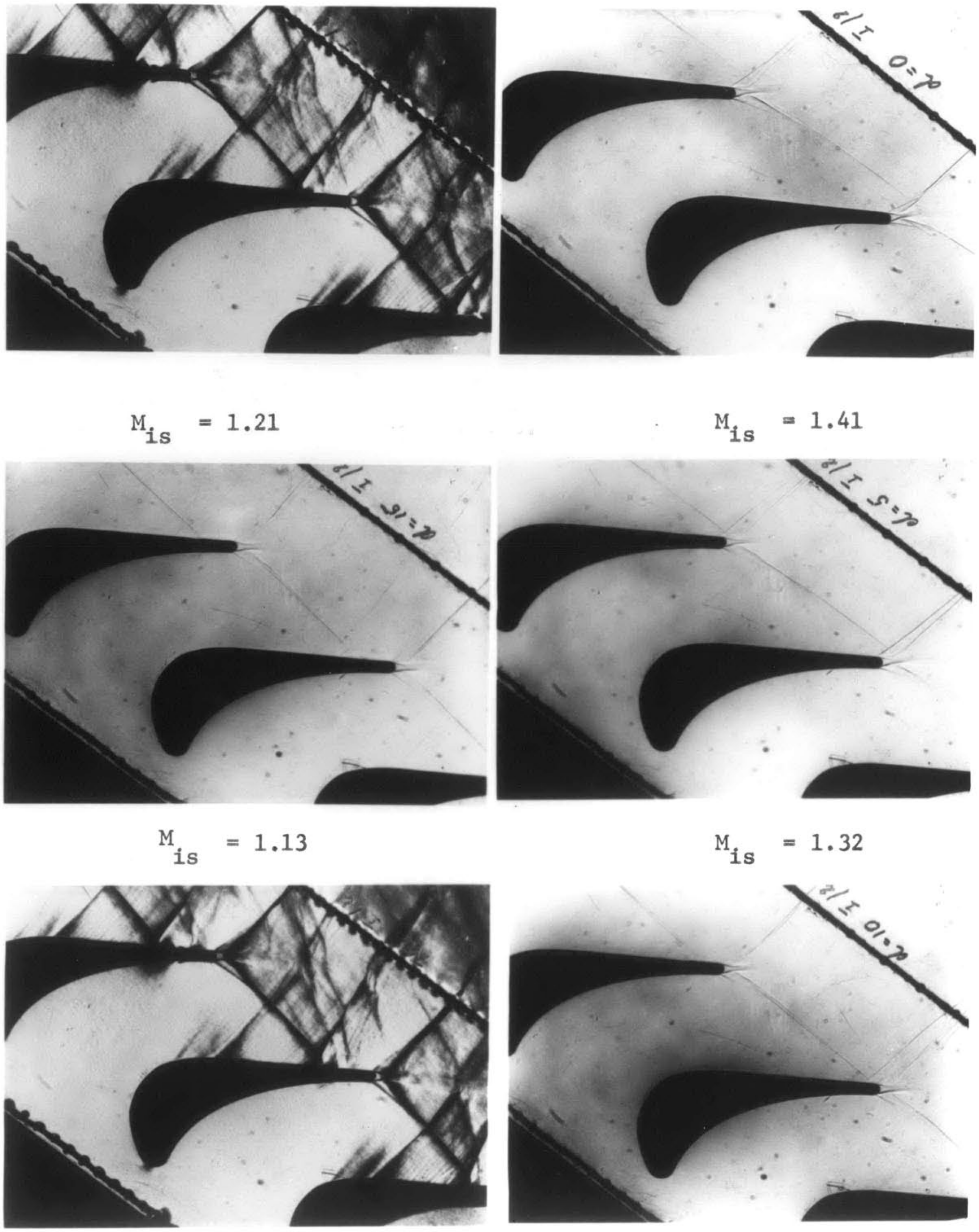

M_{is} = 1.22

M_{is} = 1.49

M_{is} = 1.21

M_{is} = 1.41

M_{is} = 1.13

M_{is} = 1.32

Figure 4.24c Reference Blade 1 Schlieren photos g/c = 0.81 contd.

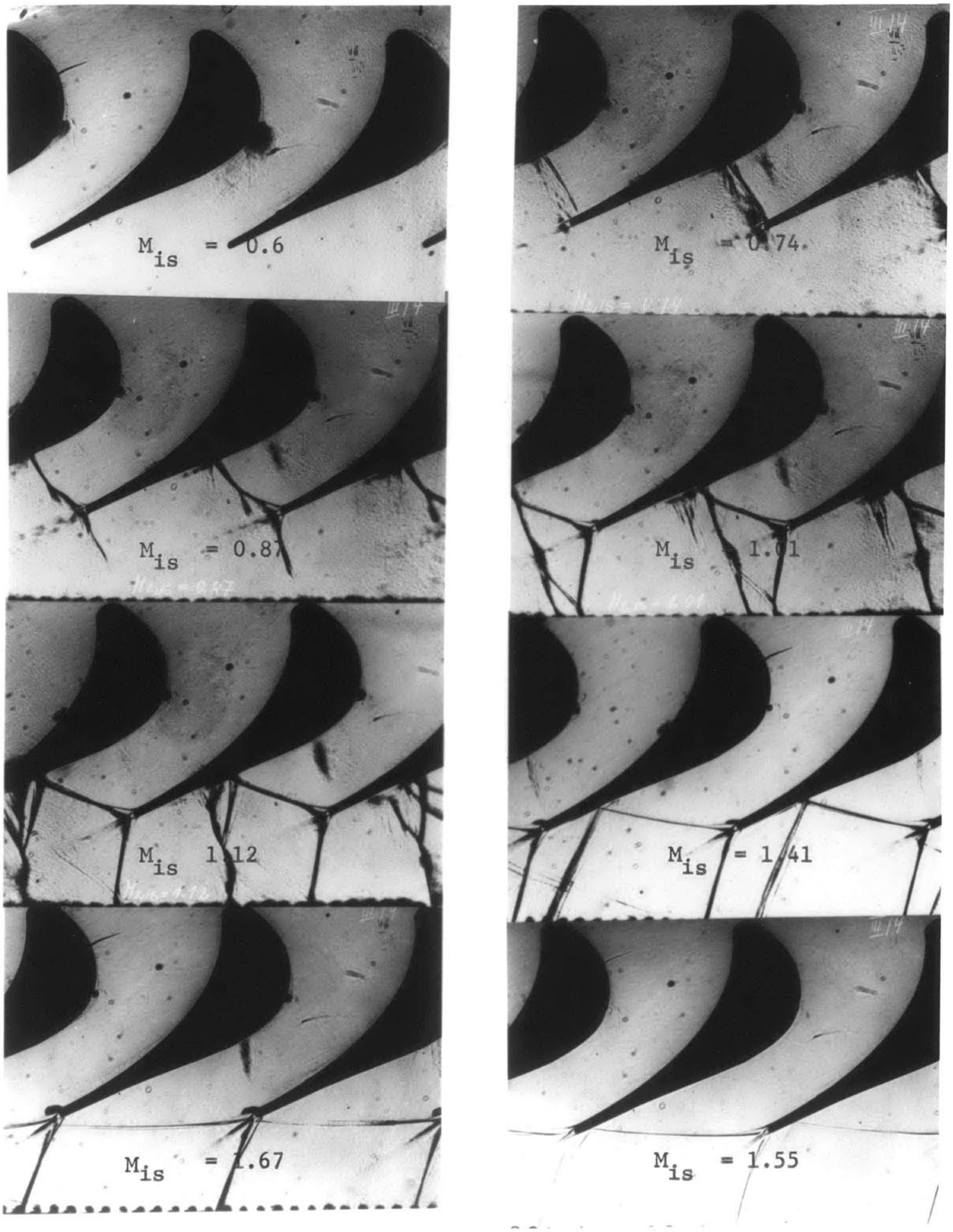

Figure 4.25 "Plug Nozzle" Blade 3 Schlieren photos g/c = 0.695

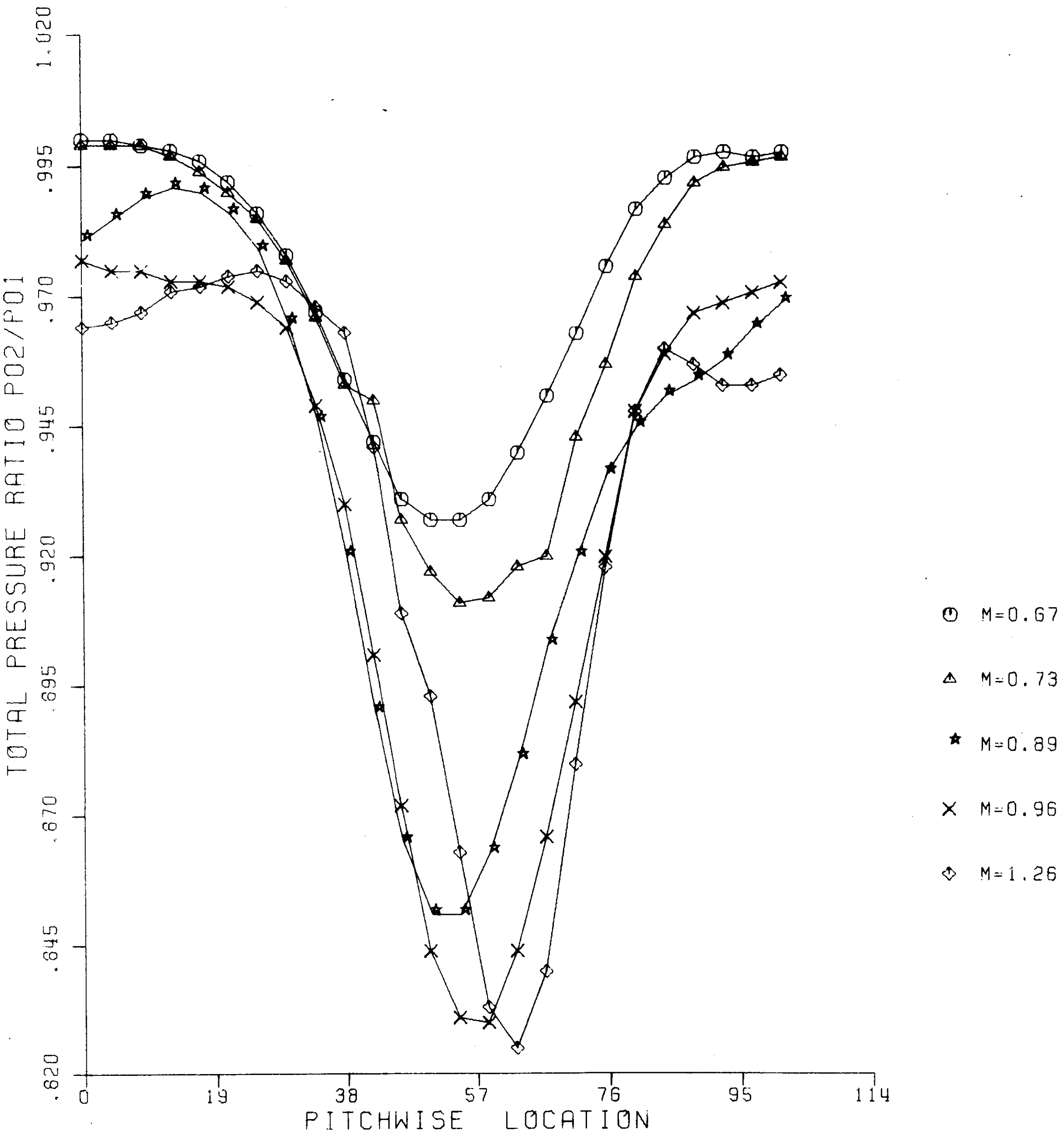

Figure 4.26 Blade 1 Downstream Wake (Stagnation Pressure ratio variation across the pitch)

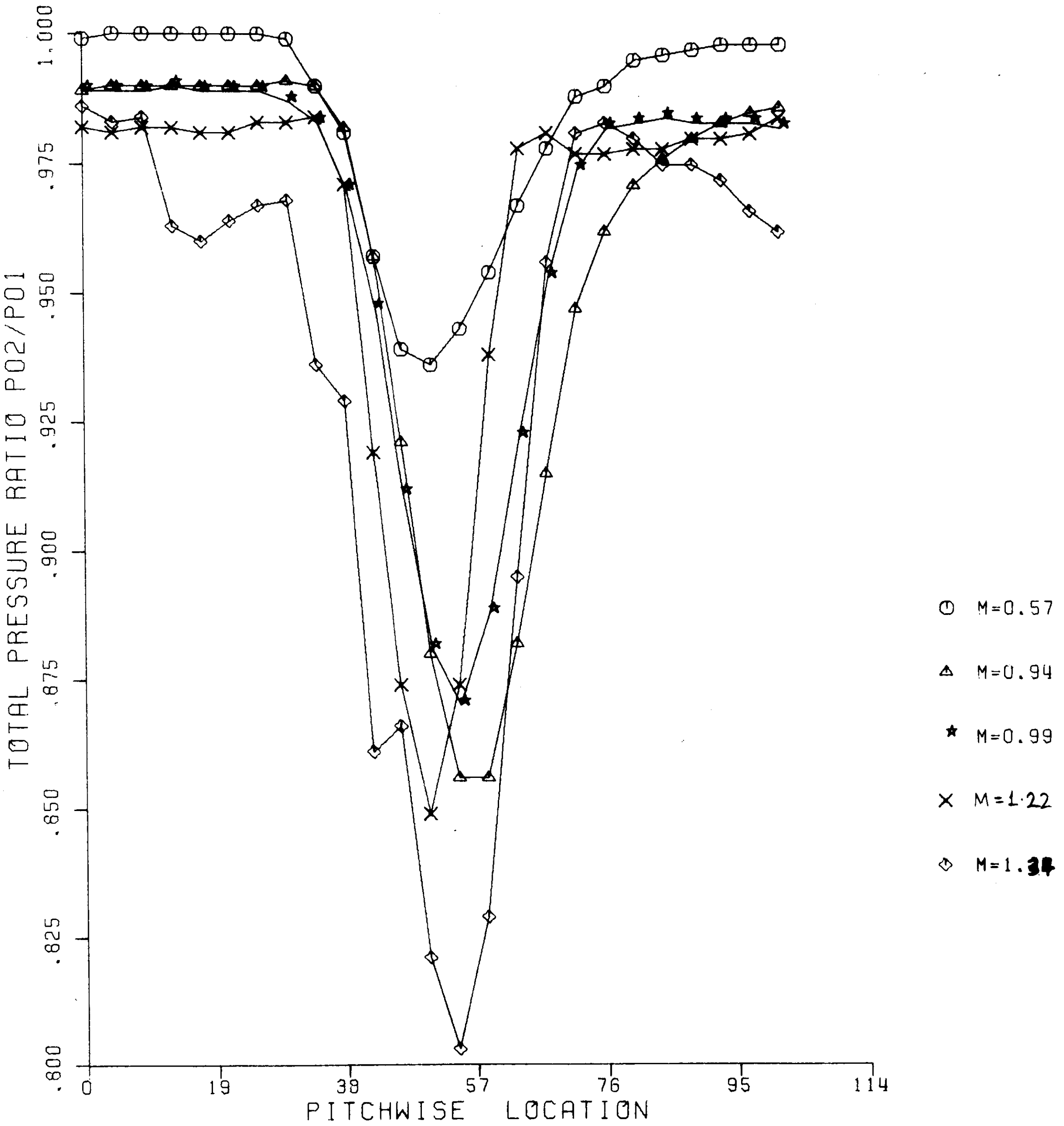

Figure 4.27 Blade 2 Downstream Wake (Stagnation Pressure ratio variation across the pitch)

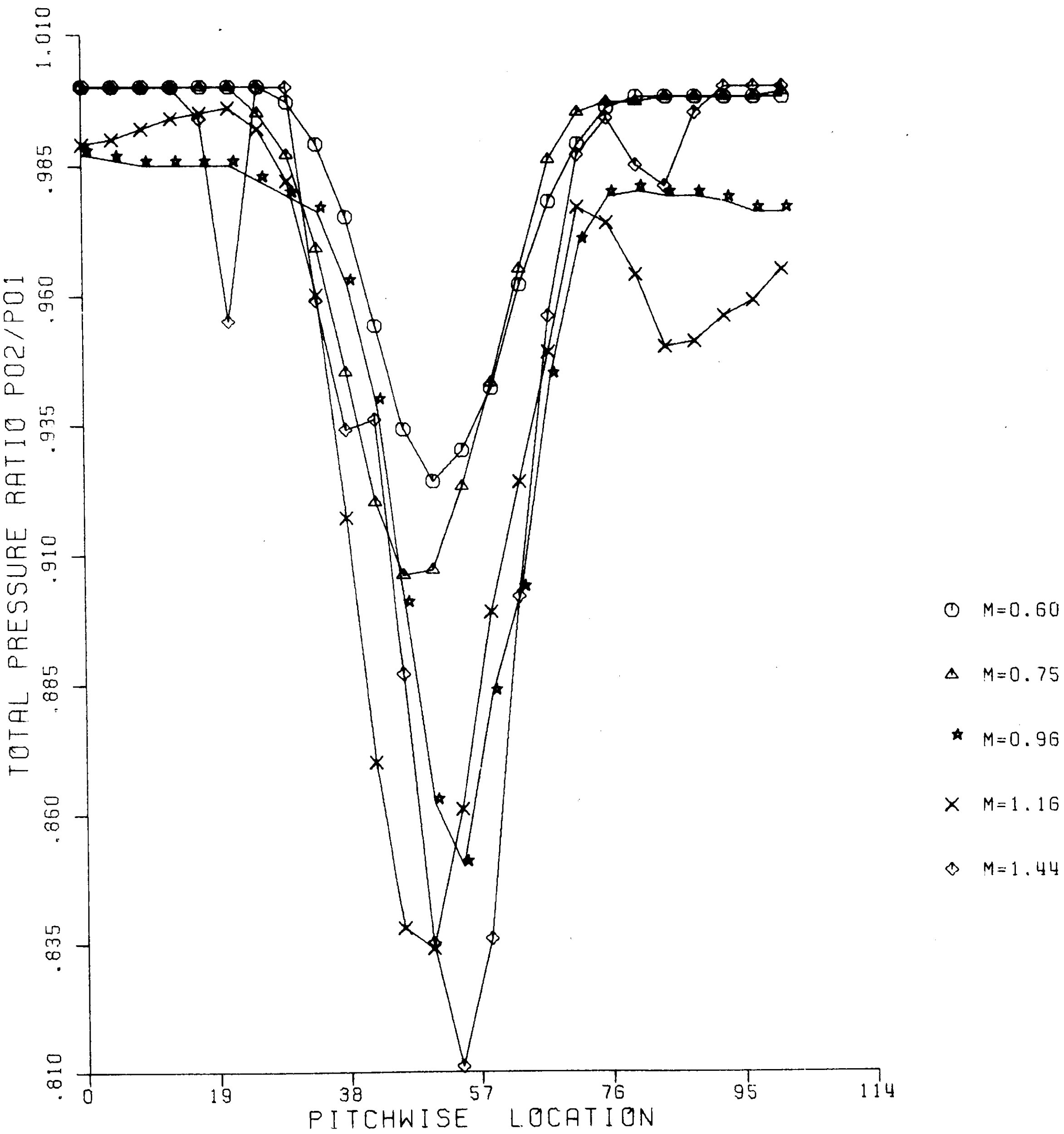

Figure 4.28 Blade 3 Downstream Wake (Stagnation Pressure ratio variation across the pitch)

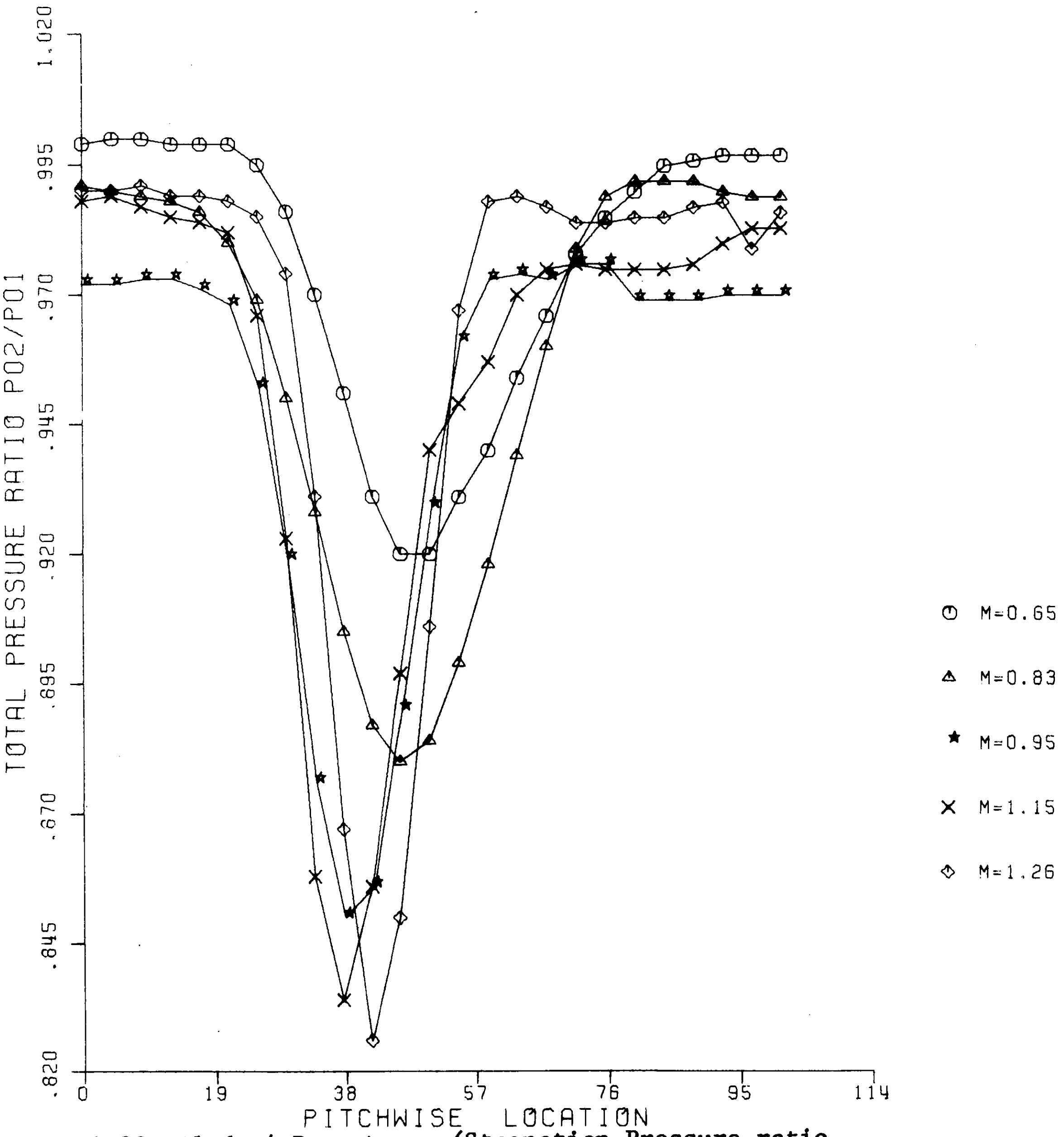

Figure 4.29 Blade 4 Downstream (Stagnation Pressure ratio variation across the pitch)

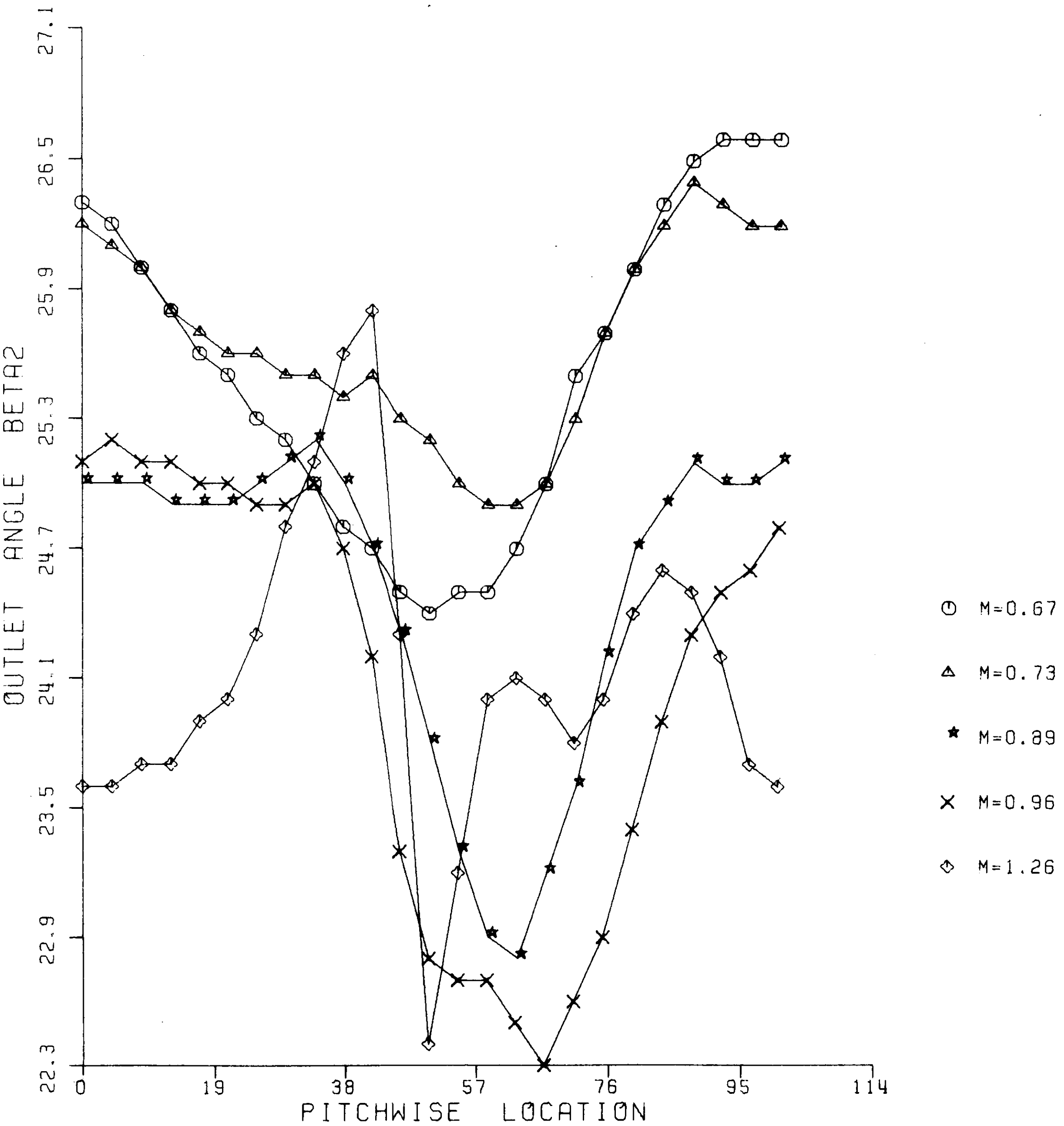

Figure 4.30 Blade 1 Exit angle Variation across the pitch.

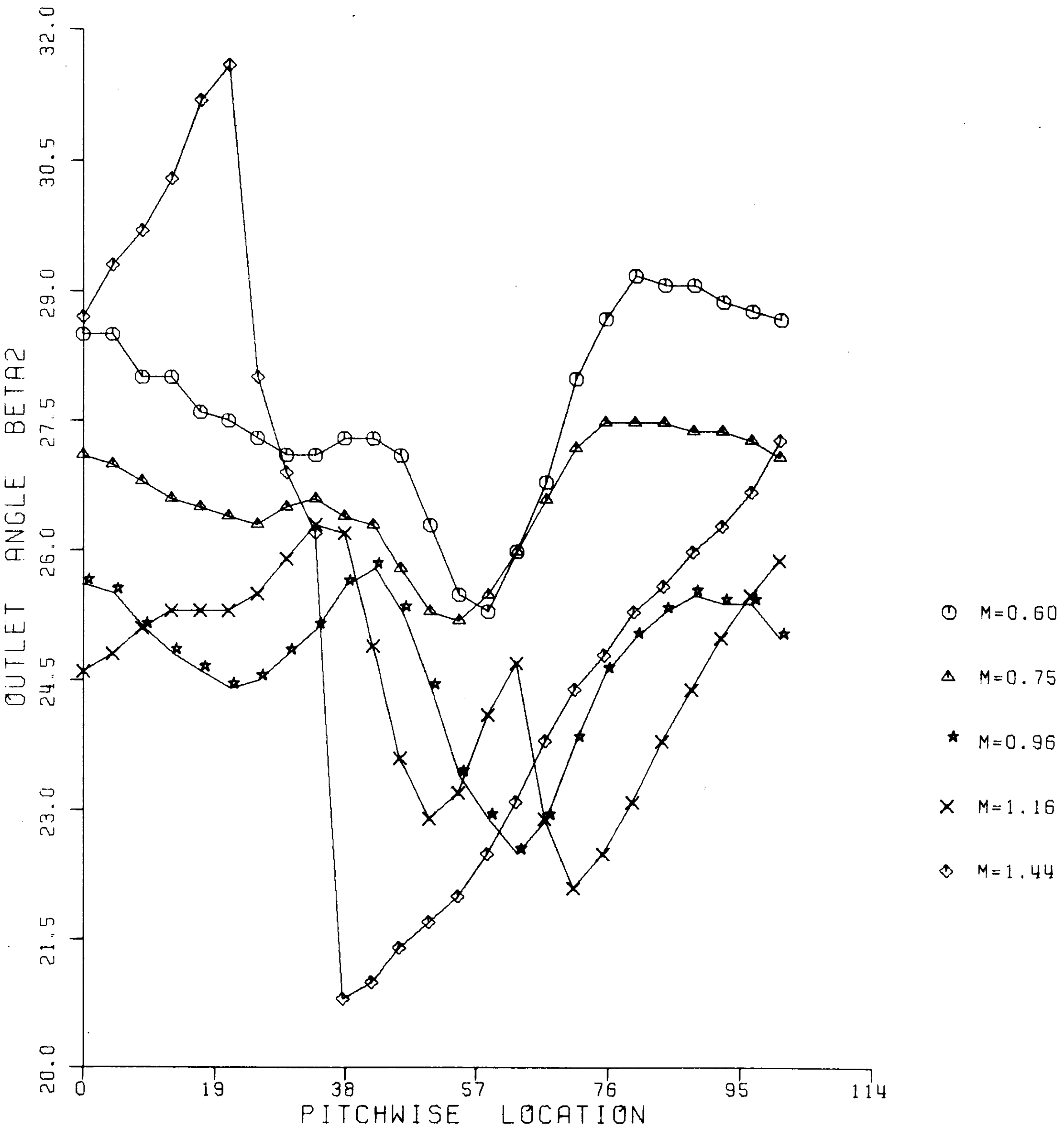

Figure 4.31 Blade 3 Exit angle Variation across the pitch.

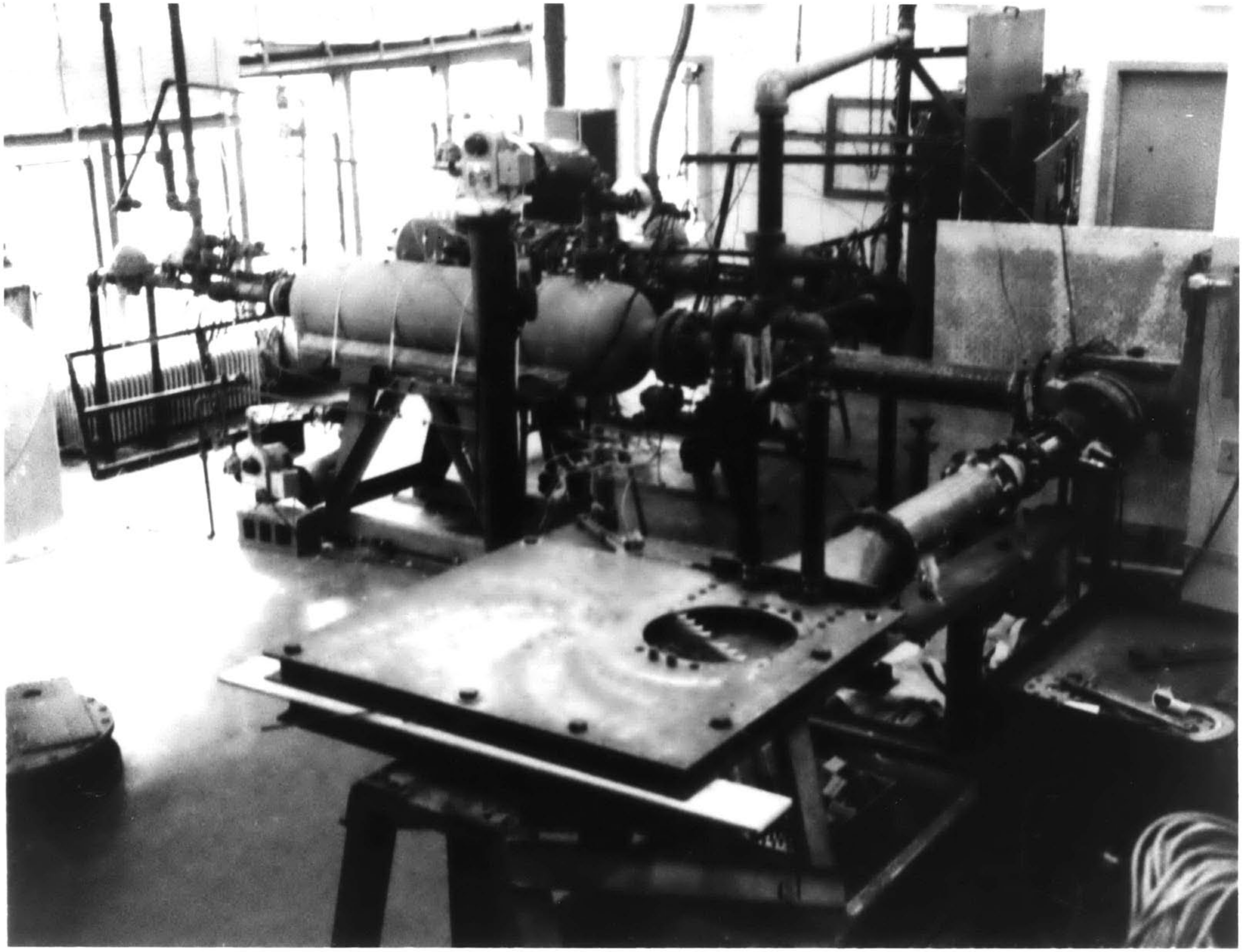

Figure 5.1 M.I.T. Hot Blowdown Cascade Facility

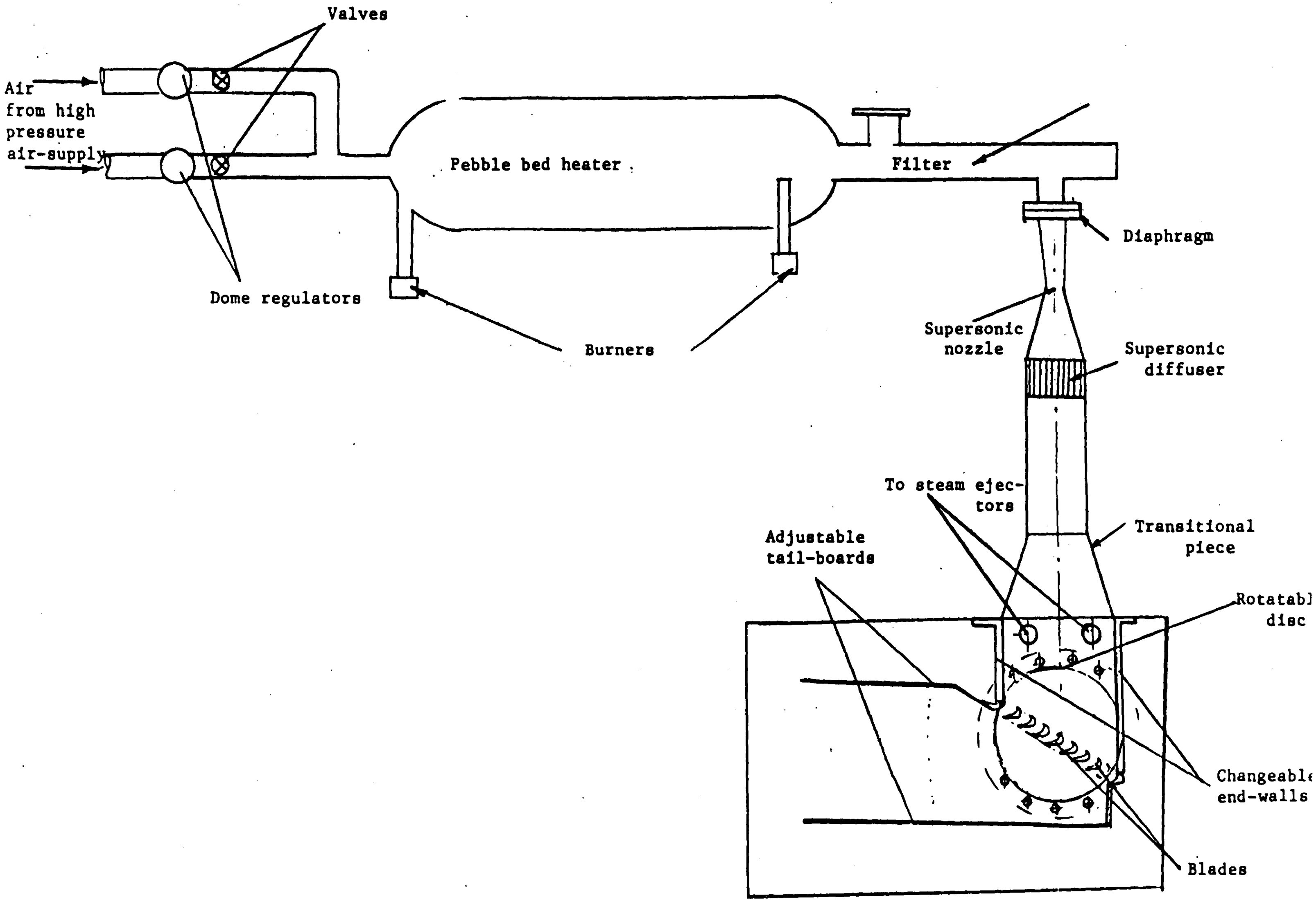

Figure 5.2 HOT-BLOWDOWN CASCADE FACILITY

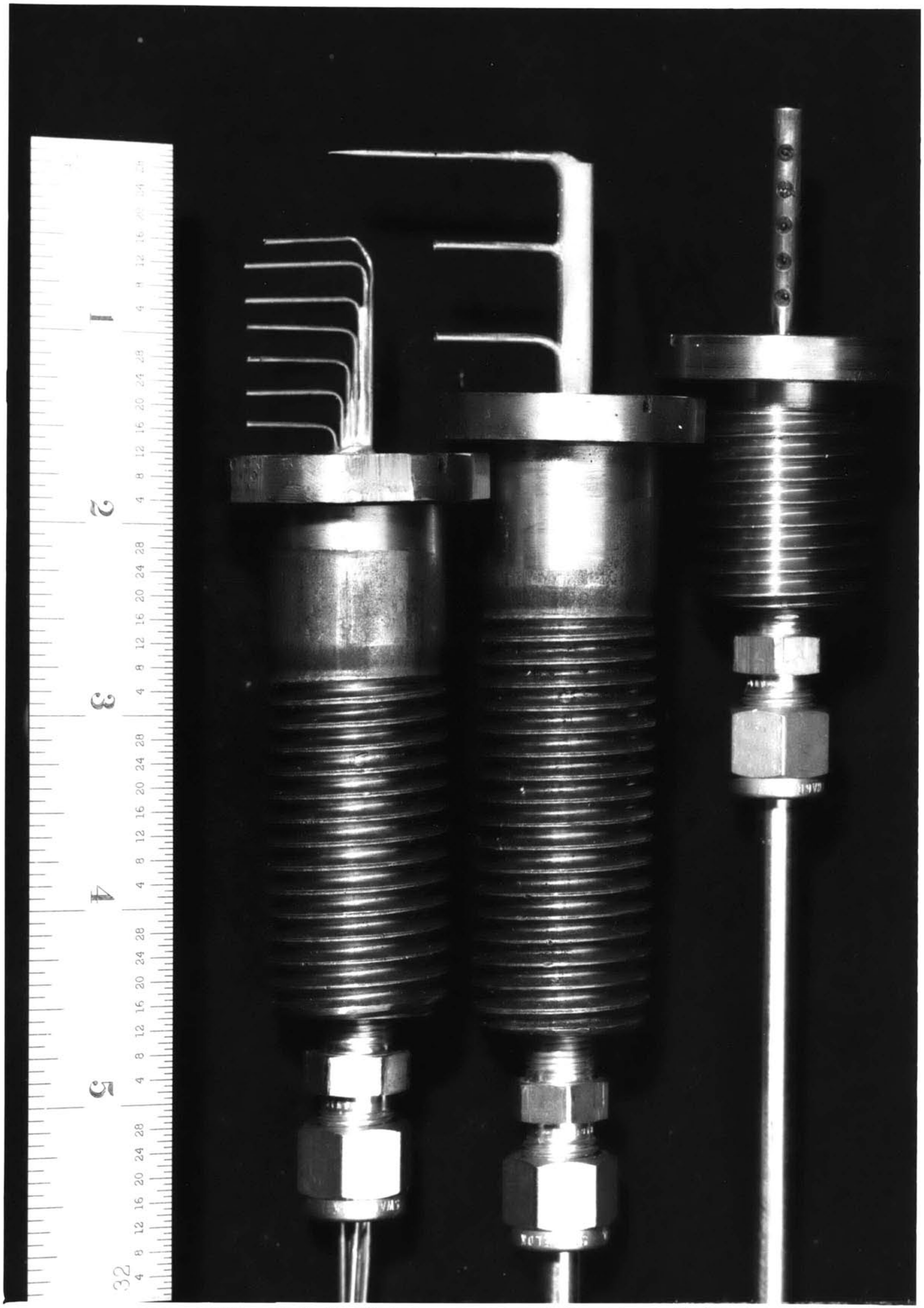

Figure 5.3 Temperature and Pressure Rakes

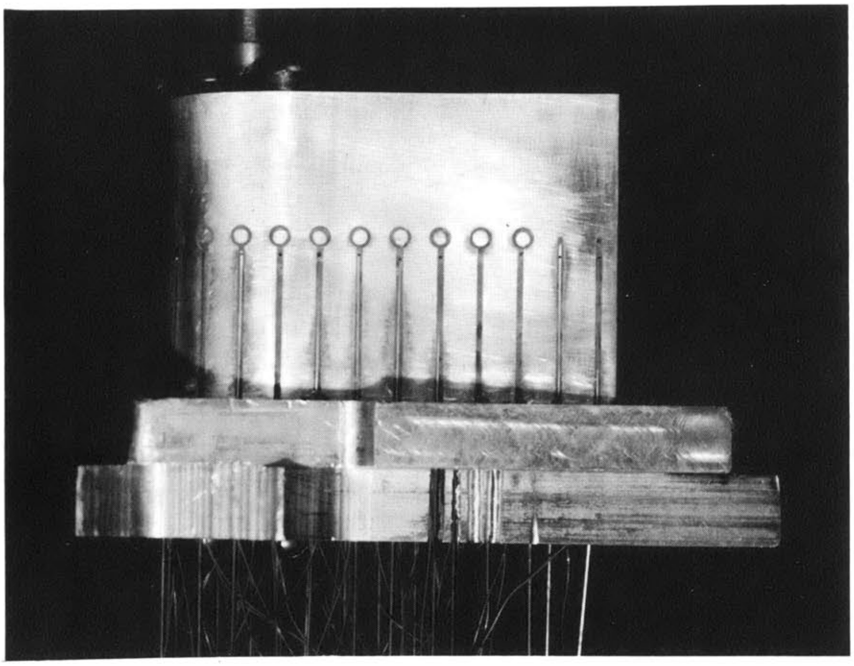

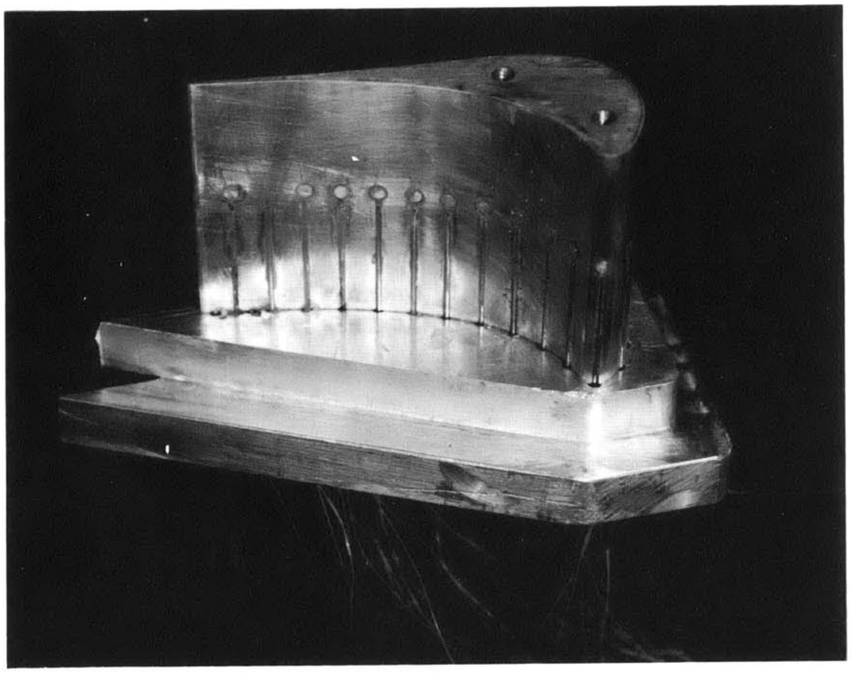

Figure 5.4 Blade Instrumentation

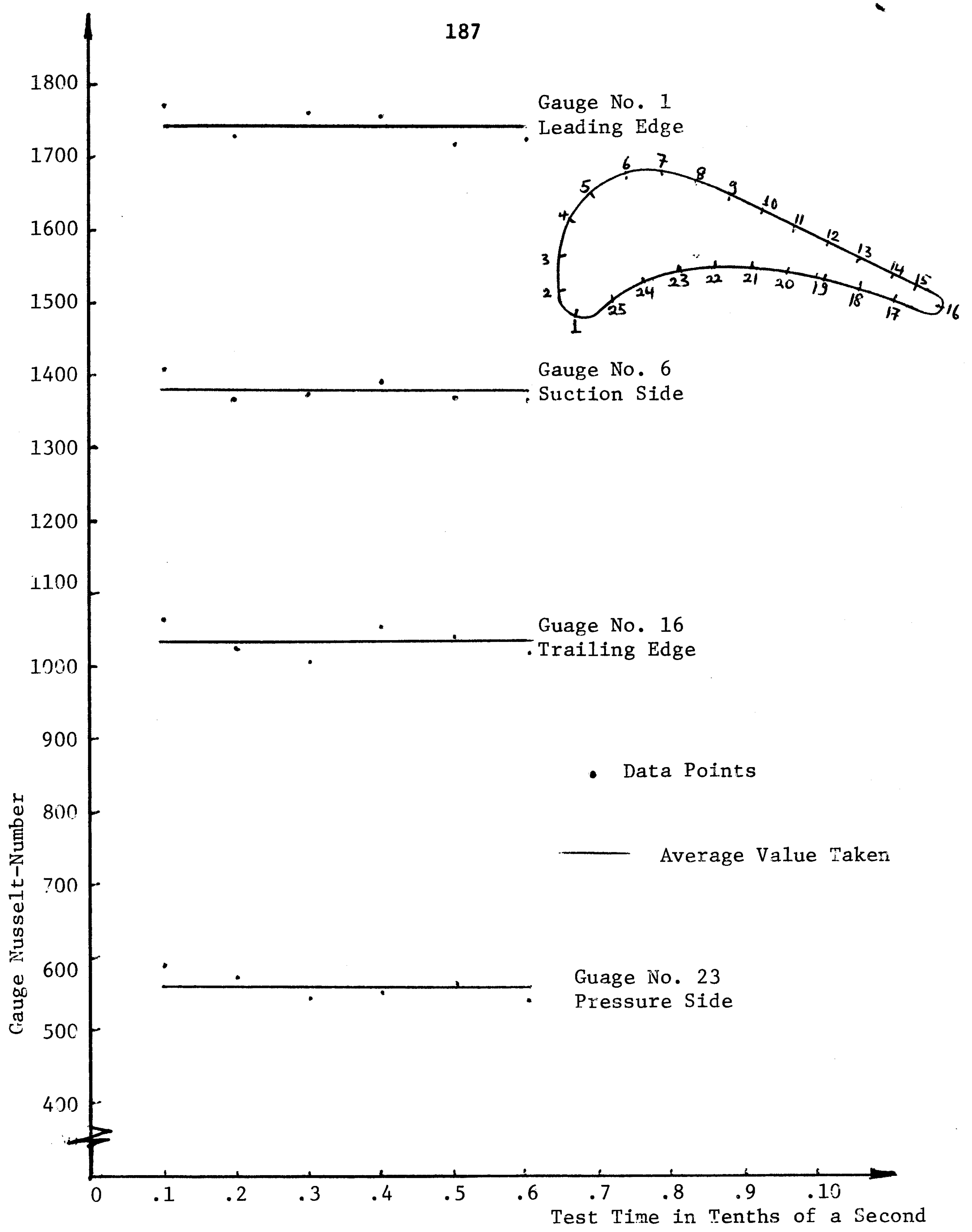

Figure 5.5a. Gauge heat transfer measurement (with correction for heat-loss) as function of time.

Figure 5.5b Inlet Stagnation Temperature and Pressure Spanwise distribution.

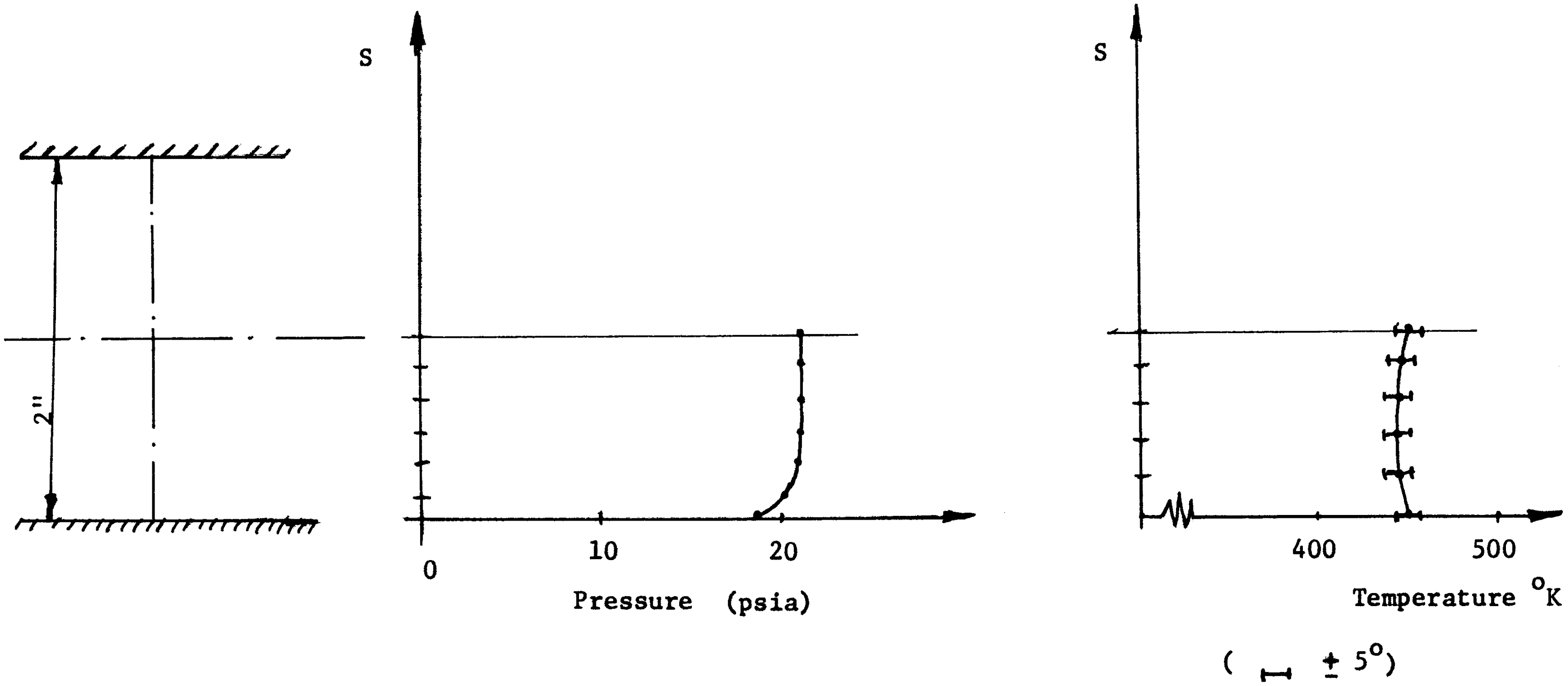

S-Spanwise Location

Figure 5.6 Blade 1 Mach number distribution tested in Hot Blowdown Cascade Facility g/c = 0.695.

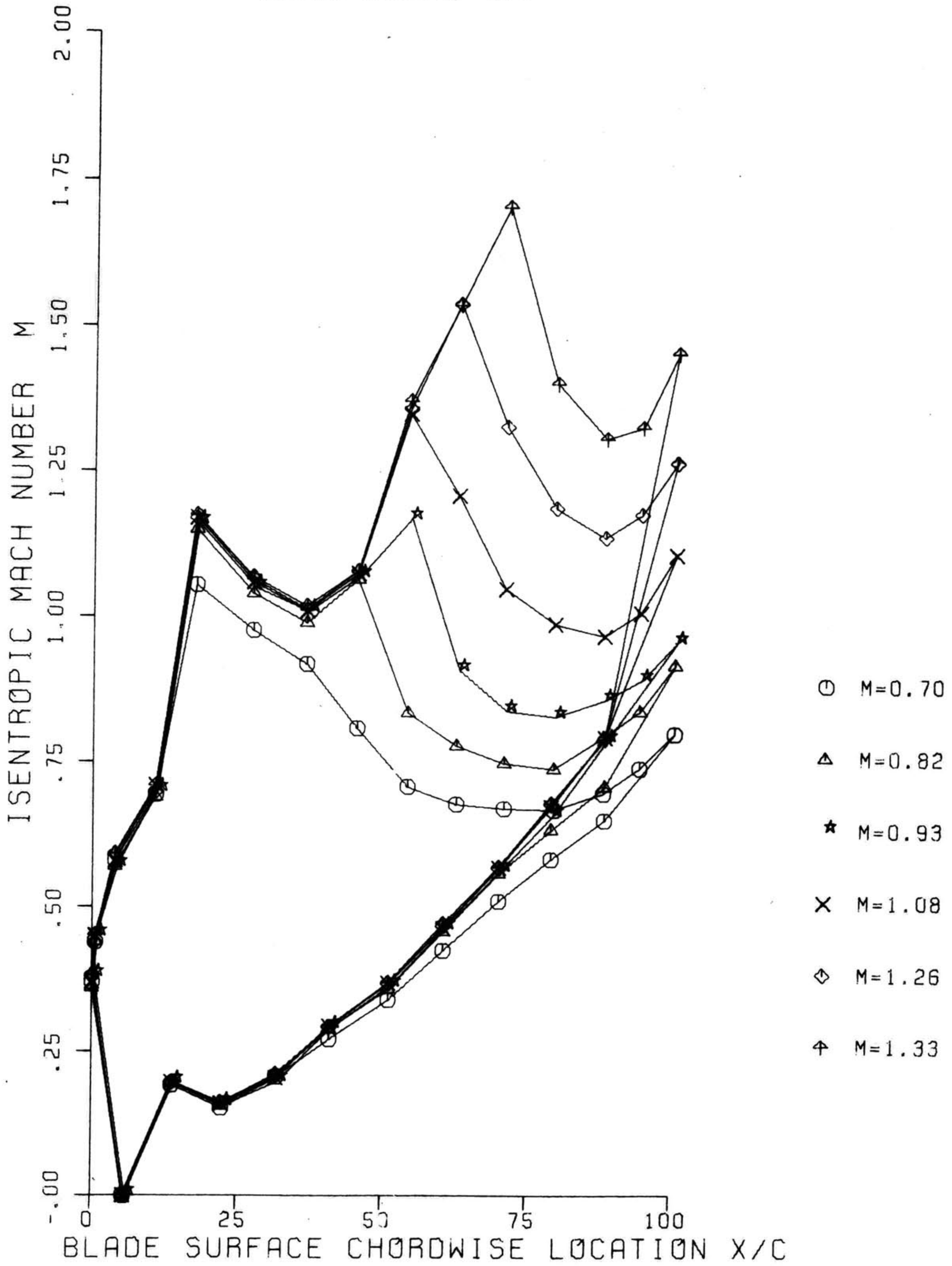

Figure 5.7 Blade 3 Mach Number distribution g/c = 0.695

(test conducted in Hot Blowdown Cascade Facility)

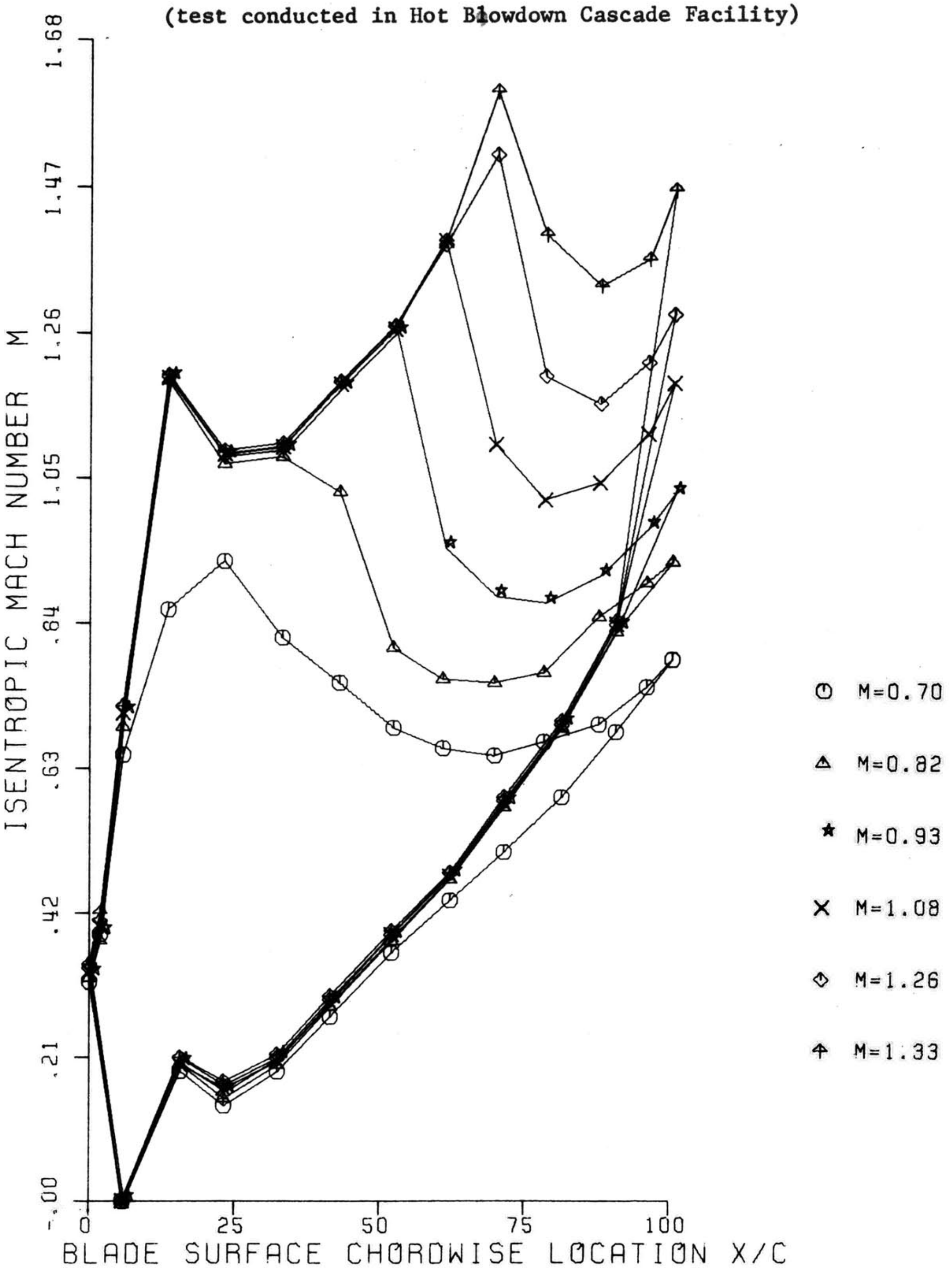

Figure 5.8 Blade 4 Mach Number distribution g/c = 0.695 (test conducted in Hot Blowdown Cascade Facility)

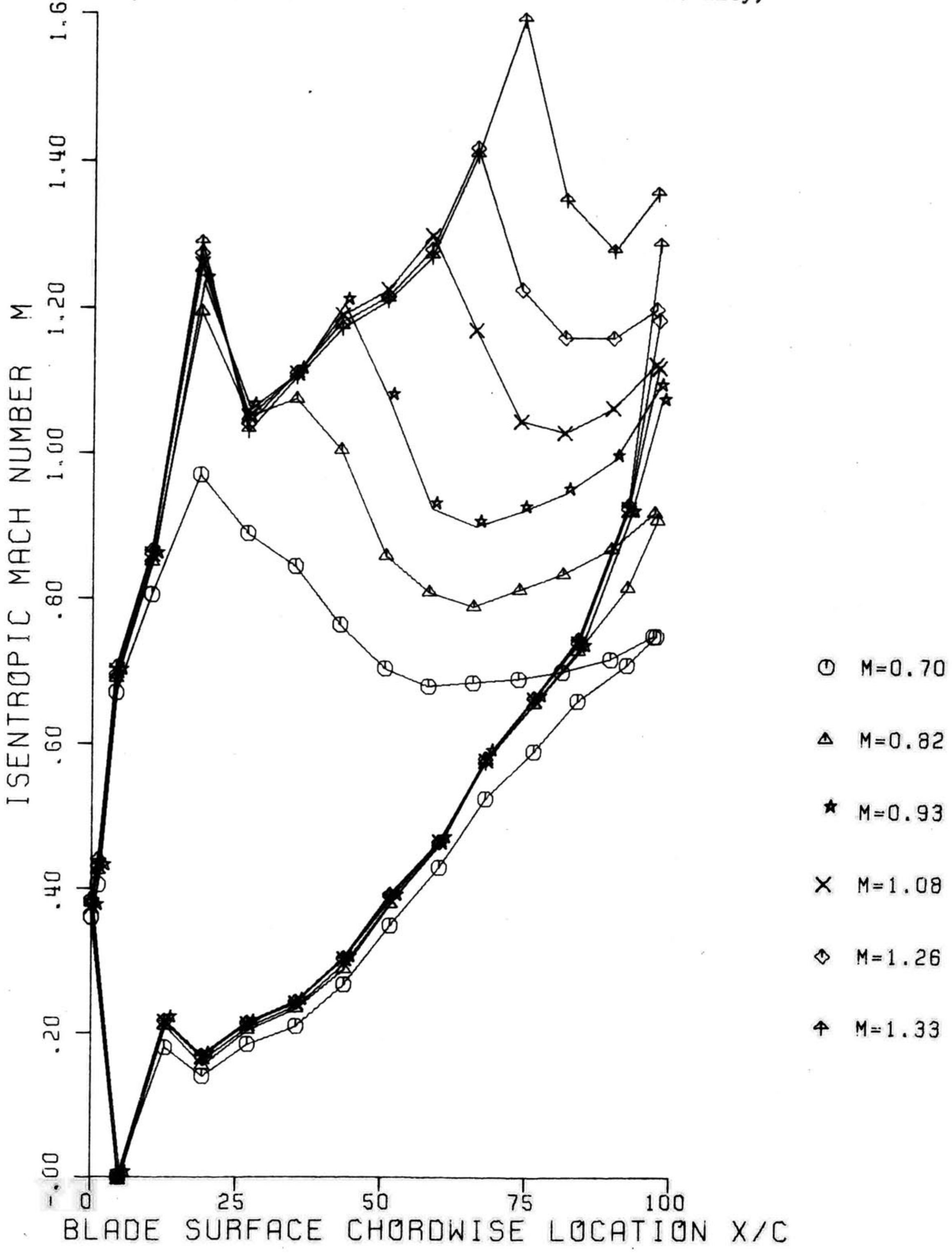

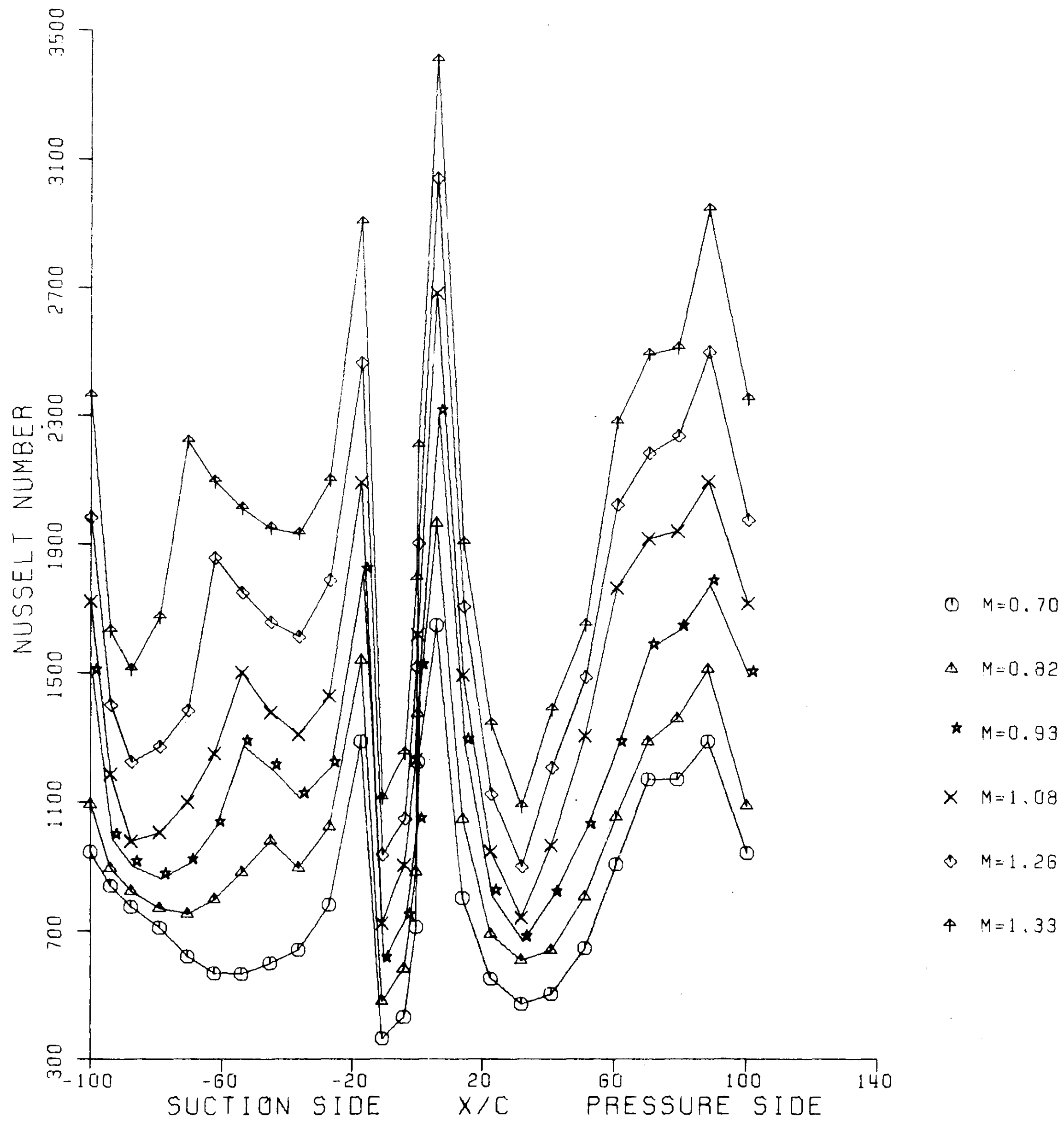

Figure 5.9 Blade 1 Nusselt number variation over the blade surface for different exit Mach Number.

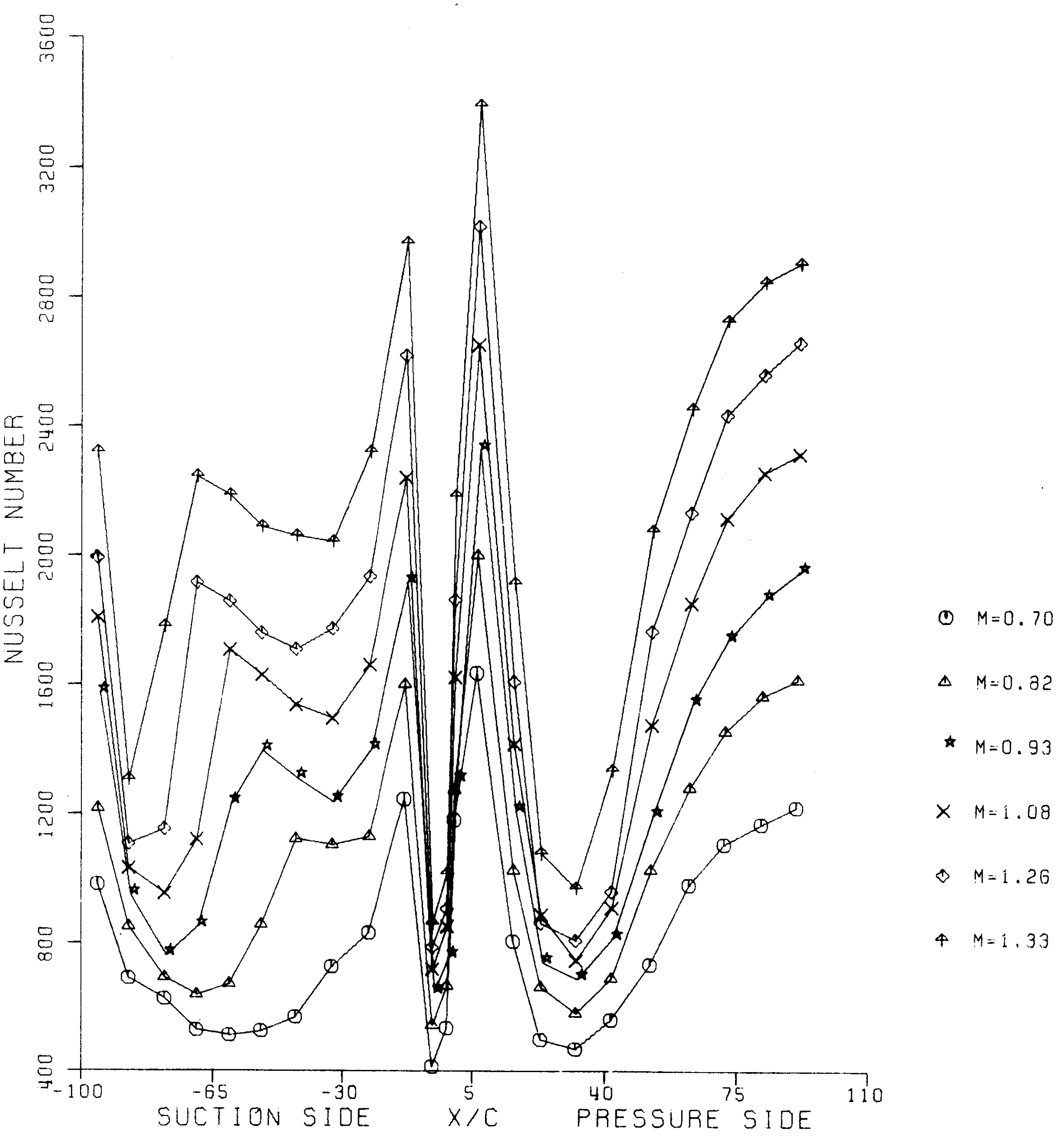

Figure 5.10 Blade 3 Nusselt number variation over the blade surface for different exit Mach Number.

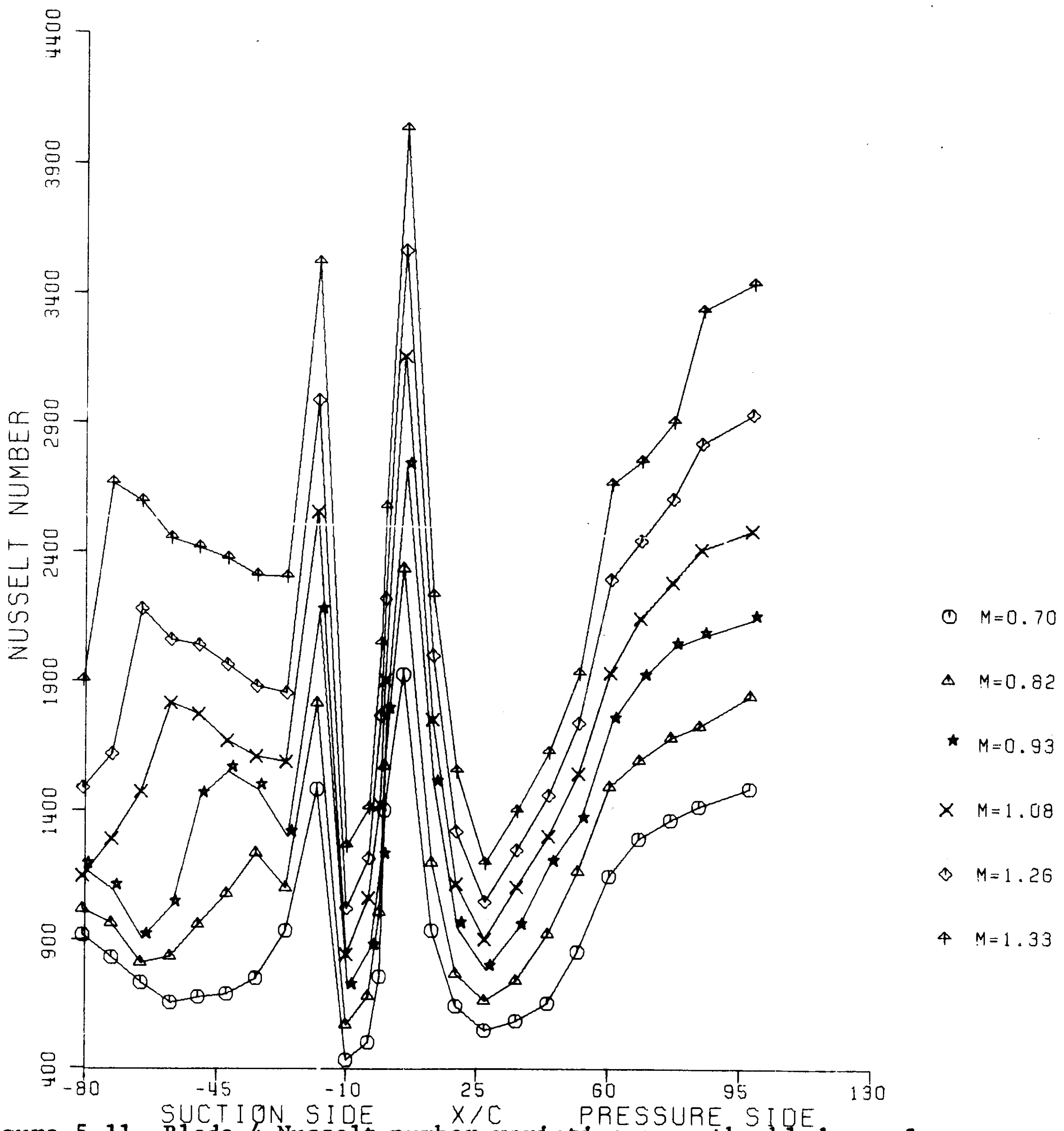

Figure 5.11 Blade 4 Nusselt number variation over the blade surface for different exit Mach Number.

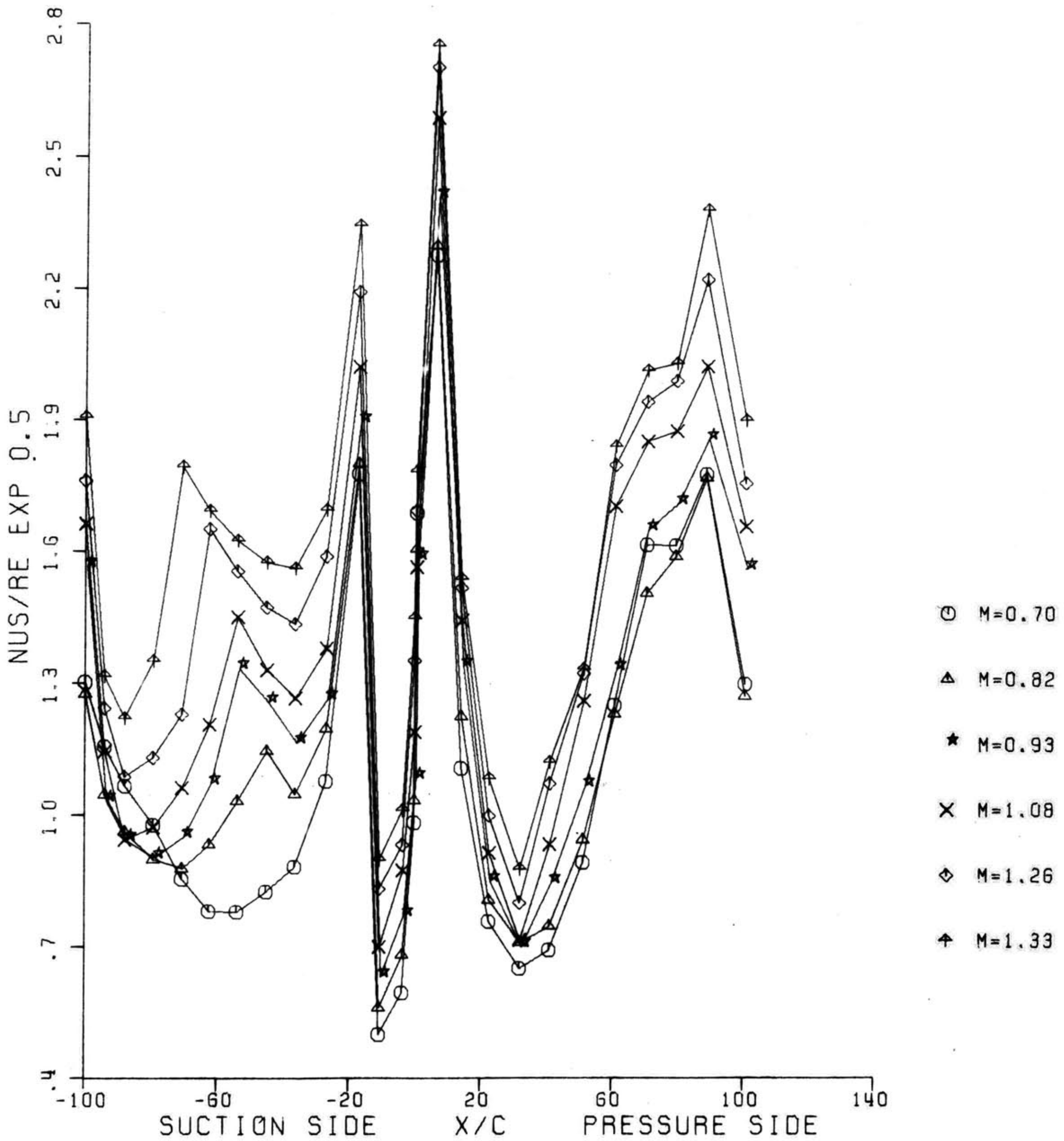

Figure 5.12 Blade 1 Distribution of $Nu/Re^{0.5}$ over the blade surface.

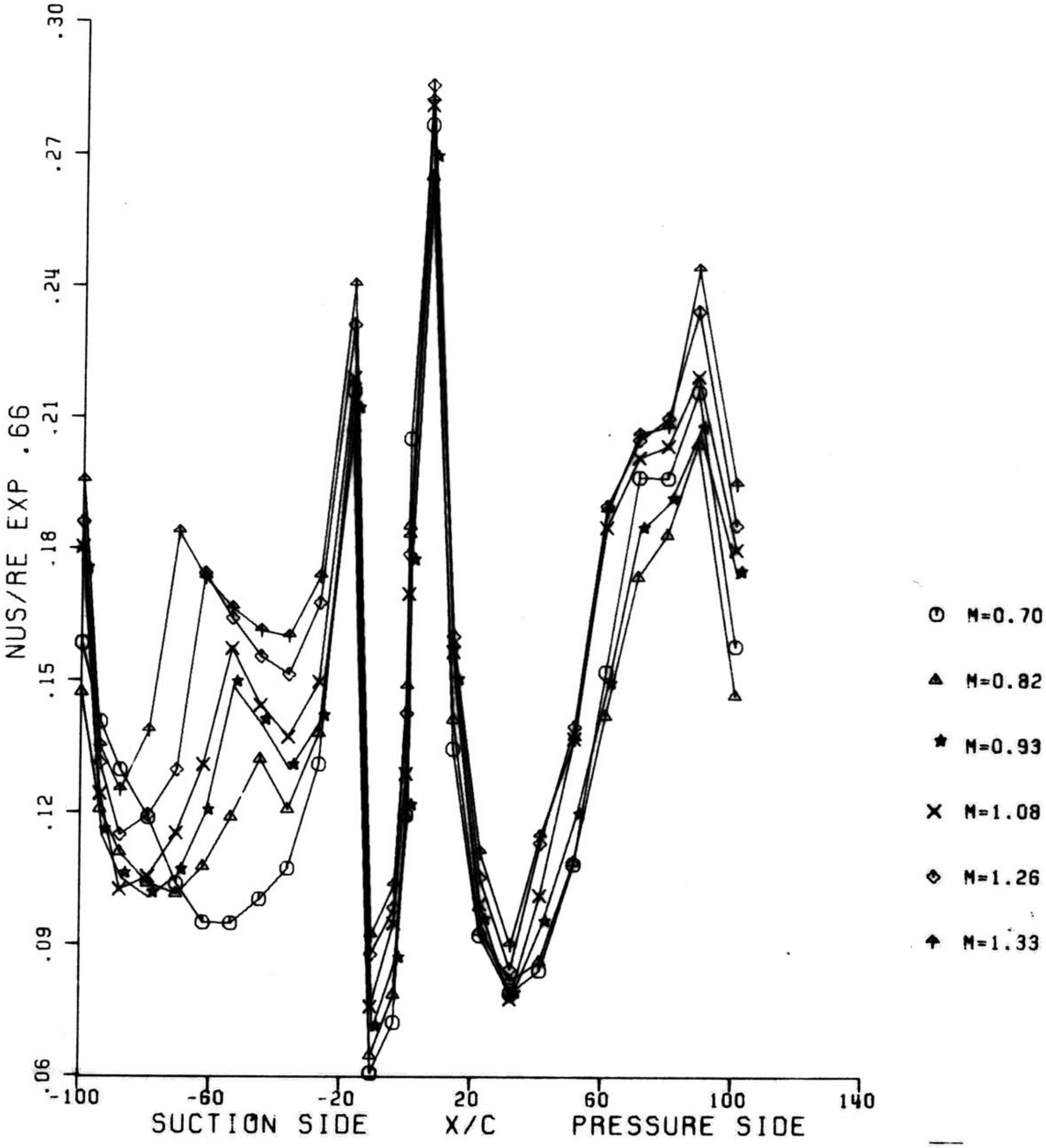

Figure 5.12 Blade 1 Distribution of $Nu/Re^{0.66}$ over the blade surface

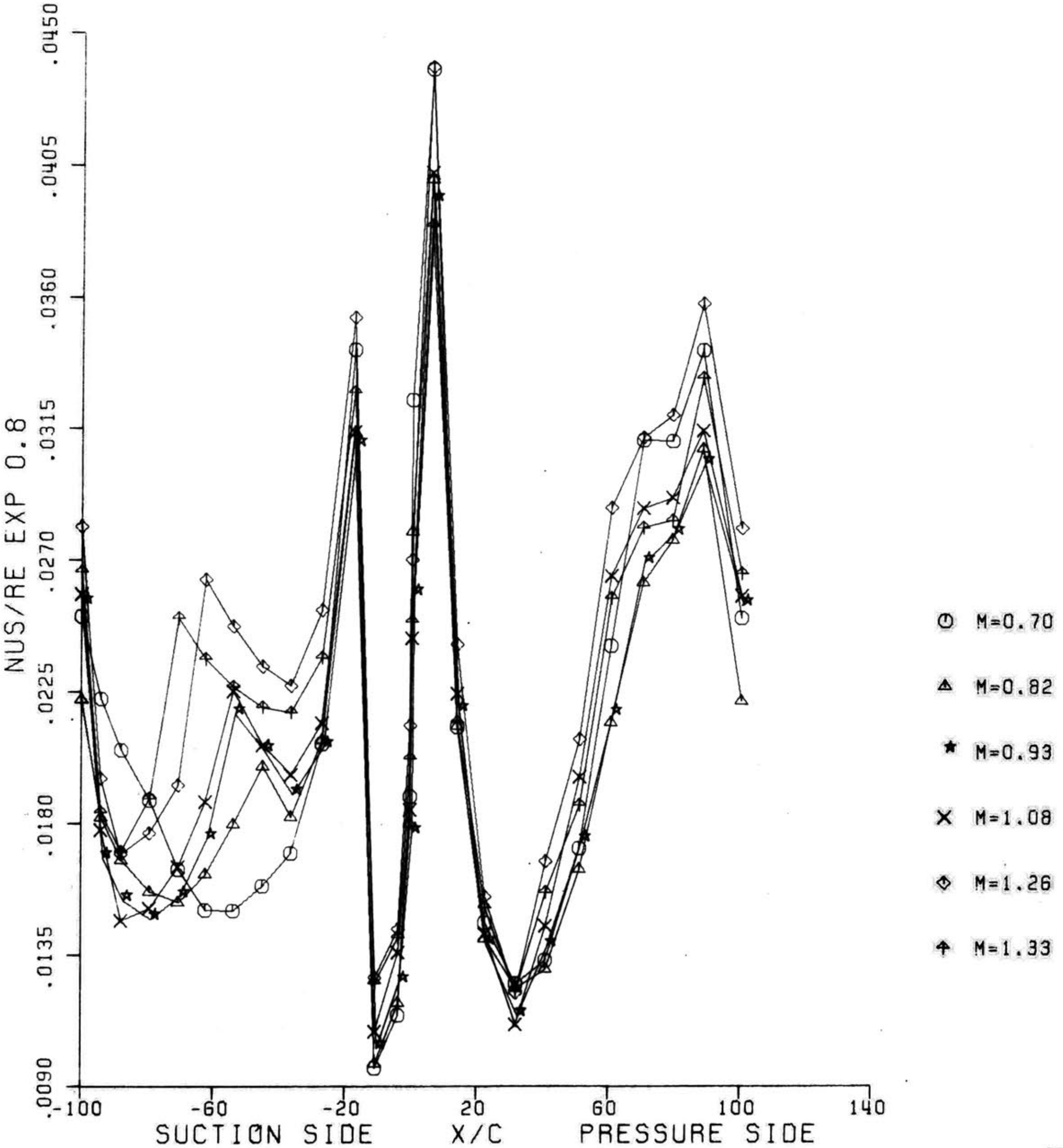

Figure 5.14 Blade 1 Distribution of Nu/Re$^{0.8}$ over the blade surface.

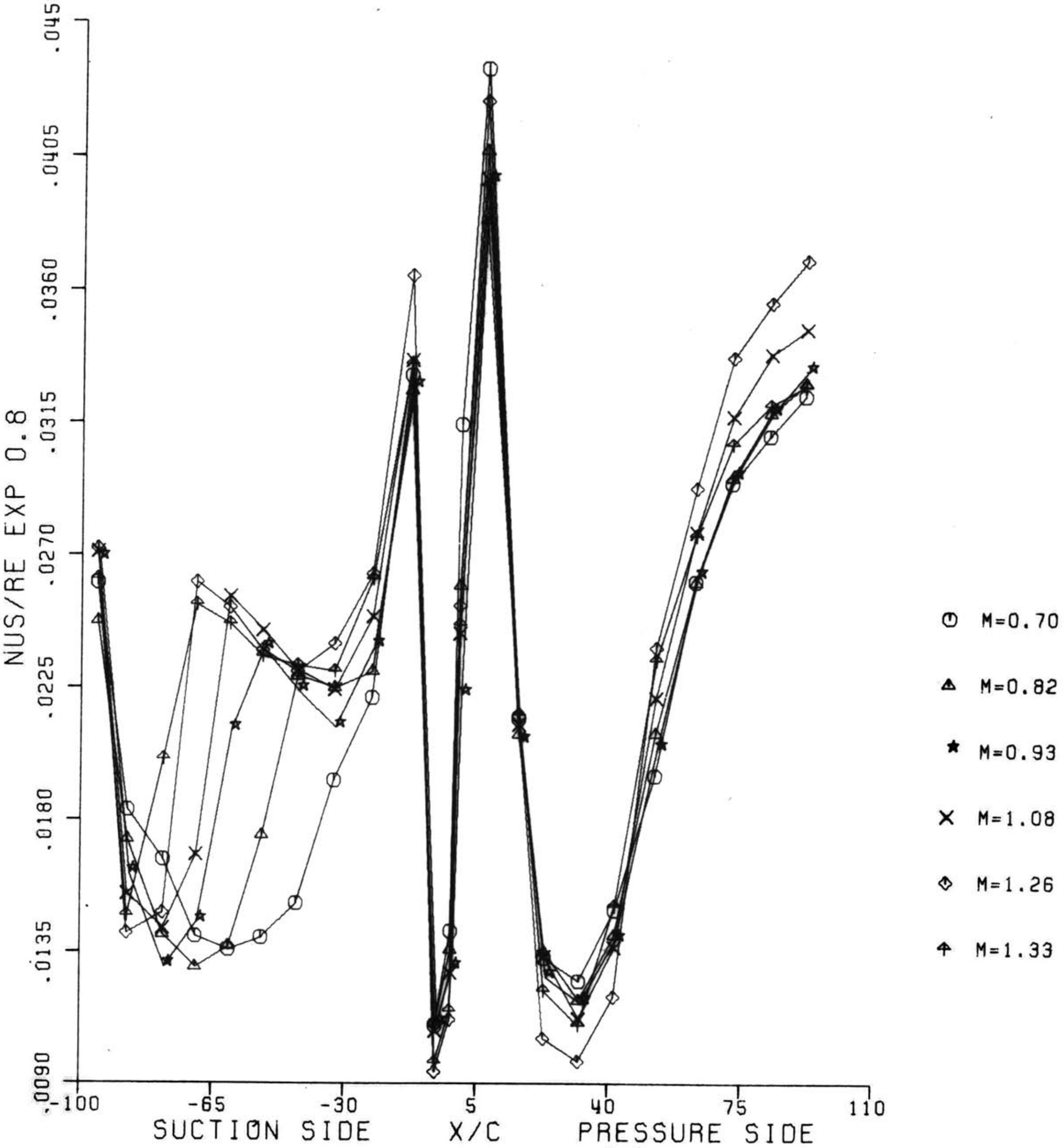

Figure 5.15 Blade 3 Distribution of $Nu/Re^{0.8}$ over the blade surface.

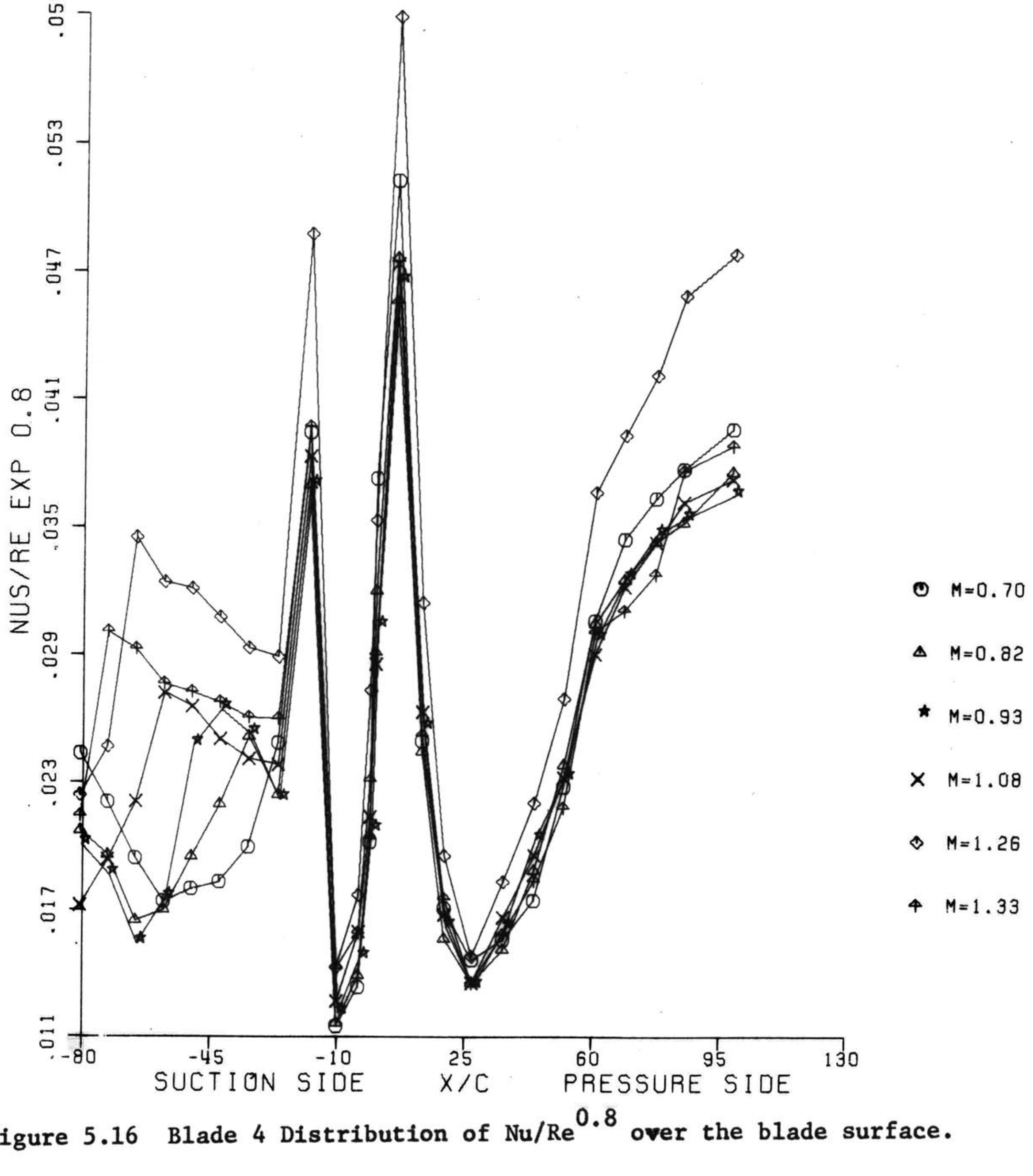

Figure 5.16 Blade 4 Distribution of $Nu/Re^{0.8}$ over the blade surface.

Figure 5.17

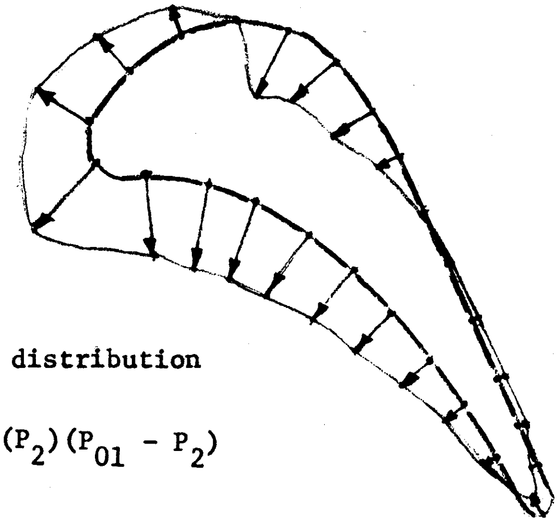

Blade 1 Static Pressure distribution

M = 0.7

$\bar{P} = (P - (P_2)(P_{01} - P_2)$

1 cm = 1 $\bar{P}$

Figure 5.18 Blade 1 Nusselt number distribution M = 0.7

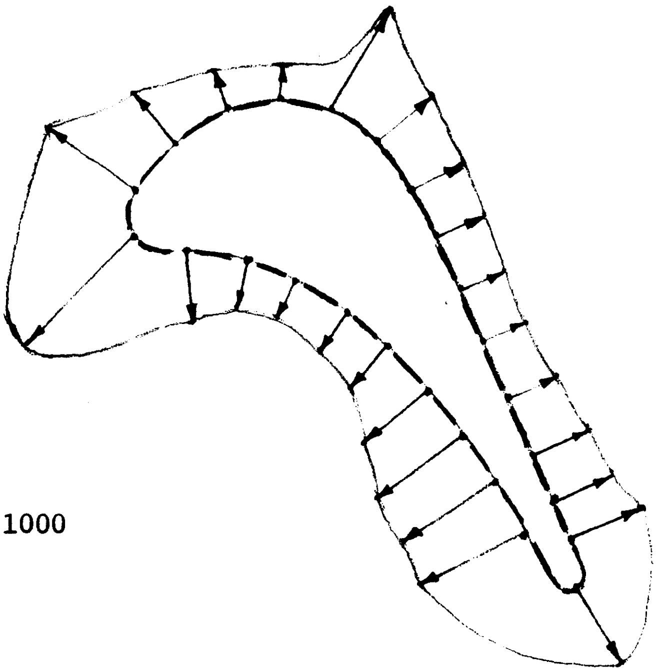

1 cm = Nu no. of 1000

Figure 5.19

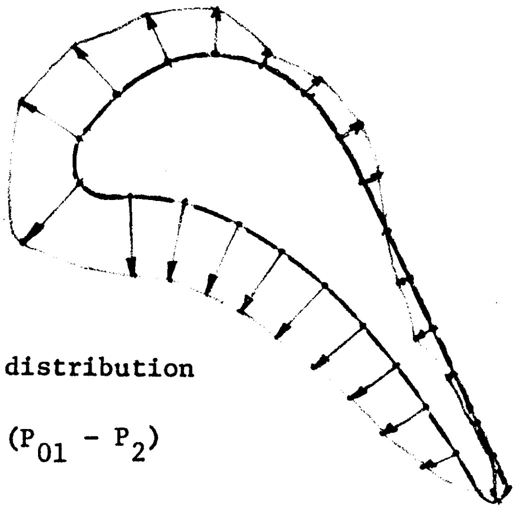

Blade 1 Static Pressure distribution

$M = 1.33$

$\bar{P} = (P-P_2)(P_{01} - P_2)$

$1 \text{ cm} = 1 \bar{P}$

Figure 5.20 ~~Blade 1 Nusselt number distribution~~ M = 1.33

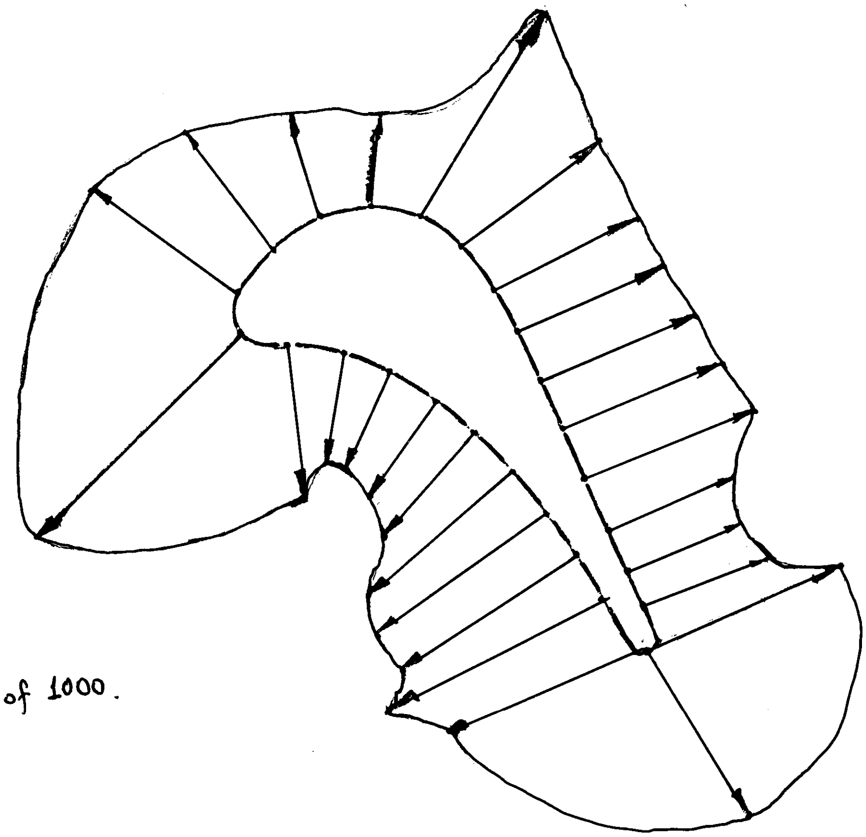

1cm ≡ Nu no. of 1000.

Figure 5.21 Comparison between $Nu_{experimental}$ and $Nu_{theoretical\ prediction}$ For Blade 1 at M = 0.7. (using hot flow high turbulence level (10%) experimental pressure distribution)

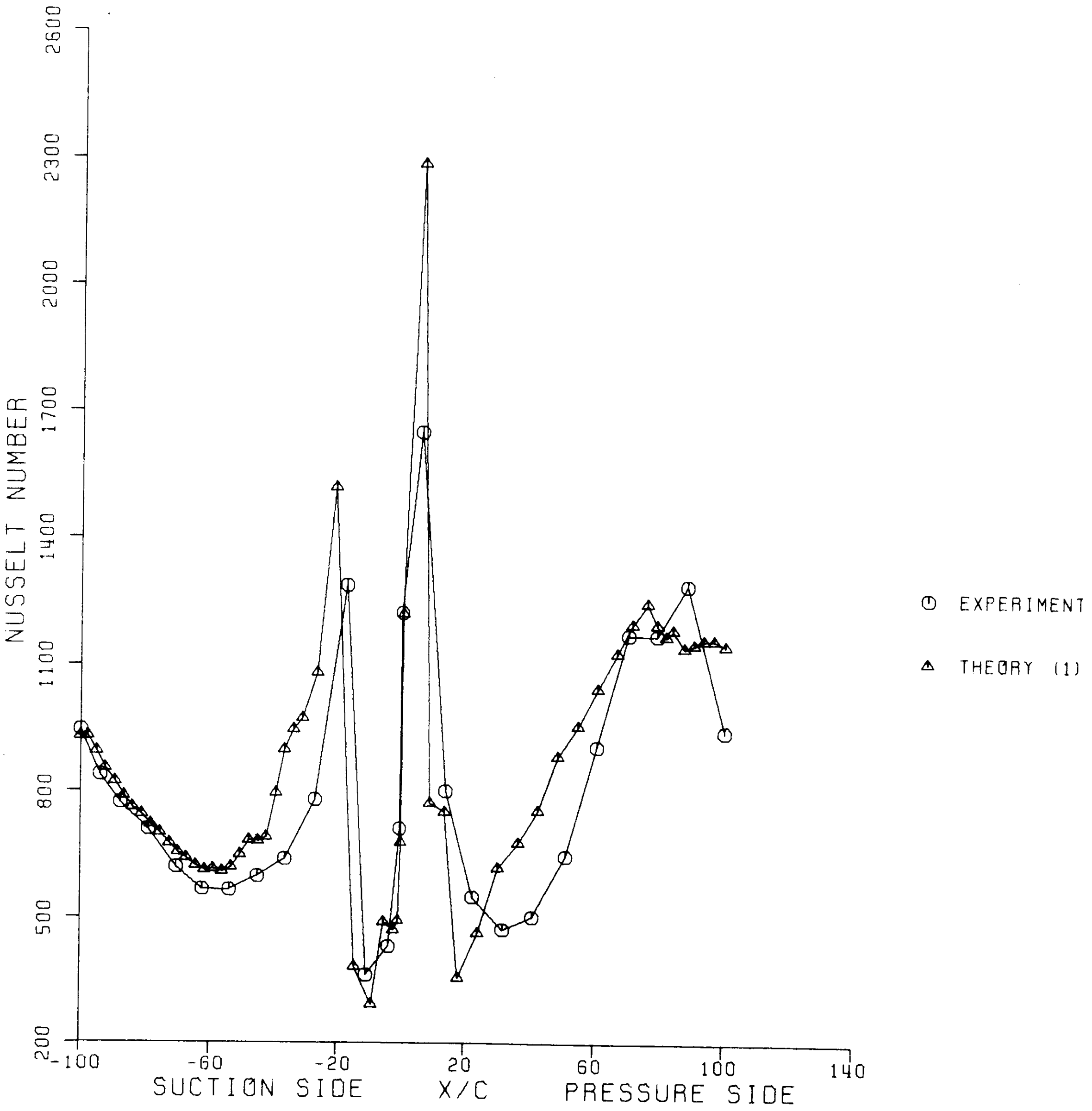

Figure 5.22 Comparison between $Nu_{experimental}$ and $Nu_{theoretical\ prediction}$ For Blade 1 at M = 1.08. (using hot flow high turbulence level (10%) experimental pressure distribution)

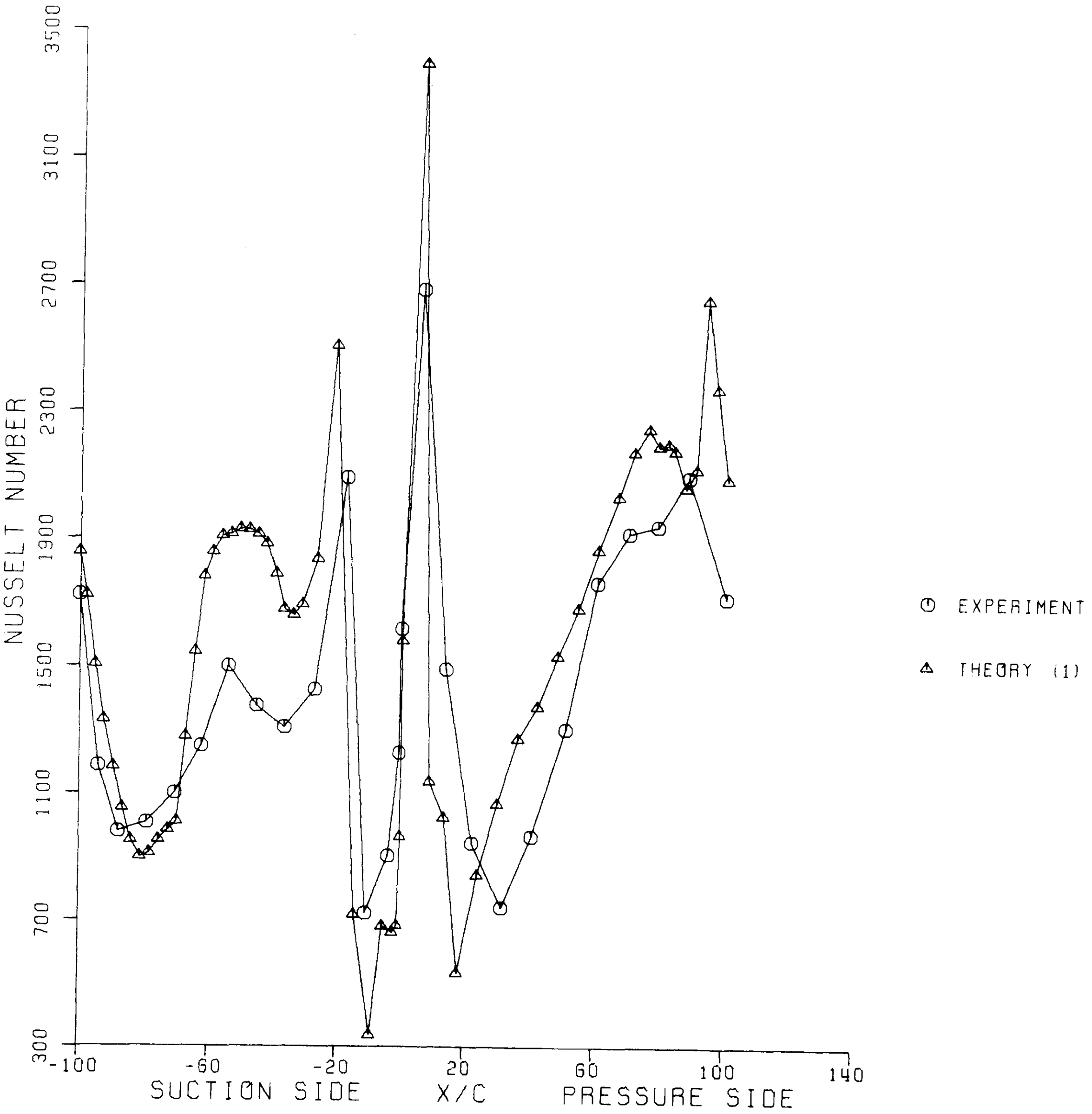

Figure 5.23 Comparison between $Nu_{experimental}$ and $Nu_{theoretical\ prediction}$ For Blade 1 at M = 1.33. (using hot flow high turbulence level (10%) experimental pressure distribution)

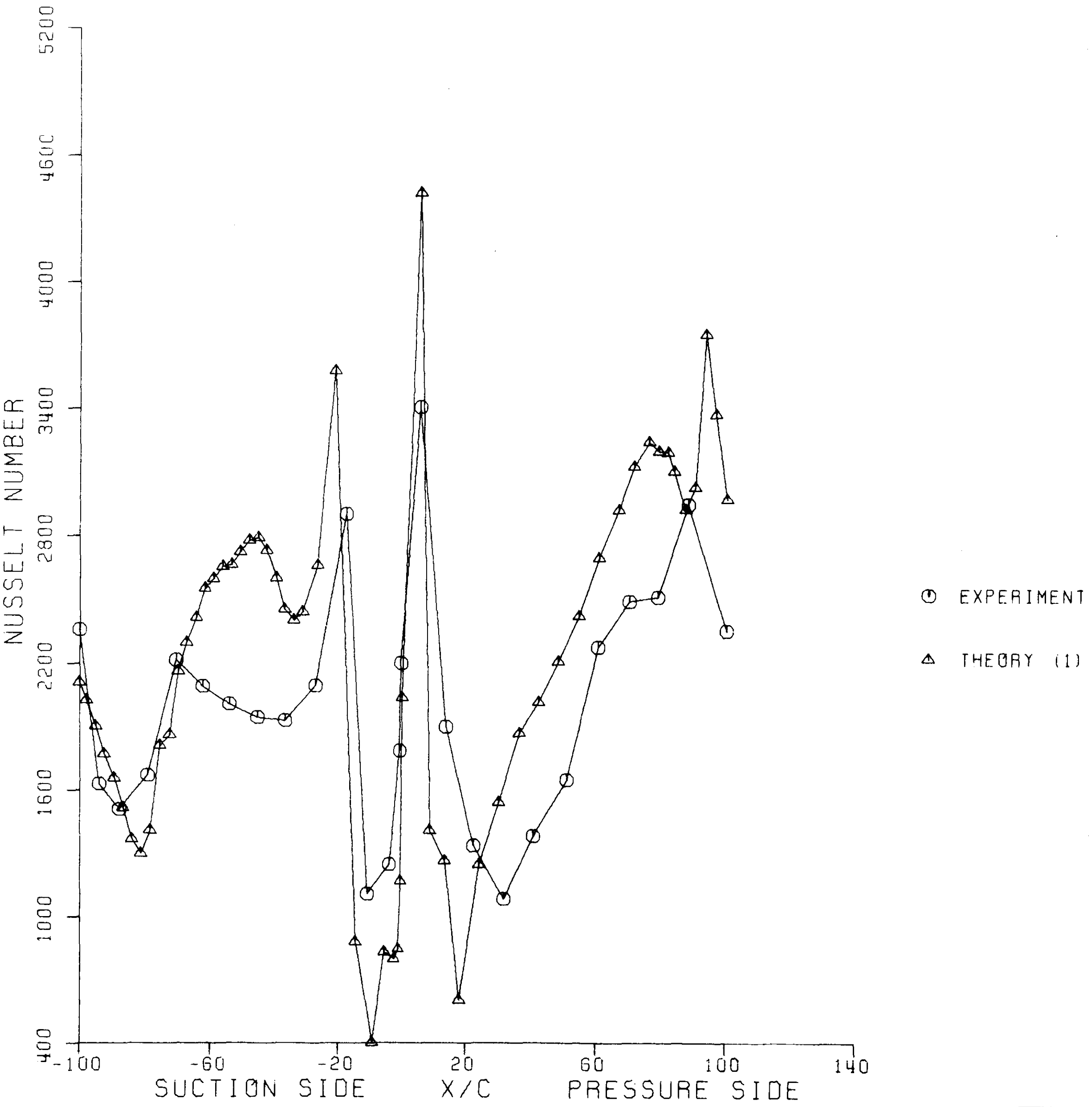

Figure 5.24 Comparison between $Nu_{experimental}$ and $Nu_{theoretical}$ prediction for Blade 3. $M_{exit} = 0.7$. (using hot flow high turbulence level (10%) experimental pressure distribution)

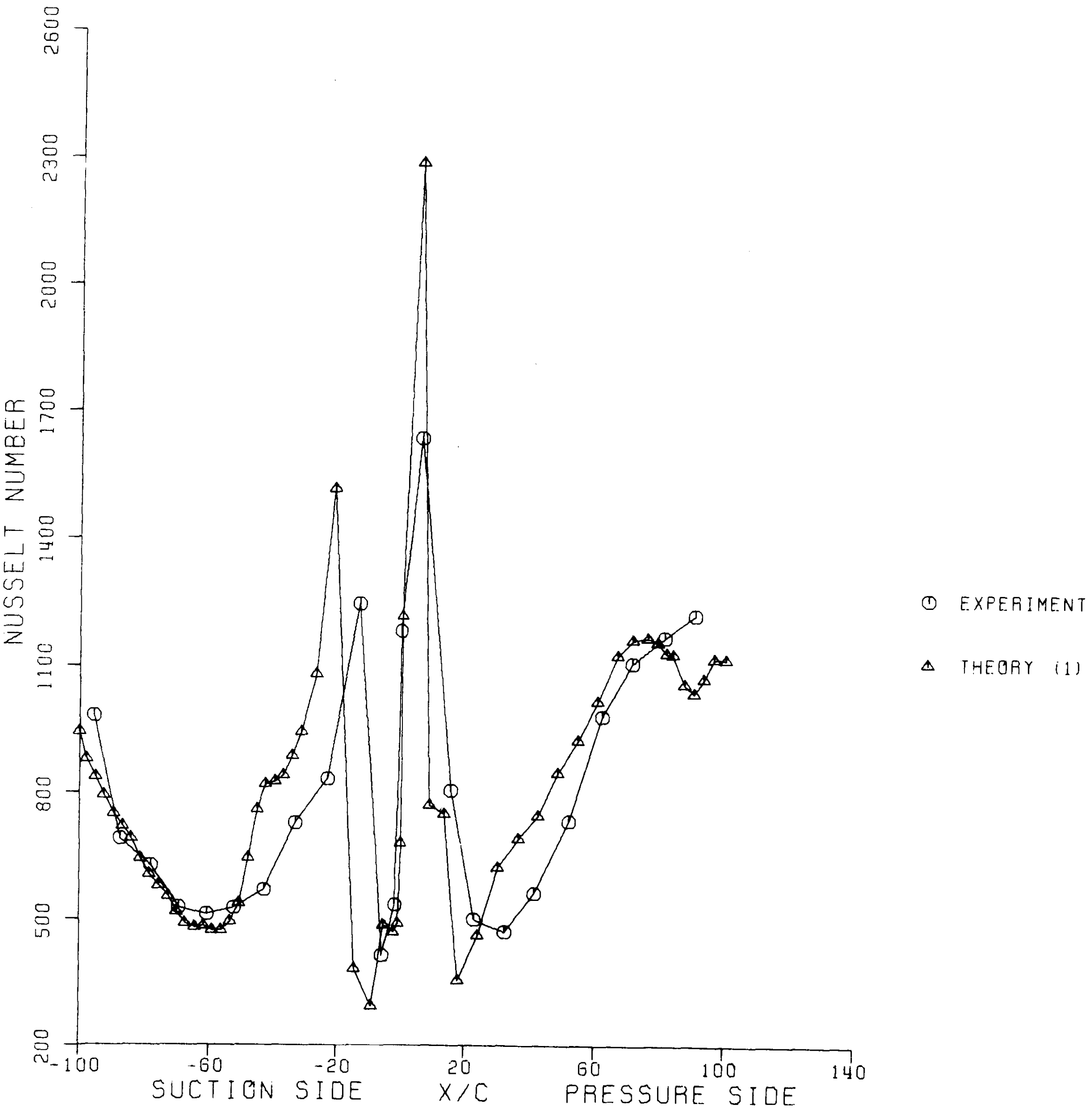

Figure 5.25 Comparison $Nu_{experimental}$ and $Nu_{theoretical}$ prediction for Blade 3. $M_{exit} = 0{,}93$. (using hot flow high turbulence level (10%) experimental pressure distribution)

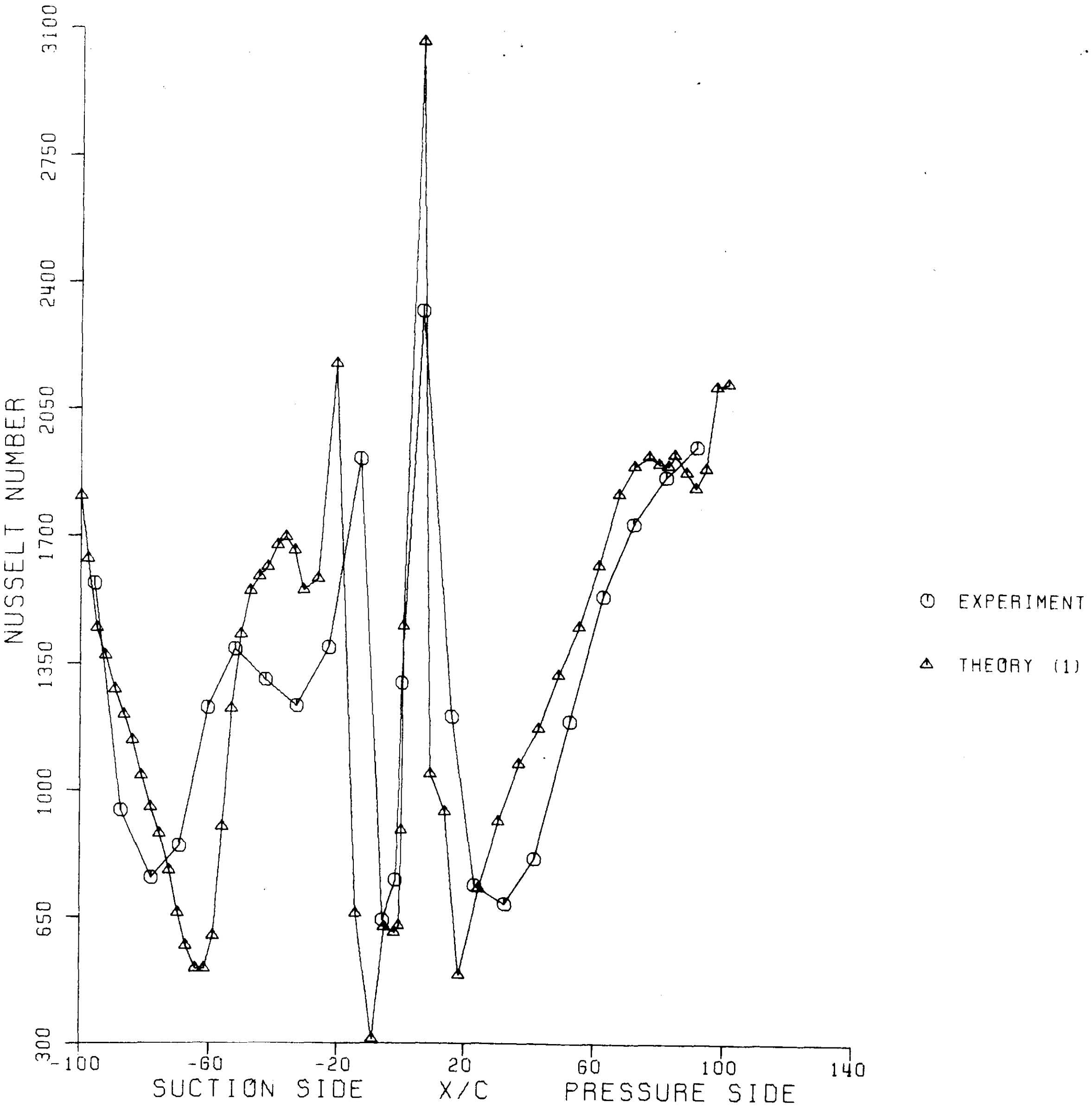

Figure 5.26 Comparison $Nu_{experimental}$ and Nu theoretical prediction for Blade 3. $M_{exit} = 1.26$. (using hot flow high turbulence level (10%) experimental pressure distribution)

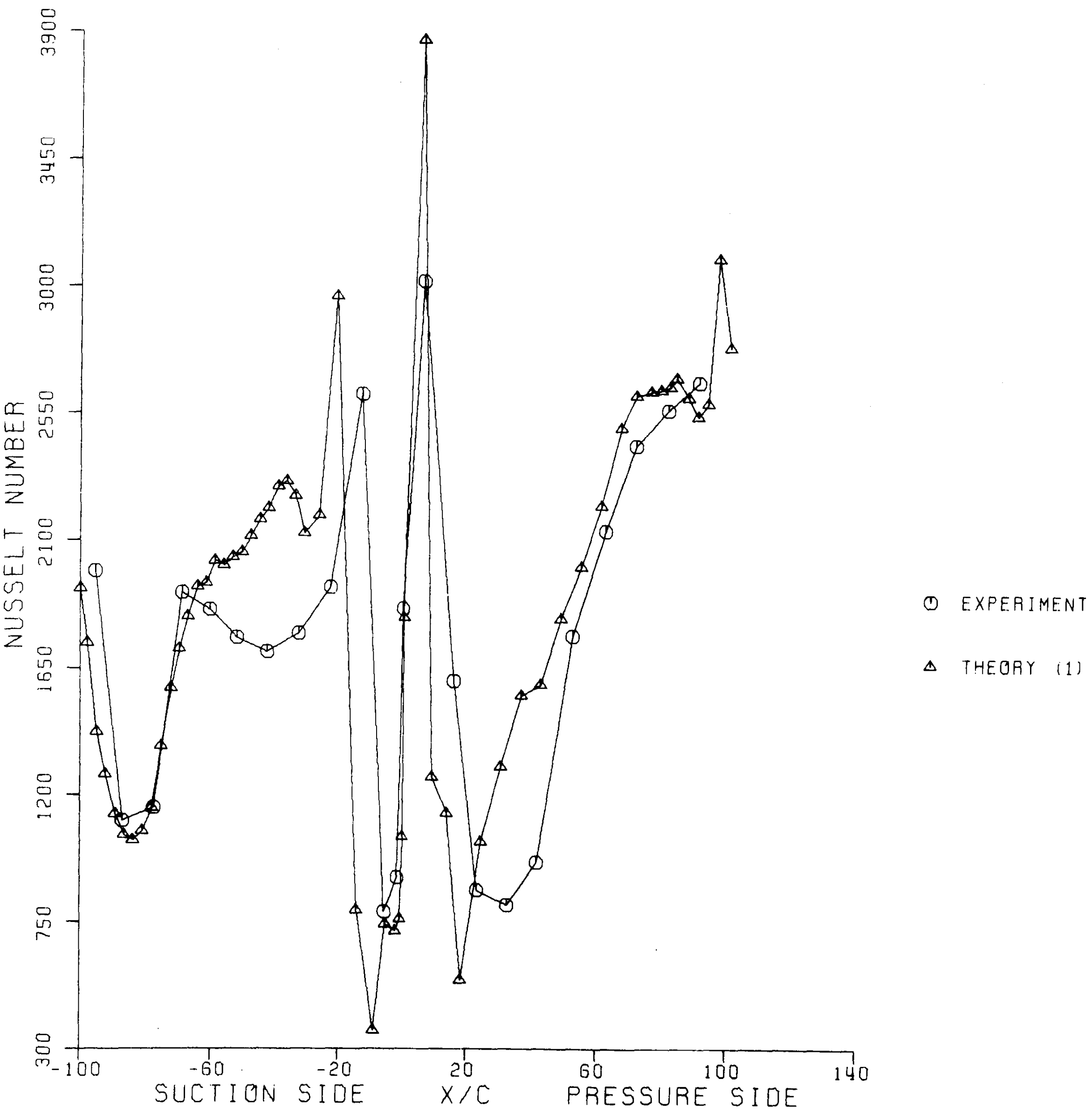

Figure 5.27 Comparison between $Nu_{experimental}$, $Nu_{theoretical\ prediction(1)}$ and $Nu_{theoretical\ prediction\ (2)}$ for Blade 1 at M = 0.7

Theory (1) is based on Hot Flow High Turbulence (10%)

Experimental Pressure Distribution

Theory (2) is based on Cold Flow Low Turbulence(0.7%)

Experimental Pressure Distribution.

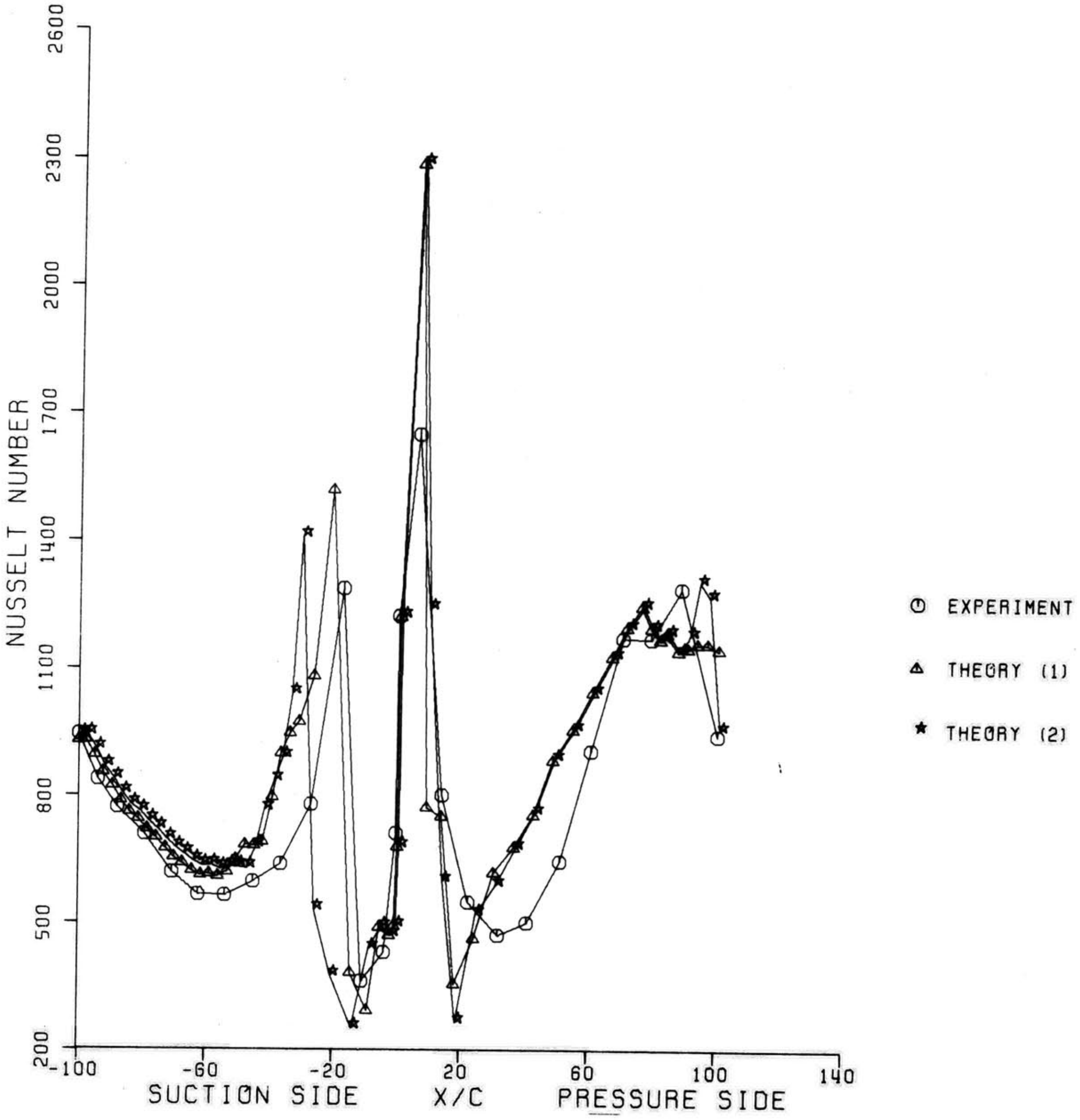

Figure 5.28 Comparison between $Nu_{experimental}$, $Nu_{theoretical\ prediction(1)}$ and $Nu_{theoretical\ prediction\ (2)}$ for Blade 1 at M = 1.08
Theory (1) is based on Hot Flow High Turbulence(10%)
Experimental Pressure Distribution
Theory (2) is based on Cold Flow Low Turbulence (0.7%)
Experimental Pressure Distribution.

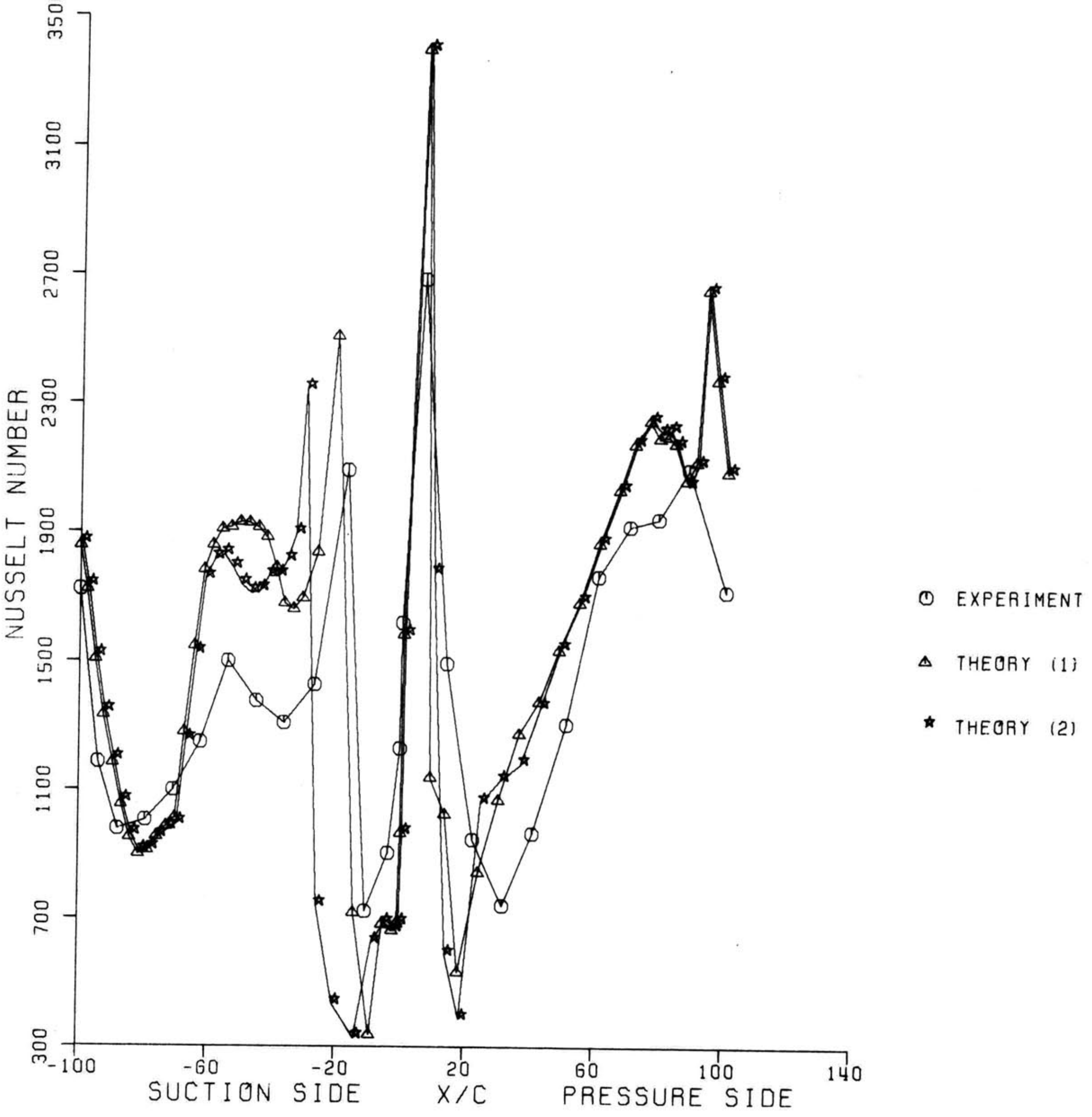

Figure 5.29 Comparison between $Nu_{experimental}$, $Nu_{theoretical\ prediction(1)}$ and $Nu_{theoretical\ prediction\ (2)}$ for Blade 1 at M = 1.33

Theory (1) is based on Hot Flow High Turbulence(10%)
Experimental Pressure Distribution
Theory (2) is based on Cold Flow Low Turbulence (0.7%)
Experimental Pressure Distribution.

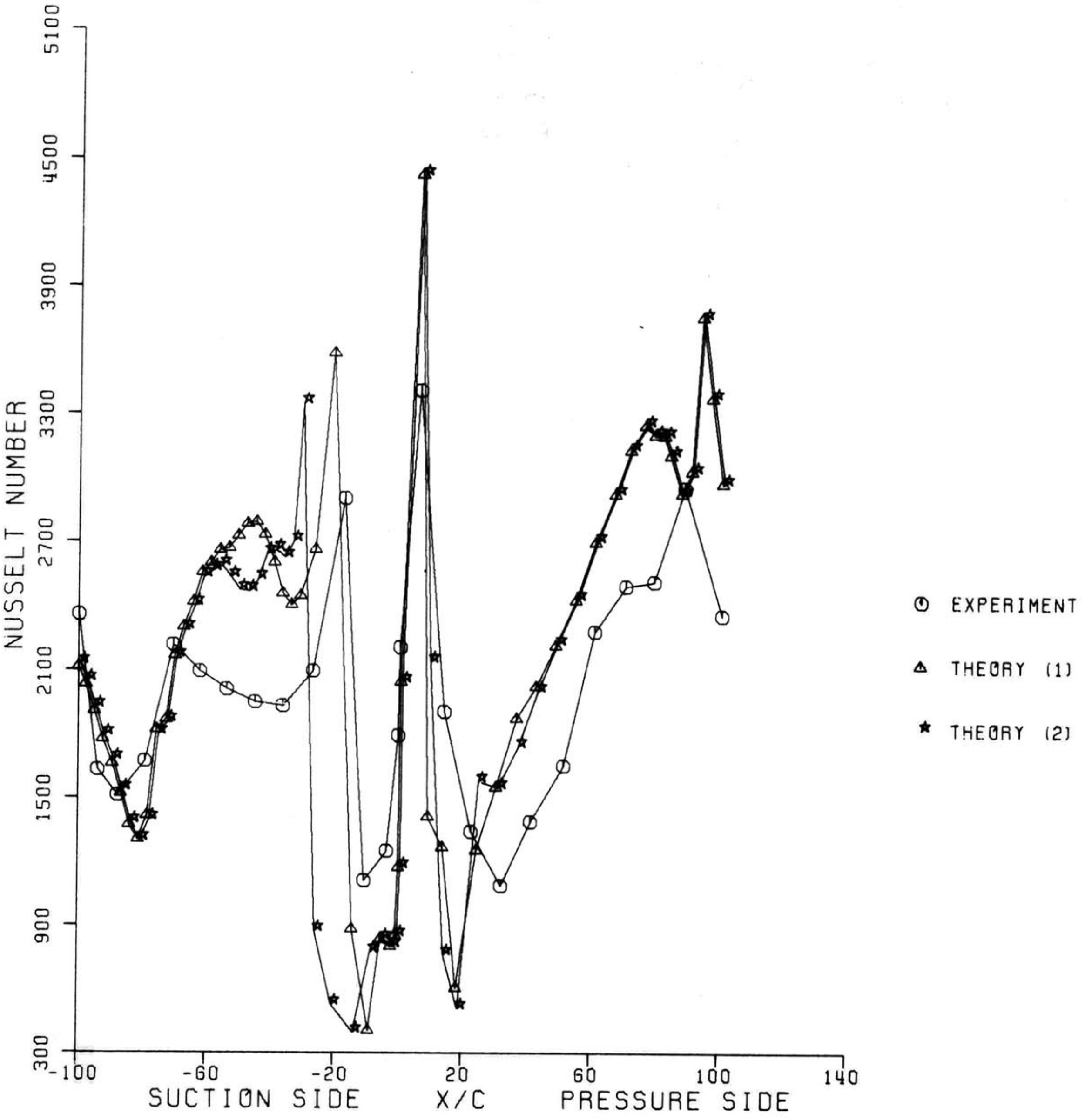

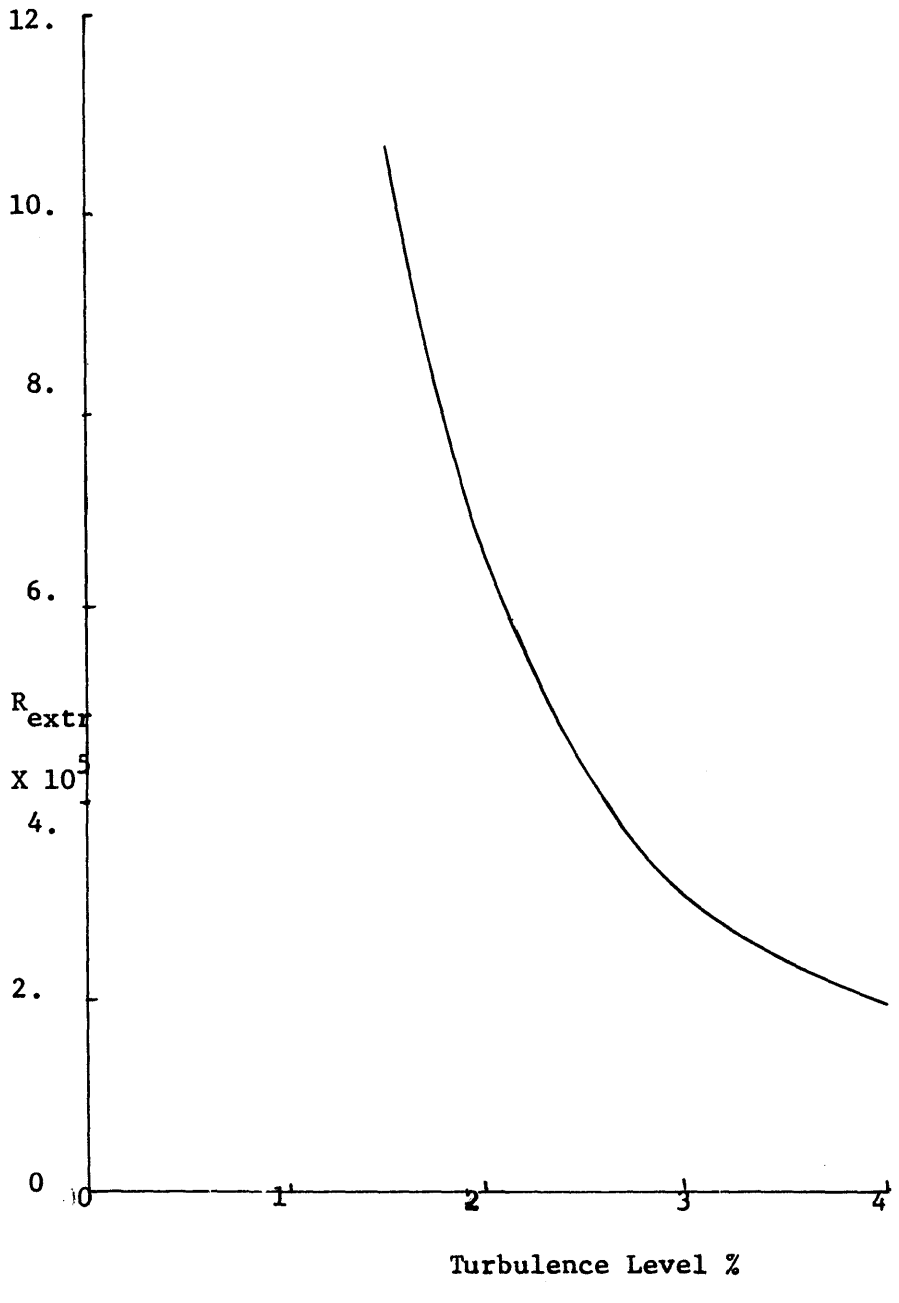

Figure 5.30 Reynolds number at the begining of transition versus degree of Turbulence, Tu, using emphirical equation of reference 54.

Figure 5.31 Heat Transfer at the Leading Zone

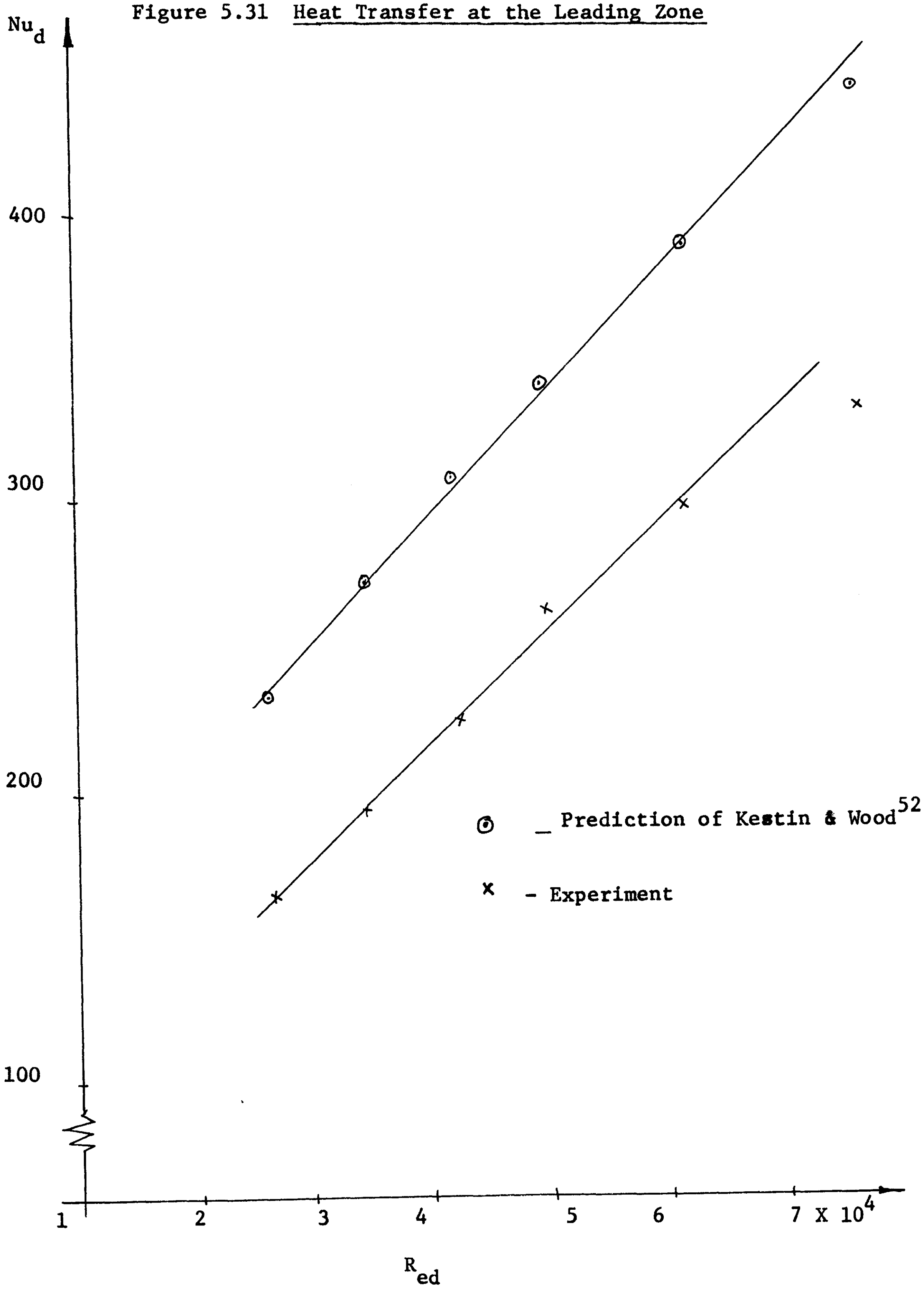

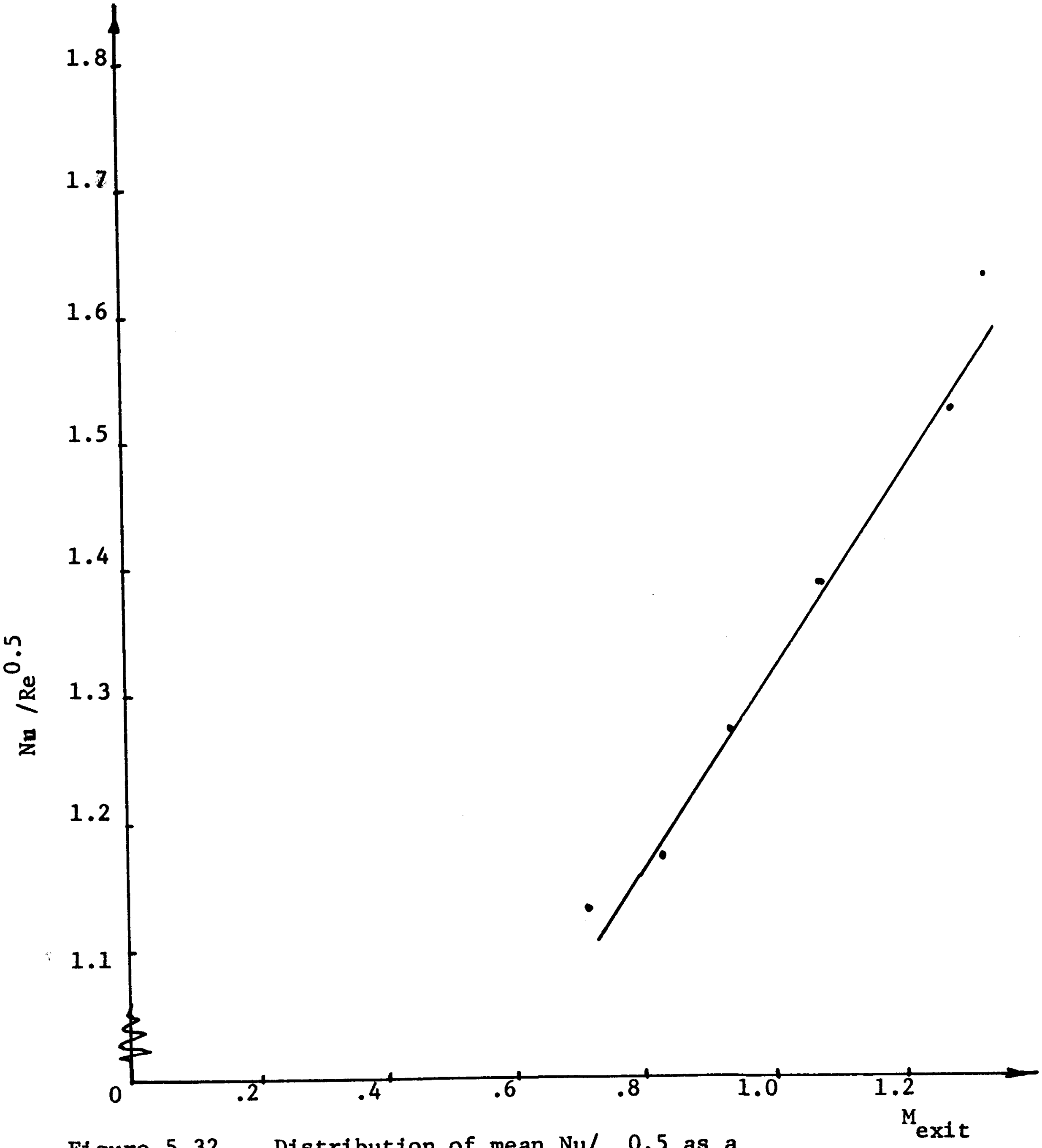

Figure 5.32 Distribution of mean $Nu/_{Re}0.5$ as a function of Exit Mach Number.

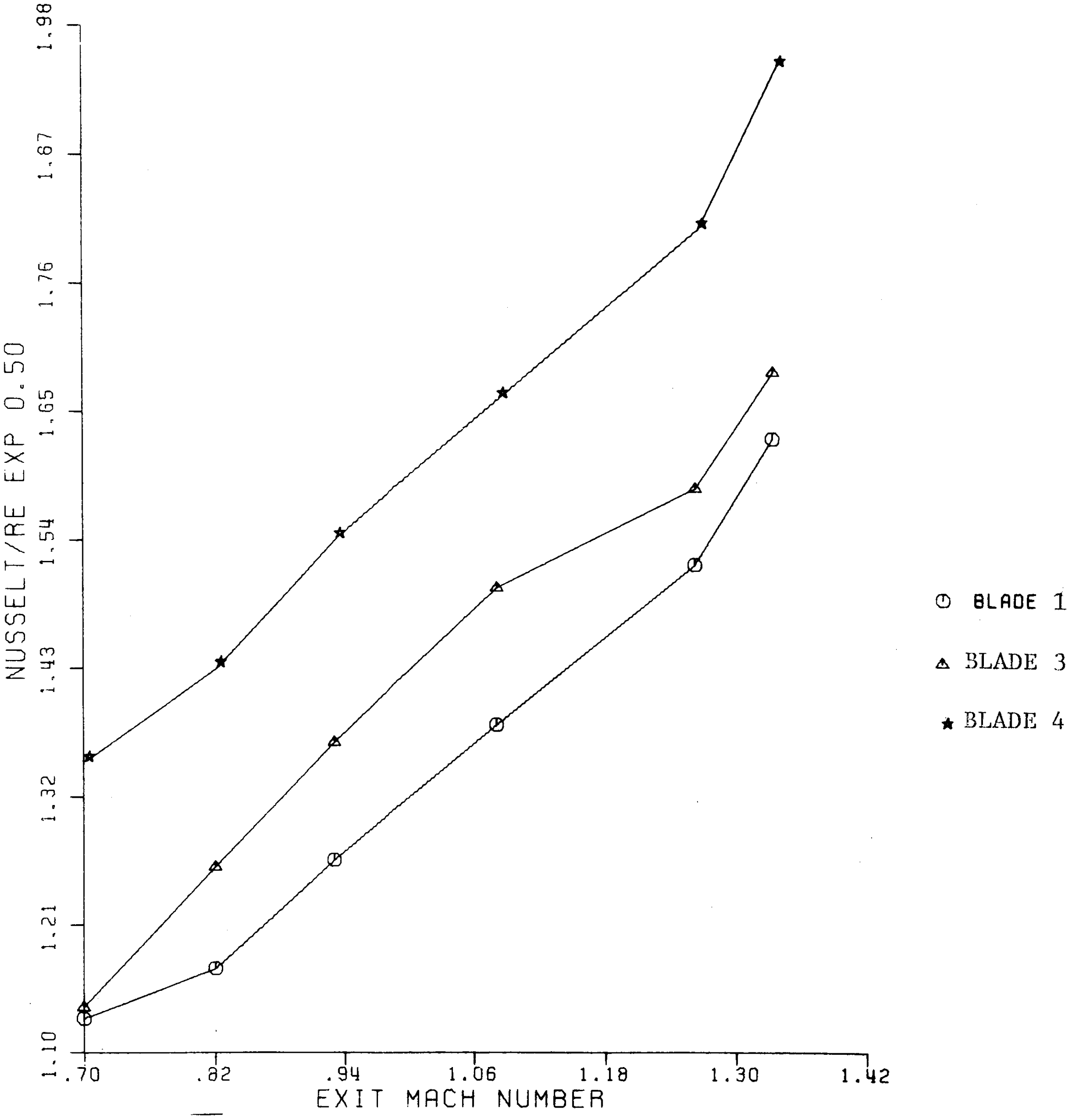

Figure 5.33 Blade average $N_u/R_e^{0.5}$

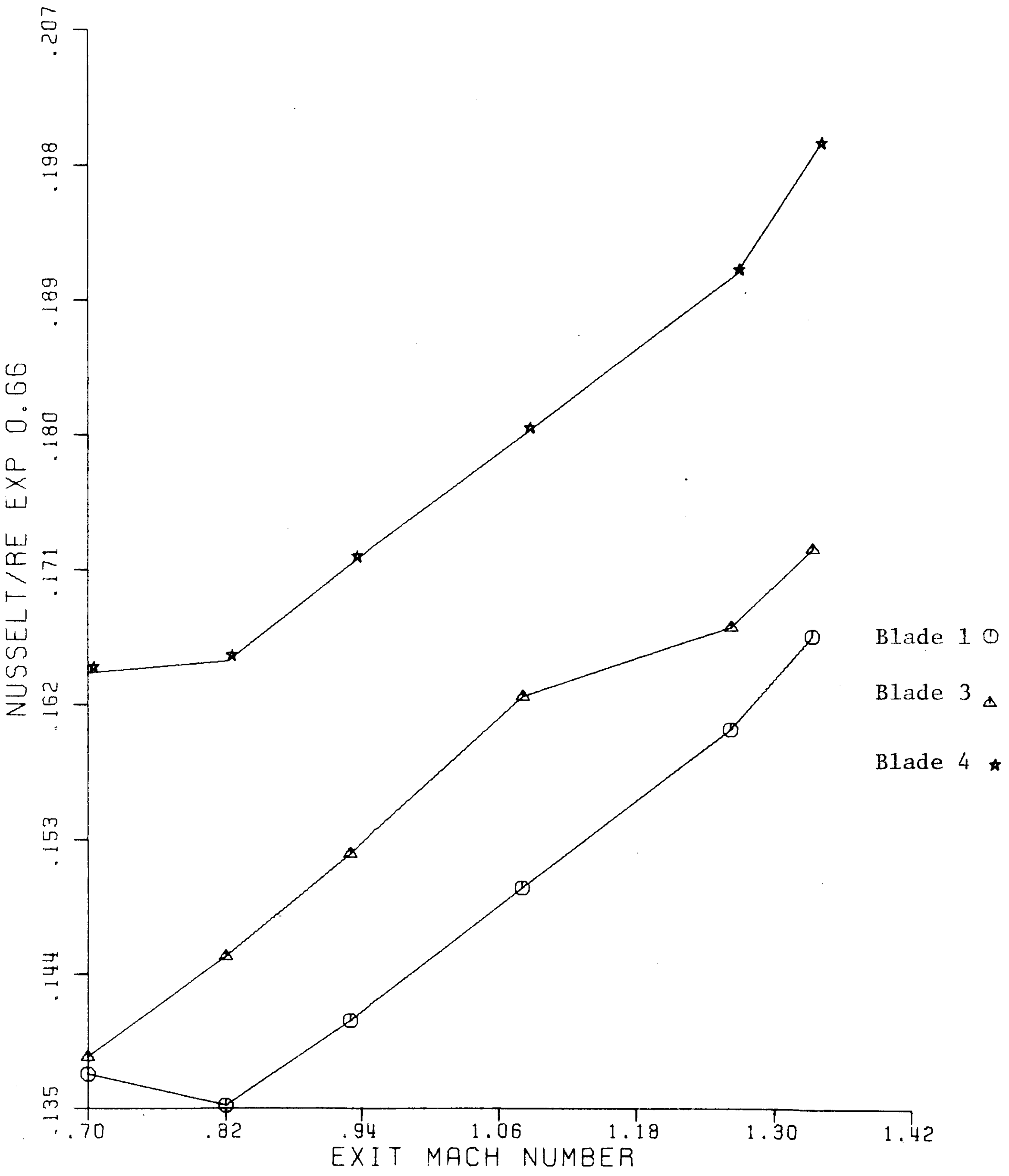

Figure 5.34 Blade average $N_u/R_e^{0.66}$

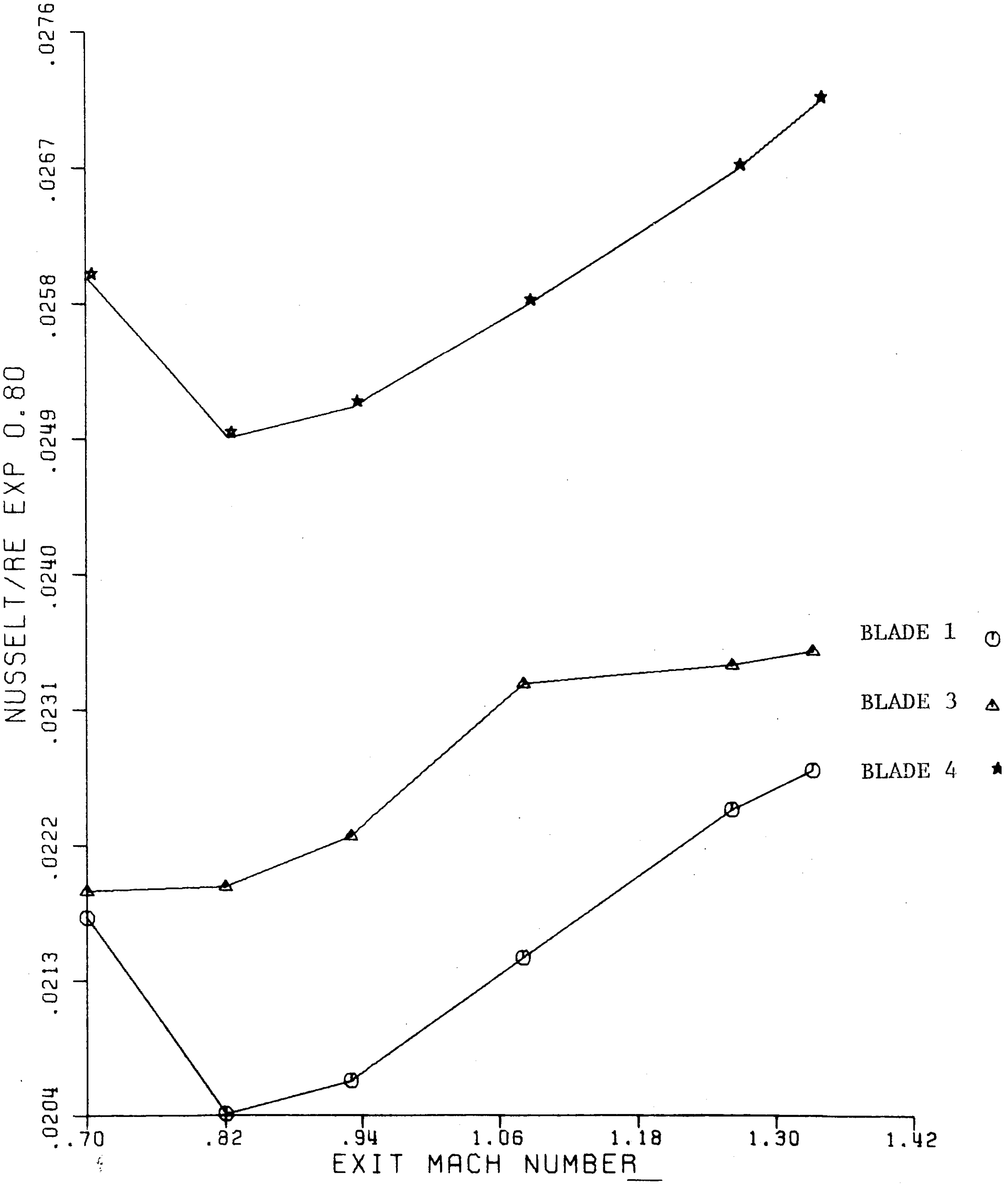

Figure 5.35 Blade average $N_u/R_e^{0.8}$

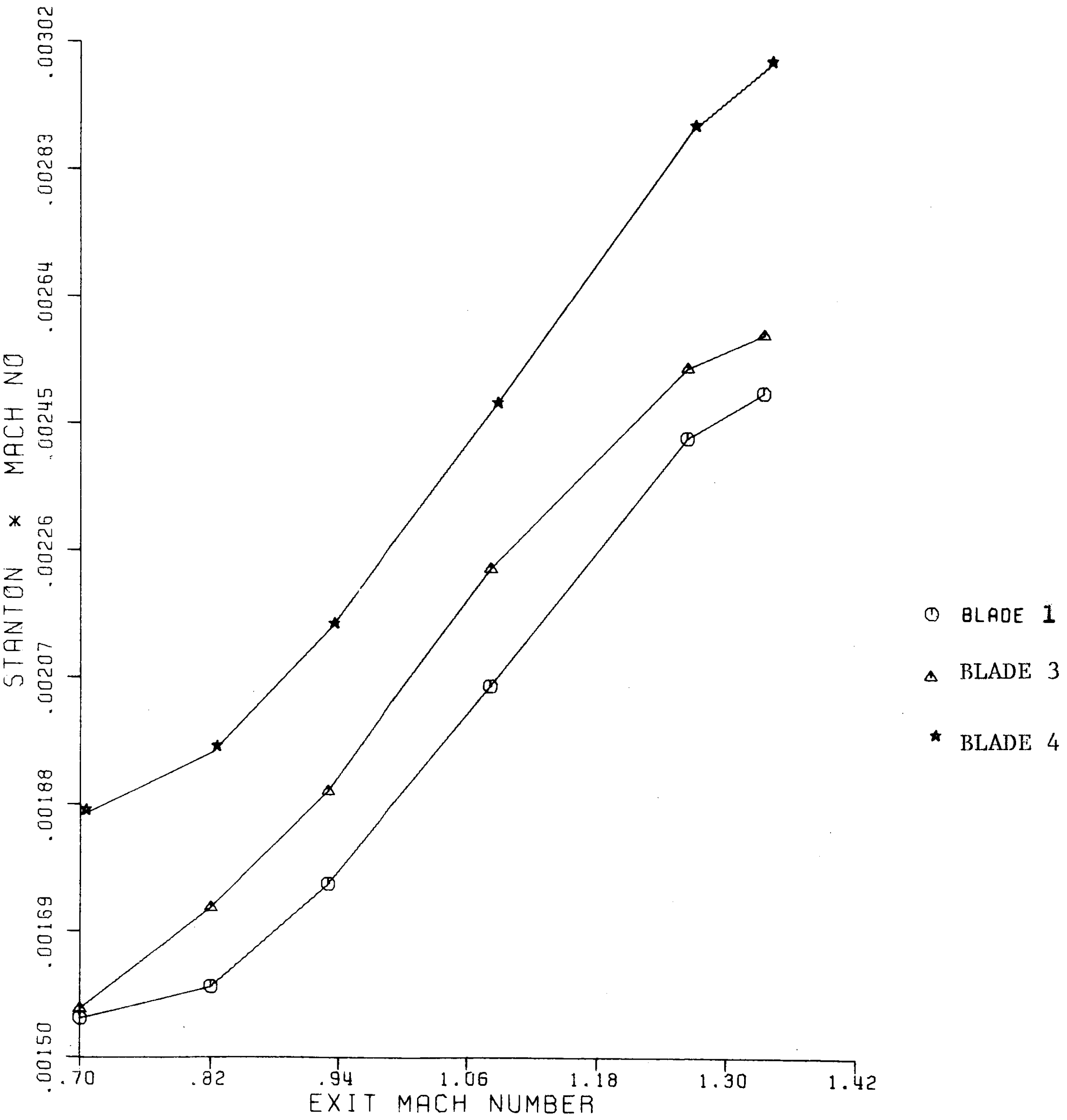

Figure 5.36 Blade average "Stanton Number x Mach Number"

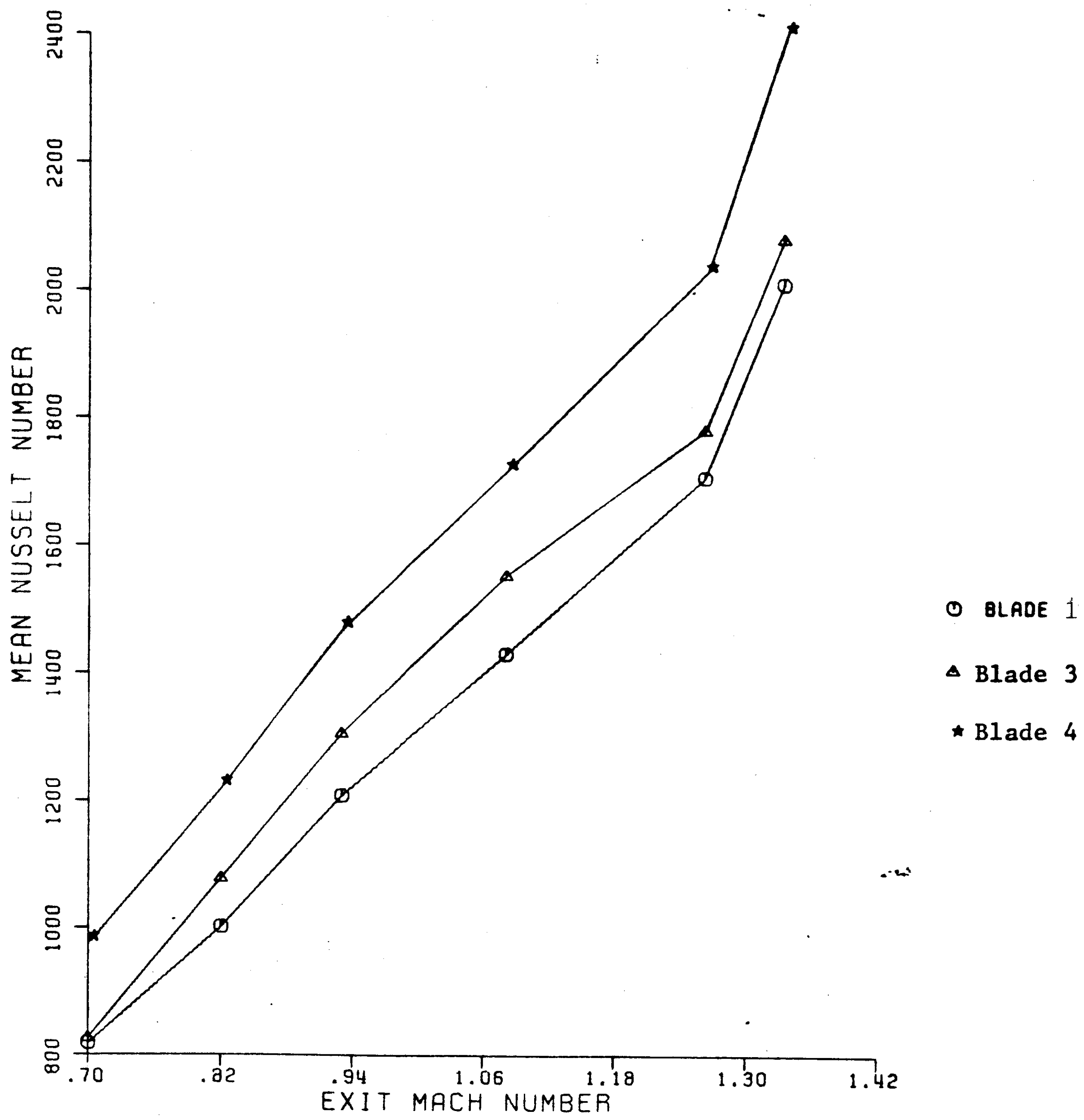

Figure 5.37 Blade average Nusselt Number

Figure 5.38 Mean Heat Transfer Results

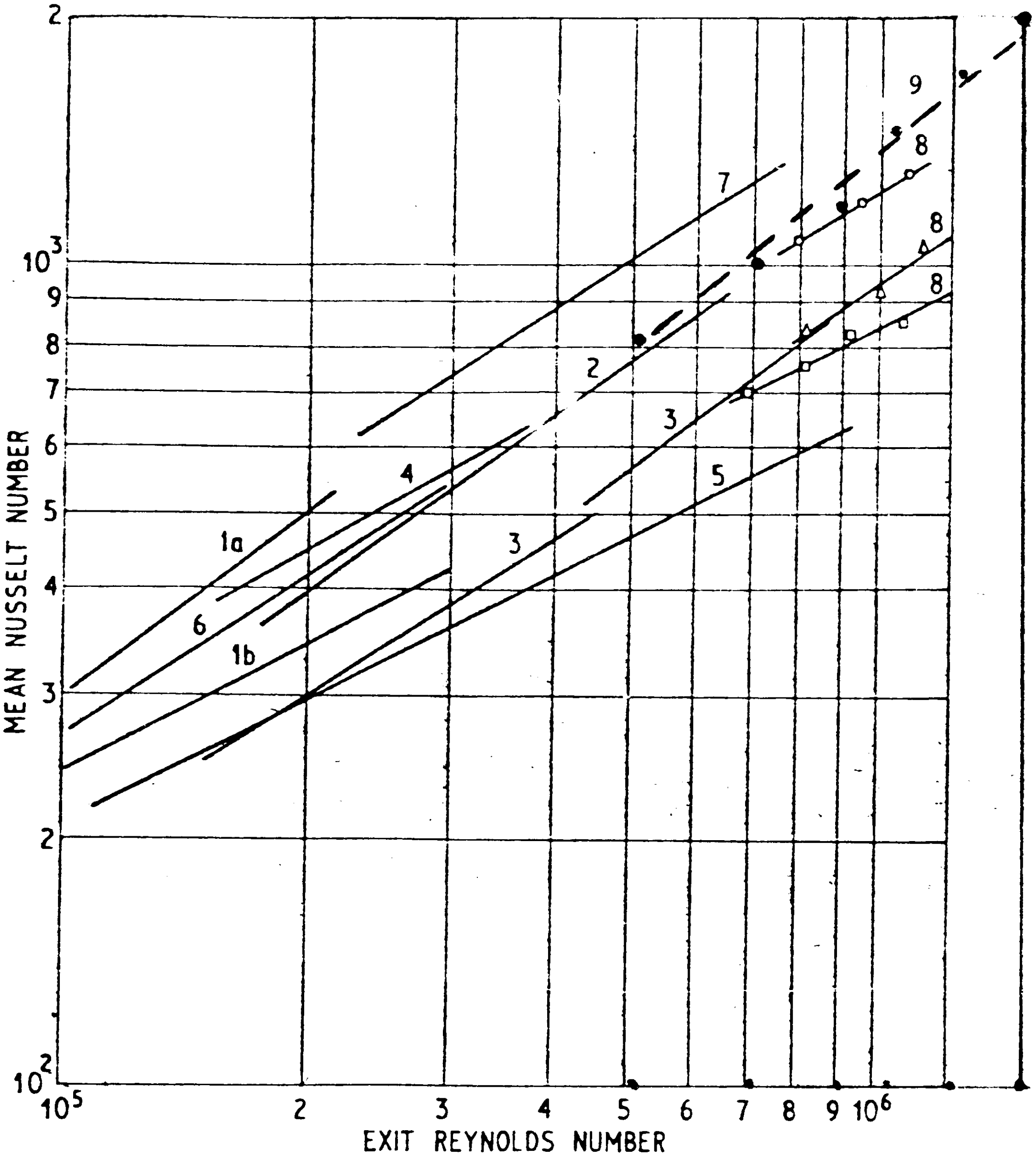

1*a* Ainley turbine (ref. 67)
1*b* Ainley cascade (ref. 67)
2 Wilson and Pope (ref. 36)
3 Hodge (ref. 68)
4 Bammert and Hahnemann (ref.69)
5 Andrews and Bradley (ref. 70)
6 Fray and Barnes (ref. 71)
7 Halls (ref. 72)
8 Turner (ref. 43)

	Symbol	Turbulence
	○	5·9%
	△	2·2%
	□	0·45%
9 Experiment	●	10%

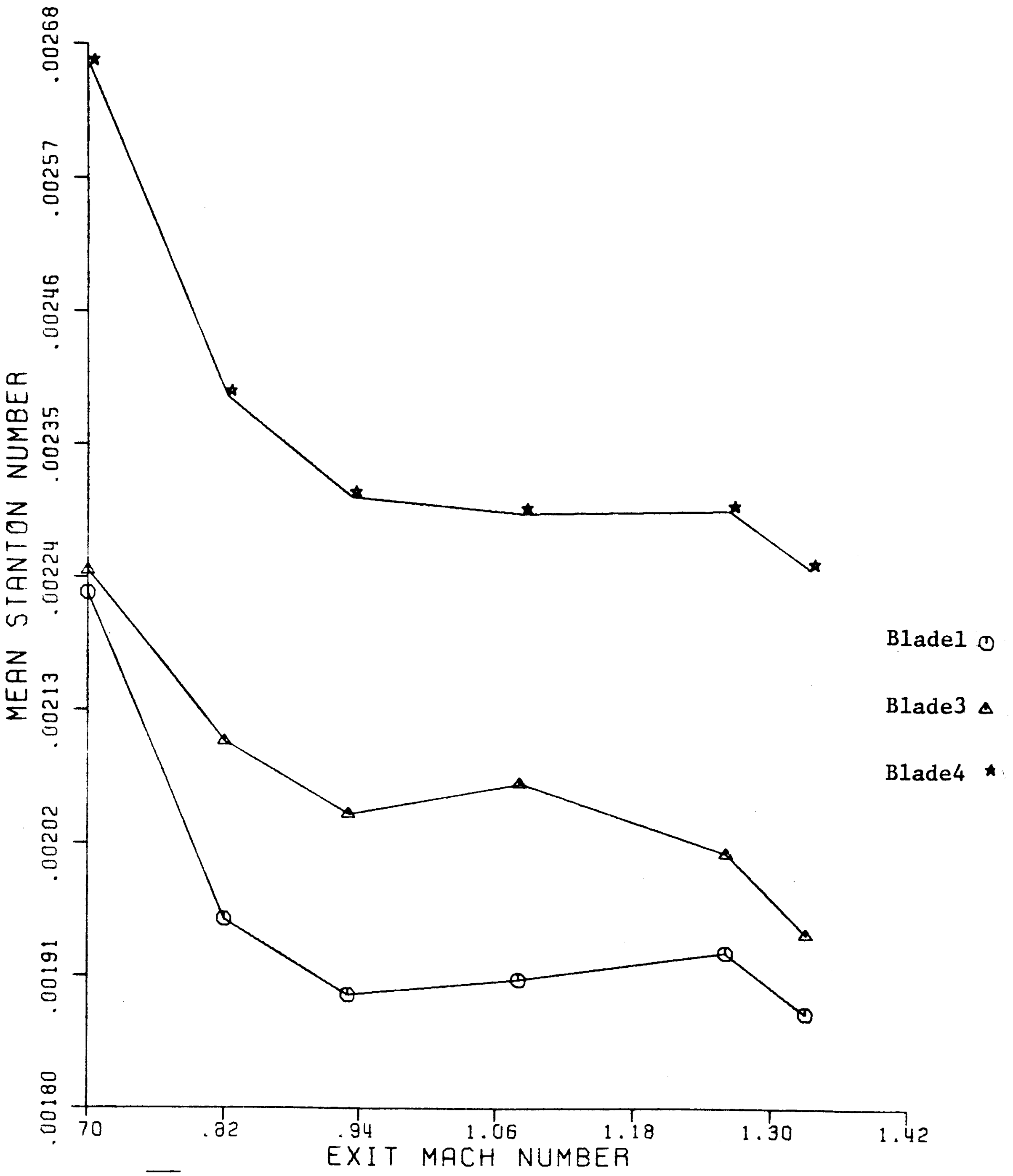

Figure 5.39 Blade average Stanton Number

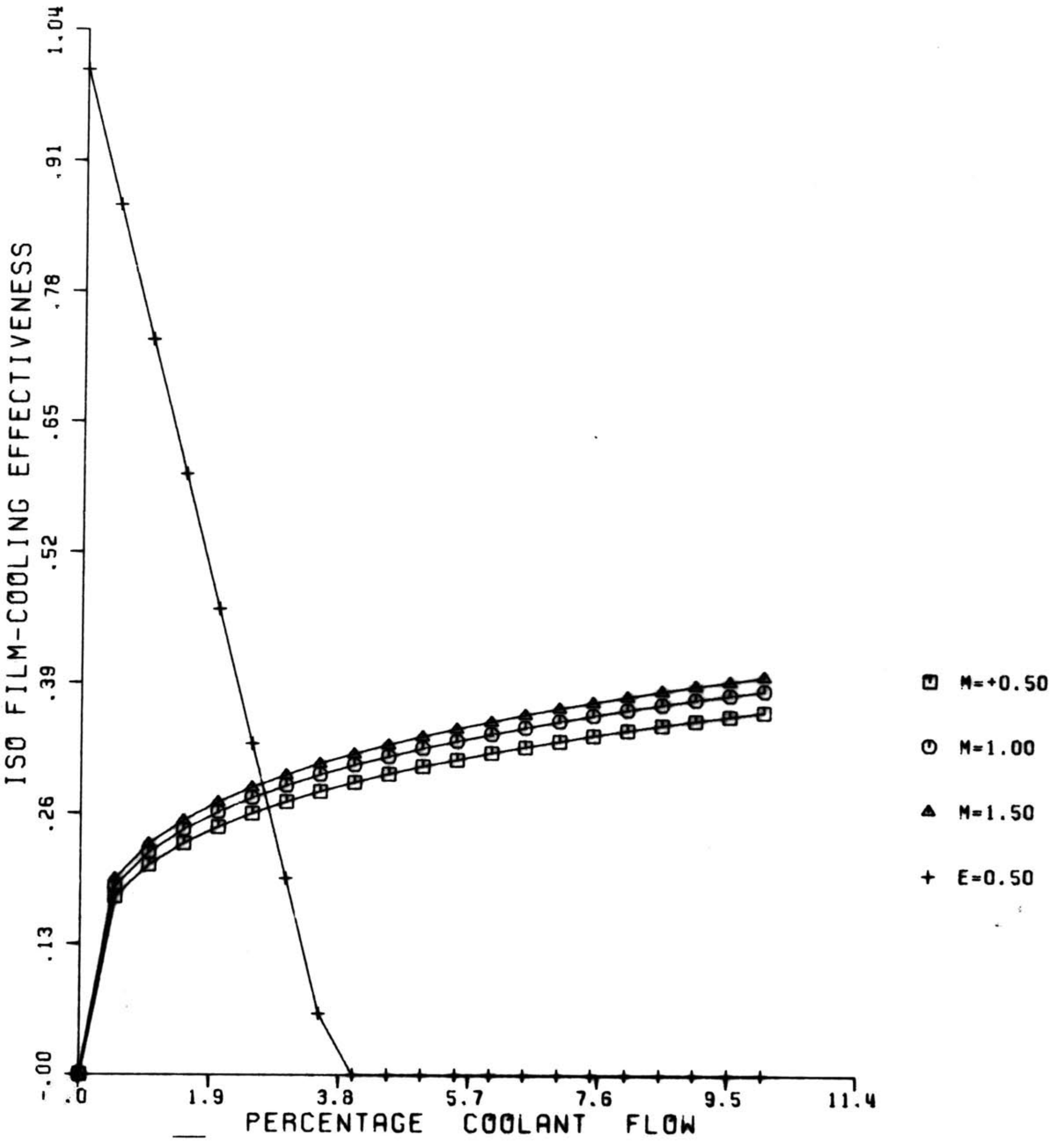

Figure 6.1 Isothermal film cooling effectiveness as a function of coolant mass flow. (transonic stage)

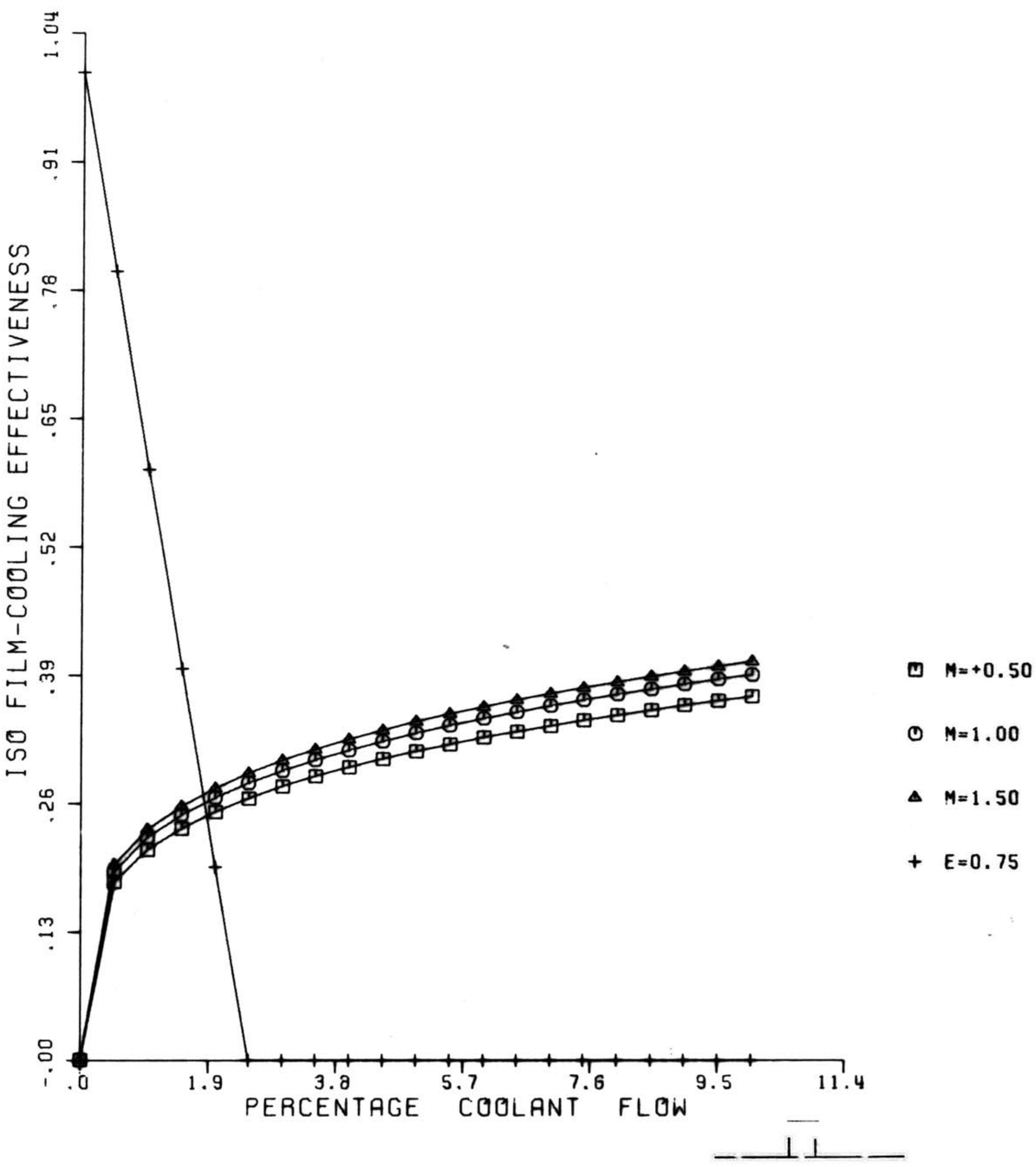

Figure 6.2 Isothermal film cooling effectiveness as a function of coolant mass flow. (transonic stage)

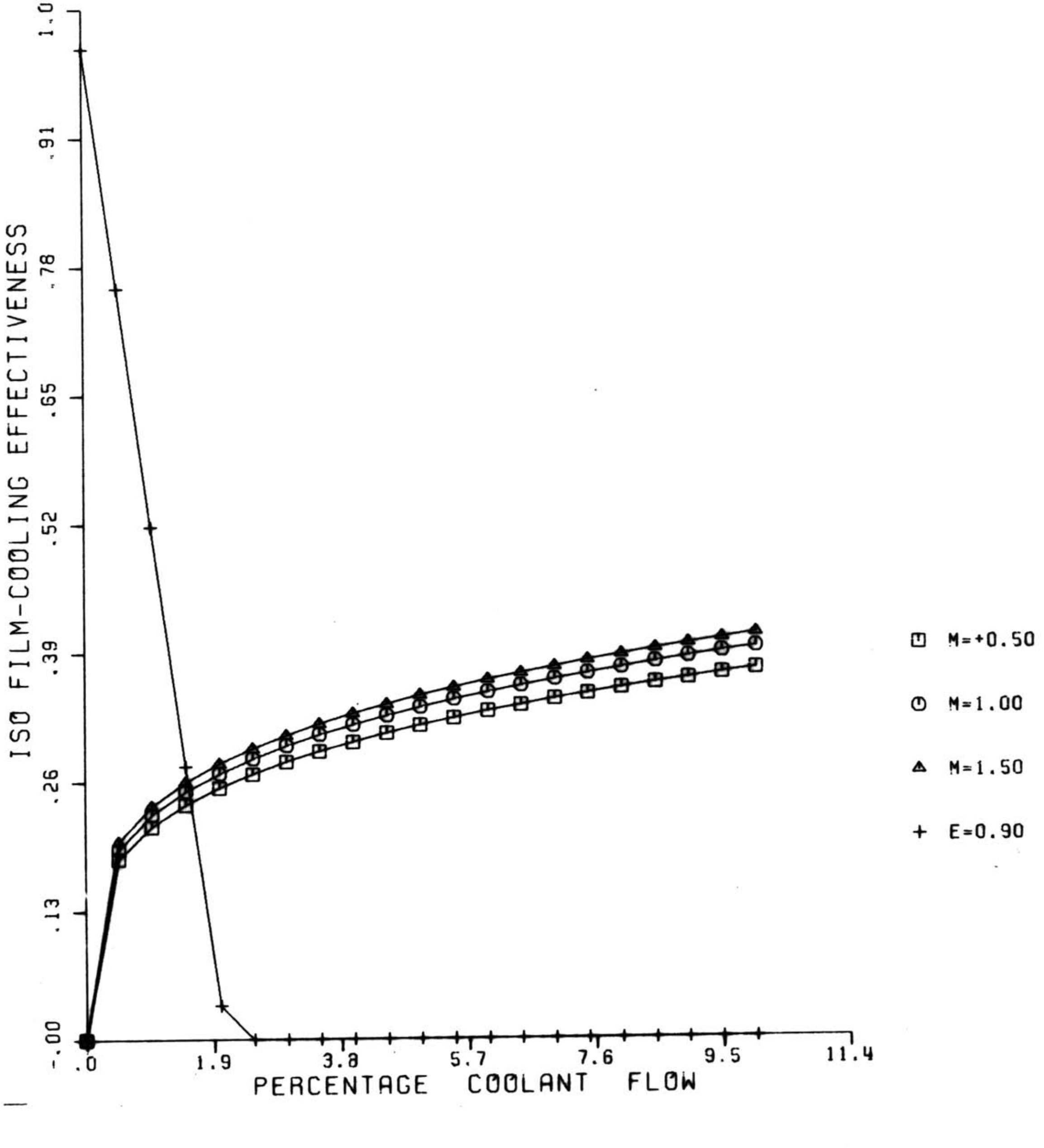

Figure 6.3 Isothermal film cooling effectiveness as a function of coolant mass flow. (transonic stage)

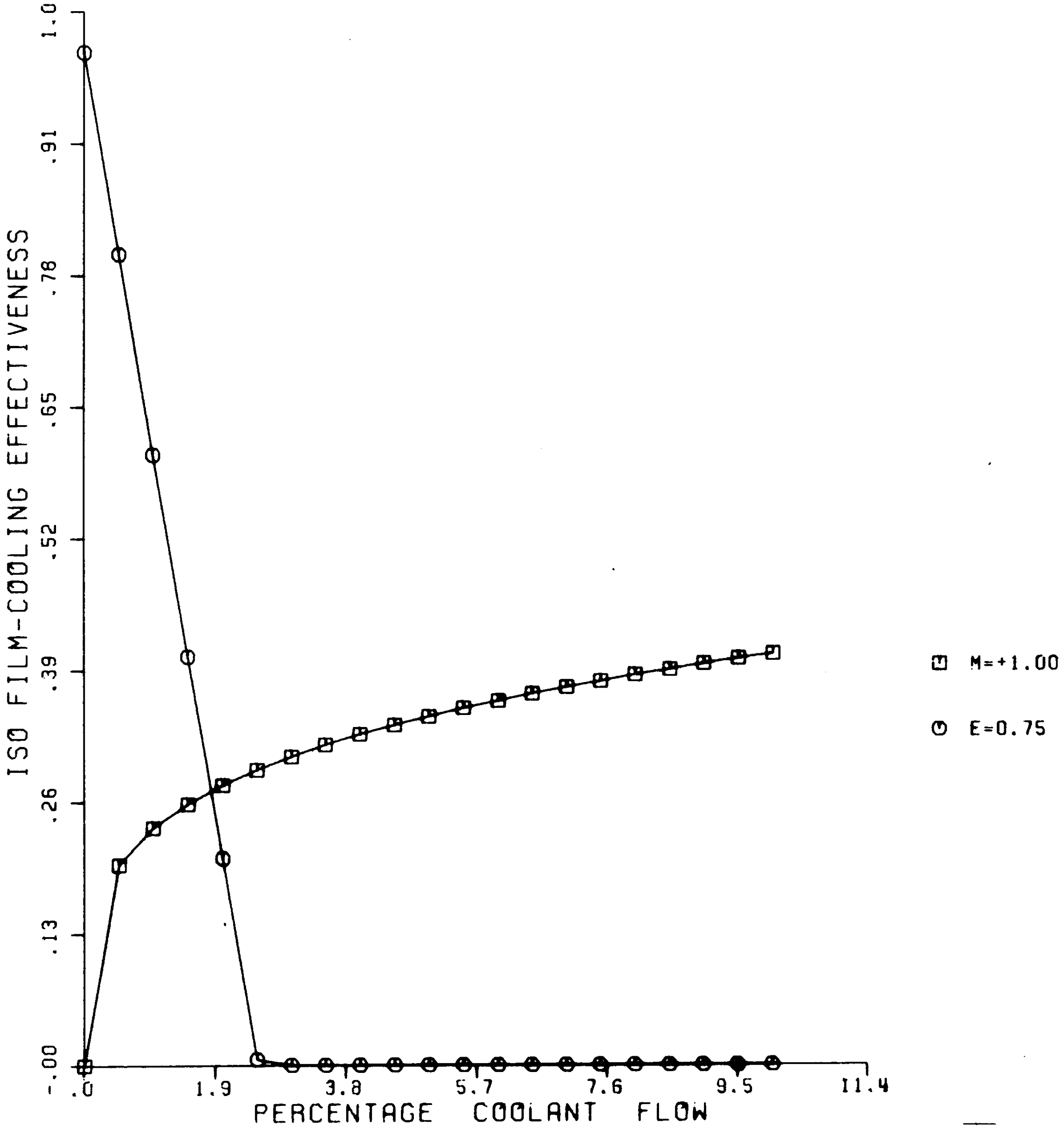

Figure 6.4 Isothermal film cooling effectiveness as a function of coolant mass flow (subsonic rotor first stage)

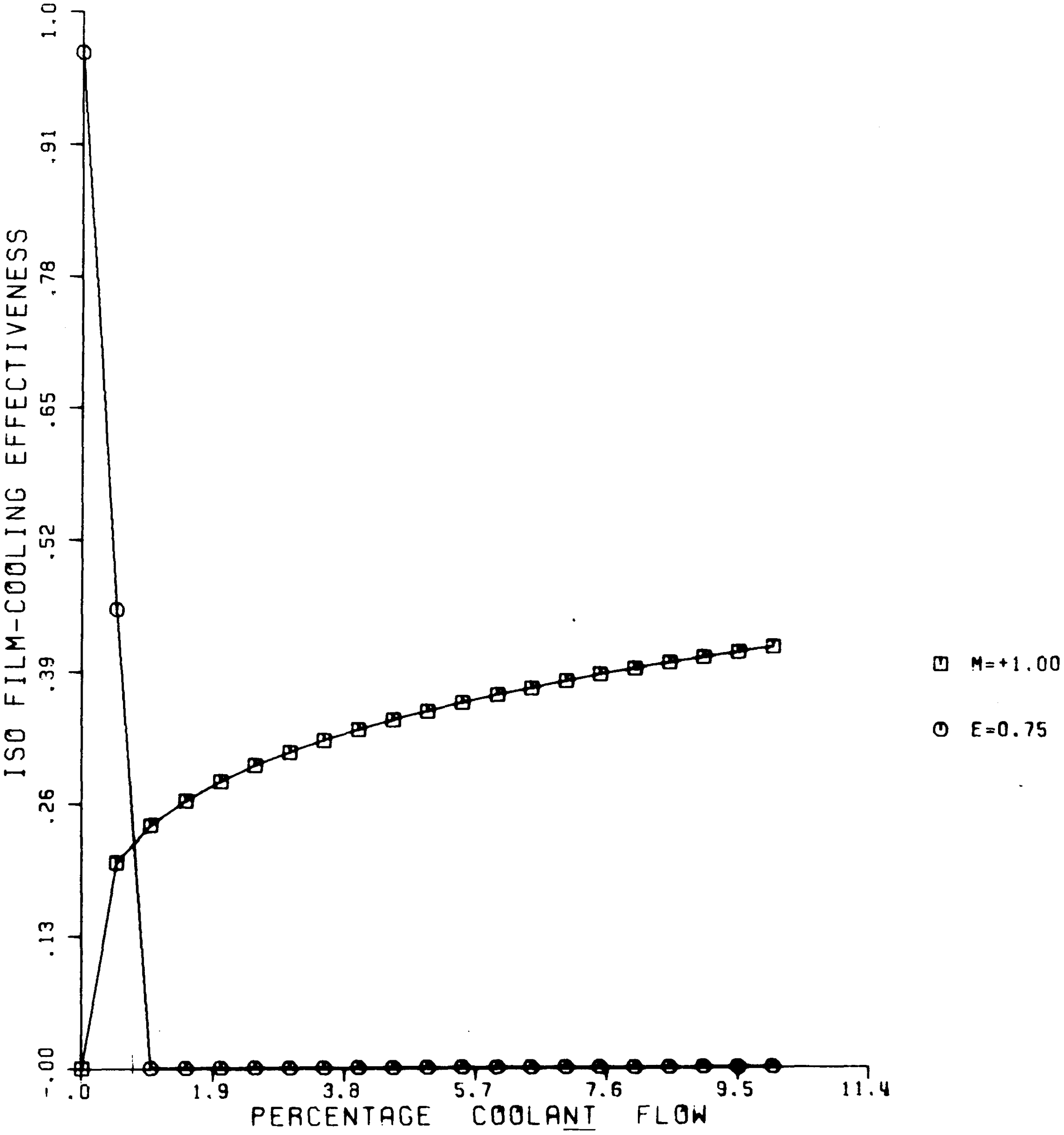

Figure 6.5 Isothermal film cooling effectiveness as a function of coolant mass flow (second nozzle of the two-stage subsonic turbine)

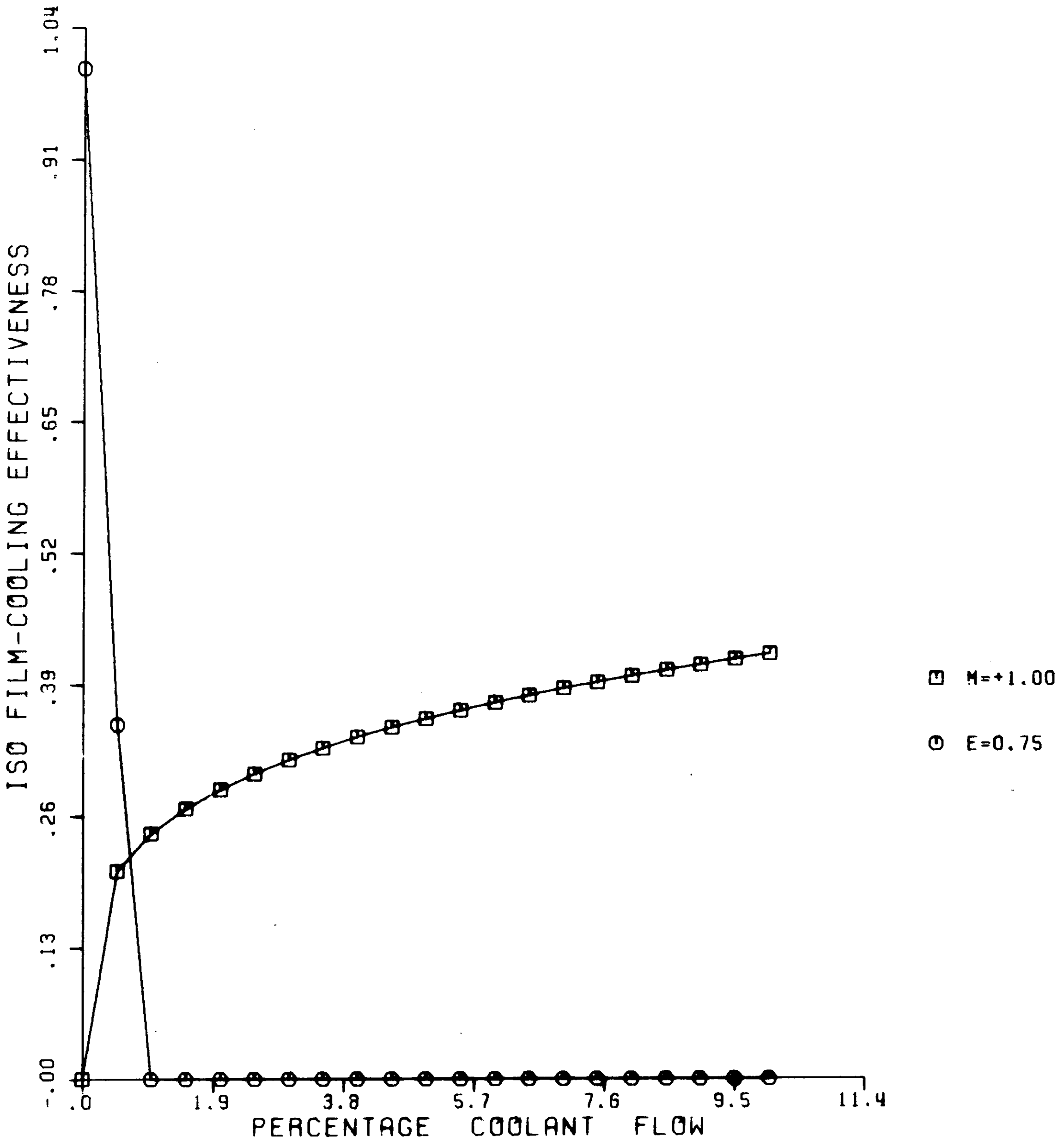

Figure 6.6 Isothermal film cooling effectiveness as a function of coolant mass flow (second rotor of the two-stage subsonic turbine)

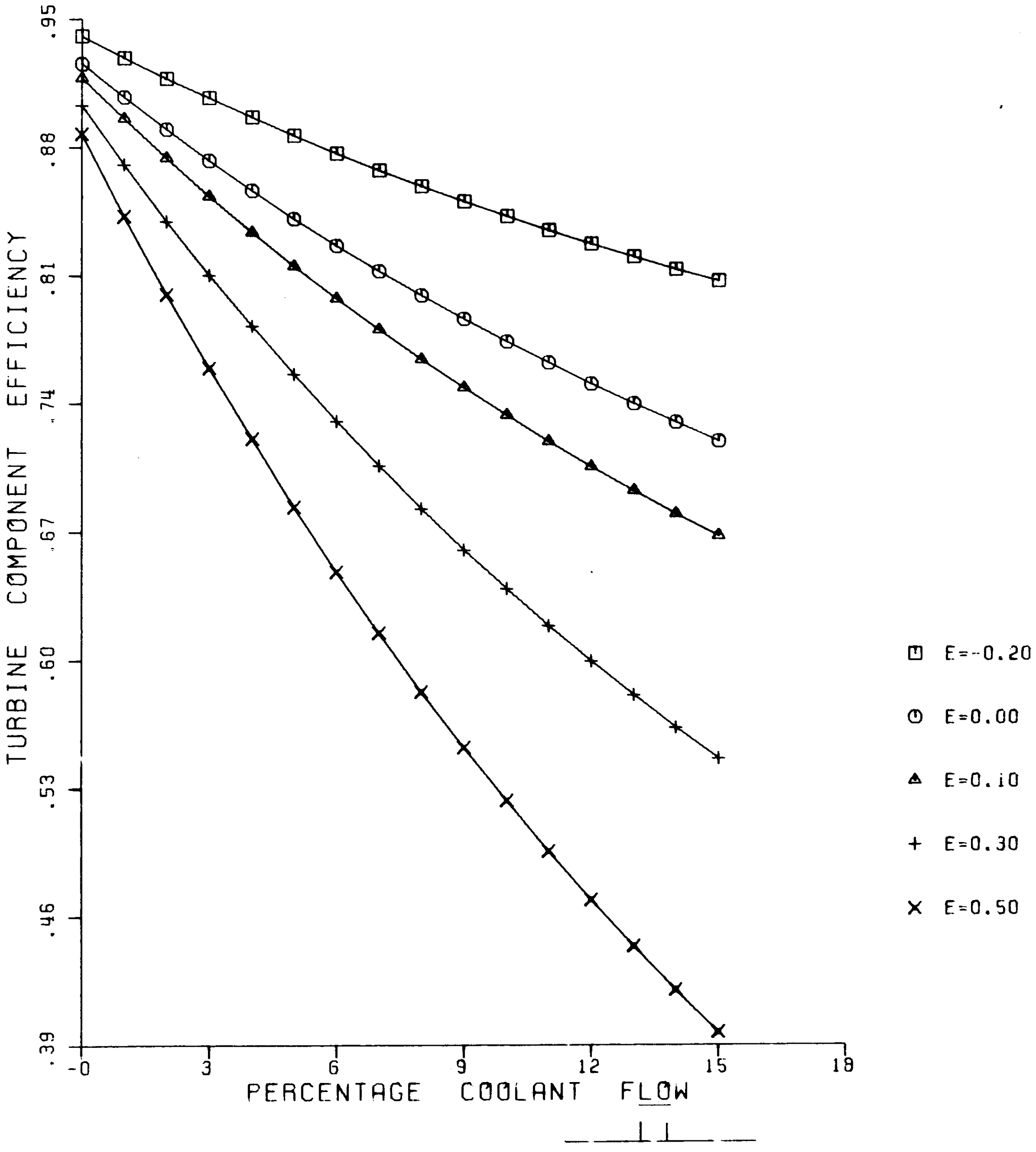

Figure 6.7 Turbine Component Efficiency as a function of coolant mass flow (2 stage subsonic turbine)

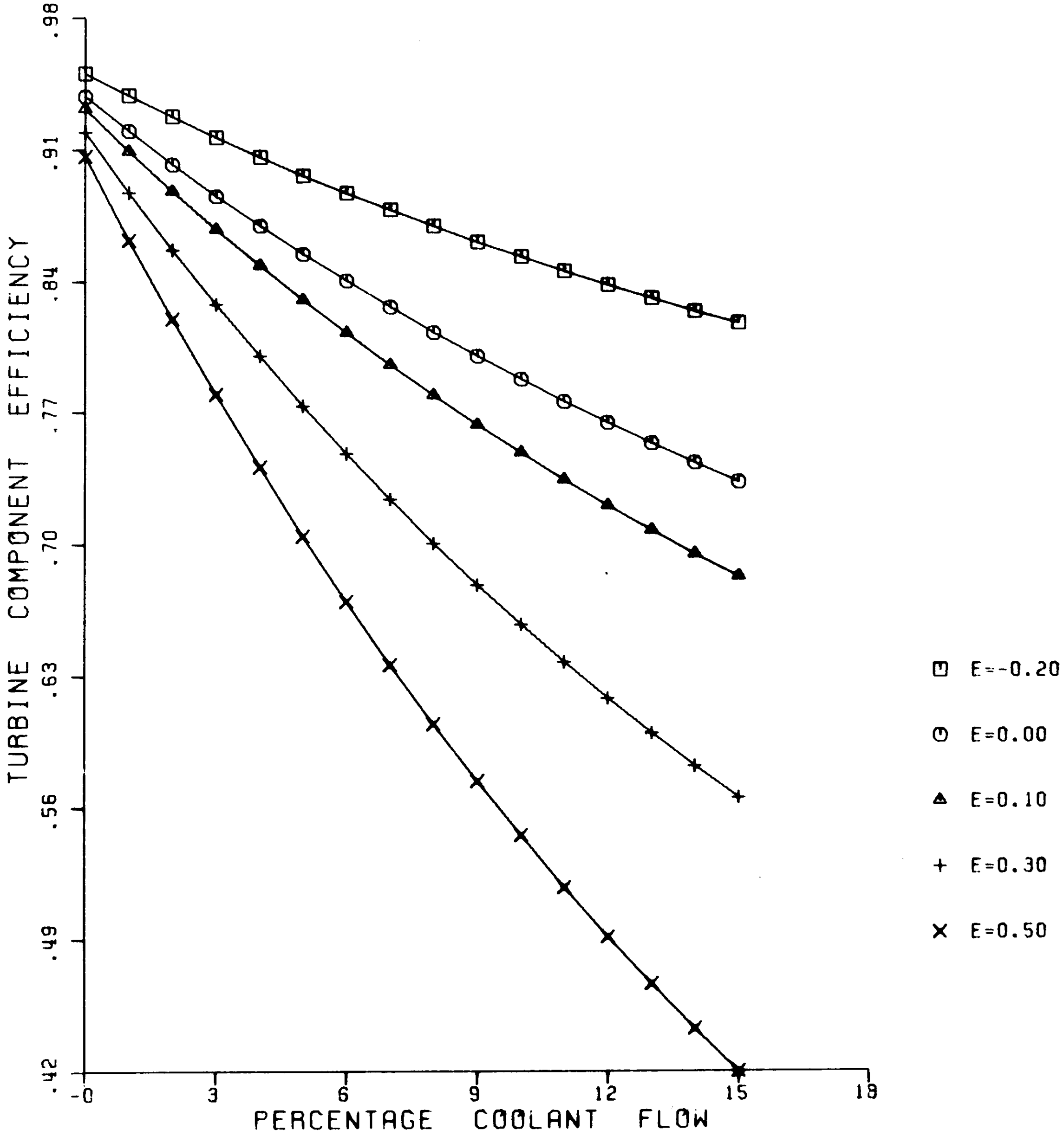

Figure 6.8 Turbine Component Efficiency as a function of coolant mass flow (transonic stage)

REFERENCES

1. Moffitt, Thomas P. "Design and Experimental Investigation of a Single - Stage Turbine with a Rotor Inlet Relative Mach Number of 2". NACA RM.E58 F20a, 1958

2. Moffitt, T.P. and Klag, F.W. Jr, "Experimental Investigation of the Partial - Admission Performance Characteristics of a Single - Stage Mach 2 Supersonic Turbine." NASA TMX - 80. 1959

3. Moffit T.P. and Klag F.W. Jr;" Experimental Investigation of Partial and Full Admission Characteristics of a Two Stage Velocity - Compounded Turbine." NASA TMX-410, 1960.

4. Johnston, I.H. and Dransfield, D.E., "The Test Performance of Highly - Loaded Turbine Stages Designed for High Pressure Ratio." Aeronautical Research Council, RM 3242, January 1959.

5. Deych, M.Y. and Troyanovskiy, B.M. Investigation and Calculation of Axial Turbine Stages. FTD - MT - 65 - 409, Wright - Patterson Air Force Base, Ohio, Issledouaniya I Raschety Stupney O Sevylch Turbin, 1964 ˙

6. Deych M. Ye and Samoylovich G.S., Fundamentals of the aerodynamics of axial turbomachine Machgiz Moscow 1959..

7. Deych M. Ye, and Gubarev A. V. "Investigation of impulse cascade at high velocities." Heat power engineering 1958 No. 12 Moscow.

8. Colclough C.D., "Design of Turbine Blade suitable for Supersonic Relative Inlet Velocities and the Investigation of their Performance in Cascades. Part II.- Experiments, Results and Discussion." Journal of Mechanical Engineering Science 8, No. 2, 1966.

9. Kantrowitz A "The Supersonic Axial Flow Compressor" NACA Report No. 974 1950.

10. Ferri, A. "Preliminary analysis of axial Flow compressors having supersonic velocity at the entrance of the Stator". NACA RM L9G06 1949 .

11. Stodola, A Steam and gas turbines 1945 1, 1964. Peter Smith, New York.

12. Shapiro, A.M. The dynamics and thermodynamics of compressible fluid flow. 1953 Volumes I & II Roland Press Co., New York.

13. Liccini, L.L. "Analytical and experimental investigation of 90° supersonic turing passages, suitable for supersonic compressors or turbines." NACA RM L9G07, 1949.

14. Liccini, L.L. "Experimental investigation of the mixing loss behind the trailing edge of a cascade of three 90° supersonic turning passages" NACA RM L5021a; 1950.

15. Busemann A. Handbook of Experimental Physics. Russian Translation Modvoe 1951.

16. Oswatitsch K. Gasdynamic Russian Translation Moscow 1952.

17. Boxer, E, Sterrett, J.R and Woldarskie, J. "Application of supersonic vortex flow theory to the design of supersonic impulse compressor or turbine blade sections." NACA RM L52B06, 1952.

18. V. Traupel. Thermal Turbomachines State power engineering publishing house. 1964.

19. Stratford, B.S., and Sansome, G.E. "Theory and Tunnel Tests of Rotor Blades for Supersonic Turbines." ARC R & M, 3275 December 1960.

20. Stratford, B.S., and Sansome, G.E., "The Performance of Supersonic Turbine Nozzles." ARC R & M #3273 June 1959.

21. Deych M.Y.
Atlas Profile of Turbine Blades. Moscow

22. Goldman, L.J. Scullin V.J. "Analytical Investigation of Supersonic Turbomachinery Blading. I - Computer Program for Blading Design." NASA - TN-D- 44421. 1968

23. Goldman L.J. "Analytical Investigation of Supersonic Turbomachinery Blading II - Analysis of Impulse Turbine Blade Sections." NASA TN-D-4422 1968.

24. Goldman L.J. and Scullin V.J. Computer Program for design of two-dimensional supersonic turbine rotor blades with boundary layer correction." NASA-TM-X-2434 Dec. 1971. Fruchtman. I.

25. Fruchtman. I. "Aerodynamic Design of Supersonic Turbines" General Applied Science Lab. Inc. Technical Memo No. 731 Final Report August 1969.

26. Shapiro A.H. & Edelman G.M. "The Method of Characteristics for two-dimensional supersonic flow." Graphical and Numerical Procedures. M.I.T. Project Meteor Report No. 7 1947.

27. Edelman Gilbert M. "The design, development and testing of two dimensional sharp-cornered supersonic nozzle. M.I.T. Meteor Report 22 1948.

28. Goldman L.T. and Vanco M.R. "Computer Program for Design of two-dimensional Supersonic Nozzle with Sharp-Edged Throat. NASA TM-X- 1502 January 1968.

29. Louis J.F., et al, "Short Duration Studies of Turbine Heat Transfer and Film Cooling Effectiveness." ASME Gas Turbine Conference Paper No. 74-GT-131, June 1974.

30. Dunavant J.C. and Erwin, J.R. "Investigation of a Related Series of Turbine Blade Profiles in Cascades." NACA TN 3802 1956.

31. Craig H.R.M; Cox H.J.A. "Performance Estimation of Axial Flow Turbines." Heat and Fluid Flow Vol. 1 No. 2 1971.

32. Zhukovskii M.I. "New Turbine Blade Profiles". Teploenergetika No. 7 1959.

33. Rausch. M. "Etude De Deux Methodes De Dessin D'aumbes (Deich et NACA) Et Calcul Des Performances Afferant Aux Profils Obtenus".

Pour L'Obetention Du Grade D'Ingenieur Civil Electro-Mecanicien. Universite De Liege, Faculte des Sciences Appliquees. Annee Academique 1971/1972.

34. Shames, M and Seashore F.L. "Design Data For Graphical Construction of Two-Dimensional Sharp-Edge- Throat Supersonic Nozzles." NACA RM E8J12 1948.

35. Lawaczeck, O; and Heinemann H.J. "Von Karman Vortex Streets In The Wakes of Subsonic and Transonic Cascades."

36. Wilson D.G, Pope J.A. "Convective Heat Transfer to Gas Turbine Blade Surfaces". Proceedings of the Institute of Mechanical Engineering vol. 134 no. 36, 1954.

37. Bodunov M.N. "Certain Results of An Experimental Investigation Into Local Coefficients of Heat Transfer To Turbine Blades." Izvestiya VUZ. Aviatsiomaya Tekhnika, Vol. 10. No. 2, pp 136-139 1967 Moscow.

38. Lokai V.I, Ivanov V.L., *High Temperature Cooled Gas Turbines* (in Russian). Mashinostroenie Moscow 1971.

39. Zhiritskii I.S. et al. *Gas Turbine Engines For Flight Vehicles.* (in Russian). Mashimostroenie 1971 Moscow.

40. Kopelev C.Z; Tihonov H.D. *Design of Turbines For Aircraft Engines.* (in Russian) Mashinostroenie 1974 Moscow.

41. Launder B.E. Laminarization of the Turbulent Boundary Layer by Acceleration. G.T.L. Report No. 77 M.I.T. November 1964.

42. Jones W.P and Launder B.E. "The Prediction of Laminarization With A Two-Equation Model of Turbulence" International Journal of Heat Transfer Vol. 15 pp. 301 - 314 1972.

43. Turner A.B. "Local Heat Transfer Measurements On A Gas Turban Blade." Journal of Mechanical Engineering Science Vol. 13 No. 1 1971.

44. Schlichting, H. Boundary Layer Theory 6th Edition McGraw-Hill 1968.

45. Dyban E.P; Gluschchenko V.G. "Investigating Heat Transfer And Gas Flow in Cascades Of Cooled Turbine Blades." Engineering Thermophysics Institute UKrSSR Academy of Sciences (in Russian) Teplofizika i Teplotekhnika, 24 pp. 39-43, 1973.

46. Lokai V.I, Gunchenko E.Il & Limanskii A.S. "Analysis of Cooled Turbine Blades". Izvestiya VUZ, Aviatsionnaya Tekhnika, Vol 17, No. 3 pp. 80-84, 1974

47. Bayley F.J.; Turner A.B. "Transpiration Cooled Turbines" Heat and Fluid Flow Vol. 2 No. 1 1972.

48. Bayley F.J.; Turner A.B. "The Heat Transfer Performance of Porous Gas Turbine Blades". The Aeronautical Journal of the Royal Aeronautical Society. December 1968.

49. Dyban Ye. P and Gluschenko V.G. "Concerning the Reliability of Existing Methods of Calculating Heat Transfer Between the Gas and the Cooled Turbine Blade." Teplofizika i Teplotekrika 23, pp. 29-34 1973 (in Russian)

50. Dyban Ye,P. and Kurosh V.D. "Heat Transfer at the Leading Edge of a Turbine Blade". Heat Transfer - Soviet Research Vol. 2, No. 1 January 1970.

51. Dyban Ye.P., Epik, E.Ya, and Kozlova L.G. "Heat Transfer in the Vicinity of the Front Stagnation Point of a Cylinder in Traverse Flow." Kiev, Teplofizika i Teplotekhnika, 24, pp 57-60, 1973.

52. Kestin J, Wood R.T. "The Influence of Turbulence on Mass Transfer From Cylinders." Journal of Heat Transfer ASME November 1971.

53. Dyban E.P. and Yerik Ye.R. "Heat Transfer in Laminat Boundary Layer with Increased Turbulence of the Outer Flow." Heat Transfer - Soviet Research Vol. 6 No. 3 May-June 1974.

54. Zysina-Molozhen L.M; and Kurosh V.D. The Effect of Turbulence of Transition in the Boundary Layer of Gas Turbine Blades." Teploenergetika Volume 18 No. 12 1971.

55. Zysina-Molozhen L.M. and Kuznetsova V.M. "Investigation of Transition Conditions in A Boundary Layer." Teploenergetika Vol. 16. No. 7 1969.

56. Kurosh V.D. and Epik E.Ya. "The Effect of Turbulence on Heat Transfer in Turbomachinery Flow Passages." Heat Transfer-Soviet Research Volume 2 No. 1 January 1970.

57. Hawthorne W.R. *Aerodynamics of Turbines and Compressors* Volume 10 High Speed Aerodynamics and Jet Propulsion. Princeton 1964.

58. Hodge J. *Cycles and Performace Estimation*. Gas Turbine Series

Volume 1. London 1955.

59. Brown T.W.F. "The Effect of the Radiation correction on Cooling Loss in High Temperature Cooled Gas Turbines". General Discussion on Heat Transfer I. Mech. E. 1951.

60. Smith M.C. and Kuethe A.M. "Effect of Turbulence on Laminar Skin Friction and Heat Transfer." Physics Fluids 1966 Vol. 9 No. 12 December 1966 p. 2337.

61. Kestin J; Maeder, P.F. and Sogin, H.H. "The Influence of Turbulence on the transfer of heat to Cylinders near the Stagnation point." Journal of Applied Maths and Physics. Vol. 7 1961 p. 115.

62. Mujumdar A.S. and Douglas W.J.M. "Some Effects of Turbulence and Wake-Induced Periodicity on Heat Transfer from Cylinders." paper presented at the 20th Canadian Chemical Engineering Conference, Sarnia, Ontario, Canada, October 1970.

63. McNally W.D. "Fortran Program For Calculating Compressible Laminar and Turbulent Boundary Layers In Abitrary Pressure Gradients." NASA TN D-5681 1970.

64. Hawthorne W.R. and Walker A.B. "The Effect of Blade Cooling on the Efficiency of a Multistage Turbine". ONR Contract N5ori-78, Task Order 21, NR-220-010. M.I.T. Gas Turbine Lab; Cambridge, Mass., TR No. 2 March 1949.

65. Rohsenow W.M. "The Effect of Turbine Blade Cooling on Efficiency of a Simple Gas Turbine Power Plant." ASME Paper No. 55-A-120 1955.

66. Colladay R.S. "Importance of Combining Convention with Film Cooling." AIAA Paper No. 72-8. January 1972.

67. Airley D.G. "An experimental single stage air-cooled Turbine Part II", Proceedings of the Institution of Mechanical Engineers. 1953, Vol. 167, pg. 351.

68. Hodge R.I. "A Turbine Nozzle Cascade For Cooling Studies, Parts I and II." A.R.C.C.P Nos. 492, 293. 1960.

69. Bammert, F and Hahnemann, H. "Heat Transfer in the Gas surrounding cooled turbine blades; Ministry of Supply, Report G.D.C. 2466 1951.

70. Andrews, S.J. and Bradley P.C. "Heat Transfer to Turbine Blades" A.R.C.C.P. No. 294. 1957.

71. Fray D.E. and Barnes, J.F. "An experimental high temperature turbine (No. 126) Part 2. The Cooling performance of a set of extruded air-cooled turbine blades. A.R.C.C.R. and M 3405 1965.

72. Halls G.A. "Air Cooling of Turbine Blades and Vanes." AGARDograph 120, Supersonic turbojet propulsion systems and components, ed. J. Chauvin, 1967.

73. Liepman H.W. and Roshko A. Elements of Gas dynamics John Wiley & Sons, Inc. New York 1967.

74. Rohsenow W.M. and Choi H.Y. Heat, Mass and Momentum Transfer Prentice Hall. 1961.

75. Horlock J.H. Axial Flow Turbines Robert E. Krieger Publishing Co. New York 1973.

76. Kerrebrock J.L. Aircraft Engines. MIT Gas Turbine Lab. Lecture Notes October 1971

77. Cohen, C.B., and Reshotko, E. "The Compressible Laminar Boundary layer with Heat transfer and Arbitrary Pressure Gradient." NACA TR 1294 1956.

78. Sasman, P.K. and Gresci, R.J. "Compressible Turbulent Boundary Layer with Pressure Gradient and Heat Transfer." AIAA Journal Vol. 4, no. 1 January 1966 pp. 19-25

79. Reshotko, E and Tucker, M. "Approximate Calculation of the Compressible Turbulent Boundary Layer with Heat Transfer and Arbitrary Pressure Gradient." NACA TN 4154 1957.

80. Stwwartson K. "Correlated Incompressible and Compressible Boundary Layers." Proc. Royal Society (London) Serial A, Volume 200, no 1060, December 22, 1949 pp. 84-100.

81. Thwaites B. "Approximate Calculation of the Laminar Boundary Layer." Aeronautical Quarterly Vol. 1 Nov. 1949 pp. 245-280.

82. Mager, Arthur. "Transformation of the Compressible Turbulent Boundary Layer." Journal of Aeronautic Science Vol. 25, no. 5. May 1958 pp. 305-311.

83. Ortiz M. "The Effect of Geometry on Film Cooling Effectiveness", M.S. thesis, Department of Aeronautics and Astronautics, Massachusetts Institute of Technology, Cambridge, Massachusetts, February, 1976.

BIOGRAPHICAL NOTE

The author was born on May 31, 1946 in Ijebu-Ode, Western State of Nigeria. He attended Ijebu-Ode Grammar School, where he obtained the West African School Certificate in 1962 and Higher School Certificate in 1964. In August 1965 he won a scholarship to study aeronautics in the Soviet Union. He got a diploma in Russian Language in June 1966 at Moscow State University. He was then admitted to the Kiev Institute of Civil Aviation Engineers, where he got his Master's degree in Aeronautics in February 1972. He holds the I.C.A.O. (International Civil Aviation Organization) Aircraft Engineer's License.

He joined the department of Aeronautics and Astronautics in September 1972 and since has been engaged in the studies on High Pressure Ratio Transonic Turbines at M.I.T. Gas Turbine Laboratory.